PhD Course in

Mathematical Models for Engineering, Electromagnetics and Nanosciences

XXXVI Cycle

COMPATIBILITY OF IONIC LIQUID ELECTROLYTES TOWARDS LI-ION AND NA-ION ELECTRODES

PhD Candidate
Giovanna Maresca
Curriculum: Materials Science

Supervisor: Dr. Giovanni B. Appetecchi
Advisor: Prof. Sergio Brutti
Tutor: Prof. Maria Assunta Navarra

2021/2023

Table of Contents

1. Introduction

1.1 Electrochemical energy storage

Fossil fuels, i.e., coal, oil, and natural gas, are the most widely used energy resource worldwide [1]. In 2022, the global consumption of primary energy for natural gas, oil, and coal was 26.7%, 31.6%, and 23.5% of the total world energy consumption, respectively (**Figure 1.1**), as published by the Energy Institute (EI) in the "2023 Statistical Review of World Energy". The contribution of fossil fuels will still account for 78% of the energy production in 2040 [2]. Risks related to the fossil fuel production, such as resource depletion, environmental pollution, and political unrest, have led to the emergence of renewable and cleaner energy sources (i.e., wind, solar, and wave) which are to be supported by energy storage systems (ESSs) [3]. In fact, the main drawback related to the renewable energy sources is the discontinuous production, resulting in a considerable difference between demand and production while destabilizing the grid. As a result, efficient, practical technologies include batteries, capacitors, and supercapacitors capable of storing electrical energy for appropriate utilization on or off the electrical grid and have drawn significant attention over the last decade [4]. The ESSs play a determinant role in the harvest and conversion of energy-requiring transportation, power generation, industry, and domestic use [5].

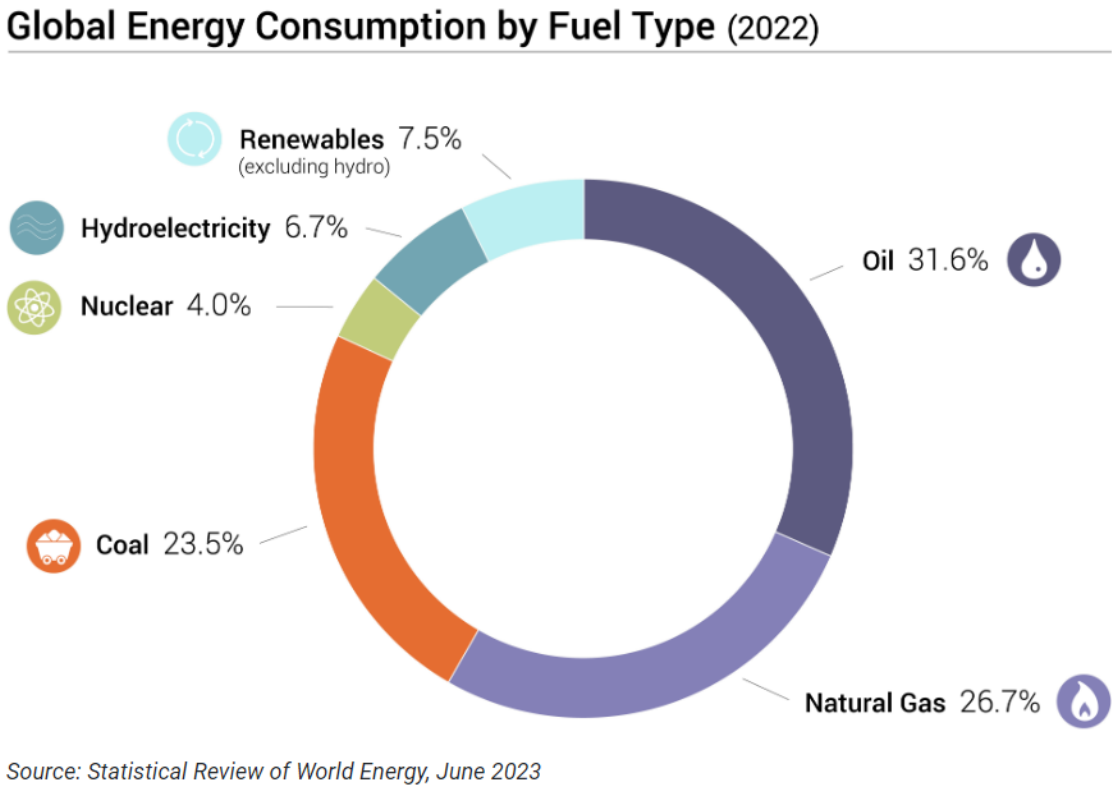

Figure 1.1: World energy consumption by source (2015).

The EESs do offer a well-established approach for improving grid reliability and utilization, and are involved in time dimension, providing electricity when is needed. Energy storage technologies available for large-scale applications can be divided into four types: mechanical, electrical, chemical, and electrochemical [6]. In **Figure 1.2** are illustrated the characteristics of several EESs in terms of power rating, which identifies potential applications, and duration of discharge.

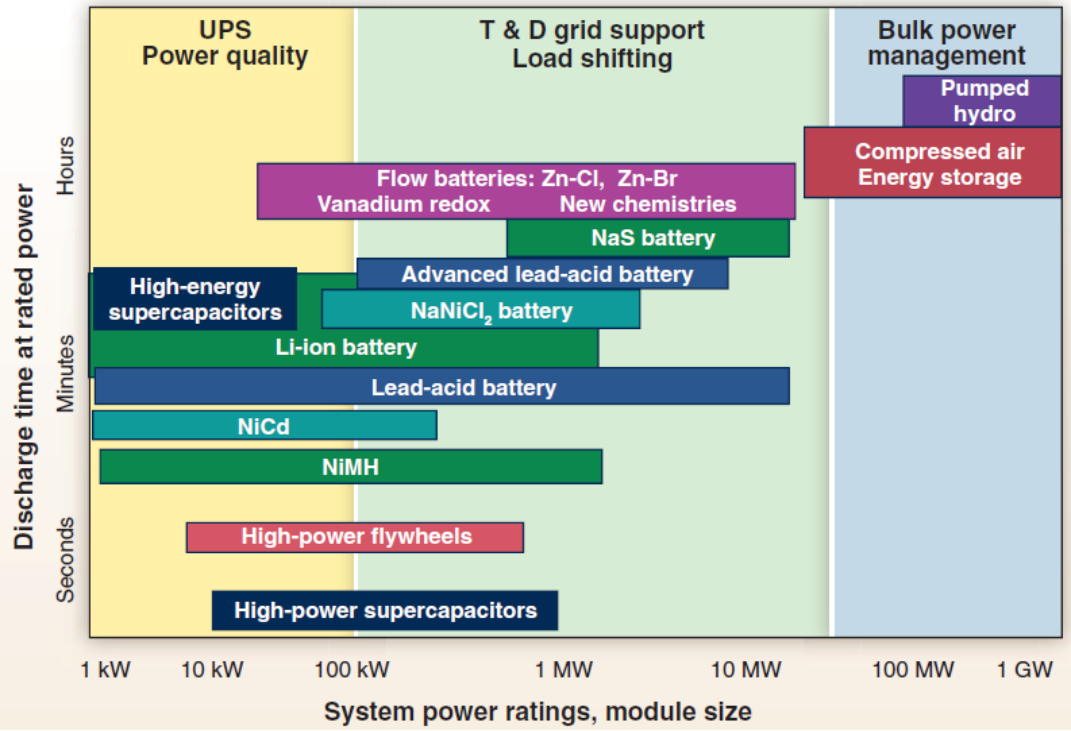

Figure 1.2: Comparison of discharge time and power rating for various EES technologies. The comparisons are of a general nature because several technologies have broader power ratings and longer discharge times than illustrated [3].

The storage can integrate the renewable resources accommodating the peak loads. Load shifting represents one of more attractive opportunities for EESs, because they can store energy when generated in excess and release it at times of larger demand [3]. As shown in **Figure 1.2**, several energy storage technologies are based on batteries. In general, electrochemical energy storage possesses several desirable features, including pollution-free operation, high round-trip efficiency, flexible power, and energy characteristics to meet different grid functions, long cycle life, and low maintenance [3]. Batteries represent an excellent energy storage technology for the integration of renewable resources. Their compact size makes them well suited for use at distributed locations, and they can provide frequency control to reduce variations in local solar output and to mitigate output fluctuations at wind farms.

An electrochemical rechargeable cell converts chemical energy directly into electric energy by means of an electrochemical oxidation-reduction (redox) reaction. A (rechargeable) battery consists

of more electrochemical cells, with external connections for powering electrical devices, connected in series and/or in parallel for providing the required voltage and capacity, respectively [3]. Each cell is composed of a positive (cathode) and a negative (anode) electrode, where the redox reaction takes place, separated by an electrolyte, i.e., usually an organic solution containing dissociated salts enabling ion transfer between the two electrodes. The electrodes are connected externally, allowing the chemical reaction to proceed with the simultaneous liberation of electrons, that provide tapped current by the users [7,8]. The energy storage properties for most of the common rechargeable batteries are shown in **Figure 1.3** [3], with additional details summarized in **Table 1.1** [3].

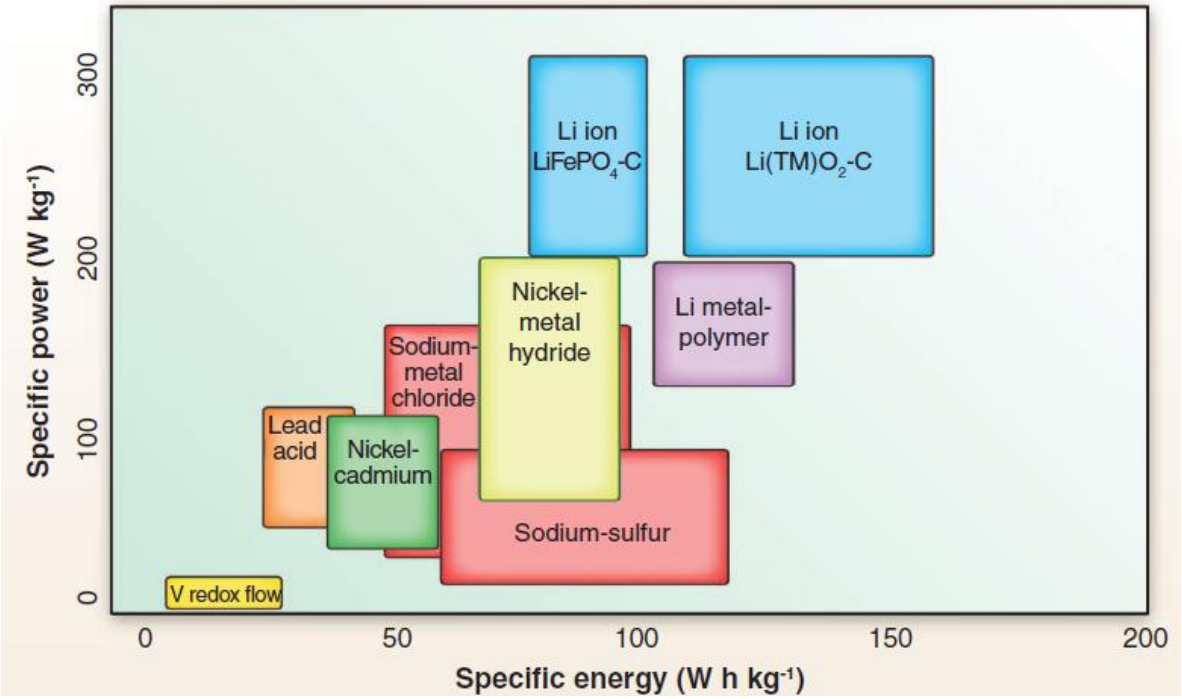

Figure 1.3: Gravimetric power and energy densities for different rechargeable batteries. Most of these systems are currently being investigated for grid storage applications [3].

Table 1.1: Energy and power characteristics for batteries being considered for grid storage applications. The range of values reflects variations associated with battery design and performance.

Battery Type	Voltage Range (V)	Energy Density (Wh/L)	Specific Energy (Wh/kg)	Specific Power (W/kg)	Cycleability
Lead Acid[52]	2.1 - 1.8	60 - 75	30 - 40	60 - 110	100 - 500
Nickel-Cadmium[53,54]	1.3 - 0.8	130 - 150	40 - 60	40 - 100	2000
Nickel-Metal Hydride[55,56]	1.3 - 0.9	250 - 330	70 - 100	70 - 200	1000
Lithium Ion - $Li(TM)O_2$ - C TM = Ni, Co, Mn[52,38]	4.2 - 2.5	200 - 250	120 - 160	200 - 300	300 - 1000
Lithium Ion - $LiFePO_4$ - C[57]	3.5 - 2.5	120 - 150	80 - 90	200 - 300	1500 - 2000
Lithium Metal-Polymer[58,59]	4.0 - 2.4	100 - 110	100 - 110	130 - 170	600
Sodium-Sulfur[60]	2.1 - 1.8	70 - 150	60 - 120	15 - 70	4000
Sodium-Metal Chloride[61]	2.6	20 - 140	50 - 100	30 - 150	3000
Vanadium Redox Flow[62]	1.6 - 1.1	10 - 20	10 - 20	1 - 4	5000

The electrochemical energy systems can be divided by the mechanism use to store energy [9]: *i*) batteries (energy storage through charge transfer reactions; *ii*) redox-flow cells (energy storage in the redox species continuously circulating through the cells); *iii*) supercapacitors (energy storage via a capacitive process arising from an electrochemical double layer at the electrode-electrolyte interface). Supercapacitor are attracting much attention for their higher power density and longer lifetime [10] with respect to batteries [7]. This technology is of interest for power quality applications, and it is expected to be used in conjunction with the batteries themselves to provide future grid storage solutions.

1.2 Li-ion batteries

The Li-ion batteries (LIBs), firstly commercialized in 90's by Sony, are based on the reversible intercalation of the Li^+ species, e.g., the Li ions migrate across the electrolyte sandwiched between the two electrodes as reported in **Figure 1.4**. The anode material is a graphitic carbon able of hosting Li^+ cation between its layers whereas the cathode is a Li-intercalation compound, usually an oxide because of its higher potential that often is characterized by a layered structure. Both electrodes, separated by a non-aqueous electrolyte able of transporting Li^+ ions, are able of reversibly inserting and removing lithium ions into/from their respective structures [11]. On charging, Li^+ cations are removed (deintercalated) from the layered oxide (cathode) and intercalated into the graphite (anode) layers. Electrons are released from the cathode and move towards the anode side through an external electric circuit. During the discharge process, the reverse process occurs. Cell reactions of a typical LIB can be defined as follows:

Charge process:

$$LiCoO_2 \rightarrow Li_{1-x}CoO_2 + xLi^+ + xe^- \quad (1.1)$$

$$xLi^+ + xe^- + C_6 \rightarrow Li_xC_6 \quad (1.2)$$

Discharge process:

$$Li_{1-x}CoO_2 + xLi^+ + xe^- \rightarrow LiCoO_2 \quad (1.3)$$

$$Li_xC_6 \rightarrow xLi^+ + xe- + 6C \quad (1.4)$$

The benefits related to the Li-ion technology lies in its low molecular weight, small ionic radius (promoting its motion through electrolyte and electrodes) and low redox potential ($E°_{(Li+/Li)}$= - 3.04 V vs. standard hydrogen electrode (SHE) [12]). The latter enables high output voltages and, therefore, high energy densities. These favorable properties, coupled with its long cycle life and rate capability, have enabled the Li-ion technology for the portable electronic market and, moreover, for powering the next generation of hybrid (HEVs) and plug-in hybrid (PHEVs) electric vehicles, also considering that further improvements can be achieved in terms of performance, cost, and safety [13].

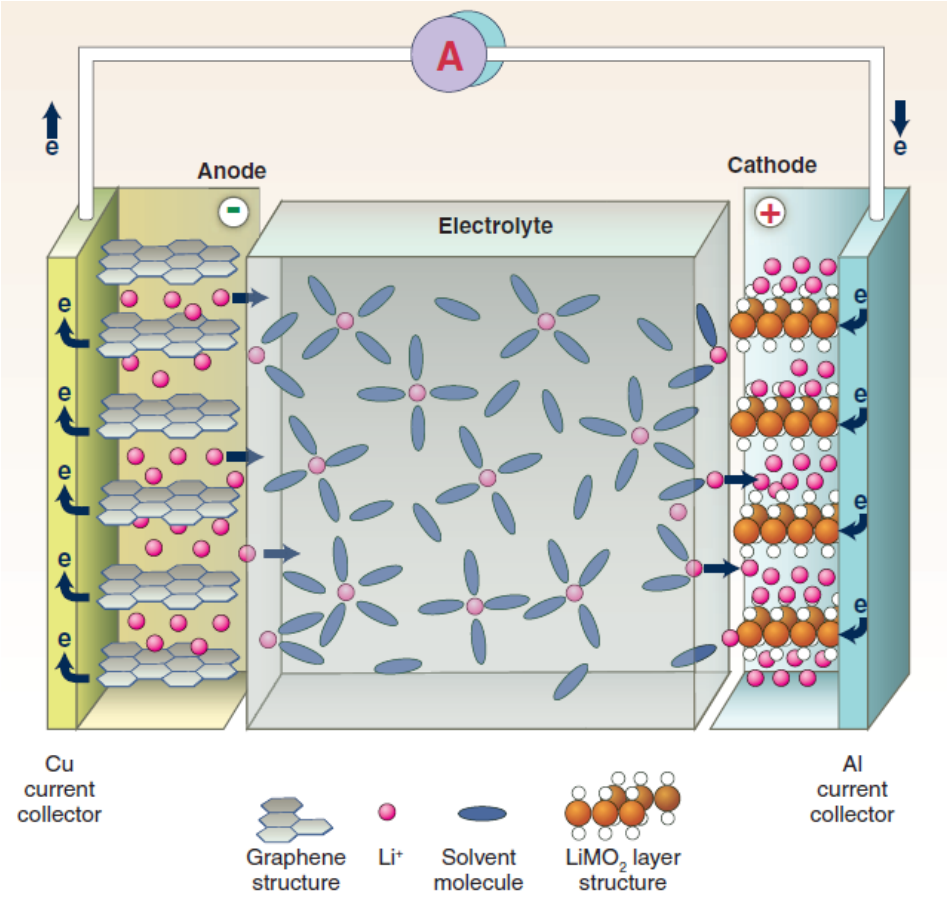

Figure 1.4: Scheme of a LIB system.

Many advances have been made in the LIB field in terms of particle size, composition, structure, and morphology aiming to optimize the electrode/electrolyte components [14]. For instance, an improvement of the electrode material has been achieved using sub-micrometer and smaller sized active materials combined with carbon-coating approach, obtaining core-shell morphologies [15]. Moving from bulk materials to nanosized particles has enabled: *i*) use of new Li reaction mechanisms, such as conversion-reaction electrodes which show enormous capacity gains [16]; *ii*) introduction of anode electrodes based on alloy reactions, such as Tin (Sn) and Silicon (Si)-based materials [17]; *iii*) identification of poorly conducting polyanionic compounds or fluorine-based compounds displaying excellent electrochemical performance [18]; and *iv*) transformation of the poorly conducting lithium iron phosphate ($LiFePO_4$) electrode into the most used electrode material for electric vehicles [19]. $LiFePO_4$ is very attractive for its lower cost, safety, and operating voltage, highly compatible with the thermodynamic stability of the major of electrolytes [3]. Particularly, $LiFePO_4$-based batteries are being evaluated in stationary energy storage systems [3].

Actually, the scientific community is moving towards the development of electrode materials based on abundant and available chemicals, in particular synthesized through ecofriendly processes and containing sustainable 3D metal redox elements such as Manganese (Mn) (lithium-manganese

oxide $LiMn_2O_4$), Iron (Fe) ($LiFePO_4$, Li_2FeSiO_4) and Titanium (Ti) (TiO_2, $Li_4Ti_5O_{12}$) [20]. Also, attention is attracted by low-temperature-solution chemistry routes, i.e., hydro(solvo)thermal, ionothermal, and bio-mineralization processes requiring temperatures > 500°C lower than traditional powder synthesis [21].

1.3 Na-ion batteries

LIBs are currently the most used energy storage technology, but the increasing worldwide energy demand for the large-scale applications is expected to skyrocket the price of lithium, affecting reserves as well, as it is not a naturally abundant element [22]. The overall global consumption was nearly 21280 tons in 2008 and present mineable resources could be sustained for approximately 65 years at a maximum average growth rate of 5% per year [23,24].

Sodium is the fourth most abundant element on the Earth [25], with 23 billion tons of soda located in the United States alone. The high abundance of Na resources and the lower cost related to the production, about $135- 165 per ton for sodium carbonate against about $5000 per ton in 2010 for lithium carbonate, provide a compelling reason for the development of Na-ion batteries (SIBs) [26,27]. The electrochemical mechanism and the battery component of LIBs and SIBs are basically the same, except for their ion carriers, as displayed in **Figure 1.5**.

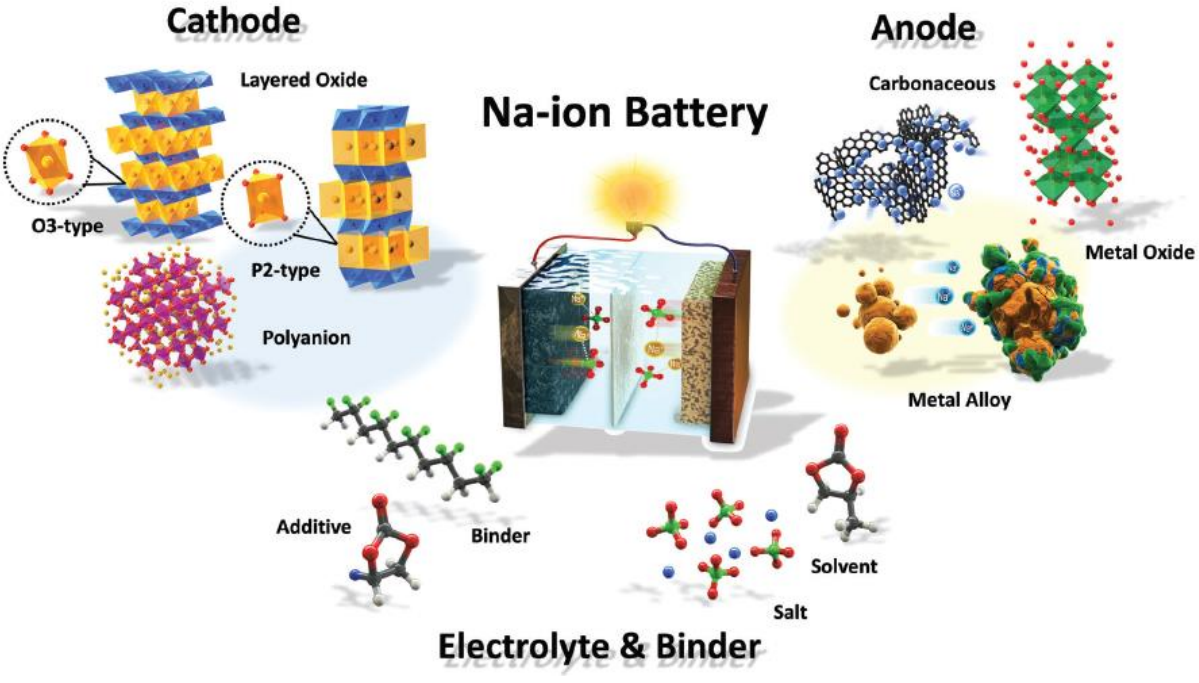

Figure 1.5: Schematic representation on SIBs [22].

The intercalation chemistry of sodium in cathode materials is very similar to that of lithium, making it possible to use similar compounds for both systems [22]. However, even if the knowledge

gained from the Li-ion technology is being transferred to the Na-ion one, new generations of Na-intercalation compounds will be required for the development of sustainable and environmentally benign room-temperature Na-ion cells [28]. For instance, there are some obvious differences between these systems. Na^+ ions (1.02 Å) are larger compared to Li^+ ions (0.76 Å), which affects the phase stability, transport properties, and interphase formation [29]. Sodium is also heavier than lithium (23 g mol^{-1} compared to 6.9 g mol^{-1}) and has a higher standard electrode potential (-2.71 V vs. SHE as compared to -3.02 V vs SHE for lithium); thus, SIBs will always fall short in terms of energy density [22]. However, the weight of cyclable Li or Na is a small fraction of the mass components, and the capacity depends by the characteristics of the electrodes. Hence, there should be no dramatic energy density consequences of the transition from LIBs to SIBs [26]. Moreover, the aluminum can be used as anode current collector in SIBs (no alloy with Na^+ cations), which is a cost-effective alternative to the heavier and more expensive copper [30]. However, significant efforts are still needed for enhancing the capacity value/retention of the electrode materials with high initial coulombic efficiency [30], thus allowing the NIB technology of penetrating into the market. Different types of cathode materials were studied, especially based on intercalation reactions, showing high capacity and good cyclability [22]. These electrode materials can be classified in three main groups: layered oxides, polyanionic materials (phosphates, pyrophosphates, fluorosulfates, oxychlorides), and NASICON (Na super ionic conductor) types, included Prussian blue analogues [22]. These materials show reversible intercalation of Na^+ through minimal structural change, with good cycle life. However, the continuous Na^+ insertion in the host structure leads to structural evolution because of the large Na^+ size (coordination number 6: 1.02 Å) relative to that of Li^+ (coordination number 6: 0.76 Å). In addition, sodiated transition metal materials are highly hygroscopic, even if briefly exposed to external [31], causing formation of NaOH (insulating compound) on its surface that degrades the electrode performances.

In contrast with the wide variety of cathode materials, the sustainable choice is more limited for the anode materials [32]. The search for an anode with appropriate voltage storage, large reversible capacity, and high structural stability remains an obstacle for development of SIBs. Sodium titanium oxides operating via intercalation reactions show low cyclability and alloy-based materials may suffer from practical bottlenecks derived from the large volumetric changes related to their redox operation. Therefore, only intercalation materials, especially the carbon-based ones have proved viability [32]. Graphite, which is common anode material in LIBs, does not properly intercalate Na ions [33,34]. Instead, non-graphitic carbonaceous materials (carbon black [35], pitch-based carbon fiber [35], and hard carbon [36]) allow the insertion of Na ions. Particularly, hard carbons (HCs), generally

synthetized from bio-waste precursor at high temperature [37–39], are considered the "first generation" anode choice for SIB systems.

As well as for lithium batteries, the sodium systems did not consider, till now, Na metal as the anode due to dendrite growth-up, high reactivity, and unstable passive layer observed in the most organic electrolytes. These issues, here just mentioned, are even more problematic than in Li-metal cells [22]. In addition, the low melting point of sodium (97 °C) represents further safety hazards for Na metal cells [40].

1.4 Electrolytes

The electrolyte system, providing the migration of the active species between the two electrodes (in the potential range used for the cell cycling), needs to display several topic peculiarities: *i*) fast ion transport properties (i.e., ionic conductivity above of 10^{-3} S cm^{-1} for LIBs and SIBs); *ii*) electrochemical and thermal stability within the operative voltage (up to 4.5 V) and temperature (from – 20 to 50 °C) of LIBs and SIBs; *iii*) high flash point; *iv*) chemical compatibility with both negative and positive electrode materials. These requirements are well matched by electrolytes composed by an organic solvent mixture (**Figure 1.6**) and a suitable lithium (or sodium) salt containing non-coordinating anions such as hexafluorophosphate (PF_6), perchlorate (ClO_4), tetrafluoroborate (BF_4) or triflate (CF_3SO_3). Low viscosity solvents such as diethylcarbonate (DEC) [41] or dimethyl carbonate (DMC) are combined with high dielectric constant solvent such as ethylene carbonate (EC) [42] or propylene carbonate (PC) [43,44].

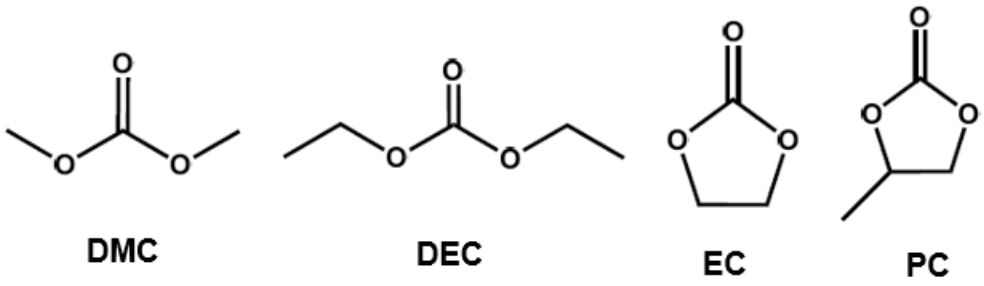

Figure 1.6: Chemical structure of the most common organic solvents for LIB electrolytes.

However, the above cited organic electrolytes suffer of safety concerns, associated with their high flammability and volatility [45]. The major safety drawback is represented by the thermal runaway, which encloses a series of chain exothermic reactions within the battery [45]. This phenomenon can be promoted by mechanical, electrical, and thermal abuse, leading to sharp rise in the internal battery temperature and, consequently, destabilizing the inner battery structure until failure [45]. In order to improve the safety and reliability of LIBs different strategies have been developed such as: *i*) incorporation of a wide variety of additives designed for this specific roles including flame retardant,

overcharge protector, SEI or lithium salt stabilizer etc. [41,46–49]; *ii*) addition of alternative lithium salts to the common $LiPF_6$ to reduce toxicity related to HF formation by hydrolysis [50,51]; *iii*) replacement of the commercial organic solutions with ceramic, polymeric and ionic liquid (IL) electrolytes [52–54].

1.5 Ionic Liquids

The first paper describing an ionic liquid (IL) was published on 1914 by Paul Walden, who observed the special physical properties of ethylammonium nitrate ($[EtNH_3][NO_3]$; m_p= 13 °C, T_d = 250 °C). Ionic liquids are room temperature molten salts, composed of ions only [55], and exhibit weak ion-ion interactions, owing to the combination of large cations with charge-delocalized anions. This results in low tendency to crystallize due to flexibility (mainly anions) and asymmetry (mainly cations) of ions [56,57]. The chemical structure of the most common IL cations and anions for LIBs is reported **in Figure 1.7**: imidazolium, pyridinium, alkylammonium, alkyphosphonium and pyrrolidinium are the most investigated cations whereas halides, BF_4^-, PF_6^-, and/or organic per(fluoroalkylsulfonyl)imide ($TFSI^-$ and FSI^-) are the most interesting anions (which can give hydrophobic or hydrophilic characteristics to the IL [56]). A wide variety of ILs can be obtained by the combining cations and anions, allowing to be properly designed by finely tuning the nature/structure of the anion and/or cations [55–57].

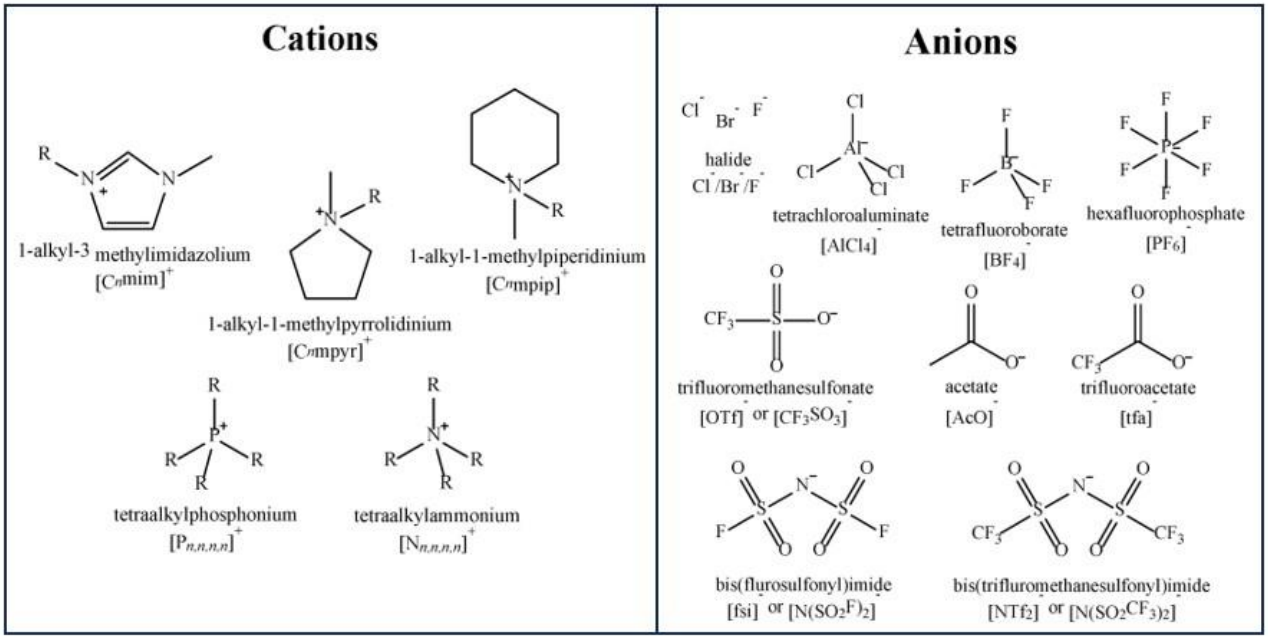

Figure 1.7: Structures of common IL cations and anions for LIBs and SIBs.

The ILs show several appealing physicochemical peculiarities including negligible volatility, flame retardancy, good-high solvent power, very good selectivity, high thermal/chemical/electrochemical

stability, low melting point, high ionic conductivity, high polarity, recyclability [56]. Therefore, they were proposed as innovative fluids for replacing the organic solvents with the aim to enhance the safety and reliability of processes and devices. For instance, ionic liquids are expected to be spread onto a wide range of today's applications at lab and industrial scale, i.e., of green and sustainable chemistry [55–57], synthesis, catalysis, cell biology, material science, physical chemistry, electrochemistry, genetics heredity, nuclear physics, medicinal chemistry, engineering, etc. **Figure 1.8** reports the publication number for ILs by area type [55]. Particularly, their favourable characteristics have been boosting an impressive raise of the publications about the use of ILs as electrolyte components for LIBs [58–60] and, recently, also for SIBs [61–63].

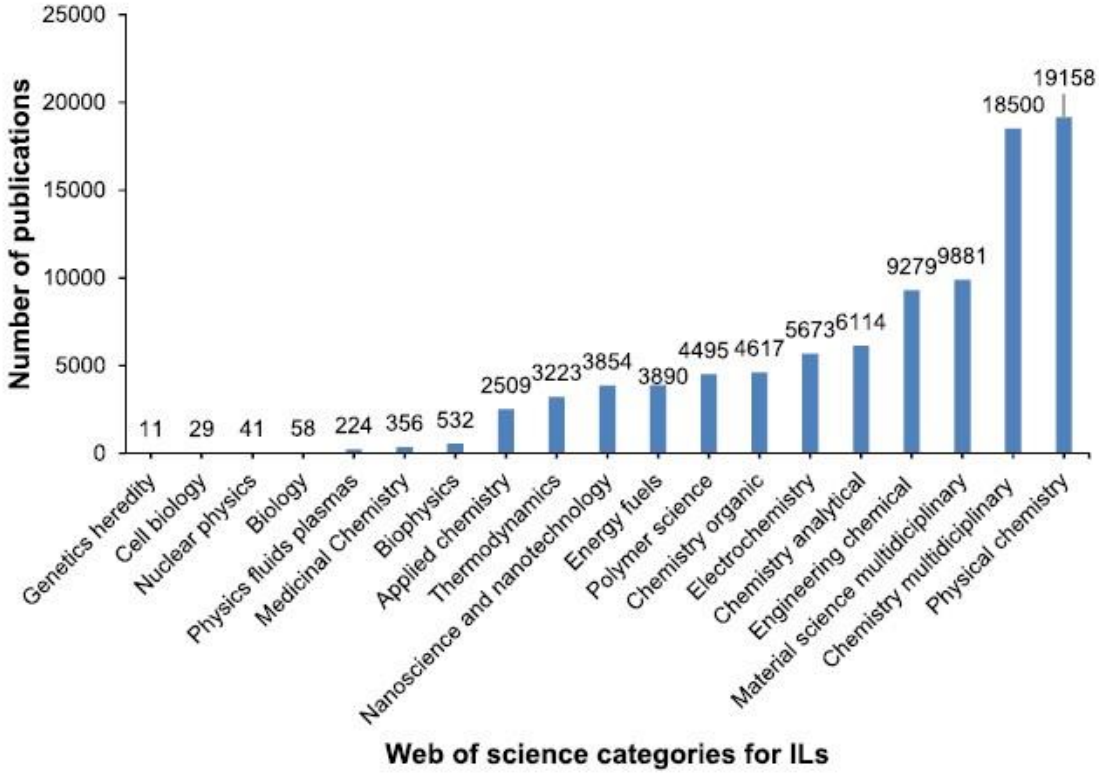

Figure 1.8: Publication number for ILs by area type (Sourced from ISI Web of Science Search) [55].

ILs have attracted growing attention as electrolyte components to replace organic solvents currently used not only for lithium batteries, but also in other electrochemical devices such as fuel cells, double-layer capacitors, hybrid supercapacitors, photoelectrochemical cells, and applications such as electrodeposition of electropositive metals [64–69], resulting in improved safety in case of electric, thermal, and mechanical abuse [58]. These remarkably improved behavior of IL electrolytes with respect to the organic ones were evidenced through flammability and volatility tests, as shown in **Figure 1.9**, where no flammability is observed even upon prolonged exposition to fire [58], and in **Figure 1.10**, where it is evidenced the increasing internal pressure of an organic electrolyte pouch

cell (panel A) due to solvent evaporation while holding the electrochemical device at 100 °C. Conversely, no volume change was exhibited by the IL-containing cell (panel B), which evidences very good vacuum retention [58].

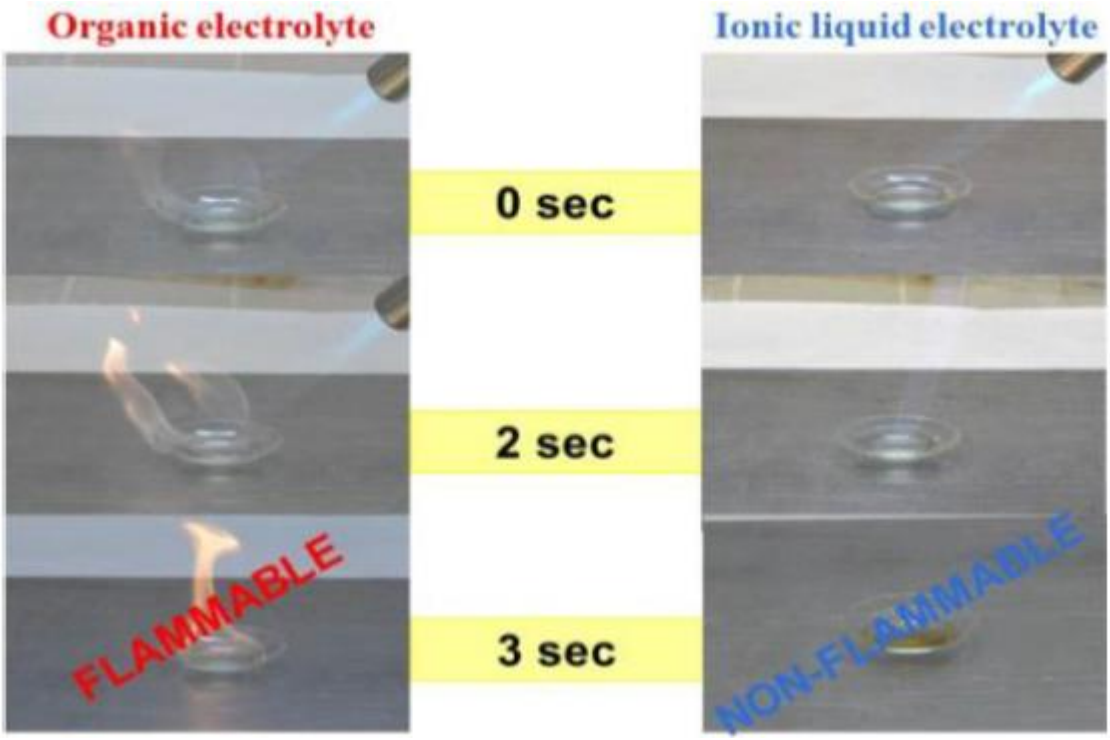

Figure 1.9: Flammability tests performed on organic (left panel) and ionic liquid (right panel) electrolytes [58].

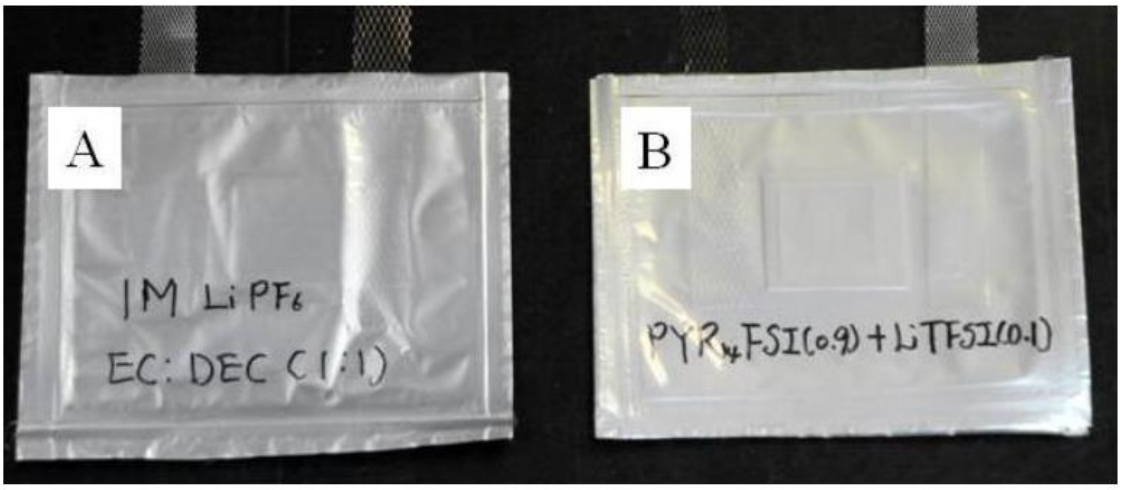

Figure 1.10: Volatility tests performed by heating of vacuum-sealed cells based on organic (panel A) and ionic liquid (right panel B) electrolytes [58].

The requirements which need to be satisfy for ILs to be used as electrolyte components in LIBs are summarized on the followings:

- high ionic conductivity ($\geq 10^{-3}$ S cm^{-1}) even at sub-ambient temperature in order to assure good Li^+ transport properties through the electrolyte;
- wide electrochemical stability (> 4.5 V vs $Li^+/Li°$) to allow Li^+ reversible intercalation even at high voltages without any relevant degradation (oxidation);
- high thermal stability for allowing utilization in high temperature devices;
- no hydrolysis, thus minimizing proton generation;
- hydrophobicity.

Such properties are mainly matched by ionic liquids formed by alkyl-imidazolium, saturated cyclic aliphatic quaternary ammonium as *N*-methyl-*N*-alkylpyrrolidinium (PYR_{1A} where the subscripts indicate the number of carbon atoms in the alkyl side chains) or *N*-methyl-*N*-alkylpiperidinium (PIP_{1A}), tetraalkylammonium (A_4N) cations in combination with hydrophobic perfluoroalkylsulfonylimide anions, e.g., FSI, TFSI, BETI, IM_{14} (where the subscripts indicate the number of carbon atoms in the fluorine-containing side chains) [58], reported in **Figure 1.7**. In **Table 1.1** are summarized the physicochemical properties of most common ILs for LIB.

The bulkiness and asymmetry of cation/anion hinder the crystal packing of the ions giving the room or sub-ambient melting point [59,70,71]. Particularly, highly asymmetric anions as IM_{14} do not allow the ionic liquid material to crystallize even in presence of symmetric cation (PYR_{11}), resulting in a very low melting point, i.e., < -40°C [72]. Also, the introduction of an oxygen atom in the side aliphatic chain was seen to sharply decrease the melting temperature because of enhanced flexibility of the ether group, this interfering with the ion packing [73,74] but affecting the thermal and electrochemical stability of the ionic liquid [72]. Aliphatic quaternary ammonium (or imidazolium) perfluorosulfonylimide ionic liquids show high thermal stability (**Table 1.1**). However, accelerating rate calorimetry measurements, reported by Dahn and co-workers [75], have shown that not all ionic liquids are safer than standard organic solvents used in lithium battery electrolytes. Particularly, imidazolium FSI behaves worse than conventional carbonate-based electrolytes. Otherwise, TFSI ionic liquids have been found to be much safer. The cations with a quasi-planar, two-dimensional structure (i.e., imidazolium species) show higher value of ionic conductivity with respect to the three-dimensional one of tetraalkylammonium cations [59,70,76]) leads to lower viscous drags [72]. Conversely, ionic liquid based on pyrrolidinium and piperidinium cations, having an intermediate structure, exhibit a much wider cathodic stability, e.g., exceeding 5 V, than non-cyclic quaternary ammonium cations [72] and, especially, unsaturated cyclic [74,77] because of the absence of acidic protons and double bounds in the cation ring. However, a molten state conductivity around 10^{-3} S cm^{-1} (or higher) is generally exhibited at room temperature. It is to note how the ionic conductivity is in good relationship with the viscosity values.

Per(fluoroalkylsulfonyl)imides were successfully proposed as anions for lithium battery electrolytes [67,78]. Among them, TFSI was found to be a good compromise because of its high anodic potential stability, good conductivity and thermal stability, hydrophobicity, e.g., acting as non-hydrogen bonding anion [78]. Particularly, McFarlane *et al*. [79–82], Passerini *et al*. [83–85] and Tatsumi *et al*. [74,86] have demonstrated the feasibility of pyrrolidinium TFSI ionic liquids as lithium battery electrolyte components, improving the performance, kinetics, cyclability and long-term stability of the electrochemical device. Comparable behaviour in respect TFSI was displayed by the TSAC anion as reported by Tatsumi *et al*. [86]. A remarkable interest has been progressively attracted by the FSI anion since its reduced steric hindrance guarantees lower viscosity and, therefore, higher conductivity [87,88]. In addition, FSI ionic liquids exhibit remarkably lower melting point than the corresponding TFSI materials, resulting in large ionic conductivity even at sub-ambient temperatures, i.e., 1.3 mS cm^{-1} at -10 °C for $PYR_{14}FSI$ [89]. On the other hand, the FSI anion leads to a reduction of the electrochemical and, especially, thermal stability since the reactivity of the fluorine atoms directly bound to the sulfonyl groups [90,91].

Table 1.1: Physicochemical properties of various lithium battery ionic liquids. Melting point: m. p.; thermal stability: ther. stab.; viscosity: η (from references [72,87,92]).

Ionic Liquid	m.p./°C	Ther. stab. / °C		η / mPa s		σ / mS cm^{-1}		ESW / V
		N_2	Air	20°C	60°C	- 10°C	20°C	20°C
$PYR_{11}TFSI$	131.0	405.1	390.0	solid	solid	$< 10^{-5}$	2×10^{-5}	solid
$PYR_{12}TFSI$	91.8	----	----	solid	solid	$< 10^{-5}$	----	solid
$PYR_{13}TFSI$	11.4	----	----	72	17	$< 10^{-5}$	2.7	5.84
$PYR_{1iso3}TFSI$	6.0	----	----	solid	solid	$< 10^{-5}$	$< 10^{-5}$	Solid
$PYR_{1n4}TFSI$	-6.5	392.2	381.1	95	21	6.2×10^{-4}	1.8	5.83
$PYR_{1iso4}TFSI$	6.0	----	----	----	----	4.0×10^{-4}	2.3	6.09
$PYR_{1sec4}TFSI$	10.1	----	----	79	18	1.5×10^{-5}	1.8	3.61
$PYR_{15}TFSI$	13.6	----	----	103	23	$< 10^{-5}$	1.3	5.91
$PYR_{16}TFSI$	2.2	----	----	125	24	$< 10^{-5}$	1.0	5.95
$PYR_{17}TFSI$	16.7	389.3	373.4	131	28	$< 10^{-5}$	0.8	5.96
$PYR_{18}TFSI$	-13.7	----	----	149	28	7.4×10^{-2}	0.54	5.83
$PYR_{1,10}TFSI$	9.6	----	----	210	37	$< 10^{-5}$	0.33	5.63
$PYR_{1(2O1)}TFSI$	< -40°C	414.8	416.4	71	19	0.47	2.4	4.84
$PYR_{1(2O2)}TFSI$	< -40°C	----	----	62	17	0.41	2.1	4.38
$PIP_{11}TFSI$	127.0	443.5	439.4	solid	solid	$< 10^{-5}$	2.2×10^{-5}	solid
$PIP_{12}TFSI$	89.9	----	----	solid	solid	3.1×10^{-5}	3.7×10^{-4}	solid
$PIP_{13}TFSI$	12.3	----	----	190	33	$< 10^{-5}$	0.92	5.82
$PIP_{14}TFSI$	-10.0	427.8	420.5	240	37	2.4×10^{-4}	0.64	5.80
$PIP_{15}TFSI$	-3.5	----	----	280	41	1.5×10^{-5}	0.54	5.85
$PIP_{16}TFSI$	21.7	----	----	270	39	$< 10^{-5}$	2.0×10^{-4}	5.91
$PIP_{17}TFSI$	6.2	423.6	408.5	330	47	$< 10^{-5}$	0.26	5.89
$PIP_{18}TFSI$	-12.4	----	----	370	52	8.0×10^{-5}	0.22	5.89
$PIP_{23}TFSI$	46.8	----	----	solid	----	$< 10^{-5}$	2.0×10^{-5}	Solid
$PIP_{24}TFSI$	7.5	----	----	275	37	$< 10^{-5}$	0.53	5.00
$PIP_{25}TFSI$	3.7	----	----	285	40	$< 10^{-5}$	0.35	5.06
EMITFSI	-9.7	----	390	36	12	2.4×10^{-3}	4.7	3.98
Et_4NTFSI	103.5	----	----	solid	solid	$< 10^{-5}$	4.3×10^{-5}	solid
$PYR_{11}BETI$	133.3	----	----	solid	solid	$< 10^{-5}$	1.7×10^{-5}	solid
$PYR_{13}BETI$	6.5	----	----	204	34	$< 10^{-5}$	0.53	5.52
$PYR_{14}BETI$	8.9	----	----	348	52	$< 10^{-5}$	0.42	5.68
EMIBETI	-1.3	----	----	98	22	$< 10^{-5}$	2.0	3.72
Et_4NBETI	83.4	----	----	solid	solid	$< 10^{-5}$	1.9×10^{-5}	solid
$PYR_{11}Im_{14}$	< -40°C	----	----	720	97	0.01	0.18	5.39
$PYR_{13}Im_{14}$	< -40°C	----	----	306	54	0.024	0.30	4.79
$PYR_{14}Im_{14}$	< -40°C	----	----	556	65	0.025	0.28	5.51
$EMIIm_{14}$	< -40°C	----	----	150	30	0.15	1.1	3.69
Et_4NIm_{14}	< -40°C	----	----	790	84	4.3×10^{-3}	0.13	5.30
$PYR_{13}FSI$	-13.6	240	240	45	17	0.08	5.6	5.48
$PYR_{14}FSI$	-20.0	230	230	66	21	1.3	4.1	5.50
$PYR_{1(2O2)}FSI$	-26.3	200	200	179	36	1.3	4.1	4.97

1.6 Aim of the thesis

One of the major challenges of LIBs and SIBs is related to safety and reliability, which are mostly connected to the nature of the electrolyte. Commercial organic electrolytes show several critical issues [52–54], therefore different alternatives have been considered, such as polymers, ceramics, and ionic liquids [52–54].

The experimental activities of the present PhD thesis have been structured in five sections: the first one was focused on synthesis, characterization, and selection of IL electrolytes. The other sections were addressed to investigation of compatibility and behaviour of the selected IL electrolytes with LIB (2^{nd} and 3^{rd}sections) and SIB (4^{th} and 5^{th}sections) systems, respectively.

During the first section, different IL families were studied: in particular, imidazolium, tetra-alkyl-ammonium, and piperidinium cations, coupled with bis(perfluroalkylsulfonyl)imide anions, were considered as innovative safety electrolyte components for being addressed to LIB and SIB systems [93–95]. The synthesis purification route is reported in detail and the quality level of the synthetized ILs was validated through X-Ray fluorescence analysis, UV-Vis spectrophotometry and Karl-Fisher titration. The thermal stability of the pure ILs was analyzed by thermogravimetric analysis (TGA) under helium atmosphere, through both temperature heating scan and isothermal steps. Li^+ and Na^+-conducting electrolyte formulations, based on 1-ethyl-3-methyl-imidazolium (EMI), trimethyl-butyl-ammonium (N_{1114}), and N-alkyl-N-methyl-piperidinium (PIP_{n1}) ionic liquid (IL) families were designed and investigated. Lithium bis(trifluoromethylsulfonyl)imide, LiTFSI, and sodium bis(trifluoromethylsulfonyl)imide, NaTFSI, were selected as the salts. The ion transport properties and electrochemical stability have been investigated, analyzing the dependence from the nature of the anion and the cation aliphatic side chain length.

In the second section, LIB silicon nanowire anodes were investigated in lithium metal cells using electrolyte formulations (selected in the frame of the 1^{st} section) based on EMITFSI, EMIFSI and N_{1114}FSI ionic liquids. The lithium insertion process in the silicon anode was analyzed by cyclic voltammetry measurements, performed at different scan rates and for prolonged CV tests, combined with impedance spectroscopy analysis. The electrochemical performances were investigated by galvanostatic charge-discharge cycling tests. X-ray photoelectron spectroscopy (XPS) measurements were carried out onto the silicon nanowire electrode surface to gain knowledge about the SEI (Solid Electrochemical Interface) layer.

In the third section, LIB cobalt-free, lithium-rich, layered oxide $Li_{1.2}Ni_{0.2}Mn_{0.6}O_2$ (LRLO) cathodes were investigated in the selected IL electrolytes. The battery performances, after previous screening of the IL formulations, were evaluated by prolonged galvanostatic charge-discharge cycling

in Li/LRLO cells. The effect of the lithium salt was also assessed. The electrochemical process of Li^+-insertion was analyzed through cyclic voltammetry measurements at increasing scan rates and for prolonged cycles.

In the fourth section, SIB hard carbon (HC) anodes, obtained from natural biowaste, have been investigated in EMIFSI and N_{1114}FSI electrolytes. The Na^+ intercalation process was analyzed by cyclic voltammetry tests, performed at different scan rates for hundreds of cycles, in combination with impedance spectroscopy measurements to decouple bulk and interfacial resistances of the cells. Also, the Na^+ diffusion coefficient in the HC host was determined via the Randles-Sevcik equation. The cell performance was evaluated by room temperature galvanostatic charge/discharge cycling tests. The evolution of the SEI (solid electrochemical interface) layer grown on the HC surface, cycled in different electrolytes, has been studied by Raman spectroscopy, XPS and focused ion beam milling scanning electron microscopy (FIB-SEM) analysis.

In the last section, SIB monocline sodium manganite, α-$NaMnO_2$, cathodes were investigated in EMIFSI and N_{1114}FSI electrolytes. The Na^+ insertion process in α-$NaMnO_2$ was analyzed through cyclic voltammetry tests, carried out at different scan rates, combined with impedance spectroscopy measurements. The cell performance of α-$NaMnO_2$ electrodes was validated by galvanostatic charge-discharge cycling tests whereas the surface composition and the morphology of post-mortem cathodes were analyzed through XPS and FIB-SEM measurements.

My PhD research activities were carried out in the frame of two Projects: *i*) Si-DRIVE (Silicon Alloying Anodes for High Energy Density Batteries comprising Lithium Rich Cathodes and Safe Ionic Liquid based Electrolytes for Enhanced High VoltagE Performance), H2020-NMBP-ST-IND-2018" (Topic LC-NMBP-30-2018) Grant Agreement 814464, founded by the European Union's Horizon 2020; *ii*) National Program (Electric Research System) Agreement (Energy storage systems for electrical network, Activity LA1.7: Ionic liquid electrolytes for sodium batteries) between the Italian Ministry of Ecological Transition and ENEA.

2. Synthesis and Characterization of Ionic Liquids

2.1 Experimental Section

The IL ions were selected based on the proper peculiarities aiming to optimally match the requirements for LIB and SIB systems. Small (or planar) and asymmetric (having alkyl side chains with different length) cations were selected to combine fast ion transport properties and low melting point [58]. Also, the incorporation of hetero atoms into the cation main alkyl side chain was considered as it was seen to improve the transport properties [58]. The anions were selected among the per(fluoroalkylsulfonyl)imide family [58]: in particular, the TFSI anion was chosen for its high thermal and electrochemical stability whereas FSI was selected for its fast ion transport properties, low melting point and good SEI forming ability onto anodes. The asymmetric FTFSI anion was also considered as it is expected of exhibit lower melting point (due to its asymmetric structure) and of combining the properties of TFSI and FSI. It is worth to note that, till now, these ionic liquid families were poorly investigated for being addressed to Si anodes and SIB electrodes. **Figure 2.1** illustrates the chemical structure of the selected ions, and **Table 1.1** summarizes the IL samples designed/synthesized.

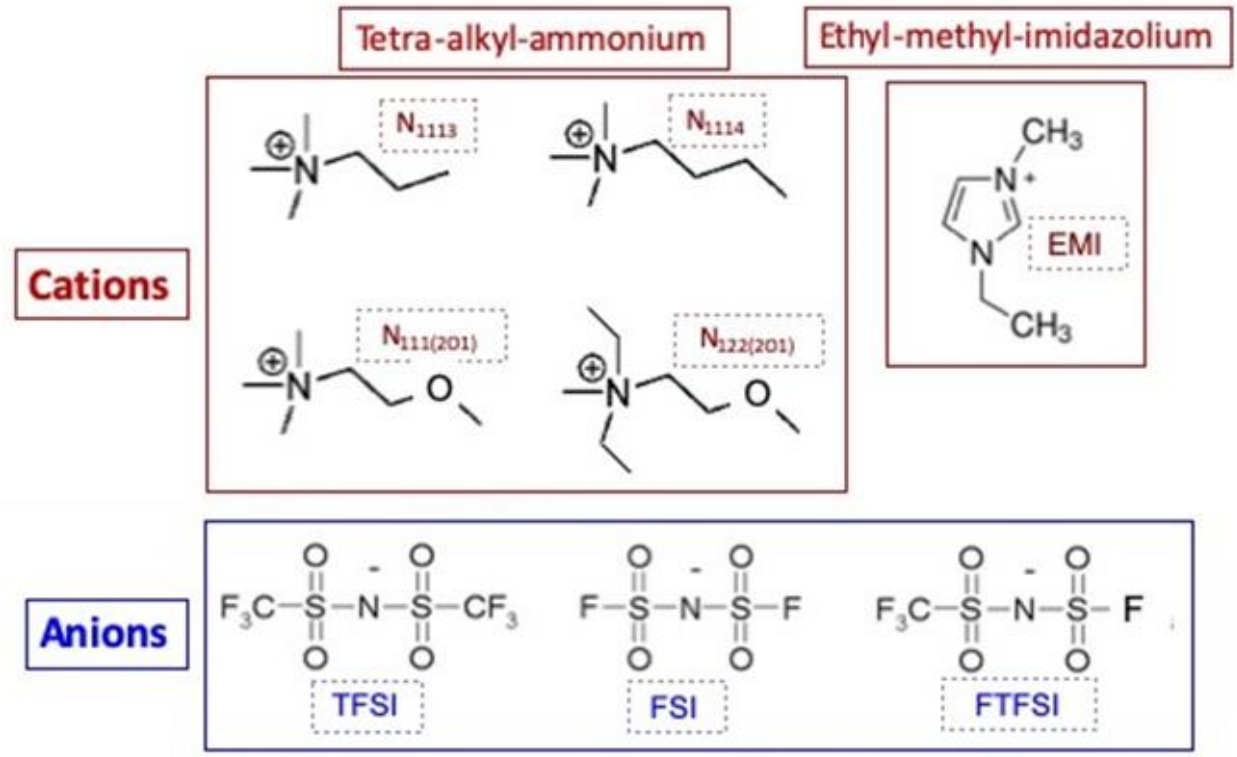

Figure 1.1: Chemical structures of the ionic liquid cations (red upper panels) and anions (blue lower panels).

Table 2.1: Summary of the ionic liquid samples synthesized and investigated.

Acronym	Ionic liquid sample
EMIFSI	1-ethyl-3-methyl-imidazolium bis(fluorosulfonyl)imide
EMITFSI	1-ethyl-3-methyl-imidazolium bis(trifluoromethylsulfonyl)imide
N_{1113}TFSI	*N*-trimethyl-*N*-propyl-ammonium bis(trifluoromethylsulfonyl)imide
N_{1114}FSI	*N*-trimethyl-*N*-butyl-ammonium bis(fluorosulfonyl)imide
N_{1114}TFSI	*N*-trimethyl-*N*-butyl-ammonium bis(trifluoromethylsulfonyl)imide
N_{1114}FTFSI	*N*-trimethyl-*N*-butyl-ammonium (fluorosulfonyl)(trifluoromethylsulfonyl)imide
$N_{1114}IM_{14}$	*N*-trimethyl-*N*-butyl-ammonium(trifluoromethylsulfonyl) (nonafluorobutylsulfonyl) (trifluoromethylsulfonyl)imide
$N_{111(2O1)}$TFSI	*N*-trimethyl-N(2-methoxyethyl)ammoniumbis(trifluoromethylsulfonyl)imide
$N_{122(2O1)}$TFSI	*N*,*N*-diethyl-*N*-methyl-*N*(2methoxyethyl)ammoniumbis(trifluoromethylsulfonyl)imide
$N_{122(2O1)}$FTFSI	*N*,*N*-diethyl-*N*-methyl-*N*(2methoxyethyl)ammonium (fluorosulfonyl)(trifluoromethylsulfonyl)imide
PIP_{13}TFSI	*N*-methyl-*N*-propyl-piperidinium bis(trifluoromethylsulfonyl)imide
PIP_{14}TFSI	*N*-butyl-*N*-methyl-piperidinium bis(trifluoromethylsulfonyl)imide

2.1.1 Materials and Methods

Most of ionic liquids investigated were synthesized/purified through an eco-friendly, sustainable procedure (developed in our laboratories), which uses deionized water as the only processing solvent [96]. The synthesis route was performed through six steps, which are schematized as the followings: *i*) synthesis of precursor (intermediate product); *ii*) purification of precursor; *iii*) anion exchange reaction; *iv*) rinsing of the ionic liquid; *v*) vacuum drying. The N_{1113}TFSI, $N_{111(2O1)}$TFSI and $N_{122(2O1)}$TFSI samples were provided by Solvionic (purity level > 99.9 %) and used as received. The chemicals used for the synthesis of the ionic liquids are summarized in **Table 2.2.**

Table 2.2. Chemicals used for the synthesis of the ionic liquids.

Chemical	Purity / %	Destination
1-methyl-3-imidazole	> 99	Reagent
N-methyl-piperidine	> 99	Reagent
N-trimethyl-*N*-butyl-ammonium bromide	> 98	Reagent
N-diethyl-*N*-methyl-*N*-methoxyethyl-ammonium bromide	> 98	Reagent
Bromoethane	> 99	Reagent
1-Bromo-propane	> 99	Reagent
1-Bromo-butane	> 99	Reagent
Lithium bis(trifluoromethylsulfonyl)imide	> 99.9	Reagent
Sodium bis(fluorosulfonyl)imide	99.7	Reagent
Acid (trifluoromethylsulfonyl)(nonafluorobutylsulfonyl)imide	> 99	Reagent
Activated carbon	n. a.	Sorbent material
Deionized water	100	Solvent

2.1.2 Synthesis/Purification of ionic liquids

i) Synthesis of precursors

The IL precursor was prepared by reacting 1-methyl-3-imidazole (or *N*-methyl-*N*-piperidine) with the proper amount of alkyl-halide (generally bromide, which represents an optimal compromise among reaction kinetics, chemical stability, and cost [96]) as schematized in **Figure 2.2**.

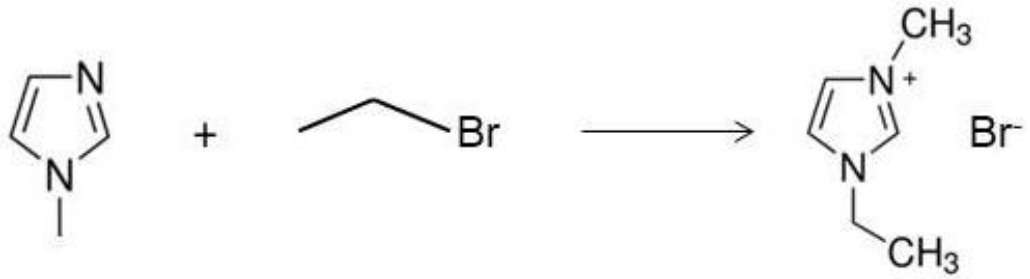

Figure 2.2: Scheme of the reaction for synthesizing the 1-ethyl-3-methyl-imidazolium bromide precursor starting from 1-methyl-3-ethyl-imidazole and bromoethane.

The amines, used in slight excess (≤ 1 wt.%) with respect to the stoichiometric amount to increase the reaction yield and minimize the halide impurities in the ionic liquid [96], was diluted in deionized water (1:1 volume ratio) and loaded into a glass reactor. Then, the alkyl bromide was loaded within the reactor: conversely to the amines, this chemical is immiscible with water and formation of two separated phases was observed (i.e., the lower phase is constituted by the alkyl bromide as its higher density than the water/amine solution).

Successively, the chemicals were stirred at 70 °C until full disappearance of the second phase (i.e., the precursor, progressively formed during the reaction schematized in Figure 2.2, is soluble in water), generally observed after 30-60 minutes. A yellowish concentrated aqueous solution of precursor was obtained with a yield approaching 100 % in mole.

ii) purification of precursors

The aqueous precursor solution (**Figure 2.3A**), obtained from step (*i*) was treated with activated charcoal (AC) to remove contaminants (coming from the chemicals). Analogously, the *N*-trimethyl-*N*-butyl-ammonium bromide and *N*-diethyl-*N*-methyl-*N*-methoxyethyl-ammonium bromide precursors (provided by Solvionic) were dissolved in deionized water. A proper AC amount (previously purified through water rinsing) was loaded (precursor: carbon weight ratio = 2:1) into the glass reactor. The resulting slurry, further diluted with deionized water to reduce the viscosity, was stirred for three hours at room temperature [8]. The solid fraction (AC) was separated from the liquid one (aqueous solution of precursor) by vacuum (oil-free pump, < 1 mTorr) filtration (polyamide filter

membranes with porosity < 0.2 μm) of the slurry. The liquid fraction (clear and colorless) was separately collected for the synthesis of the ionic liquid.

The solid fraction was rinsed in situ with deionized water in order to recover the precursor fraction (i.e., about 30 % of the overall amount) trapped through the sorbents. A water: sorbent weight ratio equal to 2:1 allows of fully recovering the precursor without any impurities release from the carbon [10]. Finally, the liquid phase from rinsing, constituted by a clear and colorless diluted aqueous solution of purified precursor, was combined with the liquid fraction (**FigureB**) obtained upon vacuum filtration.

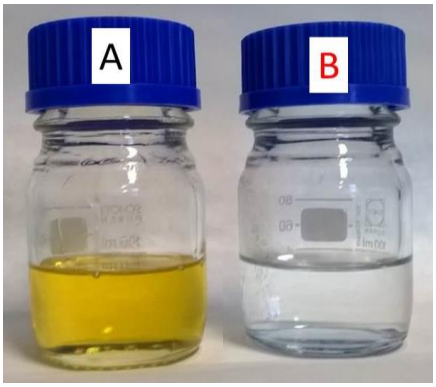

Figure 2.3: Aqueous solution of the 1-ethyl-3-methyl-imidazolium bromide precursor before (panel A) and after (panel B) purification route.

iii) Anion exchange reaction

The lithium bis(trifluoromethylsulfonyl)imide (LiTFSI) or sodium bis(fluorosulfonyl)imide (NaFSI) or (trifluoromethylsulfonyl)(fluorosulfonyl)imide (LiFTFSI) salt, previously dissolved in the minimal (deionized) water amount, was added (into the glass reactor) to the aqueous precursor solution coming from the purification step. The acid (trifluoromethylsulfonyl)(nonafluorobutyl sulfonyl)imide (HIM_{14}), provided as a 60 wt.% water solution, was directly loaded into the reactor. The precursor:LiTFSI (or NaFSI or LiFTFSI or HIM_{14}) mole ratio is equal to 1:1. However, the lithium (or sodium) salts and the HIM_{14} acid were used in slight excess (2-3 wt.%) to enhance the yield of the anion exchange reaction [8]. The ionic liquid was obtained through the reaction schematized in **Figure 2.4**.

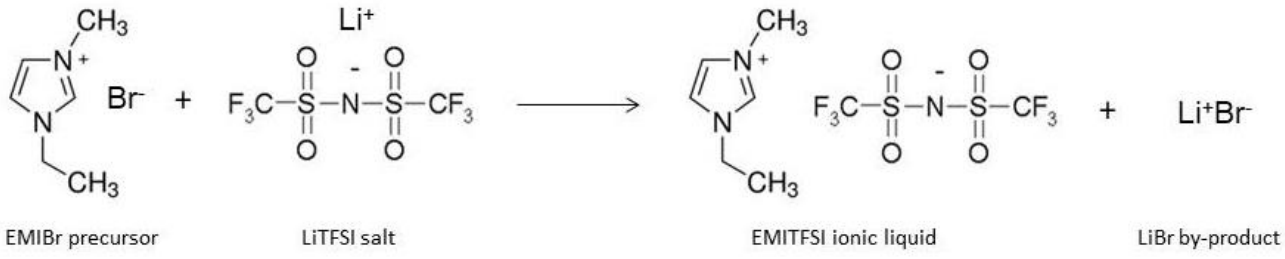

Figure 2.4: Scheme of anion exchange reaction for obtaining the EMITFSI ionic liquid starting from the EMIBr precursor and the LiTFSI salt.

Formation of hydrophobic ionic liquid, insoluble in water, was quickly observed. The solution was stirred for 1 h at room temperature and then, kept in rest at 5 °C to reduce the dissolution of the ionic liquid in the aqueous phase [96]. After 30 minutes, complete phase separation took place. The upper phase (clear and colorless), mainly constituted by an aqueous solution of LiBr (or NaBr or HBr) as the by-product of the anion exchange reaction, was separated from the lower one by vacuum aspiration. Conversely, the lower phase (colorless and slightly cloudy) is mainly formed by the ionic liquid, and very small amount of LiBr (or NaBr or HBr) and LiTFSI (or NaFSI or LiFTFSI or HIM_{14}).

iv) Rinsing of the ionic liquid

The ionic liquid obtained from the anion exchange reaction (*iii*) contains contaminants as halides and Li^+ (or Na^+), which must be carefully removed. Halides are rather unwelcome because, oxidizing to halogens, reduce the electrochemical stability window of the ionic liquid. Therefore, the ionic liquid phase, after removal of the aqueous phase, was subjected to consecutive rinsing steps with deionized water [96]. The H_2O:ionic liquid mixture (volume ratio = 1:1 in each rinsing step) was intimately mixed by magnetic stirring for 10 minutes at room temperature.

After decanting (in a refrigerator at 4-5 °C for 30 minutes), the aqueous phase was removed by vacuum aspiration. The rinsing steps was repeated until the disappearance of halides in the aqueous phase, checked by means of a 0.1 N solution of $AgNO_3$ and, eventually, highlighted by a pale-yellow solid precipitate due to AgX (highly insoluble in H_2O). Briefly, 1.0 ml of the aqueous phase was added to 1.0 ml of $AgNO_3$ solution and was centrifuged for a few minutes for better highlighting any AgX formation. No halide content was detected upon six rinsing steps. Finally, the ionic liquid was filtered under vacuum (polyamide membrane with porosity < 0.2 μm) in order to remove any finer solid particles.

v) Vacuum drying

The ionic liquid as obtained from step (iv) was vacuum dried in a rotary evaporator at 90 °C for 2-3 hours to massively remove the water content. The final drying step was carried out at 20°C for 1 hour, then at 60°C for 1 hour and finally at 120°C for additional 18 hours. **Figure 2.5** depicts a picture of a few samples of the synthesized ionic liquids.

Recovery of the ionic liquid

The ionic liquid, even if insoluble in water, undergoes a very modest dissolution (about 6 % of the overall amount) in the aqueous phase [96] due to the presence of LiBr (or NaBr or HBr) and LiTFSI (or NaFSI or LiFTFSI or HIM_{14}) excess in the aqueous phase. The Li^+ (or Na^+ or H_3O^+) cations interact with the TFSI (or FSI or FTFSI) anions, thus increasing the *ionic force* of the water solution. The ionic liquid losses are mainly localized in the anion exchange reaction instead in the rinsing step.

Therefore, the possibility to recover the IL fraction through adequate treatment of the aqueous phase (coming from the anion exchange reaction and from the rinsing steps) was studied.

The aqueous solvent was removed (and recovered) by vacuum distillation carried out, at laboratory scale, in a rotary evaporator at 90 °C for 3 h. A suspension composed by the ionic liquid and a white solid precipitate of LiX (or NaX) and LiTFSI (or NaFSI or LiFTFSI) was obtained. The lithium (or sodium) salts dispersed in the solid phase were removed (from the ionic liquid) by vacuum filtration (using a Teflon filter with porosity lower than 0.2 μm). Then, the ionic liquid was subjected to consecutive rinsing steps (stirring for 10 minutes at room temperature each one) through deionized water (H_2O:ionic liquid volume ratio = 1:1) for removing the salt fraction still dissolved. The presence of halide in the aqueous phases (removed by vacuum suction) was checked by 0.1 N $AgNO_3$. Upon six consecutive rinsing steps, no presence of halide was detected. This procedure allowed for almost full recovery of the fraction of ionic liquid dissolved in aqueous phase.

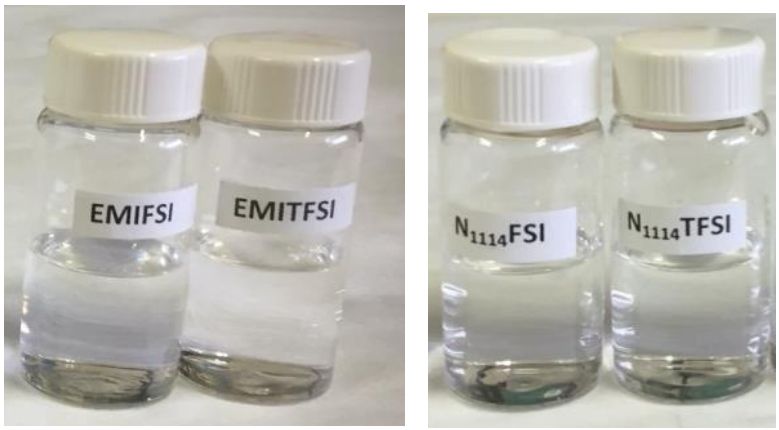

Figure 2.5: Ionic liquid samples synthesized in the present work.

2.1.3 Quality control

The synthesized ionic liquids were subjected to quality control, i.e., through X-ray fluorescence, UV-Vis spectrophotometry and Karl-Fisher titration, to check the purity level of the prepared samples.

i) X-ray fluorescence

The halide content was determined by X-ray fluorescence spectroscopic measurements performed (at room temperature) using an EDX-720 Shimadzu energy dispersion spectrometer. A rhodium foil was used as an X-ray source, which operates at an energy level of 15 (for elements from sodium to titanium) or 50 (titanium to uranium) kV. The sample under investigation was housed in a cylindrical cuvette (made in polypropylene) closed at one end by a polyester Mylar circular window (10 mm in diameter and 6 μm in thickness), which (blocked by a suitable ring) can be crossed by radiation. Care was taken in housing the IL sample in order of compactly and uniformly covering the window.

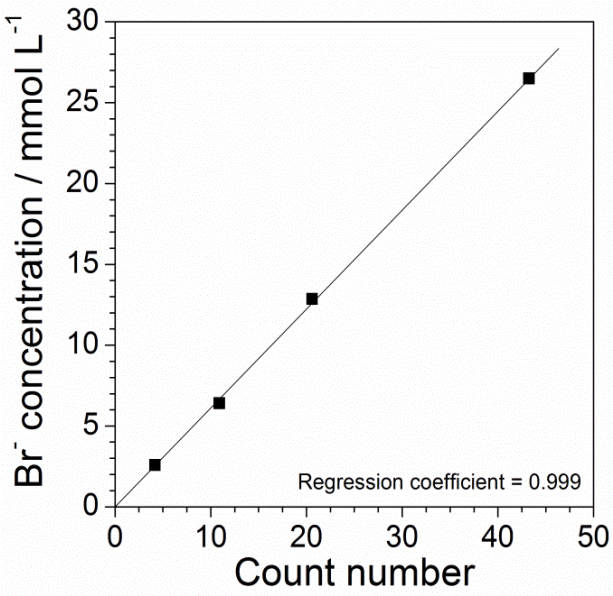

Figure 2.6: Scheme of the Br concentration vs count number dependence obtained from KBr solutions by X-ray fluorescence measurements at room temperature. The error bars fall within the data markers.

Before running the measurements on the IL samples, a calibration curve (**Figure 2.6**) was built to establish the correlation between the count number (given by the equipment) and the halide concentration. For bromides, aqueous solutions of potassium bromide (> 99.4%) at different Br^- concentrations (expressed in 10^{-3} mole L^{-1}) were used, which were subjected to X-ray fluorescence measurements. The Br^- concentration (corresponding to that of the KBr solutions) was reported as a function of the number of counts recorded during the execution of the measurements, obtaining a linear dependence (regression coefficient equal to 0.999 and absolute error equal to 0.005) represented from the equation:

$$y = 0.613x \quad (1)$$

where *y* represents the concentration of the anion Br- and *x* is the number of counts recorded by the instrument. Therefore, the bromide content in the ionic liquid samples was determined (based on the number of counts detected during the X-ray fluorescence measurement) using the equation (1).

ii) UV-Vis spectrophotometry

The overall purity level of the IL samples was checked by UV-Vis spectrophotometry, i.e., an analytical technique based on the interaction between the sample and electromagnetic radiation having a wavelength of 200-400 nm (ultraviolet radiation, UV) and 400-800 nm (visible radiation, Vis). The concentration (C) of each compound, present in the sample, is determined by the Lambert-Beer law:

$$A = \varepsilon l C \quad (2)$$

where A represents the absorbance, ε the molar extinction coefficient and l the optical path in the sample under test.

The investigated ionic liquids were previously diluted in absolute ethanol (> 99.5%) in a volumetric ratio (ionic liquid: ethanol) equal to 1: 5, so that the absorbance values did not exceed the full-scale value of the instrument. No interference on absorbance values was due to ethanol. The measurements were carried out, at room temperature, using a UV-1800 Shimadzu spectrophotometer in a wavelength range between 700 and 190 nm. The samples to be investigated (diluted in ethanol) were housed inside a quartz cuvette (with an optical path equal to 10 mm). The reference cuvette (identical to the one containing the sample under examination) was filled with pure ethanol. The spectrophotometer is able to subtract the absorbance due to ethanol from the alcoholic solution containing the ionic liquid.

iii) Karl-Fisher titration

The moisture content of the ILs was measured through the standard Karl Fisher titration, performed in a dry room (moisture level below 10 ppm) for avoiding contamination from the external, by an automatic Mettler Toledo DL32 coulometer titrator at 20°C. A sample amount (previously weighed by analytical balance) equal to about 0.5 grams is introduced into the titrant solution. The humidity value is calculated by the instrument after about twenty seconds from the introduction of the investigated ionic liquid. For correctly determining the moisture content (to avoid underestimation), the ionic liquid must be soluble in the titrant solution (based on methanol) and the water (contained in it) must be released easily from the sample (absence of strong interactions between ionic liquid and H_2O) in order to be quickly and fully available for titration.

2.1.4 Thermal stability

The thermal stability of the ionic liquids was studied by thermo-gravimetrical analysis (TGA) conducted by both variable-temperature ramps and isothermal treatments. The latter approach gives more reliable results, especially under prolonged heating time periods [58]. However, especially in case of samples with unknown thermal stability, a preliminary heating scan is mandatory in order to define, even roughly, the degradation temperature range.

The TGA measurements were carried out, by means of a Setaram Setsys Evolution 1200 TGA system, under helium atmosphere with a flux of 60 ml min^{-1}. Two different kinds of experiment were performed on each investigated IL sample: *i*) temperature heating scan, at a temperature rate of 10 °C min^{-1}, up to 700 °C; *ii*) isothermal steps at subsequent increasing temperatures. For the first type of measurements, an initial mass of about 20 mg was housed is an alumina pan before to be introduced

into the calorimeter whereas for the second one about 60 mg were loaded in the crucible. A very fast ramp (40 °C min^{-1}) was set up for adjusting the temperature step by step, i.e., the time associated to the temperature ramp between two consecutive (temperature) steps, differing in about 25 °C, is extremely short (just a few seconds). The TGA measurements have been repeated, on each IL electrolyte sample, at least twice to verify the reproducibility of the results. Each sample was previously vacuum dried at temperatures up to 120 °C for at least 24 hours in a vacuum better than 10^{-3} mbar before TGA experiments to remove undesired water, eventually absorbed during handling.

2.1.5 Ion transport properties

The ion transport properties of the ionic liquids (ILs) and their mixtures with the lithium and sodium salts were investigated in terms of ionic conductivity vs temperature dependence. The conductivity measurements were carried out in a wide temperature range, i.e., from − 40 to 80 °C, at a very slow heating scan rate (<1 °C h^{-1}) for better evidencing the phase transitions [58]. A conductivity-meter AMEL 160, allowing to run impedance measurements at a fixed frequency (i.e., 1 Hz or 1 kHz, depending on the conduction value of the sample under test) was used whereas the temperature control was allowed by a climatic test chamber (Binder GmbH MK53). The electrolytes (handled in the dry room) were housed in sealed glass conductivity cells (AMEL 192/K1) equipped with two porous platinum electrodes (i.e., the cell constant was determined through a 0.1 N KCl aqueous solution having an exactly known conductivity value). The samples solid at room temperature were molten before being placed into the conductivity cells. To fully crystallize the materials, the cells were dipped in liquid nitrogen for 60 s and then, quickly transferred into the climatic chamber at – 40 °C. This route was repeated until the frozen ionic liquid samples remained solid at − 40 °C. In previous work, it was demonstrated that the incomplete crystallization of ILs may result in pseudo-equilibrium (metastable) states affecting both their thermal and the transport properties [85]. However, a few ILs did always turn liquid as they exhibit a melting point below – 40 °C and/or no crystallization process [58]. Finally, the cells were kept at – 40 °C for at least 18 h prior starting the conductivity measurements.

2.1.6 Electrochemical stability

Lithium-conducting IL electrolytes

The electrochemical stability of the 0.2LiTFSI-0.8IL electrolytes was investigated using carbon working electrodes for better simulating the situation in battery cells [18]. The working electrodes were prepared blending 70 wt.% Super C45 (IMERYS) and 30 wt.% Na-carboxymethylcellulose (CMC, Dow Wolff Cellulosic) in water. The so-obtained slurry was cast onto aluminum (for anodic sweep voltammetry) foils (30 μm thick). The coatings were initially dried in ambient air and, then,

under vacuum at 150 °C overnight. Finally, disk electrodes of 10 mm diameter (corresponding to a geometrical area of 0.78 cm^2) were punched.

The positive electrode disks were housed, together with a lithium disk (10 mm diameter) and a Celgard 2325 separator (19 mm diameter), within El-Cell ECC-std containers. Cell manufacturing was performed in an argon filled glove box (moisture and oxygen content below 1 ppm). While assembling the cells, the selected 0.2LiTFSI-0.8IL electrolyte was spread (5 μL) onto the positive electrode before matching with the separator to facilitate its adhesion. A further amount of electrolyte (25 μL) was then dropped onto the separator. To secure a deep penetration of the viscous electrolytes into the separator pores, the wet positive electrode-separator assemblies were subjected to a vacuum step for 30 min. Finally, the cells were sealed using polyethylene O-ring and transferred into a climatic chamber kept at constant temperature (i.e., 30 °C) for the electrochemical tests.

Cyclic voltammetry (CV) tests were carried out on each 0.2LiTFSI- 0.8IL electrolyte to determine the anodic electrochemical stability limit. Additional CV measurements were run also on bare Al working electrodes for selected 0.2LiTFSI-0.8IL electrolytes to better evaluate eventual dissolution phenomena of the aluminum substrate at high voltages. The electrochemical cells have been stored in a climatic chamber at 30.0 (± 0.1) °C and tested at this temperature. The measurements were carried out scanning (1 mV s^{-1}) the cell voltage from the open circuit voltage (OCV) value towards more positive voltages and, successively, running consecutive CVs between the OCV value (vs Li/Li^+) and 5.0 V. Clean electrodes and fresh cells were used for each test which was run, using an Ivium Vertex electrochemical testing station, at least twice on different fresh cells to confirm the reproducibility of the results.

Sodium-conducting IL electrolytes

The electrochemical stability window was investigated by voltammetry analysis on Na metal cells, which were prepared using two-electrode Swagelok cells (diameter = 10 mm). Two glass fiber (Whatman™, Maidstone, UK) disk separators, soaked with a 0.1$NaClO_4$-0.9IL electrolyte solution, were placed between a Na metal (American Elements, Los Angeles, CA, USA) coin and a Pt° (Merck KGaA, Darmstadt, Germany), carbon or HC working electrode. Before sealing, the cells were subjected to a vacuum for 30 min to allow full loading of the working electrode and separator by the viscous IL electrolyte.

A preliminary study on anodic stability was conducted by linear sweep voltammetry (LSV) on Na cells, using Pt as the working electrode to define the anodic voltage cut-off (i.e., 4.6 V), which was applied as the benchmark. The LSV was run from the open circuit voltage (OCV) towards more positive voltage values at a scan rate of 1 mV s^{-1}. Then, cyclic voltammetry (CV) tests were run using

carbon-based (Super C45) working electrodes which allow much better simulation of the operative conditions in practical devices. The CV measurements were carried out by consecutively scanning the cell voltage between the OCV value and 4.6 V at a scan rate of 1 mV s^{-1}. The cathodic stability was investigated by CV analysis using HC as the working electrode by consecutively scanning the cell voltage between the OCV value and 0.01 V at a scan rate of 0.05 mV s^{-1}.

2.2 Results and Discussions

2.2.1 Preparation of lithium and sodium IL electrolytes

The synthesis route described in the previous paragraph (2.1.2) allowed the preparation of transparent, uncolored, and odorless ionic liquid samples, which were investigated also in the presence of lithium (LiTFSI) and sodium (NaTFSI) salts. The binary LiTFSI/IL and NaTFSI/IL were prepared by dissolving (magnetic stirring) the proper amount of lithium/ sodium salt in the ionic liquid at room temperature. The LiTFSI/IL mole ratio was fixed to 0.2:0.8, while for NaTFSI/IL was equal to 0.1:0.9. The formulation (in terms of mole ratio) of Li and Na binary electrolytes were chosen on the basis of the salt solubility in the IL medium. For instance, preliminary solubility tests have shown NaTFSI is fully soluble in the selected ionic liquids only up a mole fraction equal to 0.1.

2.2.2 Quality control

i) Halide content determination

The results obtained from the X-ray fluorescence investigation are reported as counter number vs applied energy (keV) trace. **Figure 2.7** plots, as an example, the diagram related to the N_{1114}TFSI ionic liquid before (blue trace) and after (red trace) rinsing through deionized water. The presence of bromide in the IL sample as obtained from the anion exchange is clearly evidenced by two sharp features, located around 13.5 keV and (in particular) 12 keV, which are seen to fully disappear (red trace) after the rinsing process. No count was detected by the instrument, i.e., the count number was below its detection limit, and, based on the equation (1), the bromide content was found to be below 5 ppm. All investigated IL samples have exhibited a halide (Br^- or I^-) content < 5 ppm, this confirming the high efficiency of the rinsing route.

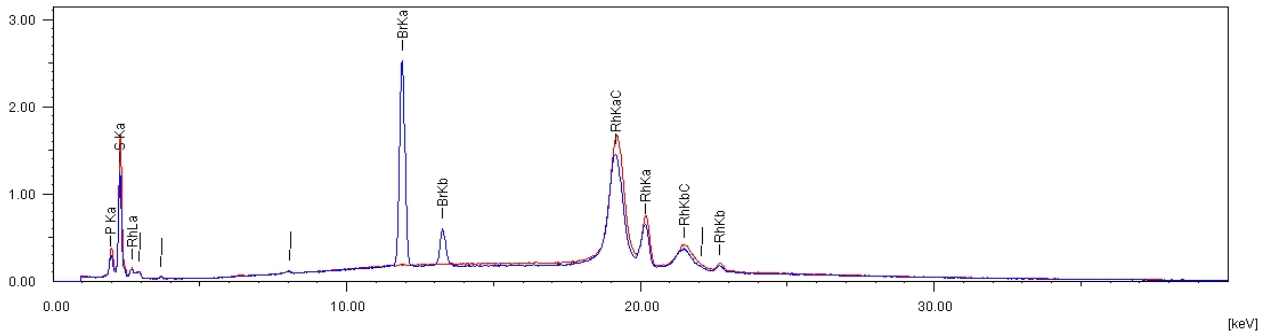

Figure 2.7: X-ray fluorescence (counter number vs energy) trace of the N_{1114}TFSI ionic liquid sample before (blue trace) and after (red trace) rinsing through deionized water [97].

ii) Overall purity level

The absorbance vs wavelength response obtained from UV-Vis measurements is characterized by various features, which are ascribable to the different impurities within the IL sample. **Figure 2.8**

reports, as an example, the absorbance vs wavelength dependence for N_{1114}TFSI (previously diluted in ethanol). In particular, the area value (error bar equal to 5%) comprised between each UV-Vis plot, recorded in the 260–600 nm range, and the X axis (i.e., reporting the wavelength number) is directly proportional to the overall amount of impurities contained in the volume of the diluted IL sample (subjected to the spectrophotometric measurement) and, therefore, to the contaminant content in the pristine ionic liquid. This correlation was previously demonstrated by plotting the impurities concentration in the IL samples *vs*. the area value delimited (in the 260–600 nm range) by the absorbance curves obtained for ethanol: IL mixtures at different volume ratios (from 20:1 to 5000:1). The results, reported in **Figure 2.9**, show a linear relationship up to an impurity content of 60 mg per liter of ionic liquid.

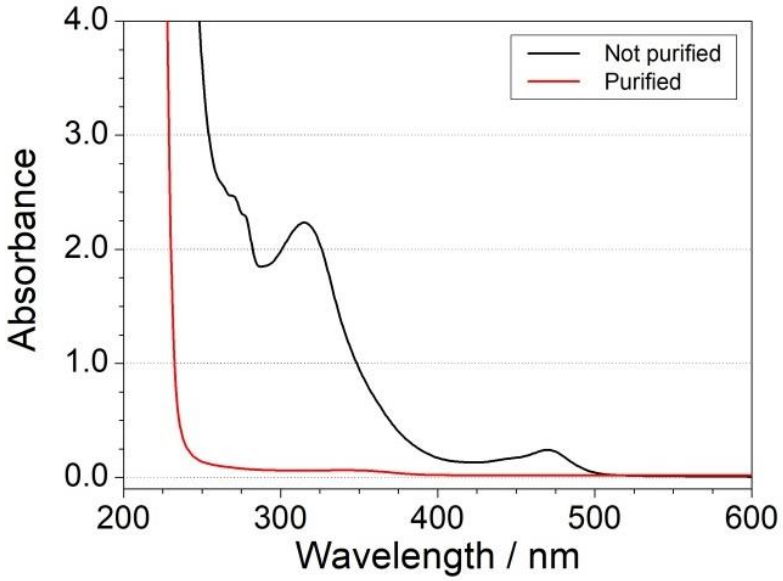

Figure 2.8: Absorbance vs wavelength traces for the N_{1114}TFSI ionic liquid (previously diluted in ethanol) [97].

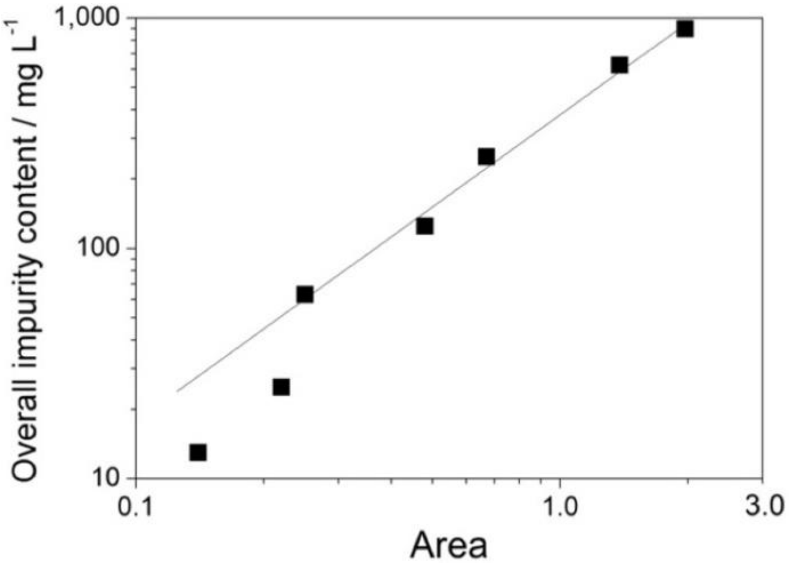

Figure 2.9: Dependence of the overall impurities content vs the area value delimited (in the 260–600 nm range) by the absorbance curves obtained for ethanol: IL mixtures at different volume ratios (from 20:1 to 5000:1) [97].

Therefore, the purity level of the investigated ionic liquids was determined by comparing the absorbance curve relative to the samples prepared through the process described in the present report (red trace of Figure 2.8) with that obtained from the same IL not subjected to any purification route (black trace of Figure 2.8). For instance, the area values, comprised between each UV-Vis plot (260–600 nm range) and the X axis were compared. The purity level of the not purified ionic liquid ranges from about 99 to 99.5 %, depending on the purity level of the starting chemicals. Therefore, all final IL samples exhibited a purity level always above 99.9 %.

iii) Moisture content

The Karl-Fisher titrations have revealed, in all investigated IL samples, a water content below 2 ppm, demonstrating the high efficiency of the vacuum drying process.

2.2.3 Thermal stability

Figure 2.10 summarizes the thermal trace obtained from ramp-temperature TGA measurements on the investigated IL samples, i.e., the relative mass variation is reported as a function of the temperature. All the ionic liquids containing the FSI anion display a lower thermal stability than their counterparts with the TFSI one, in agreement with previous data reported in literature [96,98]. The FTFSI based samples behave very similarly with respect to the FSI ones. The EMITFSI sample shows the best performance, followed by the ILs comprising the TFSI anion and the quaternary ammonium cations. Imidazolium based ILs are known to possess high thermal stability, especially when combined with TFSI anion [99,100]. Usually, these measurements are performed in scanning mode and describe the so-called short-term thermal stability. To the best of our knowledge, no information is available about the specific tetra-alkyl-ammonium ILs here investigated. Some studies of different ammonium-based liquids were reported and showed a slight lower decomposition temperature with respect to the imidazolium based ILs [100]. The previous literature pointed out that, in general, the short-term thermal stability probes the decomposition of ILs. Decomposition occurs by various mechanisms [99,100]: *i*) as a first step, the loss of the alkyl chain of cations takes place; *ii*) in other cases, the anions replace the alkyl chain or the break of the C-N bond produces alkenes; *iii*) the opening of the cation ring, for imidazolium-based ILs, occurs at much higher temperatures. The incorporation of an oxygen atom in the main cation alkyl side chain is seen to moderately affect the thermal stability, i.e., $N_{111(2O1)}$TFSI and $N_{122(2O1)}$TFSI (panel A) are seen to be stable up to 300 °C.

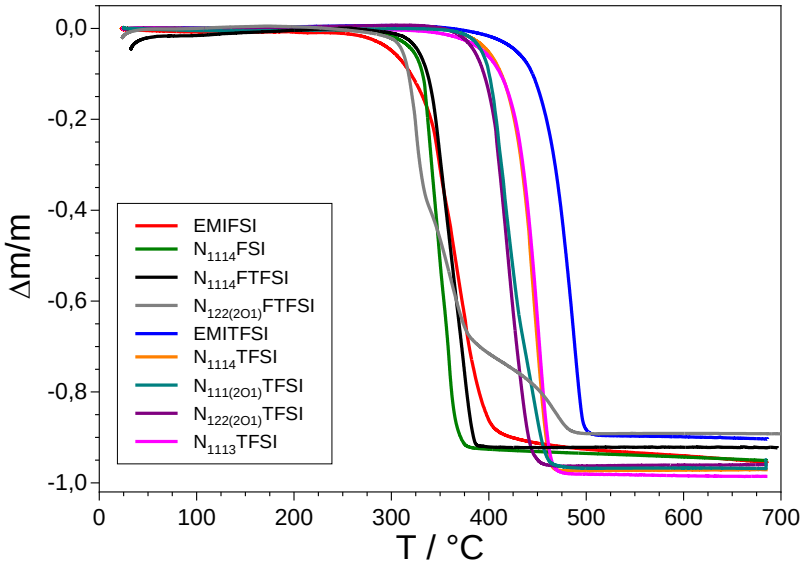

Figure 2.10: Ramp-temperature TGA trace summary, related to the investigated ionic liquids, obtained in He atmosphere with a flux of 60 ml min^{-1} and a scanning rate of 10 °C min^{-1} [101].

The main purpose of the isothermal TGA measurements is to investigate the (thermal) behavior of the IL samples as a function of time (long-term thermal stability). **Figure 2.11** compares the (isothermal) curves obtained for all investigated ionic liquids at different temperatures. At a first sight, all investigated ILs show lower thermal stability than that observed in the ramp-temperature traces, this fact is ascribable to the peculiarities of the isothermal technique which allow to much better evidence the degradation phenomena than the ramp-temperature method. The two types of measurements, in general, can give different information: while scanning TGA mainly detects the decomposition of materials, the isothermal treatments are able to also study the evaporation of samples. The ionic liquids comprising the TFSI anions display a much higher stability than the FSI and FTFSI-based ones. EMIFSI and N_{1114}FSI start to exhibit a weight loss above 150 °C whereas the TFSI-based samples show no (or negligible) thermal degradation up to 225-250 °C (depending on the nature of the cation). Conversely to what was observed in the ramp-temperature traces of **Figure 2.10**, the N_{1114}FTFSI sample displays a thermal stability about 50 °C higher with respect to that of the FSI ones: this apparent discrepancy is once ascribable to the better reliability of the isothermal technique, which must be preferred for evaluating the thermal stability of the IL electrolyte especially under prolonged overheating periods. This is of relevant importance for practical devices as it gives information about the robustness of the battery system. The incorporation of an oxygen atom in the cation alkyl side chain does not seem to affect the (thermal) stability of the ionic liquids, except for the FTFSI samples. For instance, the $N_{122(2O1)}$FTFSI sample shows weight loss above 120 °C (vs 227 °C of N_{1114}FTFSI).

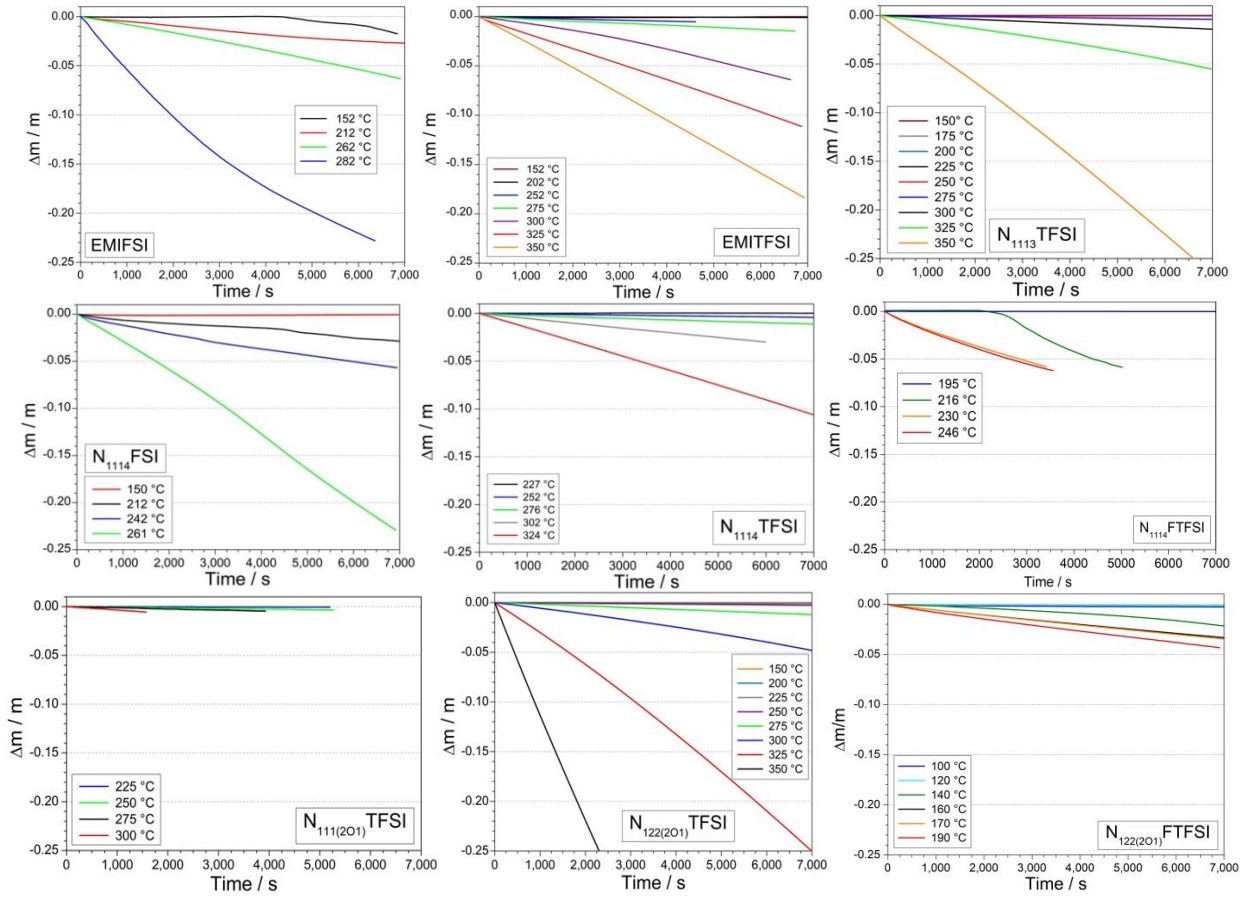

Figure 2.11: Relative mass variation (normalized to the initial sample weight) of the investigated ionic liquid samples subjected to isothermal conditions at different temperatures (increased stepwise) [101].

Table 2.3: Temperature values at which, under isothermal conditions, one observes a mass variation of 1 and 5% in 3,600 seconds [101].

Sample	T[1%] / °C	T [5%] / °C
EMIFSI	212	262
EMITFSI	300	325
N_{1113}TFSI	300	350
N_{1114}TFSI	302	324
N_{1114}FSI	212	242
N_{1114}FTFSI	216	230
$N_{111(2O1)}$TFSI	300	n. a.
$N_{122(2O1)}$TFSI	300	325
$N_{122(2O1)}$FTFSI	140-150	> 190

Table 2.3 summarizes the value of the lowest temperature where one observes a mass variation of at least 1 (T[1%]) or 5 % (T[5%]) in a time interval of 3600 seconds. All ionic liquids based on the TFSI anion display mass variation of 1% in isothermal conditions above 275 °C, while for the FSI ILs such

a temperature is reduced around 210 °C. The N_{1114}FTFSI sample behaves similarly to N_{1114}FSI, e.g., 216 vs 212 °C and 230 vs 242 °C for T[1%] and T[5%], respectively, whereas $N_{122(2O1)}$FTFSI exhibits a weight loss equal to 1 and 5 % above 140 and 190 °C, respectively (once more evidencing the detrimental effect of the oxygen incorporation within the cation alkyl chain on the thermal stability of the FTFSI ionic liquids).

2.2.4 Ion transport properties

The temperature dependence of the ionic conductivity of the pure ILs and their mixtures with LiTFSI and NaTFSI are compared in **Fig. 2.12** and **2.14**.

Lithium-based IL electrolytes

The (EMI^+)-based ILs are reported in panels **2.12A** and **2.12C** whereas the ($N_{RR'R''R'''}^+$)-based ones are illustrated in panels **2.12B** and **2.12D**. The pure EMIFSI sample shows a stable, but low conductivity values, i.e., around 10^{-7} S cm^{-1}, from -40 to about -20 ◦C, which are typical of the crystalline state [98]. Around -15 °C the ion conductivity suddenly jumps more than four orders of magnitude due to the melting of the ionic liquid. The conductivity *vs.* temperature slope of EMITFSI shows a non-linear increase prior melting, indicating that the ions gain some mobility in the solid phase. This is associated with the existence of low temperature solid-solid phase transitions [72]. For instance, the material exhibits ionic conductivity above 10^{-5} S cm^{-1} below -10 °C, which is undoubtedly interesting for a solid electrolyte. The melting point and conductivity gain, however, shift upward (from about -10 ◦C to 0 ◦C) going from EMIFSI to EMITFSI, likely due to the larger anion steric hindrance affecting both the coulombic interactions with the IL cation and the viscosity in the liquid state (leading to slower transport properties) [102]. This behavior is also observed in the conductivity plot of the ($N_{RR'R''R'''}^+$)-based samples (panel 12B). The ionic conductivity in the molten state decreases with the increase of the cation alkyl chain length, i.e., in passing from N_{1113}TFSI to N_{1114}TFSI (**Table 2.4**). This is ascribable to the larger steric hindrance of the $(N_{1114})^+$ cation with respect to $(N_{1113})^+$, leading to a viscosity increase [92]. On the other hand, the longer *N*-butyl chain (with respect to the *N*-propyl one) increases the asymmetry of the ($N_{RR'R''R'''}^+$) cation, thus hindering the ion packing, and, therefore, decreasing the melting temperature. For instance, the conductivity jump is seen to shift from above 15 ◦C to around 10 ◦C in passing from N_{1113}TFSI to N_{1114}TFSI in spite of the melting temperature shifting in the opposite direction. This behavior was also observed for pyrrolidinium [92] and piperidinium [103] ionic liquids.

Table 2.4: Summary of ionic conductivity values of all investigated ionic liquids and their electrolyte mixtures with the LiTFSI salt (mole fraction equal to 0.2) at different temperatures.

Ionic liquid sample	Conductivity (-10 °C) / S cm^{-1}		Conductivity (20 °C) / S cm^{-1}		Conductivity (50 °C) / S cm^{-1}	
	pure	with LiTFSI	pure	with LiTFSI	pure	with LiTFSI
EMIFSI	3.39×10^{-3}	1.51×10^{-3}	7.71×10^{-3}	5.97×10^{-3}	1.30×10^{-2}	1.28×10^{-2}
EMITFSI	2.42×10^{-6}	3.56×10^{-4}	4.69×10^{-3}	1.41×10^{-3}	7.90×10^{-3}	3.52×10^{-3}
N_{1113}TFSI	$< 1 \times 10^{-9}$	$< 1 \times 10^{-9}$	2.05×10^{-3}	4.12×10^{-5}	5.96×10^{-3}	3.13×10^{-3}
N_{1114}TFSI	$< 1 \times 10^{-9}$	4.98×10^{-8}	1.42×10^{-3}	3.89×10^{-4}	4.23×10^{-3}	1.93×10^{-3}
N_{1114}FSI	1.37×10^{-7}	1.62×10^{-4}	5.51×10^{-5}	1.30×10^{-3}	9.66×10^{-3}	3.91×10^{-3}
N_{1114}FTFSI	6.57×10^{-4}	9.23×10^{-5}	2.74×10^{-3}	7.77×10^{-4}	8.15×10^{-3}	2.83×10^{-3}
$N_{111(2O1)}$TFSI	5.80×10^{-9}	$< 1 \times 10^{-9}$	2.61×10^{-7}	2.86×10^{-6}	5.97×10^{-3}	3.81×10^{-3}
$N_{122(2O1)}$TFSI	2.47×10^{-4}	4.76×10^{-5}	1.76×10^{-3}	5.63×10^{-4}	5.44×10^{-3}	1.95×10^{-4}
$N_{122(2O1)}$FTFSI	5.90×10^{-4}	n. a.	2.85×10^{-3}	n. a.	7.46×10^{-3}	n. a.

Remarkable lowering of the melting point is observed, however, for the $N_{122(2O1)}$TFSI (**panel B**) sample, which does not exhibit any crystalline-liquid phase transition down to -40 °C. Such a behavior, found also in pyrrolidinium- [71,104] and imidazolium-based [105] ionic liquids upon incorporation of an oxygen atom into the cation side alkyl chain, is likely to be attributed to: *i*) enhanced flexibility of the side chain due to the ether group (i.e., higher freedom conformational degrees), even prevailing over the polarity gain with respect to the alkyl side chain [73]; *ii*) unfavorable close ion packing, resulting in lower ionic lattice energy; *iii*) reduction of the cation self-aggregation within the IL, which decreases the ion-ion interactions [106]. Surprisingly, the opposite trend is seen for the $N_{111(2O1)}$TFSI sample, i.e., the melting point increases from about 10 up to 35 ◦C in passing from N_{1114}TFSI to $N_{111(2O1)}$TFSI. Analogous raise of the melting temperature, resulting from the replacement of a methylene (–CH_2–) group with an ether oxygen in the main cation aliphatic chain, was previously recorded also in imidazolium ILs [107]. These diverging results might be due to the strong repulsive interactions of the oxygen electron lone pairs with the neighboring anions which predominate over the higher flexibility of the alkyl ether group, leading to significant ion crystal packing rearrangements. However, this behavior is not still fully clarified and deeper investigation is needed for a better understanding. As seen in **Fig. 2.12** (panels A and B), the conductivity of the pure ILs (reported for selected temperatures in **Table 2.4**) overcomes 10^{-3} S cm^{-1} in the molten state. The EMI-based ILs are found displaying faster ion transport properties with respect to those based on the ($N_{RR'R''R'''}^{+}$) cations. This behavior, previously reported in literature [58], might be ascribable to the smaller size and to the planar configuration of the imidazolium cation, which could better slide through the IL medium.

Panels C and D of **Fig. 2.12** summarize the conductivity *vs*. temperature dependence of the 0.2LTFSI-0.8IL binary electrolytes. Differently from the pure ILs, EMIFSI (panel A) in particular,

the imidazolium-based electrolytes (panel C) exhibit progressively increasing conductivities from -40 ◦C, indicating for a gained ion mobility with a knee around -25 ◦C and -20° C for 0.2LTFSI-0.8EMITFSI and 0.2LTFSI-0.8EMIFSI, respectively. Above these temperatures, both the EMI-based electrolytes are fully molten. As expected, the conductivity of 0.2LiTFSI- 0.8EMIFSI is slightly higher than that of 0.2LiTFSI-0.8EMITFSI at any temperature. The conductivity-temperature dependence of the binary mixtures based on ($N_{RR'R''R'''}^{+}$) cations (panel D) is rather like that of the pure ILs (panel B), with the exception of the 0.2LiTFSI-0.8N_{1114}FSI sample. This binary mixture, with respect to pure N_{1114}FSI, displays an almost linear trend prior the solid-liquid transition around -5 °C, suggesting a more marked variation of the ion-ion interactions and/or of the IL structural rearrangement upon incorporation of LiTFSI into N_{1114}FSI. Such a behavior, previously observed for pyrrolidinium-based ILs involving FSI and TFSI anions [108], can be likely associated to the presence of two different anions in the binary mixture. Finally, it is interesting to note that, even in the presence of a 0.2 mole fraction of the LiTFSI salt, the $N_{122(2O1)}$TFSI sample does not undergo any crystalline-liquid phase transition down to -40 ◦C. The incorporation of the LiTFSI lithium salt into the pure ILs can be regarded as the replacement of the IL cations with Li^+ to give mixed *x*Li(1-*x*)cation-TFSI or *x*Li(1-*x*)cation-*x*TFSI(1-*x*)FSI materials. **Fig. 2.13** reported as an example, compares the conductivity plot of pure N_{1114}FSI with that of the 0.2LiTFSI-0.8N_{1114}FSI mixture. The high charge density on the Li^+ cations (much higher than that of any IL cation investigated herein) results in the increase of the ion-ion interactions, in turn increasing the viscous drag and, therefore, depleting the transport properties [109]. For example, at 50 ◦C the conductivity value is seen decreasing from about 9.7 × 10^{-3} to 3.9 × 10^{-3} S cm^{-1} going from pure N_{1114}FSI to the 0.2LiTFSI-0.8N_{1114}FSI mixture (**Table 2.3**). On the other hand, the addition of the lithium salt is generally seen to lower the melting temperature of the mixture with respect to the pure IL, resulting from the disrupted ion packing associated to the strong Li^+ - anion interactions [109]. This result is particularly appealing for batteries operating at low temperatures. For instance, a gain in conductivity of four orders of magnitude, i.e., from 1.37 × 10^{-7} to 1.62 × 10^{-3} S cm^{-1} at -10 ◦C, is observed upon addition of LiTFSI to N_{1114}FSI (**Table 2.4**). Nonetheless, an opposite behavior is revealed for the N_{1113}TFSI sample, which is molten at 20 ◦C, but turns in the solid state upon addition of LiTFSI. As a result, a conductivity drop of about two orders of magnitude is found at 20 ◦C, for 0.2LiTFSI-0.8N_{1113}TFSI with respect to the pure IL (**Table 2.4**). Possible explanation could be the formation of a solid LiTFSI-IL eutectic compound, previously observed in pyrrolidinium ionic liquids [85], when the lithium salt mole fraction achieves 0.2.

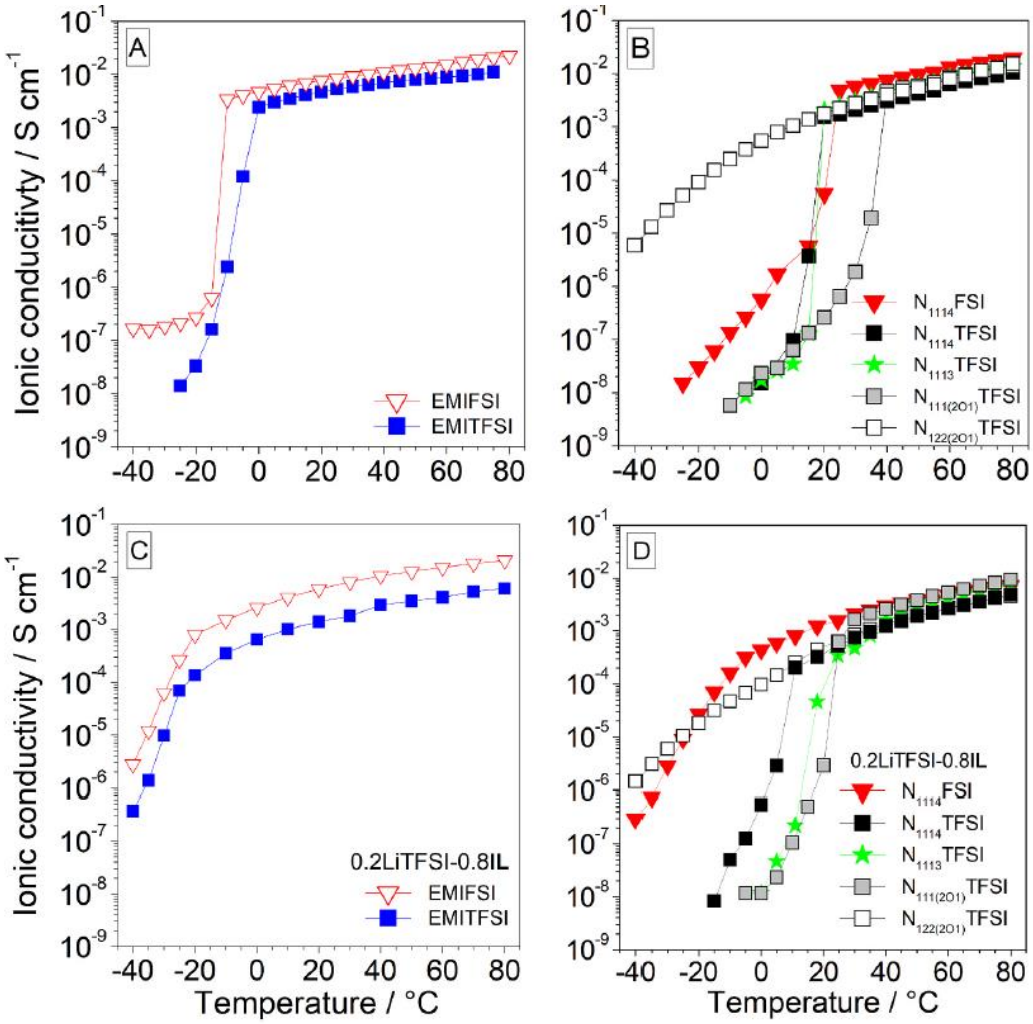

Figure 2.12: Ionic conductivity *vs*. temperature dependence of pure ionic liquids (panels A and B) and their electrolyte mixtures (panels C and D) with the LiTFSI salt (mole fraction equal to 0.2). (EMI^+)-based samples: panels A and C. ($N_{RR'R''R'''}{}^+$)-based samples: panels B and D. Heating scan rate: < 1°C h^{-1}.

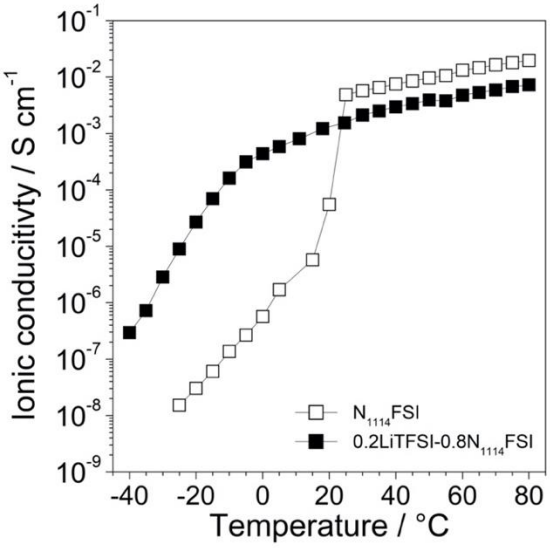

Figure 2.13. Ionic conductivity *vs*. temperature dependence for the $N_{1114}FSI$ ionic liquid and its electrolyte mixture with the LiTFSI salt (0.2 as the molar ratio). Heating scan rate: < 1 °C h^{-1}.

The conductivity *vs*. temperature dependence of the investigated ILs and their mixture with LiTFSI displays in the molten state a VTF behavior [110–112], typical of the ionic liquid materials [8]. Therefore, the conductivity value (σ) is also reported as a function of $10^3\,(T\text{-}T_0)^{-1}$ (where T_0 represents the ideal glass transition temperature) according to the VTF equation, $\sigma = \sigma^{\circ}\cdot exp\{ -Ea /[R *(T - T_0)]\}$ [113]. The results, illustrated in **Fig. 2.14**, exhibit a linear dependence of the conductivity *vs.* $10^3\,(T\text{-}T_0)^{-1}$, highlighting the good match between the experimental data and the VTF model equations. The activation energy (E_a) and T_0 parameters, calculated by fitting the experimental data into the VTF equation, are summarized in **Table 2.5**. The data analysis convergence, estimated in terms of χ^2, is also illustrated in **Table 2.4** and compared with that obtained using the simple Arrhenius fitting. First of all, the VTF equation represents with better accuracy the experimental conductivity compared to the Arrhenius one. Secondly, the convergence of the VTF fitting is much better for the LiTFSI-IL mixtures compared to the pure ILs. As reported in literature [8], but for other ILs, the ideal glass transition temperature is seen to increase with the addition of LiTFSI and the anion size (both in pure ILs and in LiTFSI-IL mixtures). Conversely, the activation energy shows a scattered trend as illustrated in **Table 2.5**, suggesting that it is differently (positively or negatively) affected by competitive phenomena. Turning to the ammonium cations, the longer alkyl side chain of N_{1114}TFSI compared to N_{1113}TFSI leads to a decrease of T_0, but an increase of the activation energy (with and without LiTFSI). Furthermore, the introduction of oxygen atoms in the alkyl chain of the ammonium cation, i.e., $N_{111(2O1)}$TFSI and $N_{122(2O1)}$TFSI, leads to a decrease of T_0 in comparison to N_{1114}TFSI (with and without LiTFSI), but more scattered changes are observed for the E_a value. This behavior is clue of remarkable variability on the local coordination of ILs and their mixtures with LiTFSI in the molten state driven by the size of the anions (TFSI *vs*. FSI), the presence of Li^+ cations, and the structural flexibility/local polarity of the cations' alkyl side chains.

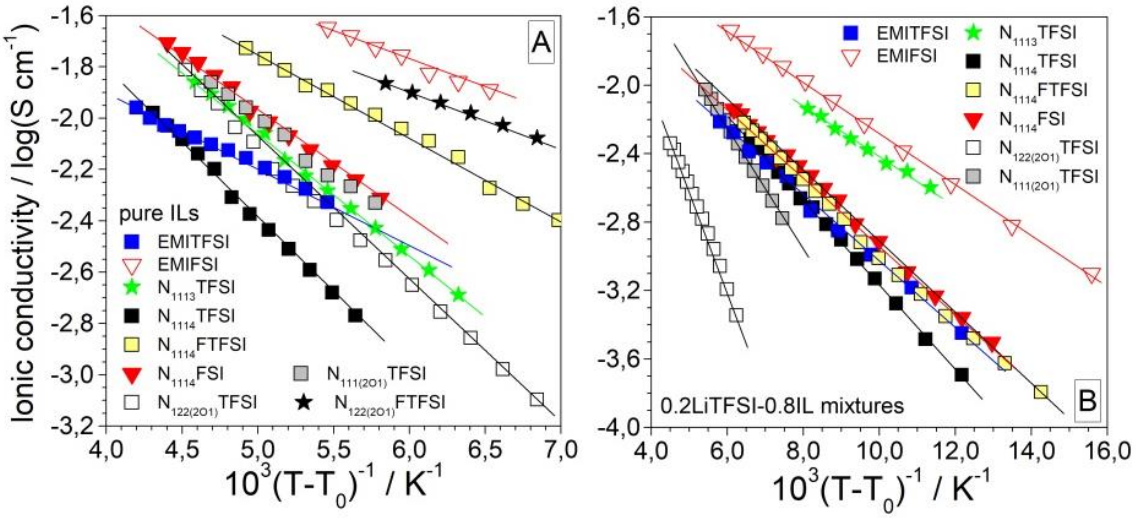

Figure 2.14: VTF conductivity plot of pure ionic liquids (panel A) and their electrolyte mixtures (panel B) with the LiTFSI salt (mole fraction equal to 0.2).

Table 2.5: Summary of the VTF fitting parameters calculated from the ionic conductivity values of the pure ionic liquids and their electrolyte mixtures with the LiTFSI salt (mole fraction equal to 0.2). Errors have been estimated by the linearized VTF fittings results assuming a 99.9% confidence.

IL sample	E_a / kJ mol^{-1}		T_0 / K	
	pure	with LiTFSI	pure	with LiTFSI
EMIFSI	90 ± 6	49 ± 1	110 ± 20	181 ± 3
EMITFSI	41 ± 1	47 ± 1	170 ± 10	189 ± 3
N_{1113}TFSI	134 ±7	60 ± 10	130 ± 20	230 ± 10
N_{1114}TFSI	169 ± 9	69 ± 4	126 ± 5	202 ± 3
N_{1114}FSI	122 ± 4	56 ± 3	121 ± 9	191 ± 3
N_{1114}FTFSI	n. a.	n. a.	160 ± 10	198 ± 5
$N_{111(2O1)}$TFSI	130 ± 10	103 ± 6	140 ± 20	169 ± 3
$N_{122(2O1)}$TFSI	170 ± 10	190 ± 10	130 ± 10	131 ± 3
$N_{122(2O1)}$FTFSI	n. a.	n. a.	182 ± 3	n. a.

Sodium-based IL electrolyte

The ion transport properties of the sodium-based electrolyte have been studied as a function of the temperature and the obtained results are reported in **Fig. 2.15A** (EMI-based electrolytes), **15B** (N_{11114}-based) and **15C** (PIP_{1A}-based), respectively. The conductivity–temperature diagram of the 0.1NaTFSI-0.9IL electrolytes containing TFSI-based ionic liquids (EMITFSI, N_{1114}TFSI, PIP_{14}TFSI) exhibits ion conduction values around 10^{-7} S cm^{-1} (i.e., typical of a crystalline solid state) [58,114,115] from −40 °C up to the melting point, evidenced by a step increase (from two to three orders of magnitude) of the ionic conductivity. Conversely, the mixtures containing FSI-based ILs (EMIFSI, N_{1114}FSI) show, in the low-temperature range, an almost linear increase in conduction, likely attributable to an ion mobility gain due to solid–solid phase transitions occurring prior the melting [89]. A similar trend is also observed for the 0.1NaTFSI-0.9PIP_{13}TFSI sample, in agreement with the conductivity results reported elsewhere for pure PIP_{13}TFSI [103]. A two-orders-of-magnitude jump (not registered for the FSI-based electrolytes) is, however, detected around the melting temperature. A comparison among the conductivity–temperature plots highlights solid–liquid transitions, recorded in the FSI-based electrolytes, occur at lower temperatures with respect to those observed in the TFSI ones. The melting point of an IL material is determined by the strength of its crystal lattice which, in turn, is controlled by competitive factors, such as surface charge density, intermolecular forces (Van der Waals) and molecular symmetry [73], which have opposite effect. Therefore, the lower Van der Waals forces, due to the smaller steric hindrance of the FSI anion, might counterbalance the higher surface charge density (which, conversely, tends to increase the melting point), thus decreasing the melting temperature with respect to the TFSI electrolytes [58].

No sudden conductivity raise is seen for the 0.1NaTFSI-0.9$N_{1114}IM_{14}$ electrolyte, indicating the absence of any solid–liquid phase transition in the investigated temperature range. This is likely attributable to the high asymmetry of the IM_{14} anion with respect to FSI and TFSI (symmetrical), which strongly hinders the ion packing and, therefore, the IL crystallization. In the molten state, the 0.1NaTFSI-0.9IL samples display a VTF behavior, typical of the ionic liquid electrolytes [58]. Further increases in temperature beyond that of the melting lead to a progressive raise in conductivity, due to the convective thermal motions within the ionic liquid media. The ionic conduction values, in the liquid state, progressively decrease with increasing the steric footprint of the anion in the following order: FSI > TFSI > IM_{14}. This behavior, reported in the literature for other IL electrolytes [58], is due to the progressive increase in viscosity (linked to the size of the ions), which slows down the mobility of the ions within the IL material [58].

In the molten state, a moderate decrease in conduction is observed for the 0.1NaTFSI-0.9PIP_{14}TFSI electrolyte with respect to 0.1NaTFSI-0.9PIP_{13}TFSI, attributable to the longer cation alkyl chain (n-butyl compared to n-propyl), which increases the steric bulk and, therefore, the viscosity of the piperidinium IL [103]. Conversely, the increase in alkyl chain length leads to a greater asymmetry of the cation, hindering the formation of the crystalline lattice and, therefore, producing a decrease in the melting temperature of the ionic liquid, i.e., the PIP_{14}TFSI electrolyte exhibits a melting point of approximately 20 °C lower than that of the PIP_{13}TFSI one, once more in agreement with the results obtained for the pure ILs [103].

The ionic conductivity data, determined at selected temperatures, of the 0.1NaTFSI-0.9IL sodium electrolytes are summarized in **Table 2.6**. At −20 °C only the EMI-based samples exhibit conduction values (i.e., from 10^{-4} to 10^{-3} S cm^{-1}) of interest for practical devices, making these electrolytes appealing for low temperature applications. At 20 °C all investigated NaTFSI-IL electrolytes, except for the NaTFSI-0$N_{1114}IM_{14}$ sample, largely overcome 10^{-4} or 10^{-3} S cm^{-1}. The EMI-based samples display higher conductivity values than those containing $(N_{1114})^+$ and piperidinium cations, due to the lower viscous drag ascribable to the smaller size and planar configuration of the imidazolium cation [58]. At 80 °C, the conductivity value of all sodium IL electrolytes largely exceeds 10^{-3} S cm^{-1}; in particular, that of EMI- and FSI-based electrolytes widely overcomes 10^{-2} S cm^{-1}.

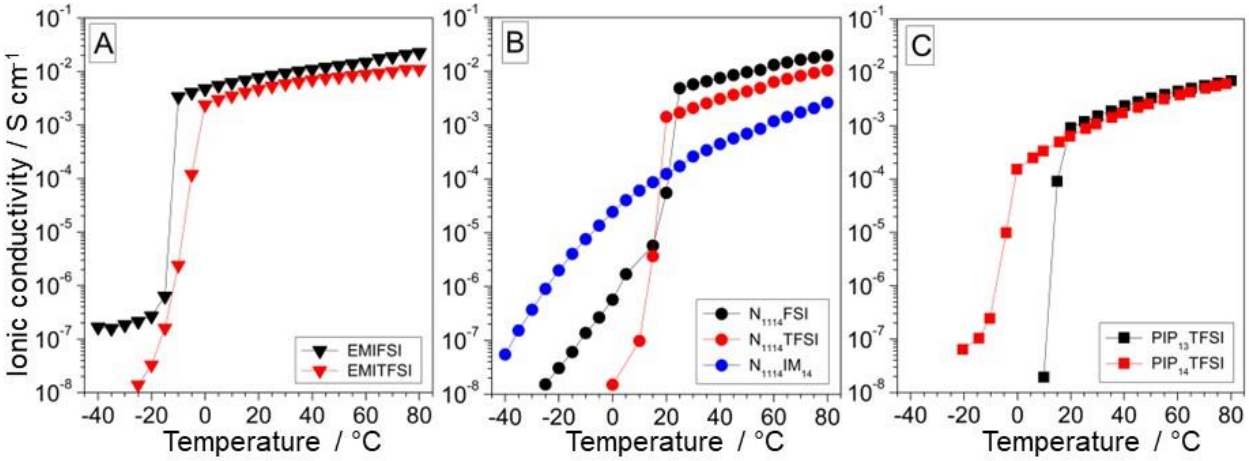

Figure 2.15: Ionic conductivity vs. temperature dependence of 0.1NaTFSI-0.9IL sodium electrolytes: (**A**) EMI-based electrolytes; (**B**) N_{1114}-based electrolytes; (**C**) PIP_{1A}-based electrolytes.

Table 2.6. Summary of ionic conductivity values of all investigated ionic liquids and their electrolyte mixtures with the NaTFSI salt (mole fraction equal to 0.1) at different temperatures.

Ionic liquid	T (-20 °C) / S cm^{-1}	T (10 °C) / S cm^{-1}	T (50 °C) / S cm^{-1}
$PIP_{13}TFSI$	< 1e^{-8}	$(1.9 \pm 0.2)\times10^{-8}$	$(3.3 \pm 0.3)\times10^{-3}$
$PIP_{14}TFSI$	$(6.4 \pm 0.6)\times10^{-8}$	$(3.9 \pm 0.4)\times10^{-4}$	$(2.6 \pm 0.3)\times10^{-3}$
$N_{1114}FSI$	$(3.1 \pm 0.3)\times10^{-8}$	$(3.2 \pm 0.3)\times10^{-6}$	$(9.7 \pm 0.9)\times10^{-3}$
$N_{1114}TFSI$	< 1e^{-8}	$(9.8 \pm 0.9)\times10^{-8}$	$(4.2 \pm 0.4)\times10^{-3}$
$N_{1114}IM_{14}$	$(2.0 \pm 0.2)\times10^{-6}$	$(6.1 \pm 0.6)\times10^{-5}$	$(7.0 \pm 0.7)\times10^{-4}$
EMIFSI	$(2.7 \pm 0.3)\times10^{-7}$	$(6.2 \pm 0.6)\times10^{-3}$	$(1.3 \pm 0.2)\times10^{-2}$
EMITFSI	$(3.3 \pm 0.3)\times10^{-8}$	$(3.5 \pm 0.4)\times10^{-3}$	$(7.9 \pm 0.8)\times10^{-3}$

2.2.5 Electrochemical stability

Lithium-based IL electrolytes

The electrochemical stability is among the most important requirements for any electrolyte, especially for those to be applied to electrochemical systems operating at high voltages. This parameter was evaluated for the 0.2LiTFSI-0.8IL binary mixtures by anodic cyclic voltammetry performed on Li/electrolyte/C cells. However, the 0.2LiTFSI- $0.8N_{1113}TFSI$ and 0.2LiTFSI- $0.8N_{111(2O1)}TFSI$ electrolytes were not investigated as they are solid at room temperature (**Fig. 2.10D**). The results, illustrated in **Fig. 2.16**, evidence relatively low current flows (normalized with respect to the geometrical area of the carbon working electrode) in the first anodic scan (dotted line). **Table 2.7** summarizes the voltage values at which the current density through the cell reached 10 and 20 μA cm^{-2} during the 1st and 2nd anodic scans: the 20 μA cm^{-2} threshold is passed at cell voltages equal or even higher than 4.7 V *vs.* $Li^+/Li°$. A remarkable reduction of the current flow is observed in the following cycles (solid traces), suggesting that the irreversible oxidation processes (taking place during the first anodic scan) are likely associated to impurities (even if in very low content) rather than to the ionic liquids and/or the LiTFSI salt [109]. Overall, the 0.2LiTFSI-0.8IL mixtures show

electrochemical stabilities against oxidation well above 4.5 V. From a more accurate analysis of the results in **Table 2.7**, it is evident that the nature of the cation plays a role in determining the oxidation stability, although this is expected to mainly involve the anion [58]. EMI-based electrolytes (panels A and B) are seen not to exceed 10 μA cm^{-2} below 4.5 V *vs.* $Li^+/Li°$ (in particular, 4.50 V for 0.2LiTFSI-0.8EMIFSI and 4.66 V for 0.2LiTFSI-0.8EMITFSI) in the 2nd anodic scan whereas current densities of 20 μA cm^{-2} are recorded only above 4.90 V. Analogously, the N_{1114}TFSI-based sample (panel D) is electrochemically more stable towards oxidation than the N_{1114}FSI -based one (panel C). These results confirm the higher stability of TFSI than FSI [72,98] due to the lower reactivity of the S-CF_3 bond with respect to the S–F one [91,116,117]. Additionally, a wider oxidation stability is observed for the ($N_{RR'R''R'''}^+$)-based mixtures, displaying current flows below 20 μA cm^{-2} even at 5 V *vs.* $Li^+/Li°$ during the second (and following) anodic scans. Finally, the ether oxygen in the cation's side chain (panel E) does not seem to affect the electrochemical stability towards oxidation of the LiTFSI-IL mixtures.

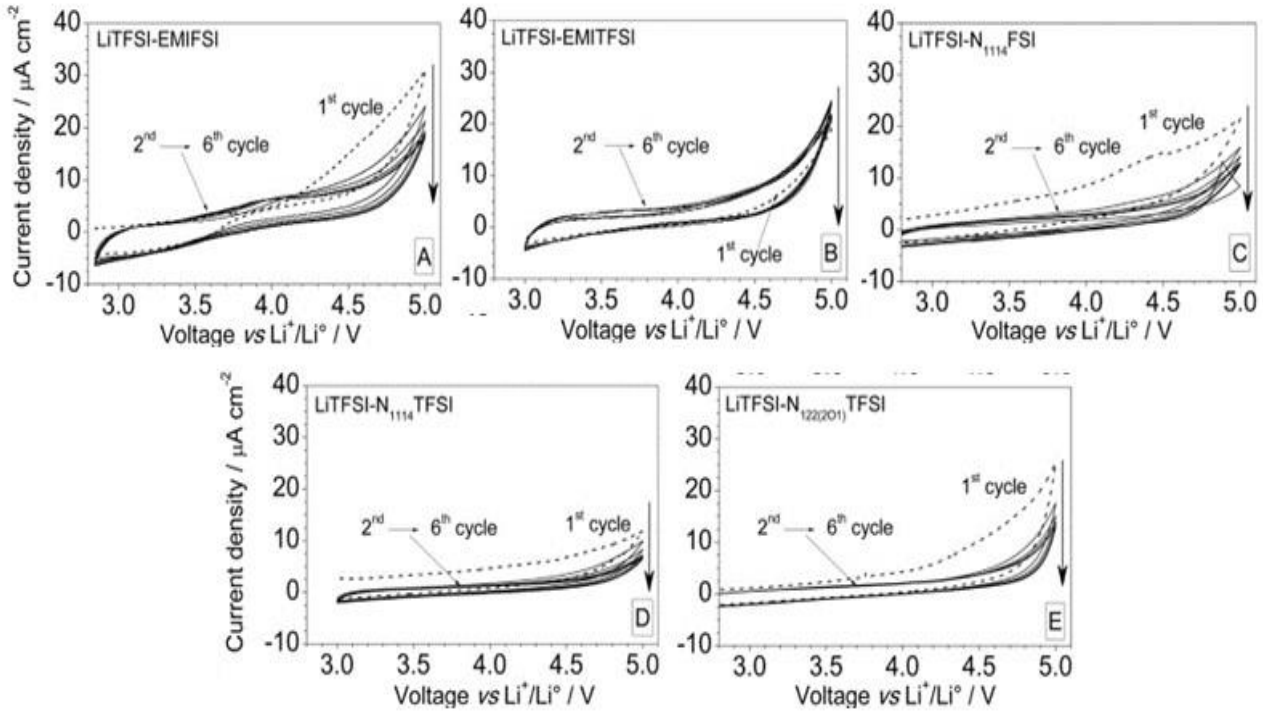

Figure 2.16: Anodic CV scans of the 0.2LiTFSI-0.8EMIFSI (panel A), 0.2LiTFSI- 0.8EMITFSI (panel B), 0.2LiTFSI-0.8N_{1114}FSI (panel C), 0.2LiTFSI- 0.8N_{1114}TFSI (panel D) and 0.2LiTFSI-0.8$N_{122(2O1)}$TFSI (panel E) ionic liquid electrolyte mixtures. Carbon as the working electrode. Lithium metal as the counter electrode. Scan rate: 1 mV s^{-1}. Temperature: 30 °C. The current density value was obtained by normalizing the current flow with respect to the geometrical surface area of the working electrode.

Table 2.7. Voltage values (vs the $Li^+/Li°$ redox couple), determined by voltammetry tests carried out on selected 0.2LiTFSI-0.8IL binary electrolyte mixtures, recorded when the current density through the cell reached 10 and 20 μA cm^{-2} during the 1st and the 2nd anodic scan. Carbon and lithium metal were used as working and counter electrode, respectively. Temperature: 30 °C.

Ionic liquid mixture	Voltage (1st scan) / V		Voltage (2nd scan) / V	
	(10 μA cm^{-2})	(20 μA cm^{-2})	(10 μA cm^{-2})	(20 μA cm^{-2})
EMIFSI	4.31	4.68	4.50	4.91
EMITFSI	4.34	4.95	4.66	4.94
N_{1114}FSI	4.23	4.93	4.75	> 5.00
N_{1114}TFSI	4.87	> 5.00	> 5.00	> 5.00
$N_{122(2O1)}$TFSI	4.48	4.90	4.84	> 5.00

Figure 2.17 depicts the results obtained from CV tests run in Li/Carbon cells containing the 0.2LiTFSI-0.8N_{1114}FTFSI and 0.2LiTFSI- 0.8$N_{122(2O1)}$FTFSI ionic liquid electrolytes. The current vs voltage profiles evidence low current flows (normalized with respect to the geometrical area of the carbon working electrode) in the first anodic scan. A remarkable reduction of the current density (< 20 μA cm^{-2}) is observed in the following cycles up to the massive degradation (oxidation) of the electrolyte samples (occurring around 4.8 V vs the $Li^+/Li°$ redox couple). This suggests that the irreversible oxidation processes, taking place during the first anodic scan, are likely associated to impurities, even if in very low content, rather than to the ionic liquids and/or the LiTFSI salt [109]. The drastic decay of the current flow through the cell after the 1st anodic sweep also supports for a high purity content of the investigated samples. Overall, the FTFSI electrolytes show electrochemical stabilities against oxidation well above 4.8 V, fully matching the Si-DRIVE targets.

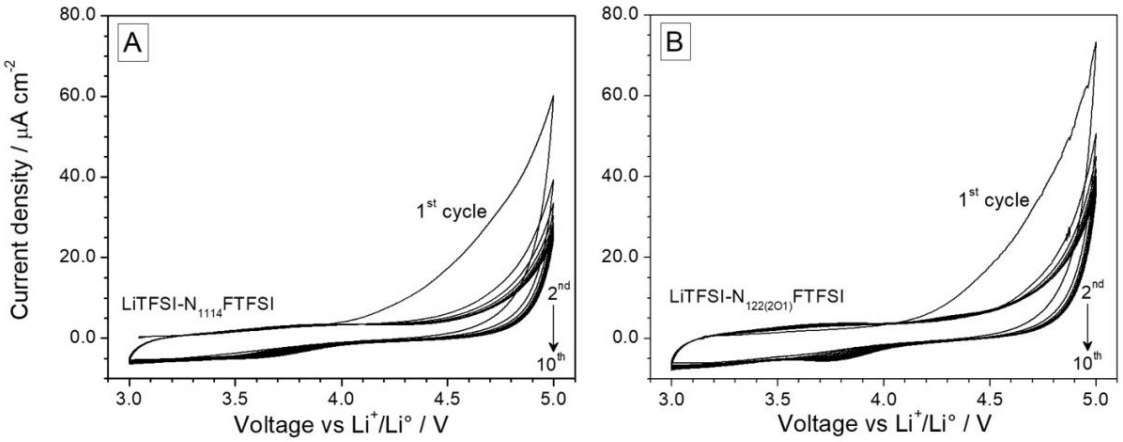

Figure 2.17: Anodic cyclic voltammetries of the 0.2LiTFSI-0.8N_{1114}FTFSI (panel A) and 0.2LiTFSI-0.8$N_{122(2O1)}$FTFSI (panel B) ionic liquid electrolytes. Carbon as the working electrode. Lithium metal as the counter electrode. Scan rate: 1 mV s^{-1}. Temperature: 20 °C. The current density value was obtained by normalizing the current flow with respect to the geometrical surface area of the working electrode.

Selected electrolytes, 0.2LiTFSI-0.8EMIFSI and 0.2LiFSI-0.8EMIFSI were subjected to prolonged (one-hundred cycles) anodic voltammetry tests carried out on Li/Carbon cells. The results, illustrated in **Figure 2.18** (panels A and B), evidence relatively low current flows (normalized with respect to the geometrical area of the carbon working electrode) in the first anodic scan (thick blue trace). A relevant reduction of the current flow, i.e., from about 50 down to 20 μA cm^{-2}, is observed in the following cycles (black traces), suggesting that the irreversible oxidation processes (taking place during the first anodic scan) are likely associated to contaminants (even if in very low content) rather than to the ionic liquids and/or the lithium salt [109,118]. Both binary electrolytes are seen to not exceed 20 μA cm^{-2} up to 4.8 vs $Li^+/Li°$ in the 2nd anodic scan whereas progressively decreasing current density values are recorded in the following scans, i.e., just 10 μA cm^{-2} are observed in the 100th cycle. No electrolyte degradation and/or parasitic phenomenon (corrosion of the Al current collector) is observed even prolonged voltammetry cycles. The results confirm, one more again, the very good electrochemical stability, i.e., up to 4.8 V, of the 0.2LiTFSI-0.8EMIFSI and 0.2LiFSI-0.8EMIFSI electrolyte formulations; no practical difference in terms of robustness towards oxidation is seen between the two electrolytes.

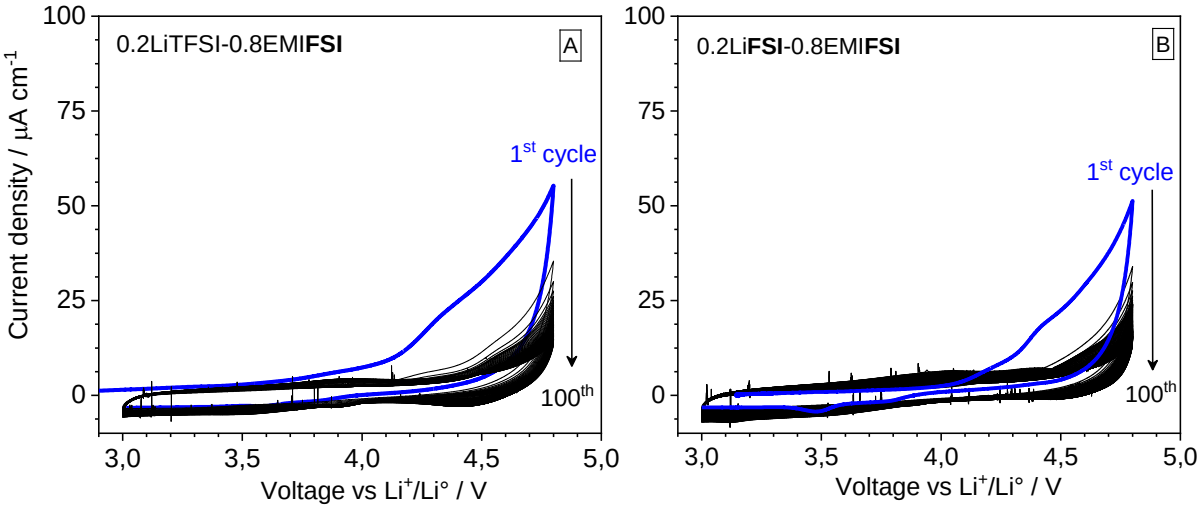

Figure 2.18: Anodic cyclic voltammetry of Li/C cells containing the 0.2LiTFSI-0.8EMIFSI (panel A) and 0.2LiFSI-0.8EMIFSI (panel B) electrolytes, respectively. Scan rate: 1 mV s^{-1}. T = 20 °C.

Compatibility with the aluminum current collector

The degradation phenomena at the current collector are an important issue in lithium battery technology, especially if the device must operate at high voltages. The TFSI and especially FSI anions are known to promote (or rather not to prevent) corrosion of the aluminum collector lacking the capability of forming an LiF passivation film upon decomposition [119–122]. Therefore, additional CV tests were carried out on carbon-coated aluminum electrodes to verify the reproducibility of the

results, as well as on bare Al collectors for comparison purpose. Analogously to the CV results presented in **Fig. 2.16**, an evident reduction of the current flow (**Fig. 2.19**) is observed in any case after the initial cycle (dashed trace). Overall, no current increase is recorded in the following cycles, both for bare and carbon-coated collectors, suggesting no evident Al dissolution during the anodic scans. Lower current flows are seen (as expected) for the smoother bare electrodes with respect to

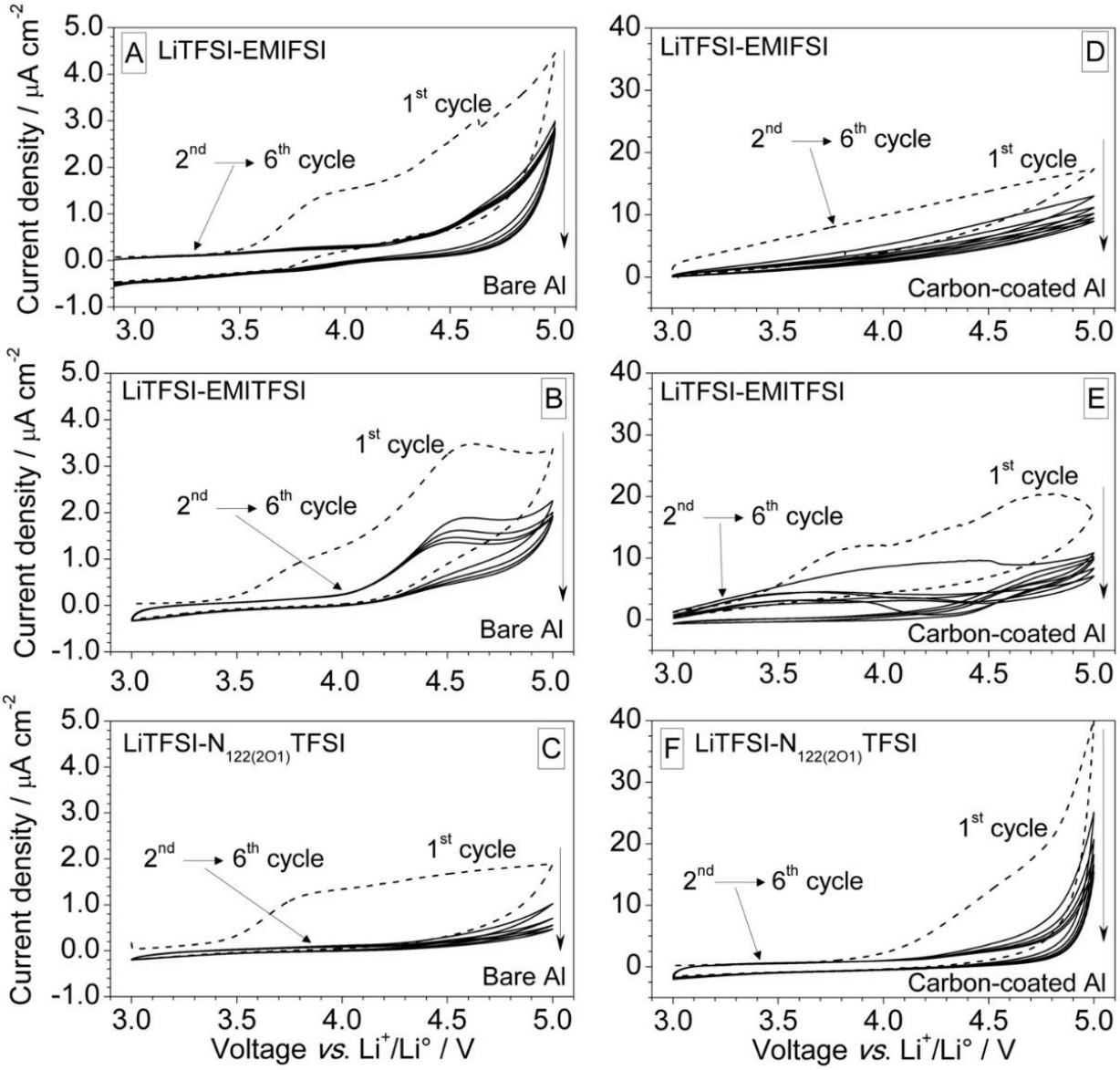

those detected for the carbon-coated ones (exhibiting a much larger surface area).

Figure 2.19: Anodic CV scans of 0.2LiTFSI-0.8EMIFSI (panels A and D), 0.2LiTFSI-0.8EMITFSI (panels B and E), and 0.2LiTFSI-0.8$N_{122(2O1)}$TFSI (panels C and F) ionic liquid electrolyte mixtures in bare (panels A, B and C) and carbon-coated (panels D, E and F) Al working electrodes, respectively. Lithium metal as the counter electrode. Scan rate: 1 mV s^{-1}. Temperature: 30 °C. The current density value was obtained by normalizing the current flow with respect to the geometrical surface area of the working electrode.

The SEM micrographs (right panels of **Figure 2.20**) taken on the cycled current collectors further support the results of the CV experiments and confirm all carbon-coated electrodes are free of obvious corrosion spots that might lead to defects in the carbon layer on-top of the Al foil. The small cracks, which are visible on all electrodes including the pristine one (analyzed for comparison purpose), can be ascribed to shrinkage of the carbon film after coating from an aqueous binder suspension and subsequent drying. This protective effect, due to the carbon coating, was previously observed in other TFSI- and FSI-based IL electrolyte systems [109,123,124]. A more detailed investigation of the corrosion phenomena on the bare Al current collectors (left panels of **Figure 2.20**) reveals the possibility of modest corrosion events, which seem to be most-pronounced in the case of the FSI-based electrolytes. For instance, the Al foils subjected to CV scans in TFSI-based ILs display hardly any significant difference to the pristine one, whereas the surface of the Al collector cycled in the FSI-based electrolyte is scattered with small amounts of contaminants that especially agglomerate near remains of the separator. However, this preliminary examination cannot fully exclude that those contaminants are simply a leftover of crystallized IL-salt after recovering the Al foils from the cycled cells. An in-depth XPS analysis upon long-term cycling tests with the different electrolytes might give more conclusive information, but it would be beyond the scope of the present manuscript. Finally, it is to note that even the purity level of the electrolyte can play an important role in promoting eventual dissolution phenomena of the Al collector [121].

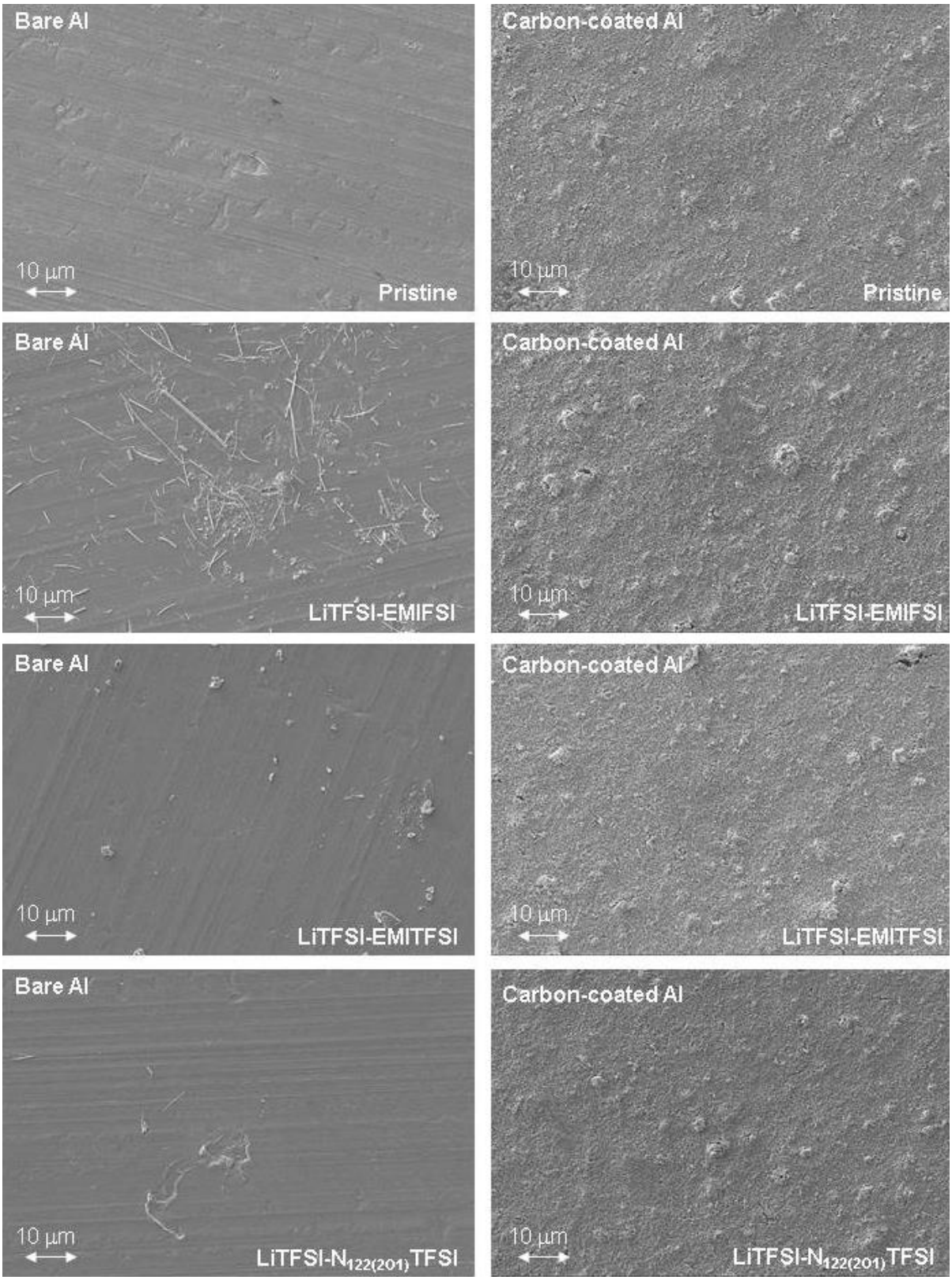

Figure 2.20: SEM micrographs taken on bare (left panels) and carbon-coated (right panels) Al current collectors upon consecutive CV scans (reported in **Figure 2.21**) in 0.2LiTFSI-0.8EMIFSI, 0.2LiTFSI-0.8EMITFSI and 0.2LiTFSI-0.8$N_{122(2O1)}$TFSI) ionic liquid electrolyte mixtures. SEM images, taken on pristine Al collectors (both bare and carbon coated) are reported for comparison purpose. Magnification: 1.00 kX [118].

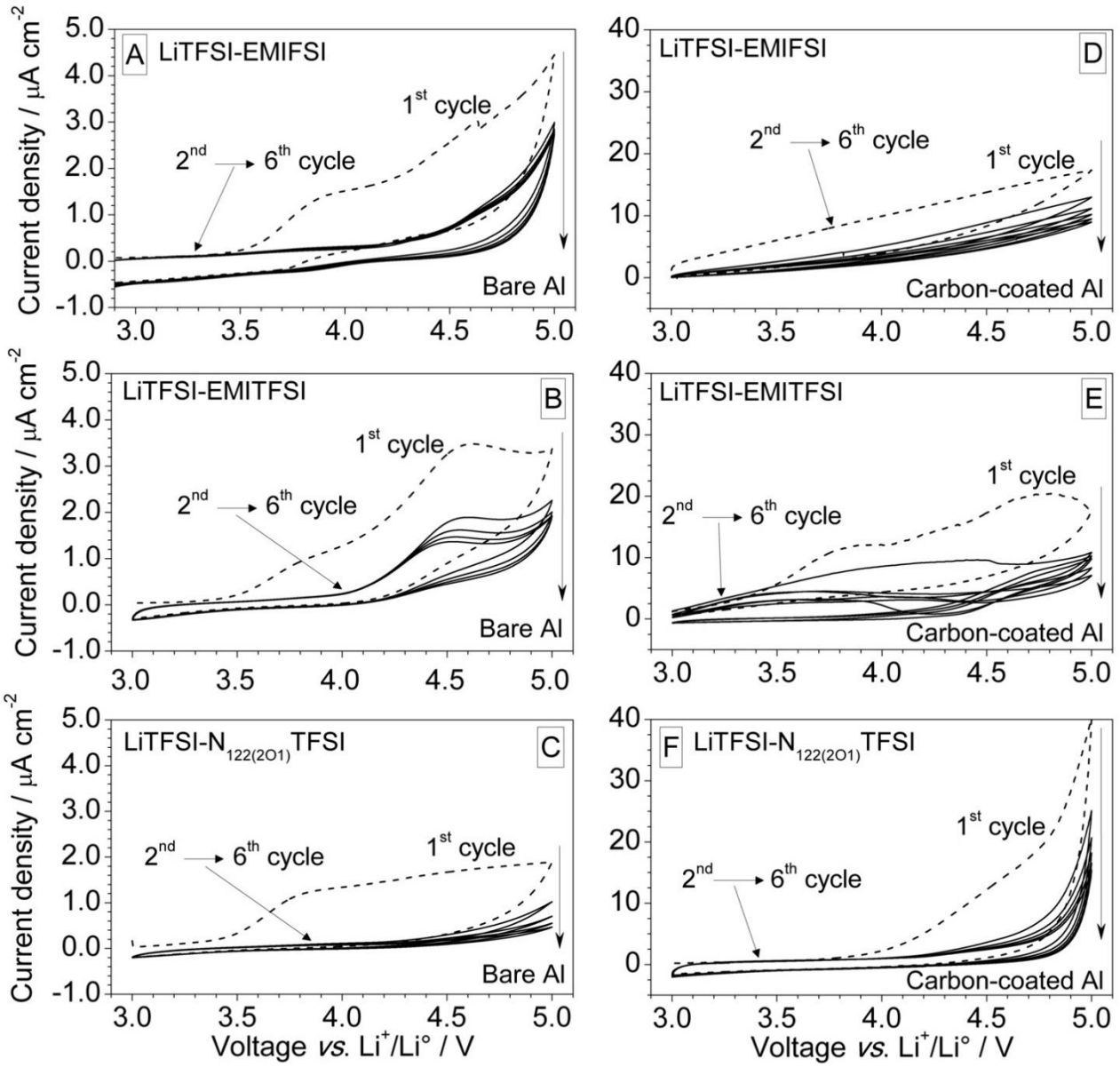

Figure 2.21: Anodic CV scans of 0.2LiTFSI-0.8EMIFSI (panels A and D), 0.2LiTFSI-0.8EMITFSI (panels B and E), and 0.2LiTFSI-0.8$N_{122(2O1)}$TFSI (panels C and F) ionic liquid electrolyte mixtures in bare (panels A, B and C) and carbon-coated (panels D, E and F) Al working electrodes, respectively. Lithium metal as the counter electrode. Scan rate: 1 mV s^{-1}. Temperature: 30 °C. The current density value was obtained by normalizing the current flow with respect to the geometrical surface area of the working electrode.

Sodium-based IL electrolytes

Preliminary LSV Test

LSV tests have been preliminarily carried out on Na/Pt cells for roughly estimating the anodic limit voltage of the Na-conducting electrolytes. The LSV-specific current curves (normalized with respect to the geometric working electrode area) relative to the cell voltage are shown in **Figure 2.22**. All samples exhibit an electrochemical stability above 4.5 V vs. $Na^+/Na°$ backed up by a very low current flow (< 5 μA cm^{-2}) up to the anodic break down voltage; this is highlighted by a steep current increase due to the massive degradation of the electrolyte at high voltages. A few IL samples show weak features (i.e., not exceeding 10 μA cm^{-2}) located from 2.0 to 3.0 V, which is probably ascribable to the irreversible oxidation of minor contaminants at the platinum working electrode. However, apart from this negligible electrochemical signal, no appreciable current increase is observed up to the massive degradation of the electrolyte. The electrolytes containing EMIFSI, N_{1114}FSI, PIP_{13}TFSI and PIP_{14}TFSI as the ionic liquid are very stable up to about 5 V (vs $Na^+/Na°$). Meanwhile, the LSV curve of the $N_{1114}IM_{14}$ electrolyte does not exhibit a sudden current increase but rather, a moderate raise around 5.3 V. This behavior, previously observed in other IM_{14} ionic liquid electrolytes [102,125], is likely due to the ability of the IM_{14} anion species to form an insulating by product upon irreversible oxidation. The accumulation of these insoluble degradation species likely leads to a resistive and less electronically conductive passive layer on the working electrode surface. Based on the LSV results, a cut-off voltage equal to 4.6 V (at which a current density lower than 10 μA cm^{-2} was observed) was adopted for the CV tests (i.e., carried out on carbon working electrodes for all sodium IL electrolytes).

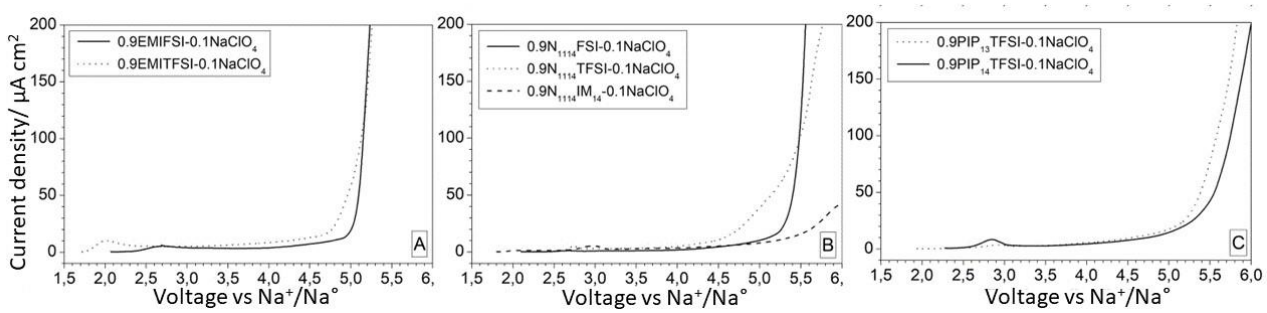

Figure 2.22 Current-voltage traces obtained through LSV tests run on Na/Pt cells containing EMI (panel (A)), N_{1114}^+ (panel (B)) and PIP_{1A}^+ (panel (C)) electrolytes. Ionic liquid: $LiClO_4$ mole ratio = 9:1. Scan rate: 1 mV s^{-1}. Temperature: 20 °C. The voltage values are referred to the $Na^+/Na°$ redox couple.

CVs on carbon electrodes

The ESW of the sodium-conducting electrolytes has been investigated by cyclic voltammetry tests run both in anodic and cathodic regions. The anodic stability was evaluated using carbon-based

electrodes, in which the electrolytes are deliberately stressed up to 4.6 V in order to evaluate their robustness under severe operative conditions. The results, reported in **Figure 2.23** as CV profiles, highlight a similar behavior for all investigated electrolytes. The undesired current increase of 20–50 µA cm^{-2} observed starting from 3–3.5 V in the first anodic scan (dotted traces), is limited to the first cycle as it disappears in the following cycles, where the current values never exceed 10 µA cm^{-2} up to 4.5 V. It is likely that the initial raise in current is due to the irreversible oxidation of contaminants

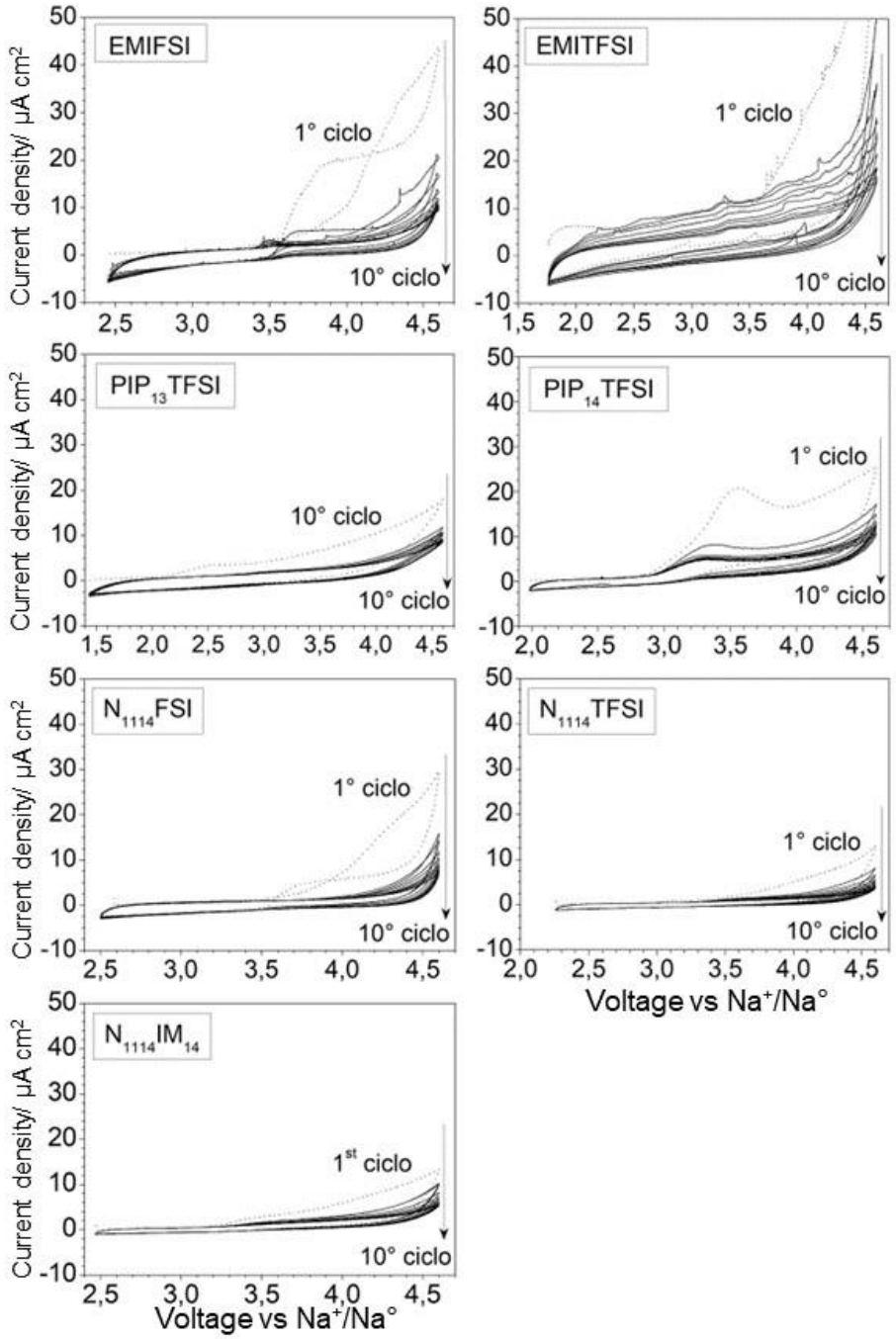

Figure 2.23: Current-voltage profiles obtained by anodic CV measurements run on Na/C cells containing different 0.1NaClO4-0.9IL electrolytes (panels from (A-G)). Scan rate: 1 mV s^{-1}. Temperature: 20 °C.

which, in our case, are fully degraded during the initial CV cycle despite their ability to catalyze the electrolyte decomposition [58]. Overall, the very low current values recorded up to the massive electrolyte degradation (mostly ascribable to the oxidation of the anion even if the cation may play a role) [58], which were highlighted by the rise onset around 4.5 V, confirms the high purity level of the IL electrolytes. The anodic limit voltage values (EA), taken when the current flow recorded during the CV measurements (**Figure 2.23**) achieves 10 (EA_1) and 20 (EA_2) µA cm^{-2}, are summarized in **Table 2.8**. All IL electrolytes show good anodic stability well above 4 V vs $Na^+/Na°$ (i.e., current values lower than 20 µA cm^{-2} are detected up to 4.6 V in the second anodic scan), fully matching the requirement for application in NIB systems. The electrolytes based on the EMI cation show current values higher than those of the IL samples consisting of piperidinium and N_{1114} cations and containing an analogous anion (FSI or TFSI), attributable (at least partially) to the greater ionic conduction of 1-ethyl-3-methylimidazolium [93]. However, as previously reported in the literature for similar types of ionic liquids [58], such behavior suggests that the nature of the cation plays an active role in the electrochemical oxidation process, although it is mainly attributable to the anion. Finally, voltammetric measurements performed on piperidinium-based electrolytes ($PIP_{13}TFSI$, $PIP_{14}TFSI$) suggest that the anodic stability does not appear to be appreciably affected by the length of the alkyl side chain linked to the cation. To summarize, the stability towards oxidation of the investigated IL electrolytes follows the sequence TFSI > IM_{14} > FSI, in agreement with the results reported in the literature [72,98,118].

Table 2.8. Anodic voltage values (EA) determined by the CV measurements (reported in Figure 2.23) run on 0.1$NaClO_4$-0.9IL electrolytes at 20 °C. The voltage, referred to the $Na^+/Na°$ redox couple, were taken when the current density through the cell reached 0.01 (EA_1) and 0.02 (EA_2) mA cm^{-2} during the 1st and 2nd anodic scan, respectively. The error bar is equal to 0.001 V.

Electrolyte mixture	**1st anodic scan / V**		**2nd anodic scan / V**	
	EA_1	**EA_2**	**EA_1**	**EA_2**
0.9EMIFSI:0.1$NaClO_4$	3.984	4.142±	4.311±	4.589±
0.9EMITFSI:0.1$NaClO_4$	3.453	3.789±	3.166	4.093
0.9N_{1114}FSI:0.1$NaClO_4$	4.092	4.372	4.514	>4.8
0.9N_{1114}TFSI:0.1$NaClO_4$	4.464	>4.8	>4.8	>4.8
0.9N_{1114}IM4:0.1$NaClO_4$	4.381	>4.8	4.598	>4.8
0.9PIP_{13}TFSI:0.1$NaClO_4$	3.947	>4.8	4.479	>4.8
0.9PIP_{14}TFSI:0.1$NaClO_4$	3.248	3.489	4.212	>4.8

Effect of contaminants on the anodic stability

The effect of the moisture content on the anodic stability of the IL electrolytes was investigated by means of CV measurements (**Figure 2.24**) performed on a selected sample (i.e., 0.1 $NaClO_4$-0.9 EMITFSI), which had been previously exposed to the external atmosphere. The adsorbed moisture content was estimated around 200–300 ppm by Karl-Fisher coulomb-metric titrations. Comparing these results with those obtained on the analogous anhydrous (<2 ppm moisture) electrolyte (Figure 21), a current increase of about one order of magnitude is observed up to the fourth CV cycle with a decrease in the subsequent ones (**Figure 2.24A**). A similar behavior is observed even if the voltammetric measurements are run up to lower cut-off voltages (i.e., 4.2 (Figure **2.24B**) and 4.0 V (Figure **2.24C**)), despite the current value throughout the cell being significantly reduced. Therefore, the increase in current recorded in the initial cycles is attributable to the presence of humidity and/or molecular oxygen, which are both able to catalyze the degradation processes (oxidation) of the electrolyte and result in a decrease in electrochemical stability. Conversely, the decrease in the current value, recorded after a few voltammetric cycles, is probably ascribable to the formation of an electronically insulating passive layer on the working electrode. These experimental findings, also reported in the literature for other ionic liquids [126,127], clearly show how the presence of impurities (such as humidity and/ or oxygen) can negatively affect the properties of electrolytes, particularly regarding the electrochemical stability.

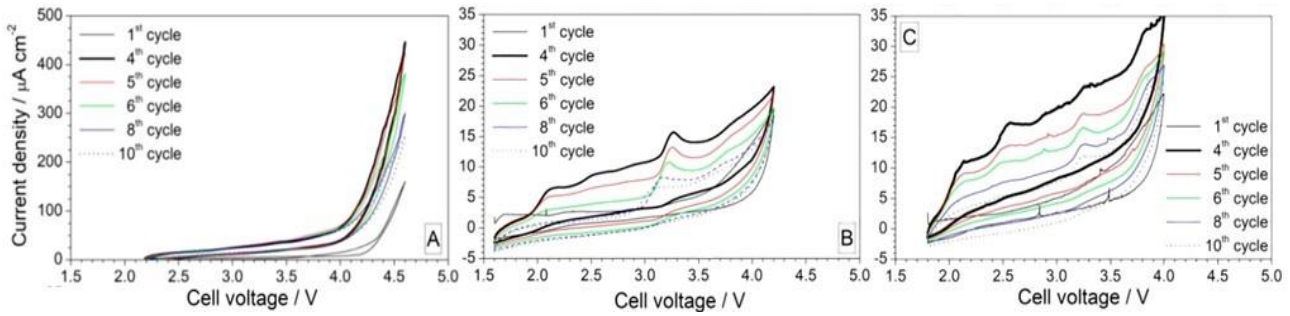

Figure 2.24. Current-voltage profiles obtained by anodic CV measurements run on Na/0.9EMITFSI-0.1$NaClO_4$/C cells in the presence of moisture contaminations at different anodic cut-offs: 4.6 V (panel (A)), 4.2 V (panel (B)) and 4.0 V (panel (C)). Scan rate: 1 mV s^{-1}. Temperature: 20 °C. The voltage values are referred to the Na^+/Na° redox couple.

Cathodic stability

The electrochemical stability towards reduction was investigated by cyclic voltammetry (**Figure 2.25**) in the cathodic range on HC working electrodes capable of reversibly intercalating sodium ions [128]. The CV measurements were carried out at a scan rate (0.05 mV s^{-1}) considerably lower than the anodic ones (1 mV s^{-1}) for promoting the intercalation (de-intercalation) processes of sodium ions

which, in cases of higher rates, may be hindered by kinetics. The FSI-based electrolytes (**Figure 2.25A and 2.25E**) show a large feature around 1 V that is present in the first cathode scan but absent in the following cycles and, therefore, is attributable to the formation of passive SEI constituted by the products coming from the electrolyte degradation [129–131] on the working electrode. Once formed, the SEI allows the reversible intercalation/de-intercalation of the Na^+ cations [128]. The reversibility of the sodium intercalation process in the HC-working electrode is further highlighted by composite peaks that appear constant when cycling at about 0.5–0.6 V in the cathode scans, whereas a symmetric feature around 0.6–0.7 V is observed in the anode scans.

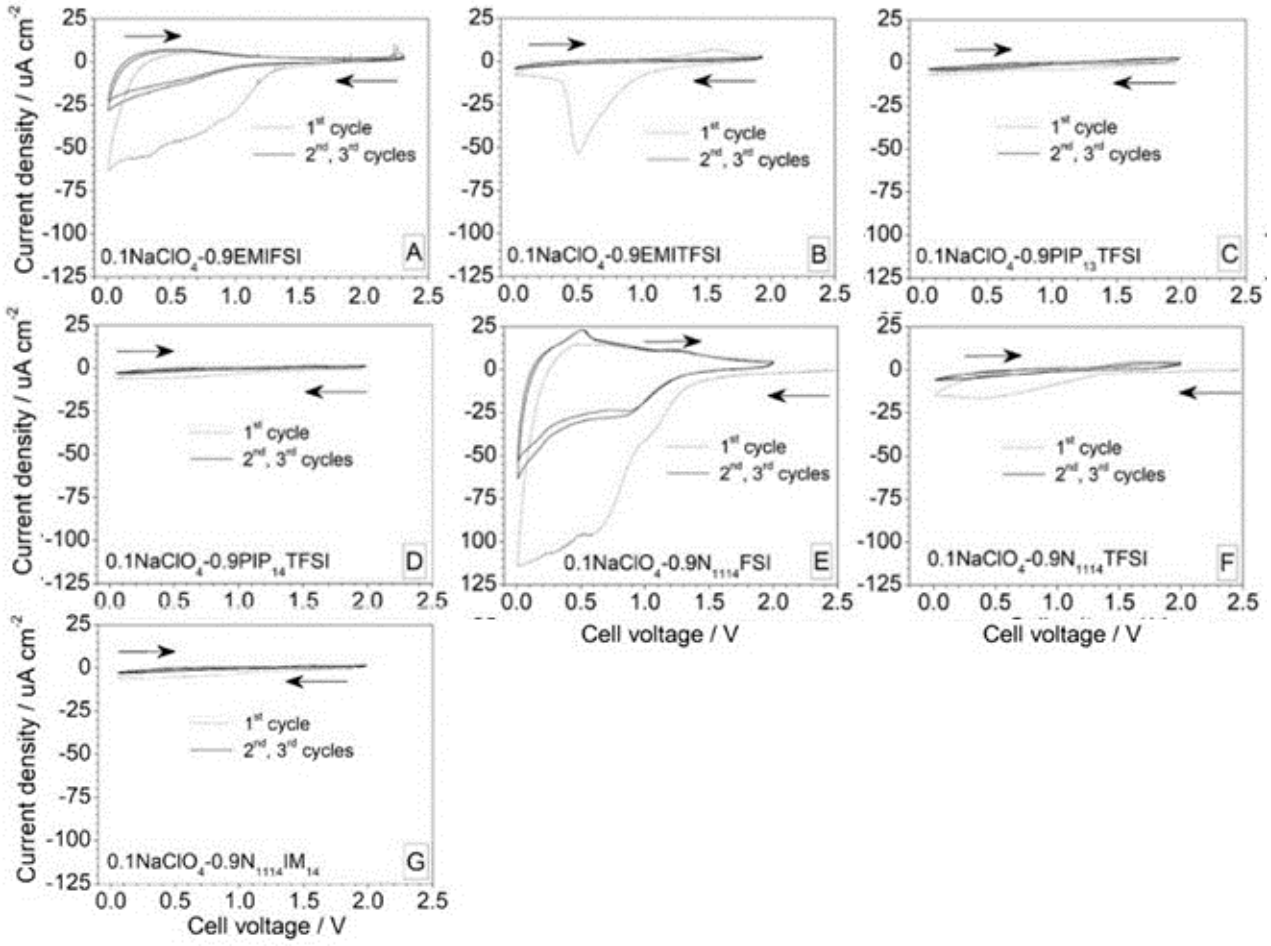

Figure 2.25: Current-voltage profiles obtained by cathodic CV measurements run on Na/HC cells containing different $0.1NaClO_4$-0.9IL electrolytes (panels from (A-G)). Scan rate: 0.05 mV s^{-1}. Temperature: 20 °C. The voltage values are based on the Na^+/Na° redox couple.

No feature related to the IL electrolyte reduction is observed up to 0.01 V, clearly showing the possibility of reversibly intercalating sodium cations. This avoids irreversible degradation phenomena of the electrolyte components, indicating how the FSI anion can form optimal interphases even on sodium-intercalating electrodes. For instance, the ability of the FSI anion to form optimal protective films on LIB anodes, such as lithium metal, graphite, and silicon, is widely reported in the

literature [58]. Conversely, the electrolyte formulations containing the TFSI (**Figures 2.25B, 2.25D and 2.25F**) and IM_{14} (**Figure 2.22G**) anions do not exhibit any significant profile attributable to the intercalation process of Na^+ ions within the HC electrode. The samples containing the ionic liquids EMITFSI (**Figure 2.25B**) and N_{1114}TFSI (**Figure 2.25F**) show a clear profile around 0.5 V in the first cathode scan due to the formation of a passive film, while the subsequent anodic scan shows an even broader peak (in particular, EMITFSI) at about 1.5 V. However, this is more likely due to the oxidative processes catalyzed by degradation products of the electrolyte, rather than the de-intercalation of sodium. Poor electrochemical activity is observed in the subsequent cycles. This behavior may be due to the poor ability of the TFSI and IM_{14} anions to form stable, passive films on anodic active materials, as previously observed in lithium batteries [58]. Overall, almost negligible cathodic currents were measured using these IL electrolytes down to 0.01 V vs. Na^+/Na, proving the strong electrochemical robustness towards reduction. To summarize, the anodic and cathodic CV measurements indicate a large electrochemical stability window up to 4.5 V and down to 0.01 V vs. Na for IL-based sodium-ion electrolytes.

3. Silicon-based anode for Li-ion batteries

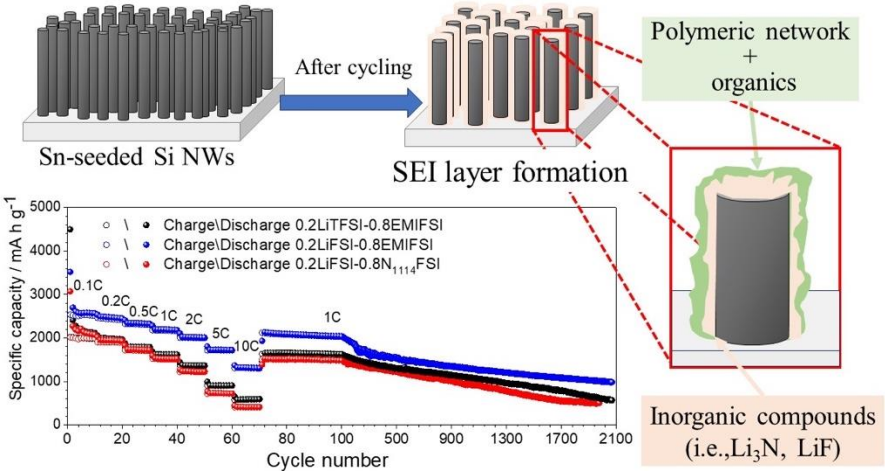

3.1 Introduction

Lithium-ion batteries (LIBs) have revolutionized the field of energy storage and are widely used in a wide variety of applications, including electric vehicles (EVs). These batteries are known for their high energy density, lightweight design, and long cycle life, making them an ideal choice for powering EVs [132–135]. The thriving EV markets have created a pressing demand for the advancement of high-energy-density storage devices aiming to achieve an energy density of 500 W h kg^{-1} or higher [136]. However, it is important to note that while lithium-ion batteries have made significant strides in the electric vehicle industry, further research and development are underway to enhance their performance, sustainability, and safety [132–135]. For example, extremely fast overcharging could promote lithium plating, resulting in detrimental effects on battery performance and safety. Moreover, lithium metal can lead to the growth of dendrites, which are conductive filaments capable of penetrating into the separator and causing short circuits, thermal runaway, and even battery fires or explosions. This risk is particularly relevant in EVs, where large numbers of lithium batteries are densely packed together [135–137].

At system level, several strategies can be approached to prevent the spread of thermal runaways, including the construction of fire-resistant casings, the use of high thermal resistance separators, and the setting of thermal barriers between the cells.

At material level, ensuring the thermal stability of the cell components such as cathode, anode, and electrolyte can significantly enhance the intrinsic safety of the LIBs. For the cathode, a protective coating can prevent the extended reaction at the cathode-electrolyte interphase, minimizing the risk of side reactions or degradation [136–138]. From the anode side, replacing the lithium metal anode with an alternative material could be an important step for improving the battery safety. In this regard, silicon has gained attention due to its high capacity for energy storage (4200 mA h g^{-1} for $Li_{22}Si_5$)

high abundancy (second most abundant element in the Earth's crust), and intermediate discharging potential (about 0.3-0.4 V vs Li^+/Li^0) which can help in preventing Li dendrite formation. However, for accommodating 4.4 Li atoms, which correspond to the $Li_{22}Si_5$ alloy, the Si structure is exposed to detrimental stress induced by a large volume change (about 400 %) which can lead to rapid degradation of the electrode and pulverization under prolonged cycling [139–141].

In 2008, Candace and coworkers demonstrated that the nanostructures (in particular, nanowires, NWs) can hold large strain without developing fractures and cracks on the NWs surface, securing a good electrical contact between the current collector and the tip of the NWs [142]. In addition, the large volume expansion in the Si anode strongly affects the stability of the so-called solid electrolyte interphase (SEI) [139]. The SEI layer is forming at the negative electrode during the initial charging process and consists of a complex heterogeneous and structurally disordered passivation layer containing organic and inorganic species coming from the electrolyte decomposition. It acts as a protective barrier, blocking further reactions between the electrolyte and the anode while allowing the transport of lithium ions [143–146]. For the Si-based anodes, the cyclic expansion and contraction of the active material expose the SEI layer to continuous cracks, forming a "fresh" Si surface that interacts with the electrolyte creating a new SEI layer [147]. This dynamic, uncontrolled, and non-uniform formation of the SEI layer can negatively impact the safety and long-term stability of the cell. Therefore, ensuring a mechanically robust and chemically stable SEI layer can be facilitated by using functional additives in the electrolyte such as vinylene carbonate (VC) and fluoroethylene carbonate (FEC) [148–150]. Although the SEI layer is essential for the safety and stability of the cell, the understanding of its nature and behavior is still very challenging. The nanometric dimension of the SEI layer (10-50 nm thick) makes its characterization challenging and easily biased by artifacts. For example, incomplete electrode post-mortem cleaning procedures (washing and drying) can leave electrolyte/salts residues whereas many SEI constituents are particularly sensitive to humidity and air pollution. As an example, ROLi and $ROCO_2Li$ can react with ambient CO_2 inducing ex-situ SEI evolution to form large amounts of Li_2CO_3. The SEI formation is affected by multiple factors: current rate, temperature, voltage, electrolyte composition, and concentration. Recently, the use of complementary techniques has been successfully demonstrated, including predictive computational models like machine learning, to gain insights into the formation and progression of the SEI layer. For the characterization of the SEI surface, the most common analysis techniques are atomic force microscopy (AFM), secondary ion mass spectroscopy (SIMS), and X-ray photoelectron spectroscopy (XPS). Additional information on the morphology of the layer can be obtained by using scanning electron microscopy (SEM) and transmission electron microscopy (TEM) [143,144,147,150,151].

Turning back to the safety concerns related to electrolytes, the most radical way to drastically reduce this issue is the substitution of flammable organic carbonates with intrinsically non-flammable ionic liquids. It has been demonstrated that quaternary ammonium cation ILs are cathodically stable on Si electrodes [152,153]. Notably, FSI-based ILs revealed better cycling behavior and higher capacity retention as compared to the TFSI ones, likely due to the formation of a more stable SEI layer onto the Si surface [154,155]. The inorganic products (LiOH and Li_2O), coming from the decomposition of the FSI anion onto the Si anode, can promote Li ion diffusion and boost the cycling performance [154].

In this scenario, the present work focuses on investigating the lithiation process of Sn seeded Si nanowire (hereafter Sn-Si NW) anodes in different IL electrolyte formulations (0.2LiTFSI-0.8EMITFSI, 0.2LiTFSI-0.8EMIFSI, and 0.2LiFSI-0.8EMIFSI). All silicon electrodes, which were investigated in the present PhD activity, were developed, synthesized, and provided by University of Limerick (EIRE) [156]. The effect of the FSI and TFSI anions was examined through cyclic voltammetry (CV) and impedance analysis. The modulation of the lithium-ion diffusivity across the SEI layer, on which the rate performance of Sn-Si NW anodes depends, was evaluated by analyzing the Li^+ diffusion coefficient. The role of the anions/cations as well as the effect of the FEC additive on the cell performance was also evaluated. Finally, the SEI layer composition was analyzed through ex-situ XPS measurements.

3.2 Experimental Section

3.2.1 Materials and Methods

Table 3.1 summarizes the weight composition of the IL electrolyte formulations selected for the investigation with Sn-Si NW anodes. The 1M Lithium hexafluorophosphate ($LiPF_6$) in ethylene carbonate:dimethyl carbonate (EC: DMC=1:1 vol.%) with 3 wt.% FEC as well as pristine FEC was provided by Solvionic and used (as received) for comparison purpose.

Table 3.1. IL electrolyte formulations selected for investigation with Sn-Si NW and a-Si anodes.

Mole fraction	Lithium salt	Mole fraction	IL	Mole fraction	Additive
0.20	LiTFSI	0.80	EMITFSI	--	--
0.20	LiTFSI	0.80	EMIFSI	--	--
0.20	LiTFSI	0.79	EMIFSI	0.01	FEC
0.20	LiTFSI	0.78	EMIFSI	0.02	FEC
0.20	LiTFSI	0.73	EMIFSI	0.07	FEC
0.20	LiTFSI	0.80	EMIFSI	+ 3 wt.%	FEC
0.20	LiFSI	0.80	EMIFSI	--	--
0.20	LiFSI	0.80	$N_{1114}FSI$	--	--

Copper silicide ($Cu_{15}Si_4$) nanowires, utilized as nanostructured hosts for amorphous silicon deposition, were prepared according to a procedure described in detail elsewhere [157,158]. The amorphous silicon (a-Si) anodes have a Si mass loading ranging from 0.1 to 0.25 mg cm^{-2}, corresponding (accounting for a Si theoretical specific capacity equal to 4,200 mA h g^{-1}) to a capacity from 0.42 to 1.05 mA cm^{-2}. The tin-seeded silicon nanowire (Sn-Si NW) anodes were synthesized in a solvent-vapor system following a method reported in the literature [159]. The Sn/Si NW anodes present a mass loading between 0.1 and 0.25 mg cm^{-2}, corresponding (accounting for nominal capacity values equal to 2,000 and 994 mA h g^{-1} for Si and Sn, respectively) to an overall capacity from 0.13 to 0.54 mA h cm^{-2}.

All materials as well as the cell manufacturing were dried, stored, and handled in an Ar-filled dry box (Jacomex, Dagneux, France, O_2, and H_2O level < 1 ppm).

3.2.2 Electrochemical measurements

The electrochemical measurements were carried out on Li metal cells using CR2032 containers. The a-Si or Sn-Si NW anodes were used as working electrodes, and a lithium metal disk (500 µm thickness, 10 mm diameter, Linyi Gelon LIB Co) acted as the counter electrode. The electrodes were separated using two glass-fiber disk (16 mm diameter) separator (Whatman TM, Maidstone, UK). The cells were kept under vacuum for 30 min to allow complete loading of the IL electrolyte into the working electrode and the separator.

An evaluation of the electrochemical processes taking place in Li/Si cells was carried out in a-Si anodes, through cyclic voltammetric (CV) analysis paired with potentiostatic electrochemical impedance spectroscopy (PEIS) measurements. The CV tests were performed from 0.01 to 2 V vs $Li^+/Li°$ at increasing scan rates, i.e., from 0.05 to 1 mV s^{-1} (four consecutive CV cycles were run at each selected scan rate), followed by 500 cycles at a constant scan rate of 1 mV s^{-1}. The PEIS was carried out on the fresh cells and at the end of each increasing scan rate CV family, in the 10 kHz – 0.1 Hz frequency range with 10 mV amplitude voltage.

Galvanostatic charge-discharge (GC) cycling tests were run on Li/Sn-Si NW cells, which were cycled between 0.01 and 2 V vs $Li^+/Li°$ at current rates from 0.1C to 10C.

All the electrochemical tests were carried out in a climate chamber at 20°C, using a Biologic (Seyssinet-Pariset, France) multichannel battery cycler.

3.2.3 Interfacial characterization

X-ray photoelectron spectroscopy (XPS) was carried out to get information on electrochemical passivation layer (SEI) formation on the Sn-Si NW surface. XPS analysis was performed under an ultra-high vacuum (~ 10^{-9} mbar) using a Kratos AXIS ULTRA spectrometer with a monochromatic Al Kα X-ray radiation source (hν = 1486.6 eV). Pass energy equal to 160 eV and 20 eV was set up

for survey spectra and narrow regions, respectively. The C 1s line at 284.8 eV was used as a charge reference. These spectroscopic studies were performed on the Sn-Si NW surface after electrochemical tests at different states of charge in Li salt-IL electrolytes: *i*) pristine material; *ii*) 1 cycle at 0.1C and *iii*) 1 cycle at 0.1C + 10 cycles at 1C. After the cell dismantling, the Si electrodes were rinsed with tetrahydrofuran (Sigma-Aldrich, anhydrous, ≥ 99.9%) at least three times for removing the residual electrolyte, vacuum-dried at room temperature and then, transferred directly to the XPS analysis chamber using a vacuum glass-oven (Buchi) to avoid contamination from external.

3.3 Results and Discussions

3.3.1 Lithium intercalation process

The results obtained from the CV measurements are displayed in **Figure 3.1**. The current value (A g^{-1}) is normalized with respect to the Si electrode mass loading. A broad feature located around 1.2 V vs Li^+/Li was observed during the first cathodic scans in all three cases (**Figure 3.1A, B, and C**), which relates to the passivation layer (SEI) formation onto the Si anodes [152,160]. This peak disappears in the subsequent cycles, suggesting stabilization of the electrode/ electrolyte interface.

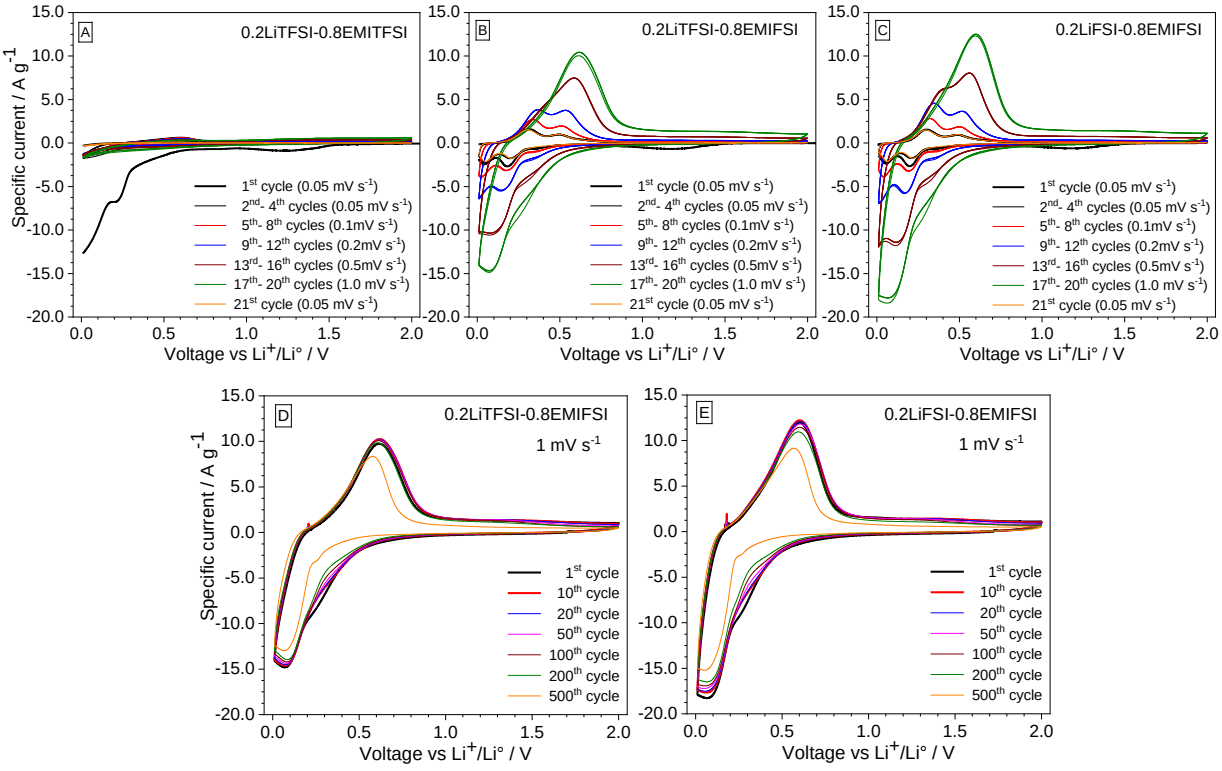

Figure 3.1: Cyclic voltammetry of Li/Si cells containing 0.2LiTFSI-0.8EMITFSI (panel A), 0.2LiTFSI-0.8EMIFSI (panel B), and 0.2LiFSI-0.8EMIFSI (panel C) electrolytes at different scan rates and for prolonged cycles with a scan rate of 1 mV s^{-1}carried out on 0.2LiTFSI-0.8EMIFSI (panel D) and 0.2LiFSI-0.8EMIFSI (panel E) based cells. T = 20 °C.

The Li/Si cells with 0.2LiTFSI-0.8EMITFSI show the peaks relative to the a-Si lithiation in the first cathodic scan: conversely, no evident feature can be noticed in the following cycles, suggesting non-optimal SEI formation (instead progressive lithiation of the amorphized Si anode) [152,160] and highlighting for large irreversible capacity (and, consequently, low initial coulombic efficiency and poor reversibility of the lithium dealloying). The progressive replacement of the TFSI anion with FSI, initially in the IL (**Figure 3.1B**) and then also in Li salt (**Figure 3.1C**), results in very beneficial effect on the cycling behavior. The lithiation of Si initially causes the formation of the amorphous phase Li_xSi, which turns into a crystalline phase below 0.06 V vs Li^+/Li [153], corresponding to two well-defined peaks located at 0.15 and 0.05 V vs Li^+/Li, as can be observed in **Figure 3.1B** and **3.1C**. In the reverse scan, two similar features around 0.3 and 0.5 V vs Li^+/Li arise from the two-phase reaction from crystalline $Li_{15}Si_4$ to amorphous Li_xSi ($x\approx2$), followed by the formation of the delithiated amorphous Si [153,161]. This indicates good reversibility of the delithiation process during the anodic scan, i.e., leading to much higher stored and delivered capacity, possibly due to an optimal SEI growth onto the silicon electrode, given by the much better film-forming ability of the FSI anion with respect to the TFSI one [152,153]. The complete overlap of the voltammograms, even at high scan rates and for prolonged cycles (**Figures 3.1D** and **3.1E**) suggests good reversibility and high coulombic efficiency of the alloying/dealloying process during cycles in the 0.2LiTFSI-0.8EMIFSI and 0.2LiFSI-0.8EMIFSI electrolytes. The increase of the scan rate results in a progressive enhancement of the current flow through the cell, leading to more pronounced and defined current vs voltage features in both verses, with only a moderate shift of the maximum value due to diffusive processes that take place into the electrolyte, according to the Randles-Sevcik equation [162,163]. At 0.2 mV s^{-1} two distinguished profiles are still observed, both in the cathodic (Li^+ alloying) and anodic (Li^+ de-alloying) verse, whereas at faster scan rates no split is recorded. Larger specific current values, resulting in higher capacity involved in the (de)lithiation process, are recorded in the 0.2LiFSI-0.8EMIFSI cells with respect to the 0.2LiTFSI-0.8EMIFSI ones. Prolonged CVs were run only on 0.2LiTFSI-0.8EMIFSI and 0.2LiFSI-0.8EMIFSI cells, after CV tests displayed in **Figure 3.1B** and **3.1C**, to investigate the reversibility of the Li^+ alloying process under hard operative conditions, i.e., 500 cycles at 1 mV s^{-1}. The results, illustrated in **Figures 3.1D** and 3.**1E**, show two defined features around 0.25 and 0.1 V (cathodic scan) and around 0.6 V (anodic scan). A very good reversibility of the lithium alloying process is observed even after 500 cycles, witnessed by the good correspondence between the cathodic and anodic features. A remarkable reproducibility of the cyclic voltammetry traces is recorded for the first 200 cycles, whereas a progressive, even modest, decrease of the CV profile is observed up to the 500^{th} cycle. To summarize, the 0.2LiFSI-0.8EMIFSI electrolyte exhibits

comparable voltammetric features to those of 0.2LiTFSI-0.8EMIFSI, however evidencing higher capacity decay (i.e., more depleted CV profile) after prolonged CV tests (> 200 cycles).

The mobility of lithium ions at electrolyte/silicon interface directly depends on the redox reaction rate according to the Randles-Sevcik equation [162,163], and can be modulated by the SEI layer formed onto the silicon particles, which can enhance the rate performances and reduce the lithium trapping [164]. Therefore, the interfacial lithium diffusion coefficient D_{Li+} (cm^2 s^{-1}) was calculated for a-Si anode cycled into the 0.2LiTFSI-0.8EMIFSI and 0.2LiFSI-0.8N_{1114}FSI electrolytes, evaluating the CV tests recorded at different scan rates (**Figure 3.1B** and **C**) described in the previous paragraph. The D_{Li+} value was calculated by the Randles-Sevcik equation (eq. 1) [165,166] for a semi-infinite diffusion of lithium-ion:

$$Ip = 0.4463\ n\ FAC\ (nFvD_{Li+} / RT)^{1/2} \quad (1)$$

where the I_p is the peak current, R, F, and T are the gas and Faraday constant, and the temperature (K), respectively. A (cm^2) is the active surface area of the a-Si anode, n is the number of electrons in the reaction, C (mol cm^{-3}) is the Li^+ ion concentration in the electrolyte, and v (V s^{-1}) is the scan rate. The relationship of the cathodic and anodic current peaks (I_c and I_a) with the square root of the scan rate is reported in **Figure 3.2**. The current peaks, in the anodic A_n and cathodic C_n scans taken into consideration for the evaluation of D_{Li+}, are displayed in **Figure 3.3**. The slope of the linear fit (**Figure 3.4**) between I_p and $v^{0.5}$ was used to estimate the D_{Li+} [167–169]. Both systems show a linear behavior, indicating diffusion-controlled reaction [170] and a peak current ratio (I_{pa}/I_{pc}) ≈ 1, i.e., reversible lithiation process and no parasitic reaction associated with the electron transfer [166]. The D_{Li+} was found to be equal to (9.6 ± 0.5)×10^{-10} cm^2 s^{-1} for 0.2LiTFSI-0.8EMIFSI and (2.5 ± 0.1) ×10^{-10} cm^2 s^{-1} for 0.2LiFSI-0.8EMIFSI, comparable with the results reported in literature for Li_xSi phases in organic electrolytes and obtained through different technique [171,172]. The error related to the D_{Li+} values is equal to 5 %.

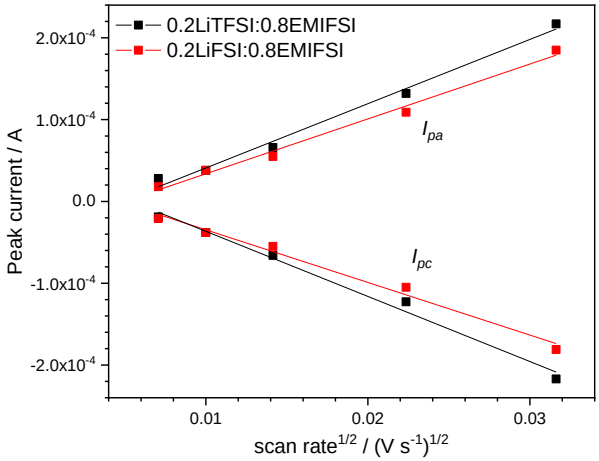

Figure 3.2: Linear fits for the anodic and cathodic peak currents vs square root of the scanning rates of a-Si electrodes in 0.2LiTFSI-0.8EMIFSI and 0.2LiFSI-0.8EMIFSI electrolytes. T = 20 °C.

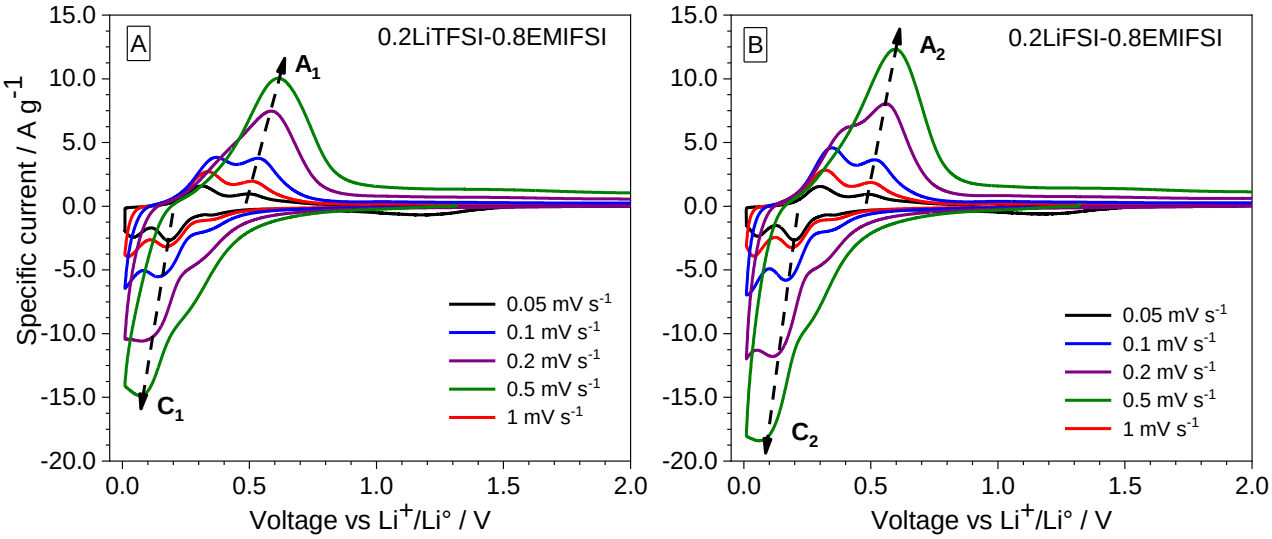

Figure 3.3: CV curves of Li/a-Si cells with 0.2LITFSI-0.8EMIFSI (panel A) and 0.2LiFSI-0.8EMIFSI (panel B) electrolytes at different scan rates. T = 20 °C.

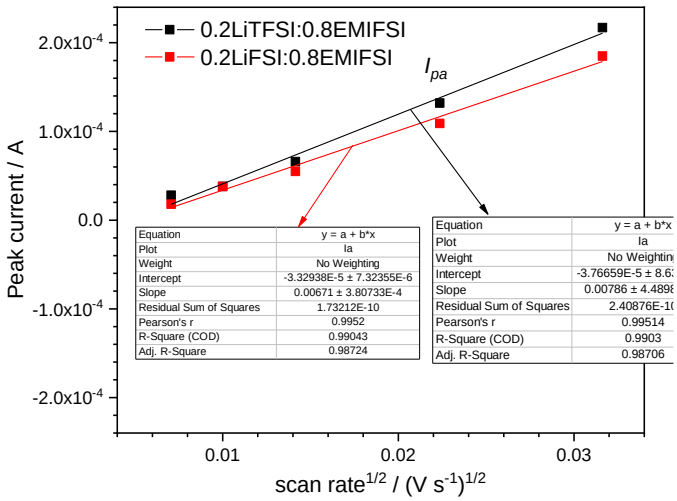

Figure 3.4: Peak current vs scan rate square root dependence for the lithiation of a-Si electrodes in 0.2LiTFSI-0.8EMIFSI and 0.2LiFSI-0.8EMIFSI electrolytes. The related linear fit is also reported. T = 20 °C.

3.3.2 Impedance measurements

Impedance measurements were conducted after each CV family tests run at different scan rates (**Figure 3.1**) and reported in **Figure 3.5** as Nyquist plots. The AC responses display a semicircle pattern at medium-high frequencies and a straight-line at low frequencies, in agreement with other studies on similar anode materials in ionic liquid electrolytes [170,173]. The high-frequency intercept with the real axis corresponds to the bulk resistance (R_{bulk}) of the IL [174–176], and the semicircle diameter gives the overall interfacial resistance R_{int} [177–179]. **Figure 3.6** plots the dependence of R_{bulk} (panel A) and R_{int} (panel B), determined from the AC responses (**Figure 3.5**) taken (in OCV condition) after each CV family of **Figure 3.1**, as a function of the scan rate. The resistance values,

summarized in **Table 3.3**, were evaluated through the equivalent circuit models depicted in **Figure 3.7** where Q_{dl} is the constant phase element accounting for the double layer capacitance and, C_l is the electrode limit capacitance [174–176]. R_{bulk} values equal to 1.7, 1.6, and 1.3 Ω cm were detected (at 20 °C) for the 0.2LiTFSI-0.8EMITFSI, 0.2LiTFSI-0.8EMIFSI, and 0.2LiFSI-0.8EMIFSI cells, respectively, i.e., close to those reported in previous work and summarized in **Table 3.2** [180].

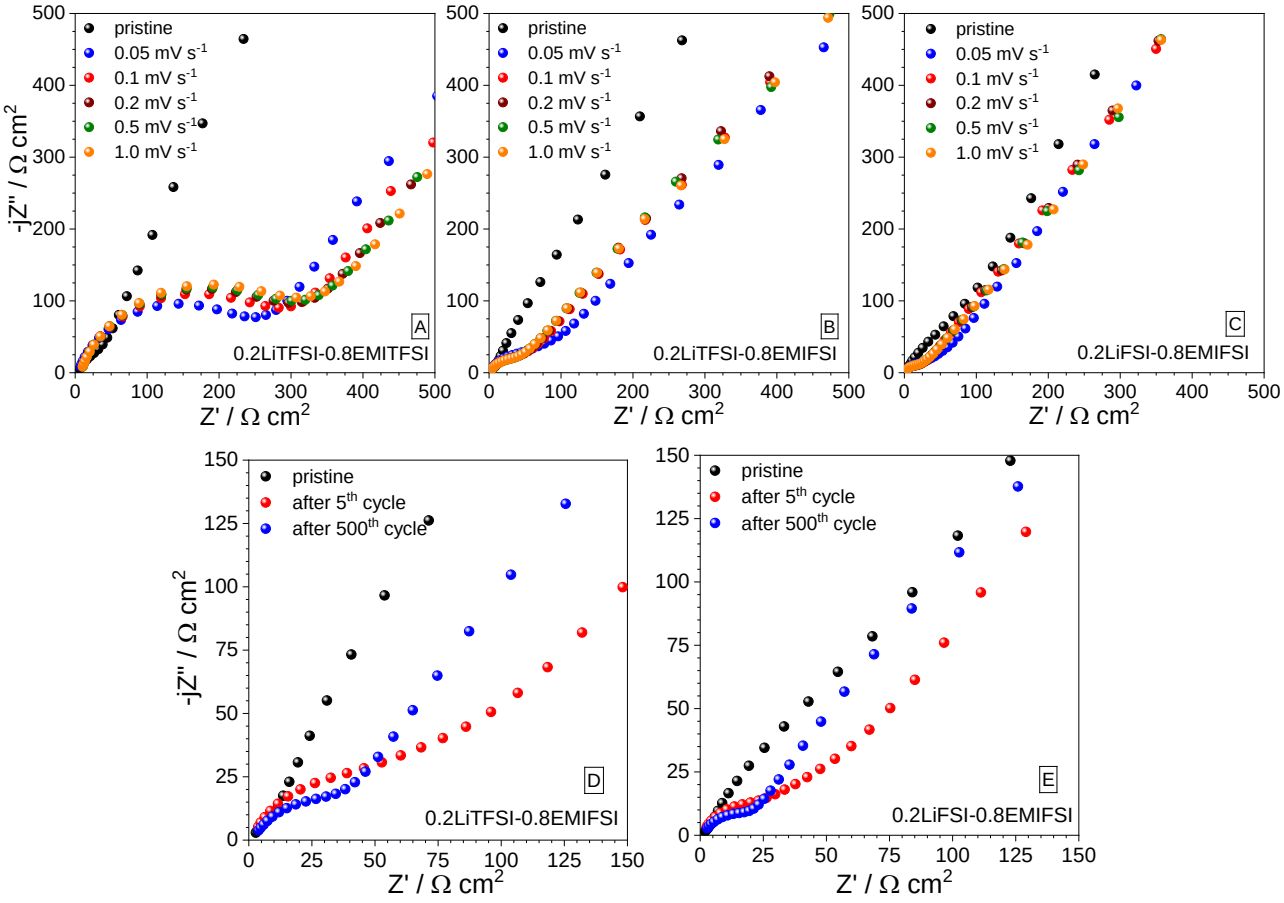

Figure 3.5: AC responses, taken under OCV condition, of Li/Si cells containing the 0.2LiTFSI-0.8EMITFSI, 0.2LiTFSI-0.8EMIFSI, and 0.2LiFSI-0.8EMIFSI electrolytes. The impedance measurements, run after each CV family tests run at different scan rates (Figure 3.1), were carried out at different scan rates (panels A, B, and C) and CV tests at 1 mVs^{-1} (panels D and E). Frequency range: 10 kHz – 1 Hz. Voltage amplitude: ΔV = 10 mV. T = 20 °C.

Significantly, no change of R_{bulk} is observed during the CV tests, confirming the good electrochemical stability of the IL-based electrolytes and the negligible lithium depletion from the electrolyte. However, the replacement of the TFSI anion with FSI results in sharp decrease of R_{int}. For instance, more than 200 Ω cm^2 are recorded for the 0.2LiTFSI-0.8EMITFSI cells (**Figure 3.5A**) whereas only 40 and 20 Ω cm^2 are approximately exhibited by those with 0.2LiTFSI-0.8EMIFSI (**Figure 3.5B**) and 0.2LiFSI-0.8EMIFSI (**Figure 3.5C**), respectively. These results, in very good agreement with the

voltammetry data of **Figure 3.1**, indicate a large decrease in interfacial resistance accompanying the transformation of the original discrete a-Si into a stable porous network (nano-ligaments) [152,160]. Once more, it highlighted the beneficial effect of the FSI anion at the interface with the Si electrode, playing a key role in determining the SEI composition and, therefore, the active material morphology. For instance, a suitable SEI layer leads to a larger surface area offered for the alloying process by the a-Si network and to the accommodation of more facile charge transfer at the electrode/electrolyte interface. Conversely, the TFSI anion is not able to promote the growing-up of suitable SEI, leading to poor Li^+ alloying and, therefore, low performance. This issue is in good agreement with both the CV results of **Figure 3.1**. The AC response recorded after 500 cycles (shown in **Figure 3.5D** and **3E**) exhibit a similar shape with respect to that of the Nyquist plots of the first family cycles (**3.5B** and **3.5C**). No practical change of R_{bulk} is observed whereas more slightly depressed semicircle is exhibited by the 0.2LiFSI-0.8EMIFSI cells, nevertheless demonstrating the electrochemical reliability of the 0.2LiTFSI-0.8EMIFSI and 0.2LiFSI-0.8EMIFSI electrolytes. An overall interfacial resistance lower than 100 Ω cm^2 is recorded in both electrolyte formulations. To summarize, the a-Si anodes seem to show comparable behaviour in both 0.2LiTFSI-0.8EMIFSI and 0.2LiFSI-0.8EMIFSI.

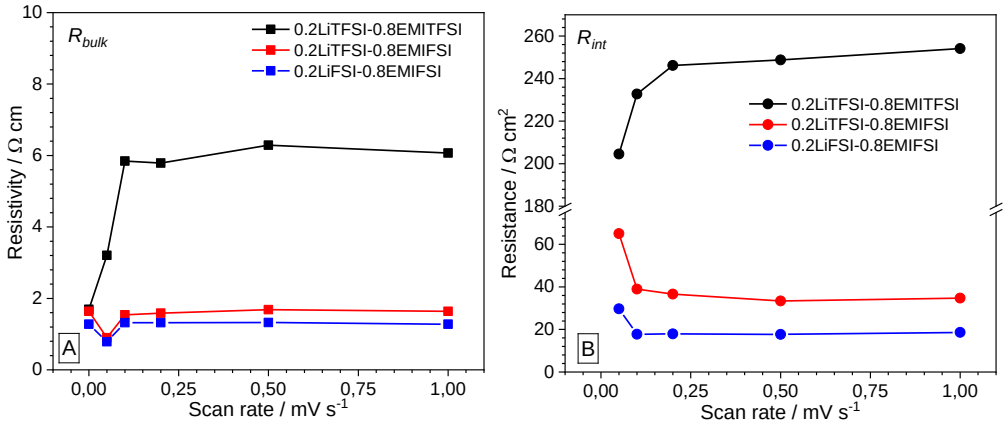

Figure 3.6: Evolution of the electrolyte R_{bulk} (panel A) and overall interfacial R_{int} (panel B) resistance, during CV tests run at different scan rates (Figure 3.1), for Li/a-Si cells in 0.2LiTFSI-0.8EMIFSI and 0.2LiFSI-0.8EMIFSI. T =20 °C.

Table 3.3. R_{bulk} (Ω cm) and R_{int} (Ω cm^2) parameters, associated with Li/a-Si cells containing the 0.2LiTFSI-0.8EMITFSI, 0.2LiTFSI-0.8EMIFSI and 0.2LiFSI-0.8EMIFSI electrolytes, determined in OCV condition after each CV family tests run at different scan rates (Figure 3.1). T = 20 °C.

Scan rate / mV s^{-1}		Pristine	0.05	0.1	0.2	0.5	1
0.2LiTFSI-0.8EMITFSI	R_{bulk}	1.7 ± 0.2	3.2 ± 0.3	5.8 ± 0.6	5.8 ± 0.6	6.3 ± 0.6	6.1 ± 0.6
	R_{int}	--	200 ± 20	230 ± 20	250 ± 30	250 ± 30	250 ± 30
0.2LiTFSI-0.8EMIFSI	R_{bulk}	1.6 ± 0.2	0.9 ± 0.1	1.5 ± 0.2	1.6 ± 0.2	1.7 ± 0.2	1.6 ± 0.2
	R_{int}	--	65 ± 6	39 ± 4	37 ± 4	33 ± 3	35 ± 3
0.2LiFSI-0.8EMIFSI	R_{bulk}	1.3 ± 0.1	0.8 ± 0.1	1.3 ± 0.1	1.3 ± 0.1	1.3 ± 0.1	1.3 ± 0.1
	R_{int}	--	30 ± 3	18 ± 2	18 ± 2	18 ± 2	18 ± 2

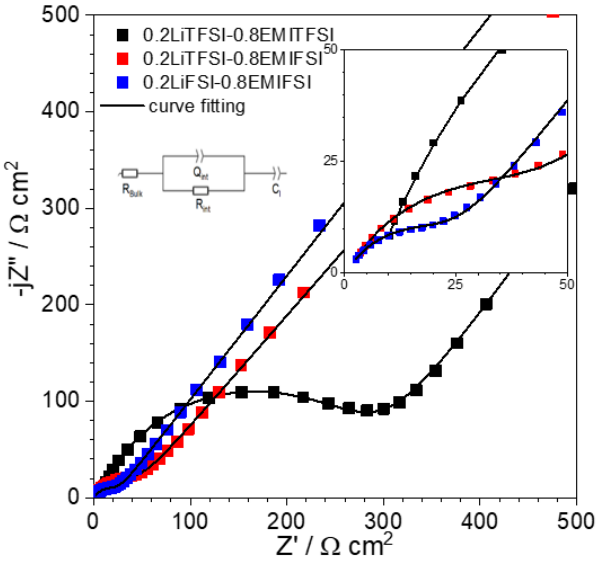

Figure 3.7: AC response of Li/Si cells in 0.2LiTFSI:0.8EMITFSI, 0.2LiTFSI:0.8EMIFSI and, 0.2LiFSI:0.8EMIFSI electrolytes. The high-medium frequency region (and the related curve fitting) is magnified in the insert. The equivalent circuit model adopted for fitting is included.

3.3.3 Cycling behavior

The CV investigation on a-Si anodes has evidenced how EMIFSI is the most suitable IL for silicon electrodes. Therefore, this IL was used as electrolyte solvent for further investigations on Sn-Si NW anodes. The N_{1114}FSI IL was employed for comparison purpose.

3.3.3.1 Effect of Sn/Si ratio

The influence of the Si/Sn weight ratio was preliminarily evaluated through cycling tests. The data, depicted in **Figure 3.8** in terms of capacity (referred to as the overall silicon/tin material weight) evolution as a function of the cycle number, show high and reproducible performance only at Si/Sn ratios above 2.6:1.

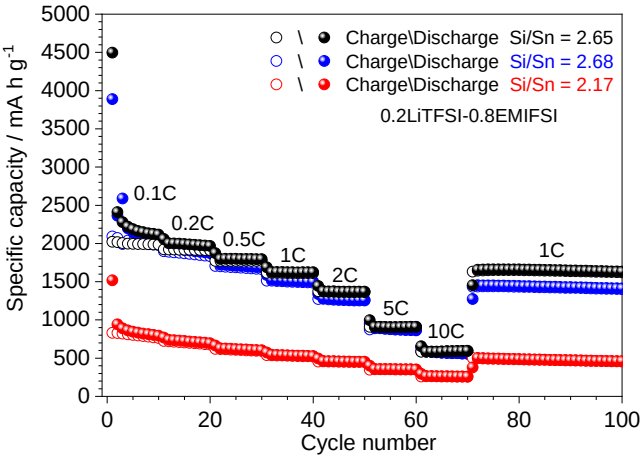

Figure 3.8: Cycling performance of Li/Si cells in 0.2LiTFSI-0.8EMIFSI electrolyte, comparing Si-Sn NW anodes at different Si/Sn weight ratios. Current rates from 0.1 to 10C. T = 20°C.

These results are observed in different electrolyte formulations subjected to various current rates, suggesting that a Sn content above 28 wt.% depletes the overall electrochemical behavior of the electrodes. Further investigation would be needed to better clarify this issue. It is also possible to hypothesize a threshold for the Si/Sn ratio (around 2.6), which must be overcome to allow high cell performance. Therefore, only Si-Sn NW samples having a Si/Sn weight ratio above 2.6 were investigated.

3.3.3.2 Effect of anion and cation

The voltage-capacity profile of the 1st charge-discharge cycle for Sn-Si NW electrodes in EMIFSI and N_{1114}FSI electrolytes is reported in **Figure 3.9A**. A series of features, between 1.2 and 0.2 V, can be noticed during the first discharge curve at 0.1C, likely due to the IL electrolyte degradation leading to SEI layer formation onto the electrode surface [152,160]. These features are followed by two plateaus located around 0.25 and 0.15 V, ascribable to the lithiation process. The value of the initial coulombic efficiency (η) and the nominal capacities (Q) delivered during the rate capability tests on Li/Sn-Si NW cells are reported in **Table 3.4**. The 0.2LiFSI-0.8EMIFSI cell shows the lowest initial irreversible capacity (Q_{irr}), amounting to 28%, with respect to 0.2LiTFSI-0.8EMIFSI and 0.2LiFSI-0.8N_{1114}FSI cells which shown a Q_{irr} equal to 55% and 35%, respectively but quickly levelling to 99% in all cases, as it can be seen in **Figure 3.9A**. A stable capacity value is observed in all electrochemical formulations up to 100 cycles even at very high rates (10C). Higher capacity values were delivered by the 0.2LiFSI-0.8EMIFSI cells at different scan rates, with a gain of ~ 550 mA h g^{-1} up to 1C and of ~ 800 mA h g^{-1} at higher current rate (> 2C) with respect to the other electrolyte systems investigated. The full-FSI cell can deliver above 50 % (1300 mA h g^{-1}) of the nominal capacity at 10 C, meanwhile, the 0.2LiTFSI-0.8EMIFSI and 0.2LiFSI-0.8N_{1114}FSI cells deliver less than 29 and 16 %, respectively, of their nominal capacity at the same current rate. The 0.2LiTFSI-0.8EMIFSI and 0.2LiFSI-0.8N_{1114}FSI electrolyte formulations show very similar capacity values which, at high rates (> 1 C) slightly decay for the N_{1114}FSI cells, likely due to the faster ion transport properties of the EMIFSI ionic liquid with respect to N_{114}FSI [180]. The best performances of the full-FSI cell configuration, in agreement with the CV results, are attributable to the better film-forming ability of the FSI anion with respect to TFSI [152,153]. Conversely, the N_{1114}FSI ionic liquid displays a lower affinity towards Sn-Si NW anodes than EMIFSI. **Figure 3.10** displays the voltage vs capacity profile of Sn-Si NW anodes in different electrolyte formulations and increasing scan rates. The potential of Si alloying plateaus is distributed around 0.1 V and the dealloying plateaus are at about 0.4 V, as reported in the literature [161,181,182]. The presence of Sn in the working electrode is evidenced by the two less-defined plateaus in the potential range of 0.45 – 0.6V (**Figure 3.10**), attributable to the two-phase alloying reaction that involved the formation of the dominant phases

Li_2Sn_5 and LiSn [161,183]. The increase of the current rate from 0.1 to 5C does not result in a significant qualitative change of the voltage profile shape, but it does lead to an increase of lithiation/de-lithiation plateau slope attributed (as well as to an increase in ohmic drop) to diffusive phenomena within the IL electrolyte, especially at high rates.

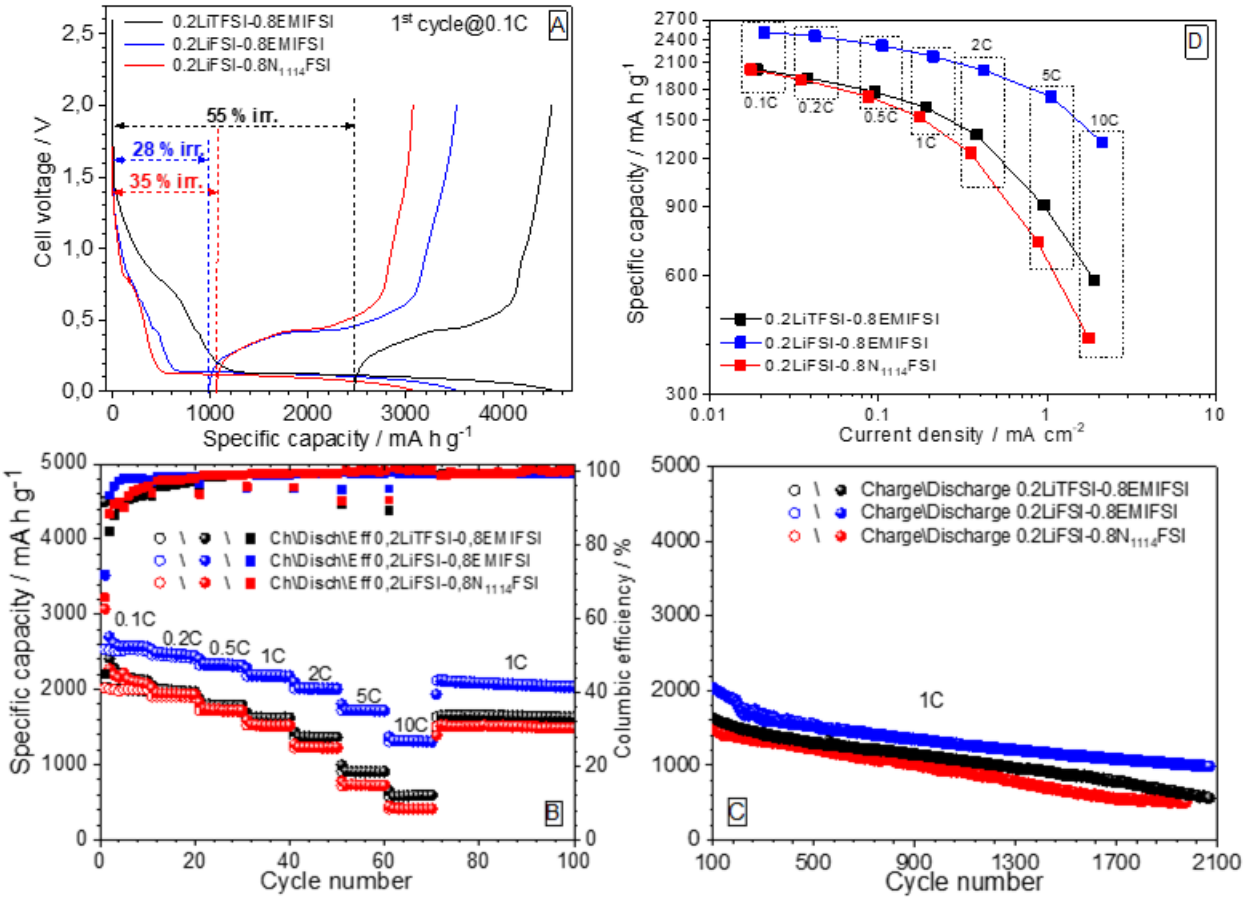

Figure 3.9: 1st discharge-charge curves (panel A), cycling performance at different rates (panels B and C), and reversible capacity vs current density dependence (panel D) of Li/Si cells in 0.2LiTFSI-0.8EMIFSI, 0.2LiFSI-0.8EMIFSI and 0.2LiFSI-0.8N_{1114}FSI electrolytes. The cycling behaviour of Li/Si cells in organic electrolyte (1M $LiPF_6$ in EC:DMC 1:1 v/v + 3 wt.% FEC) is reported for comparison purposes. T = 20°C.

Prolonged tests run at 1C (**Figure 3.9C**) subsequently to the rate capability tests, show a capacity recovery up to the starting value at 1C (**Figure 3.9B**). Very interesting capacity retention, despite a decay observed after 100 cycles, is generally exhibited by these electrolyte formulations, i.e., 1005 (0.2LiFSI-0.8EMIFSI cells), 608 (0.2LiTFSI-0.8EMIFSI) and 509 (0.2LiFSI-0.8N_{114}FSI) mA h g^{-1} are still delivered after 2000 consecutive charge-discharge cycles (1C) at 100 % of DoD, corresponding to 46 % (capacity fading equal to 0.027 per cycle), 37 % (0.031 % per cycle) and 33 % (0.034 % per cycle) of the initial capacity discharged at 1C. The remarkably enhanced performances of the 0.2LiFSI-0.8EMIFSI electrolyte, comparable to or overcoming those observed

in alkyl carbonate and other IL electrolytes [152,160], are once more likely ascribed to the better film-forming ability of the FSI anion, in combination with the transport properties of the EMI cation. The reversible (charge) capacity vs. current density dependence of the Li/Sn-Si NW Sn cells (**Figure 3.9D**) evidences a lower rate region, where the capacity is limited by the diffusion phenomena taking place within the Si electrode [184,185], distinguished by the higher rate one characterized by a more pronounced slope of the capacity vs current density curve due to diffusive phenomena occurring in the ionic liquid electrolyte [184,185]. The lower rate region limit is around 0.3 mA cm^{-2} for the 0.2LiTFSI-0.8EMIFSI and 0.2LiFSI-0.8N_{1114}FSI electrolytes: above this current rate the electrochemical behavior of the Li/Si cells is governed by diffusive phenomena. Interestingly, the lower rate region extends up to 1 mA cm^{-2} in 0.2LiFSI-0.8EMIFSI, cells, indicating that diffusion processes become predominant in this electrolyte at much higher current density with respect to that observed in 0.2LiTFSI-0.8EMIFSI and 0.2LiFSI-0.8N_{114}FSI. To summarize, the 0.2LiFSI-0.8EMIFSI electrolyte exhibits, among the investigated IL formulations, the best cycling behavior in Sn-Si NW anodes.

Table 3.4: Initial Coulombic efficiency (η) and reversible capacity, delivered at different scan rates, of Li/Sn-Si NW cells in different electrolyte formulations.

Electrolyte formulation	**1st cycle**	**Reversible capacity / mA h g^{-1}**							
	***η* / %**	**0.1C**	**0.2C**	**0.5C**	**1C**	**2C**	**5C**	**10C**	**1C$_{100th}$**
0.2LiTFSI-0.8EMIFSI	45	1995	1918	1774	1611	1363	904	586	1622
0.2LiFSI-0.8EMIFSI	72	2522	2442	2317	2175	2006	1720	1313	2027
0.2LiFSI-0.8 N_{1114}FSI	65	1998	1905	1715	1512	1226	731	414	1494

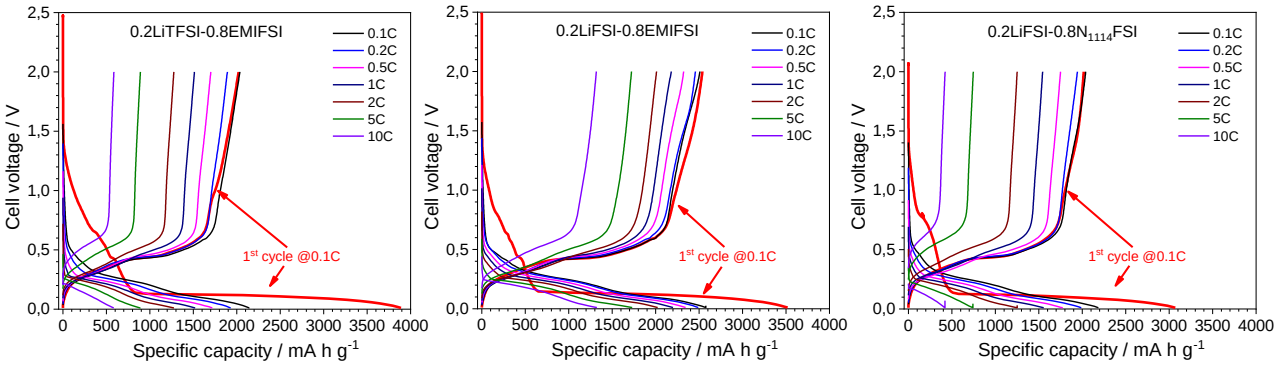

Figure 3.10: Selected voltage vs. capacity profiles of Li/Sn-Si NW cells in 0.2LiTFSI-0.8EMIFSI (panel A), 0.2LiFSI-0.8EMIFSI (panel B) and 0.2LiFSI-0.8N_{1114}FSI (panel C) electrolytes at different current rates (from 0.1C to 10C). T = 20°C.

3.3.3.3 Effect of FEC organic additive

The Sn-Si NW anodes have been also studied in the presence of FEC organic additive to investigate a possible improvement of the electrolyte/electrode interface [148]. The cycling tests, reported in **Figure 3.11**, were carried out in LiTFSI-EMIFSI electrolytes containing different FEC molar fractions (summarized in **Table 3.1**). The first discharge profile at 0.1C (**Figure 3.11A**) exhibits the typical features of silicon electrodes (already discussed in the previous paragraph), however, the progressively increasing FEC content is seen to enhance the features located in the 1.7-0.2 V range and ascribable to irreversible electrolyte decomposition. Particularly, at a FEC content equal to 3 wt.%, a very wide plateau is observed around 0.4 V, leading to a much larger irreversible capacity. The reversible nominal capacity, as well as the initial coulombic efficiency (i.e., from 45 to 55%) and the cycling behavior (even at 10C) up to about 100 cycles, is seen slightly increasing (i.e., from 2000 to about 2100 mA h g^{-1}) after incorporation of a FEC mole fraction equal to 0.01, which exhibits at 1C and 10C a delivered capacity of 1800 and 750 mA h g^{-1} (vs. 1650 and 450 mA h g^{-1} of the FEC-free cells), respectively. Further increases of the FEC up to 3 wt.% content lead to performance decay: for instance, the nominal capacity and the coulombic efficiency fall to 1500 mA h g^{-1} and to 14 %, respectively. Therefore, the presence of FEC mole fractions > 0.01 in IL electrolytes seems to support larger consumption of electrolytes and/or to hinder the formation of an optimal SEI onto the Sn-Si NW surface. As reported in literature [186,187], the uncoordinated FEC can passivate the anode surface by forming LiF, which can promote formation of HF in the presence of even very small amount of water, causing dissolution of the SEI on the Si anode surface. However, more prolonged discharge-charge tests (panel C) reveal progressive decay in performance. For instance, after 1000 cycles the 0.01 FEC cells exhibit lower capacities (950 mA h g^{-1}) than those delivered by the FEC-free ones (1,200 mA h g^{-1}), even approaching the values (900 mA h g^{-1}) shown by the 0.07 FEC and 3 wt.% FEC cells (i.e., no practical difference is seen for FEC mole fractions exceeding 0.07). This means an increase in capacity fading from 0.03 % (FEC-free cells) to 0.05 % per cycle.

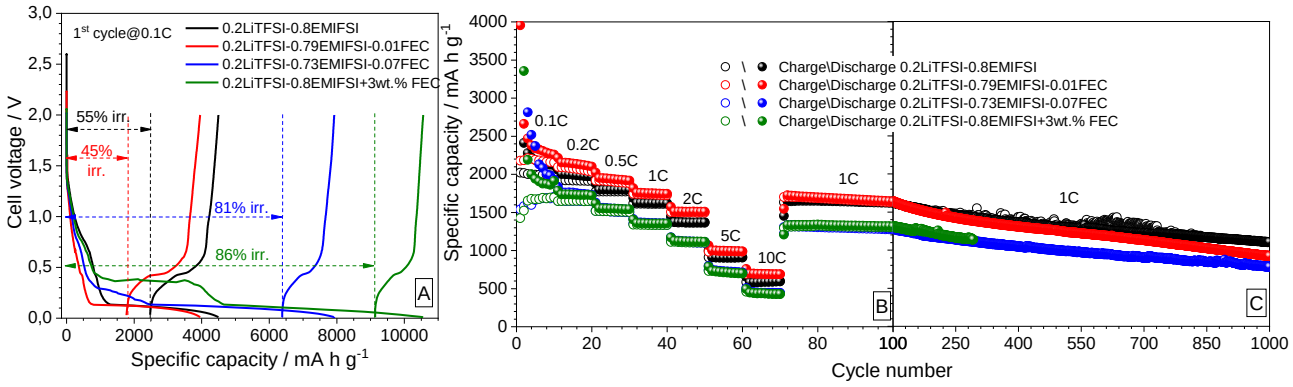

Figure 3.11: 1st discharge-charge curves (panel A) and cycling performance at different rates (panel B and C) of Li/ Sn-Si NW cells in LiTFSI-EMIFSI electrolyte with different FEC contents. T = 20°C.

3.3.4 XPS analysis on Sn-Si NW anode surface

To get insight into the SEI layer composition formed on the Sn-Si NW anodes, ex-situ XPS analysis was carried out on pristine electrode, after the first charge-discharge cycle and several cycles (reported in **Figure 3.12**). For avoiding the BE shifts associated with charging phenomena and to gain good accuracy of the peak assignments, the XPS spectra were collected in the de-lithiated state. The atomic concentrations of the post-mortem Sn-Si NW anodes are summarized in **Table 3.5** (the pristine electrode is reported for comparison). The SEI layer of the Si electrodes cycled in FEC-based and 0.2LiTFSI-0.8EMIFSI electrolytes exhibits high concentration of fluorine and a bit lower oxygen concentration, in conjunction with a larger silicon concentration onto the anode surface after several cycles, suggesting a thinner passive layer onto silicon electrode as previously reported in literature [188,189]. Otherwise, the silicon anodes in 0.2LiFSI-0.8EMIFSI and 0.2LiFSI-0.8N_{1114}FSI show high sulfur concentration which depends on the degradation products of the LiFSI salt [187].

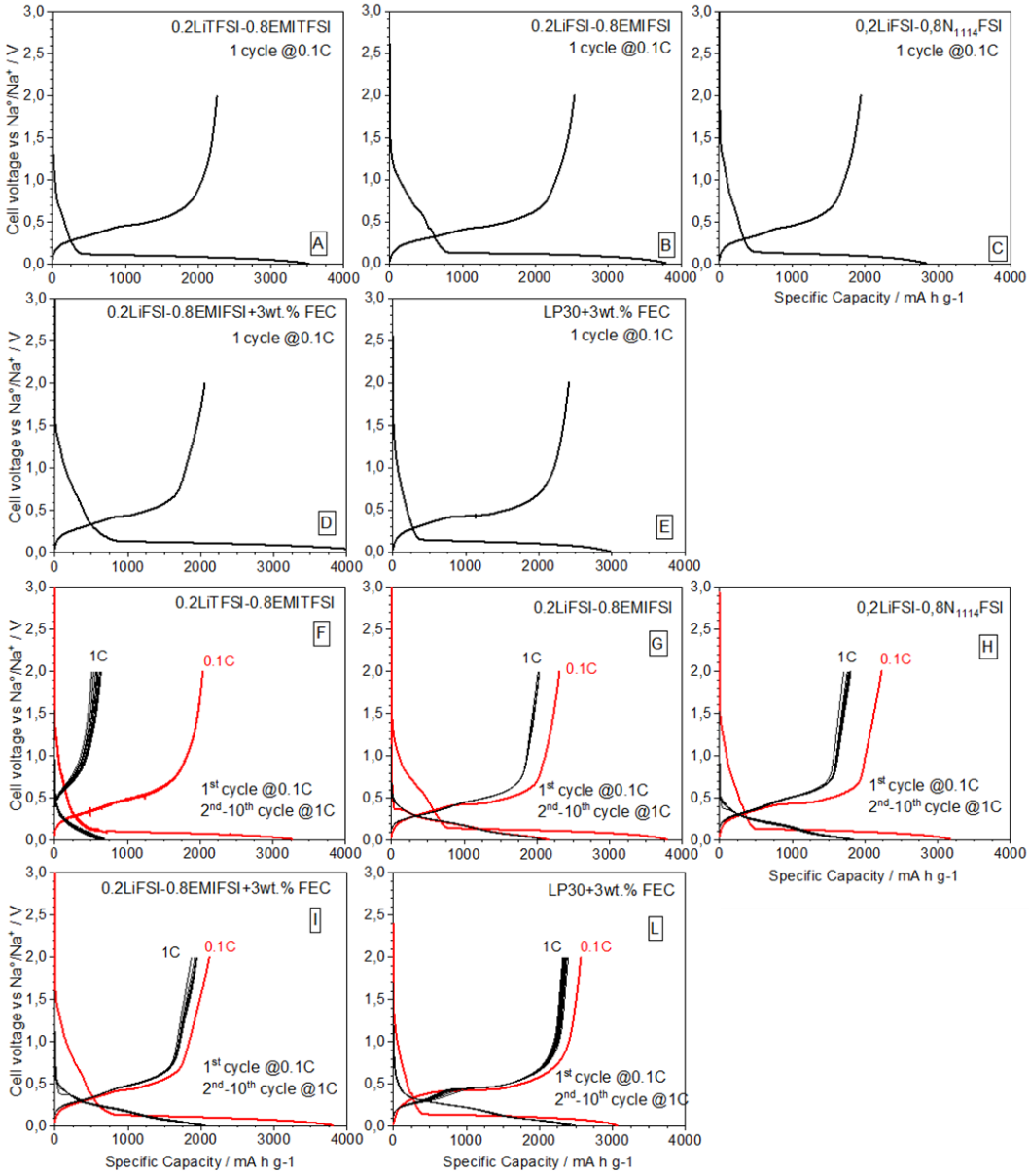

Figure 3.12: Voltage vs capacity profiles, referred to selected charge-discharge cycles, of Li/Si-Sn NW cells cycled in different electrolytes. T = 20 °C.

Table 3.5: Surface composition (atom percentage) of pristine and cycled Sn-Si NW electrodes.

		O 1s	C 1s	N 1s	F 1s	S 2p	Si 2p	Li 1s	P 2p
Pristine		14.8	56.3	--	--	--	28.0	--	--
0.2LiTFSI-0.8EMITFSI	1st cycle	31.2	33.0	1.5	4.0	1.1	2.2	26.6	--
	10th cycle	27.9	32.4	3.9	8.2	2.4	0.9	23.8	--
0.2LiFSI-0.8EMIFSI	1st cycle	31.1	33.1	3.4	2.0	5.2	0.9	24.0	--
	10th cycle	31.5	31.7	3.7	2.1	5.5	1.3	24.3	--
0.2LiFSI-0.8 N_{1114}FSI	1st cycle	30.0	30.8	3.8	3.8	7.3	2.0	21.9	--
	10th cycle	31.2	29.7	3.6	3.1	6.7	0.9	24.6	--
0.2LiFSI-0.8EMIFSI + 3 wt. % FEC	1st cycle	28.5	36.7	4.4	4.6	4.0	1.6	20.0	--
	10th cycle	30.7	33.0	2.8	5.6	2.6	0.5	24.6	--
1M $LiPF_6$ in EC:DMC 1:1 v:v + 3 wt.% FEC	1st cycle	31.6	29.6	--	5.9	0.3	1.2	30.8	0.1
	10th cycle	29.5	30.6	--	6.8	0.2	1.4	31.3	0.1

High-resolution XPS spectra of C 1s, Si 2p, F 1s, Li 1s, S 2p, O 1s, and N 1s, collected for each sample after the first charge-discharge cycles, are displayed in **Figures 3.13** and **3.14**, whereas those taken after several cycles are displayed in **Figures 3.15** and **3.16**. The Si 2p spectra of pristine Sn-Si NW anode exhibits a narrow feature at 99.8 eV corresponding to the bulk silicon, and the presence of silicon oxides at 100.5 and 102.5 eV [188,190], also confirmed by the O 1s spectra at 532.4 eV [188,190].

The N 1s XPS region of the Sn-Si NW (**Figure 3.15**) electrodes, cycled in IL electrolytes, highlights three well separated peaks: the first two are related to the cation (-C-N-, N^+), i.e., EMI^+ (401.5 eV) and N_{1114}^+ (402.6 eV) [191,192], and the anion, which appears around 400 eV (C-N, N-SO) for both $TFSI^-$ and FSI^- [187,193]. The presence of the IL signals is probably due to the IL caught in the porous structure of the Si anodes [194]. The last peak at 398.5 eV is ascribable to Li_3N/ LiC_xH_yN or -N=C- double bond in a polymeric network [195–198]. These compounds are associated with the reduction of the electrolyte, which gave place to graphitic carbon [194], evidenced in C 1s spectra (**Figure 3.15**) with the sp2 graphitic carbon feature at 284.8 eV. The relative atomic concentration increases upon cycles for the all-TFSI-based electrolyte, decreases for LiFSI-N_{1114}FSI and LiFSI-EMIFSI + 3 wt.% FEC and, finally, remains unchanged in LiFSI-EMIFSI, suggesting growing-up of stable Li_3N/LiC_xH_yN polymeric network during the first cycle.

The high-resolution XPS spectra of C 1s (**Figure 3.15**) display four main features centered around 284.8, 286.1, 288.5, and 289.5 eV in all cases, associated with C-C/C=C [187,199], C-O/C-N [196,200,201], O-C=O/C-F and CO_3^{2-} [187,199,202] species, respectively. The C-C/C=C, C-O/C-N and CF groups arise from the decomposition of IL (i.e., EMI^+, N_{1114}^+, $TFSI^-$, and FSI^-). For Si-based

electrodes cycled in LiTFSI-EMITFSI, the C 1s spectra show a very small peak at 293 eV associated with the CF_3 group [191,193] derived by the TFSI anion, also confirmed by the well-pronounced peak at 688.6 eV in the F 1s XPS spectra (**Figure 3.15**). The CO_3^{2-} can be assigned to Li-$OCOOC_2H_5$ and/or Li_2CO_3 arising from FEC degradation [191] but also from salt decomposition, as it was demonstrated in other works [195,203]. The presence of this compound was also detected in the Li 1s spectra at 54.7 eV. This peak is more prominent in FEC-based electrolytes and in LiTFSI-EMITFSI. The area ratio of $C_{286.1}/C_{288.5}$ does not substantially change for LiFSI-EMIFSI and organic electrolyte during cycling, indicating growth-up of a stable SEI during the first cycle. The C 1s spectra of the Sn-Si NW cycled in organic electrolyte reveal quite similar features to those detected in ILs, as already reported in previous paper [194].

The deconvolution of O 1s spectra (**Figure 3.16**) highlights the presence of carbonate species, already observed in the C 1s spectra, and evidenced around 532 eV [187,204]. Lithium silicate species (i.e., Li_xSiO_y), related to the lithiation of Si oxide [188,190,205], can be attributed to the peak at 531 eV, which are visible also in the Si 2p spectra at 100.5 eV [187,204]. As described in detail elsewhere [206–208] the broad peak at 533.6 eV, ascribable to O-C=O species, depends on solvent and/or additive polymerization, and it was also observed in the C 1s spectra at 286.1 eV. In all electrolytes, the Si surface is rich in carbonate species as confirmed by the features in the C 1s and O 1s spectra (**Figures 3.15 and 3.16**).

A big LiF peak at 684.8 eV [187,209] can be observed in the F 1s spectra, in agreement with the Li 1s spectra at 55.6 eV [187,209], due to the decomposition of salt (LiTFSI, LiFSI, and $LiPF_6$) by the electrochemical reduction of S-F bond [190] and during cycling can be observed that TFSI-based and FEC-based electrolytes exhibit a higher amount of LiF. As described by Piper *et a*l. [192] FSI^- and $TFSI^-$ are subject to quite different reduction processes, where the FSI^- rapidly release F^-, forming LiF, and SO_2, which suggests the formation of SEI rich in small inorganic compounds. Conversely, $TFSI^-$ can form different products, such as -SO_2CF_3. The -SO_2 species can be also observed at 168.8 eV in the S 2p spectra, where results more prominent in the FSI-based systems. The fast release of F^- and SO_2 may be correlated to the high cycling performance shown by Si- Si NW anode in LiFSI-EMIFSI electrolyte. This speculation derived from modeling studies performed on the FEC system [210], demonstrating its ability to rapidly release F^- (to form LiF) during its decomposition. The SiOF signal at 686.8 eV corresponds to the Si substrate, indicating the thickness of the SEI layer: in organic electrolyte it might be covered by the $LiPF_6$ signal, resulting from incomplete removal during the electrode rinsing and/or from intermediate decomposition products with similar binding energy to $LiPF_6$ [208,211]. This feature is more pronounced in LiFSI-EMIFSI and organic (1M $LiPF_6$ in EC:DMC 1:1 v:v + 3 wt.% FEC) electrolytes, indicating a thinner SEI onto the Si surface. The

presence of residual lithium salts (LiTFSI, LiFSI, and $LiPF_6$) and/or their incomplete decomposition products are detected around 688 eV [190,209], in the case of LiTFSI is completely overlapped by the CF_3 signal at 688.6 eV and the SiOF is not visible.

The S 2p deconvolution (**Figure 3.16**) results in a rather complex spectrum for the Si anode cycled in IL-based electrolytes. It can be divided into three main components. The first one is represented by the $Sp_{3/2}$ peak, which confirms the presence of residual LiTFSI and/or LiFSI salt at 168.8 eV and 169.1 eV [209], respectively. Although, the second one encloses several features, in the range between 169.8 and 168 eV, due to degradation products of imide-based salts that might be assigned to S=O bonds [209,212]. The last weak component, at around 167 eV, is also related to the reduction of Li-imide salt, but this process can be also induced by the X-ray beam [187,208]. The s 2p spectra display very weak peaks, probably due to residual traces of electrolyte.

The Si 2p spectra show the peak related to the bulk silicon at ~98 and ~99 eV [187,188], which in the case of LiFSI-EMIFSI tends to increase, meaning a reduction of the SEI layer thickness and in agreement with the results from impedance measurements discussed in Paragraph 3.2. A signal at 100.5 eV can be attributed to Li_xSiO_y, as already previously described, and the last peak at 102.8 eV is associated with the SiO_2 specie.

The XPS results suggest a bilayer SEI onto the Si surface, i.e., an outer part composed of organic compounds within a polymeric network that can provide flexibility and good mechanical stability against the volume changes during the Si cycling, and an inner layer dominated by inorganic compounds such as Li_3N, LiF, delivering high Li-ion conductivity, as well as a graphitic network that provides electronic conductivity [194,195,203]. The different cycling performances can be due to the different density and porosity of the SEI onto the Si surface. The SEI layer onto the Si anodes cycled in LiFSI-EMIFSI and organic electrolytes is likely rich in stable LiF and -Si-F compounds which, thanks to their high bonding energy, do not decompose during cycling and promotes a stable interface with the electrolyte [213,214]. Although, in the other case, the surface layer can contain less stable compounds, such as metastable and less dense, linear alkyl carbonates (-Si-$OCH_2CH_2OCO_2Li$, -Si-$CH_2CH_2OCO_2Li$, $R(OCO_2Li)_2$) and, due to their low bonding energy, can continue to decompose upon cycling, thus feeding irreversible redox reactions that promote silicon dendritization and pulverization, as has been shown by Bongiorno *et al* [215]. The low density of the SEI layer allows the transition of the electrolyte during the Li^+ insertion, which cause the breakup of the -Si-Si- network bond giving rise to porous structure and cracking.

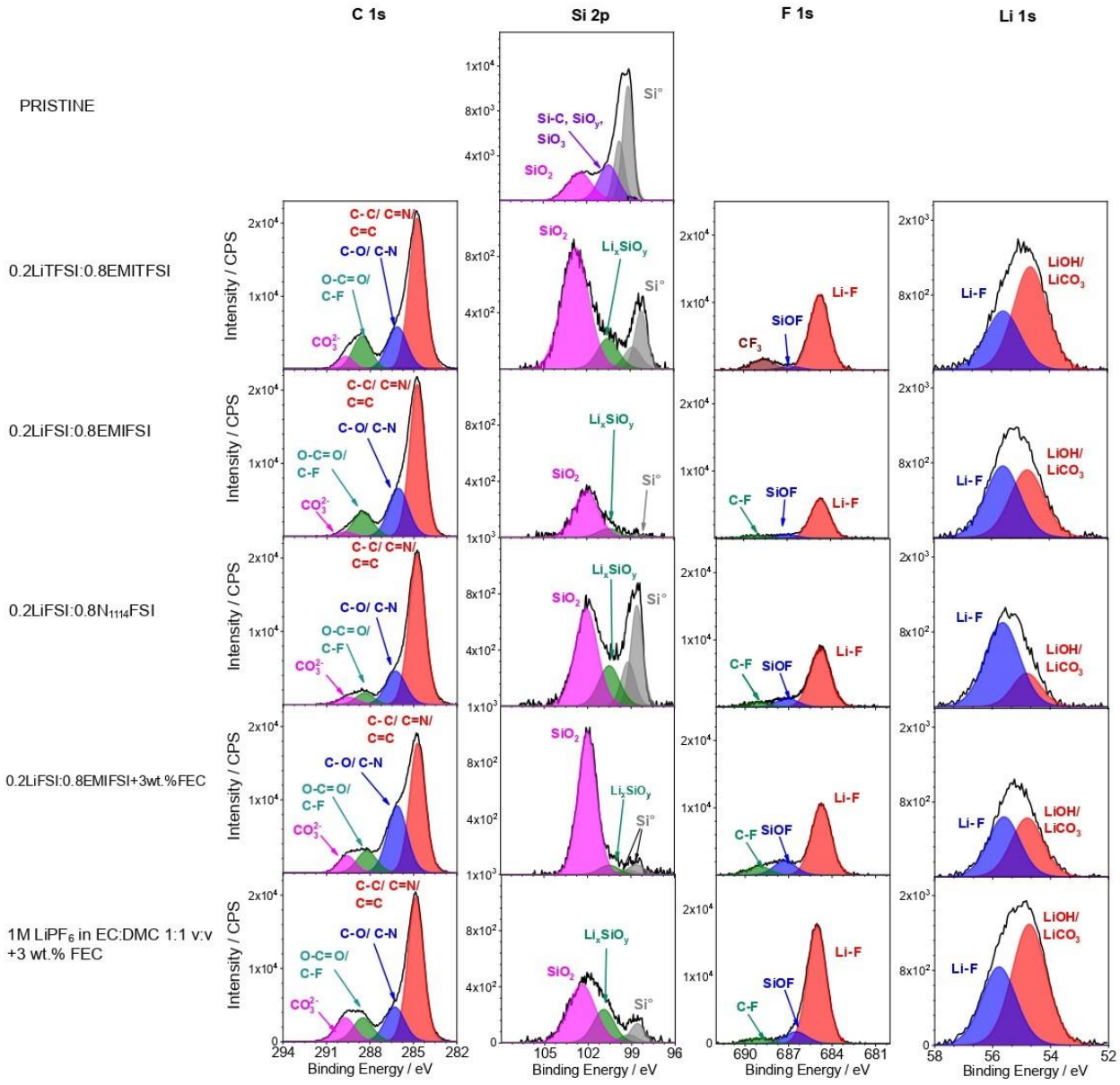

Figure 3.13: High-resolution C 1s, Si 2p, F 1s, and Li 1s core level spectra obtained on pristine Si-Sn NW anodes and after one charge-discharge cycle in different electrolyte formulations.

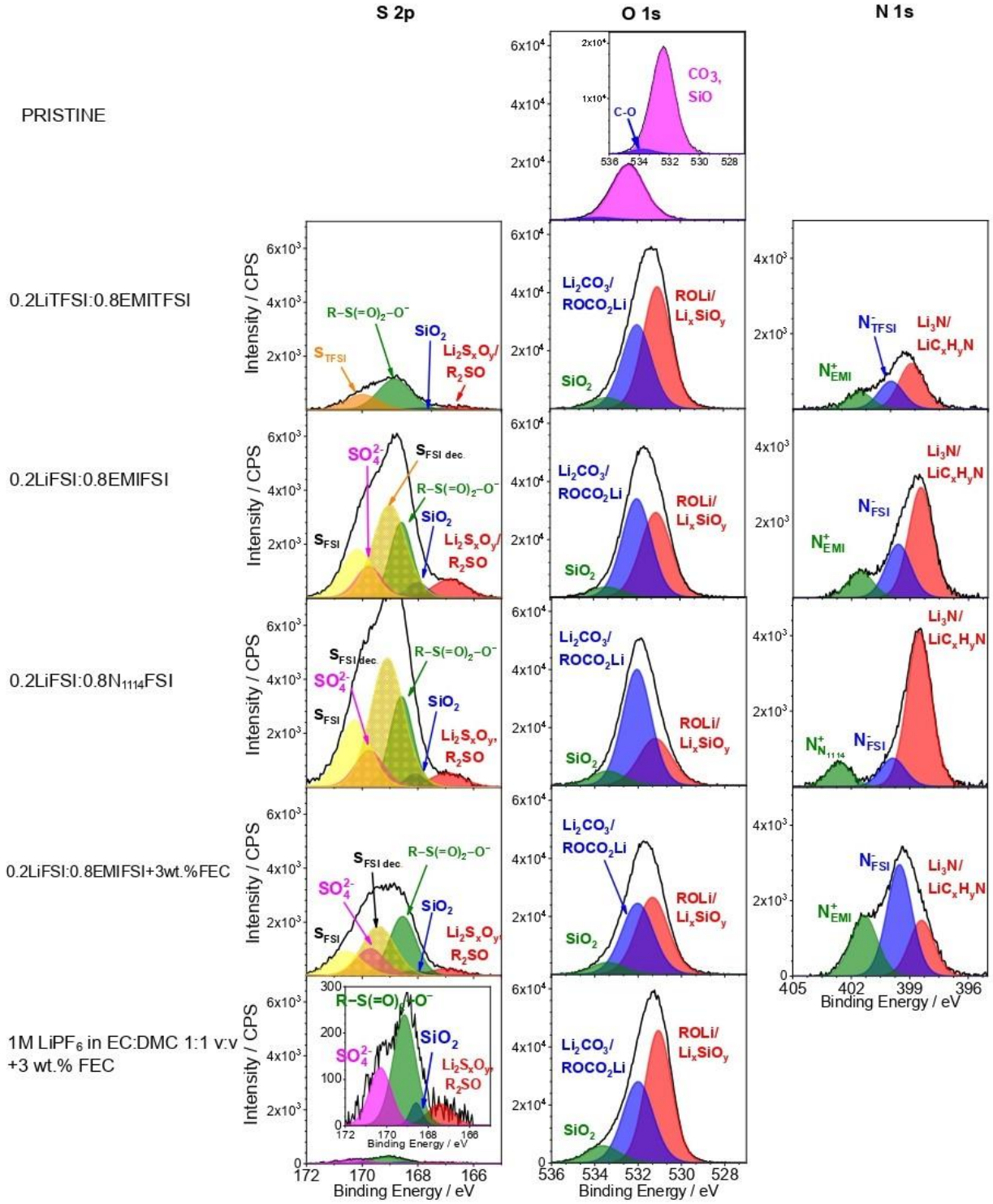

Figure 3.14: High-resolution S 2p, O 1s, and N 1s core level spectra obtained on pristine Si-Sn NW anodes and after one charge-discharge cycle in different electrolyte formulations.

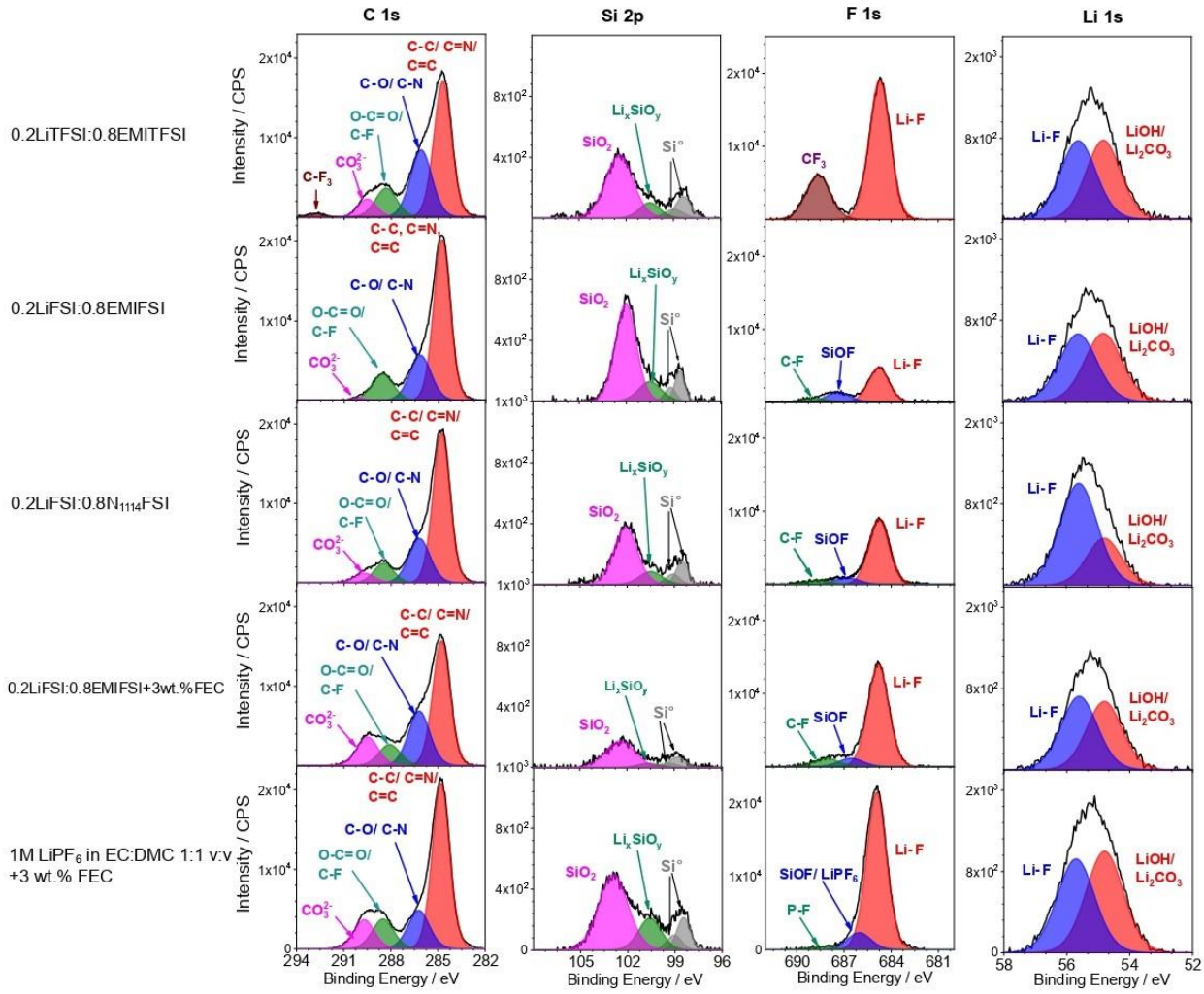

Figure 3.15: High-resolution C 1s, Si 2p, F 1s and Li 1s core level spectra obtained on the Sn-Si NW anodes after consecutive lithiation/de-lithiation steps in different electrolyte formulations (see legend).

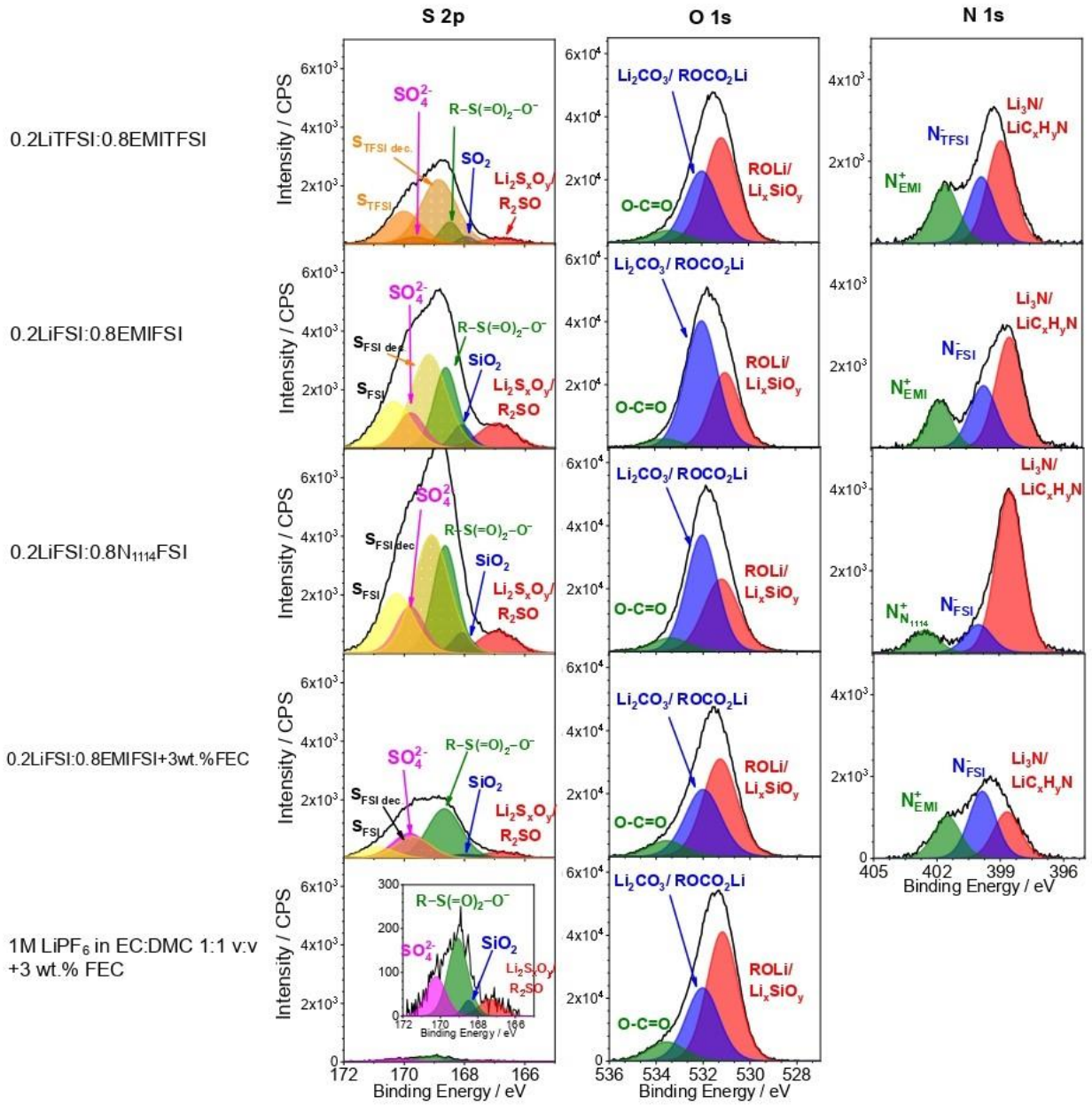

Figure 3.16: High-resolution S 2p, O 1s, and N 1s core level spectra obtained on pristine Sn-Si NW anodes and after consecutive lithiation/de-lithiation steps in different electrolyte formulations (see legend).

3.4 Conclusions

The lithiation process of Sn-Si NW anodes in different ionic liquid electrolyte formulations was investigated through electrochemical and XPS measurements. High reversibility and reproducibility of the Li^+-allowing process is observed for 0.2LiTFSI-0.8EMIFSI and 0.2LiFSI-0.8EMIFSI electrolyte systems, through cyclic voltammetry analysis carried out at increasing scan rates and for prolonged cycles. Conversely, the full-TFSI electrolytes do not show evident features related to the electrochemical processes, meaning poor reversibility of the lithiation process. The full-FSI cells

display higher specific current even after prolonged CV test (> 200 cycles), indicating larger charge amount involved in the lithiation process.

The Li^+ diffusion coefficient (D_{Li+}), evaluated using the Randles-Savcik equation, results to be equal to $(9.6 \pm 0.5)\times10^{-10}$ cm^2 s^{-1} and $(2.5 \pm 0.1) \times10^{-10}$ cm^2 s^{-1} in the 0.2LiTFSI-0.8EMIFSI and 0.2LiFSI-0.8EMIFSI electrolytes, respectively. These results are consistent with those reported in literature for organic electrolytes.

The interfacial properties of Li/Si cells were investigated by impedance spectroscopy analysis combined with CV tests. A stable bulk resistance is recorded during CV tests, confirming the good electrochemical stability of the IL-based electrolytes. Although, a marked improvement in interfacial resistance is observed after replacing the TFSI anion with the FSI. These results, in agreement with the CV tests, are ascribable to the good film-forming ability of the FSI anion,

Reversible capacities exceeding 1000 mA h g^{-1} are delivered after 2000 charge-discharge cycles at 1C, corresponding to 46 % of the initial value. LiFSI-based electrolytes are seen to better behave with respect to the LiTFSI ones. The electrode performances of Sn-Si NW anodes are seen to increase with the Si/Sn weight ratio: for instance, in passing from a Si/Sn ratio of 2.17 to 2.68, 2400 mA h g^{-1} (about 89 % of the nominal capacity = 2700 mA h g^{-1}) are still delivered at 1C and 1000 mA h g^{-1} are even exhibited at 10C (4 mA cm^{-2}). These are ones of the best, if not the best, results observed till now for Si anodes in ionic liquid electrolytes. A moderate increase in capacity is observed in the presence of modest contents (0.01 as the mole fraction) of FEC; further addition of FEC, however, does result in performance decay.

A SEI layer, externally composed by a polymeric network and a graphitic network inside, on the Sn-Si NW anode surface was revealed by XPS analysis. The supposed high density of the SEI layer, which hinders the crack formation on the Si surface in the case of 0.2LiFSI-0.8EMIFSI and organic (1M $LiPF_6$ in EC:DMC 1:1 v:v + 3 wt.% FEC) electrolytes, can support for the better cycling behavior.

To summarize, the 0.2LiFSI-0.8EMIFSI electrolyte has shown very high compatibility and excellent behavior in lithium cells with Sn-Si NW anodes and, therefore, it can be considered a very appealing electrolyte, as alternative to the commercial organic ones, for realizing safer and more reliable, highly performant lithium-ion battery systems.

4. Li-rich cathode for Li-ion batteries

4.1 Introduction

High-voltage lithium batteries are the best candidates for the next generation power sources because of their superior energy and power densities with respect to other commercially available electrochemical energy storage systems [13,216]. For such reason, remarkable efforts are currently devoted aiming to enhance their performance For enabling long-range electric/hybrid vehicles and the exploitation of electric energy from renewable sources. Additionally, the electronic consumer market is always requiring better performing batteries to cope with the development of electronics. One of the most followed approaches for enhancing the energy density of battery systems is the adoption of cathode materials with large specific capacities and, ideally, operating at high potentials, i.e., above 4 V. Among these, lithium-rich, layered oxide (LRLO) positive electrode materials are considered very promising. More specifically, $Li_{1.2}Ni_{0.2}Mn_{0.6}O_2$ (LRNM) delivers a nominal specific capacity beyond 250 mA h g^{-1}, while operating in a potential range well above 4 V [217]. Besides the promising electrochemical properties, the LRNM is cobalt-free making it a more sustainable cathode material that does not require the use of critically rated and expensive cobalt. However, the increase of the overall energy density of the batteries enhances their intrinsic danger related to its sudden release via unwanted, direct chemical reactions, thus requiring for better safety. Therefore, the electrolyte does play a key role in determining behavior, performance, and safety of LIB systems. the LRMN electrodes, which were investigated in the present PhD activity, were developed, synthesized, and provided by the Karlsruhe Institute of Technology (KIT)-Helmoltz Institute of Ulm (HIU) (Germany) [218].

4.2 Experimental Section

4.2.1 Materials and Methods

The IL electrolytes, selected for the compatibility investigation with LRMN cathodes based on the results obtained from conductivity and voltammetry measurements, are reported in **Table 4.1**.

Table 4.1: IL electrolyte formulations investigated with LRMN cathodes.

Mole fraction	Lithium salt	Mole fraction	IL
0.20	LiTFSI	0.80	EMITFSI
0.20	LiTFSI	0.80	EMIFSI
0.20	LiFSI	0.80	EMIFSI
0.20	LiTFSI	0.80	N_{1114}TFSI
0.20	LiTFSI	0.80	N_{1114}FSI
0.20	LiTFSI	0.80	$N_{122(2O1)}$TFSI

The LRMN cathodes (namely $Li_{1.3}Ni_{0.2}Mn_{0.6}O_2$, Gen1.3, and $Li_{1.4}Ni_{0.2}Mn_{0.6}O_2$, Gen1.4), have a weight composition equal to 85 % (LRMN active material), 5 % (Super C65 carbon, IMERYS, as the electronic conductor) and 10 % (PVdF, Solef 6030, Solvay, as the polymer binder). The LRMN electrodes were prepared using both sieved and not sieved active material. The LRMN mass loading ranges from 3 to 4 mg cm^{-2}, corresponding (taking in account a theoretical specific capacity for LRMN equal to 270 mA h g^{-1}) to a capacity from 0.8 to 1.1 mA h cm^{-2}. The electrodes, provided as 12 mm diameter disks (surface area equal to 1.13 cm^2) supported onto an aluminum foil (20 μm thickness), were previously vacuum dried at 120 °C for 24 hours and then, transferred in an argon-controlled atmosphere glove box (Jacomex, O_2 and H_2O content < 1 ppm) for the cell manufacturing.

4.2.2 Electrochemical measurements

The electrolyte formulations were investigated in Li/LRMN coin-cells, which were manufactured (within the glove box) through the same protocol described in detail for the Li/WE ones (see section 3.2.2) except for the LRMN cathode which was used in the place of the working electrode (WE). The Li/LRMN cells were tested at 20 °C (Binder climatic chamber) by a BioLogic BCSC multi-channel battery cycler. The reproducibility of the results was verified by running the electrochemical tests, for each electrolyte formulation, on at least two identical cells, using always fresh electrolyte and electrode samples for each electrochemical test.

Galvanostatic charge-discharge (GC) measurements were carried out on Li/LRMN cells, which were cycled between 2.5 and 4.7 V vs $Li^+/Li°$ at 0.1C for the first cycle, and between 2.5 and 4.6 V vs $Li^+/Li°$ at current rates from 0.1C to 10C for the following cycles.

The Li/LRMN cells were subjected to cyclic voltammetric (CV) analysis paired with potentiostatic electrochemical impedance spectroscopy (PEIS) measurements to gain information about the reversibility and kinetics of the lithiation process. The CV tests were performed between 2.5 to 4.8 V vs $Li^+/Li°$ at increasing scan rates, i.e., from 0.05 to 1 mV s^{-1} (four consecutive CV cycles were run at each selected scan rate), followed by 500 cycles at a constant scan rate of 1 mV s^{-1}. The PEIS was carried out on the fresh cells and at the end of each increasing scan rate CV family, in the 10 kHz – 0.1 Hz frequency range with 10 mV amplitude voltage.

All the electrochemical tests were carried out in a climate chamber at 20°C, using a Biologic (Seyssinet-Pariset, France) multichannel battery cycler.

4.3 Results and Discussions

4.3.1 Screening of IL electrolyte formulation

The 0.2LiTFSI-0.8IL electrolytes were screened by cycling charge-discharge testing performed in Li/LRMN cells to assess their performance on the cathode side. The results are illustrated in **Figures 4.1** (EMI based electrolytes) and **4.2** (ammonium-based electrolytes), respectively, which report selected cell voltage *vs*. capacity profiles (panels A–B of **Figure 4.1** and panels A-B-C of **Figure 4.2**) and capacity *vs*. cycling behaviour (panels C–D of **Figure 4.1** and panels D-E-F of **Figure 4.2**) at different current rates. For all investigated electrolytes, the 1st charge profile differs with respect to the following ones for the structural reorganization occurring in the material, resulting from the involvement of oxygen in the redox reactions [217]. In the first discharge and in all following charge/discharge cycles, rather featureless voltage slopes are observed. These voltage profiles are in good agreement with the expected de-lithiation mechanism proposed in literature for the lithium-rich, oxide materials [219–221]. Overall, the use of the IL-based electrolytes does not alter the expected reaction mechanism occurring in these materials. Both EMI-based electrolytes exhibit an initial reversible capacity approaching 200 mA h g^{-1}(at 0.05C rate), i.e., corresponding to 80 % of the LRMN

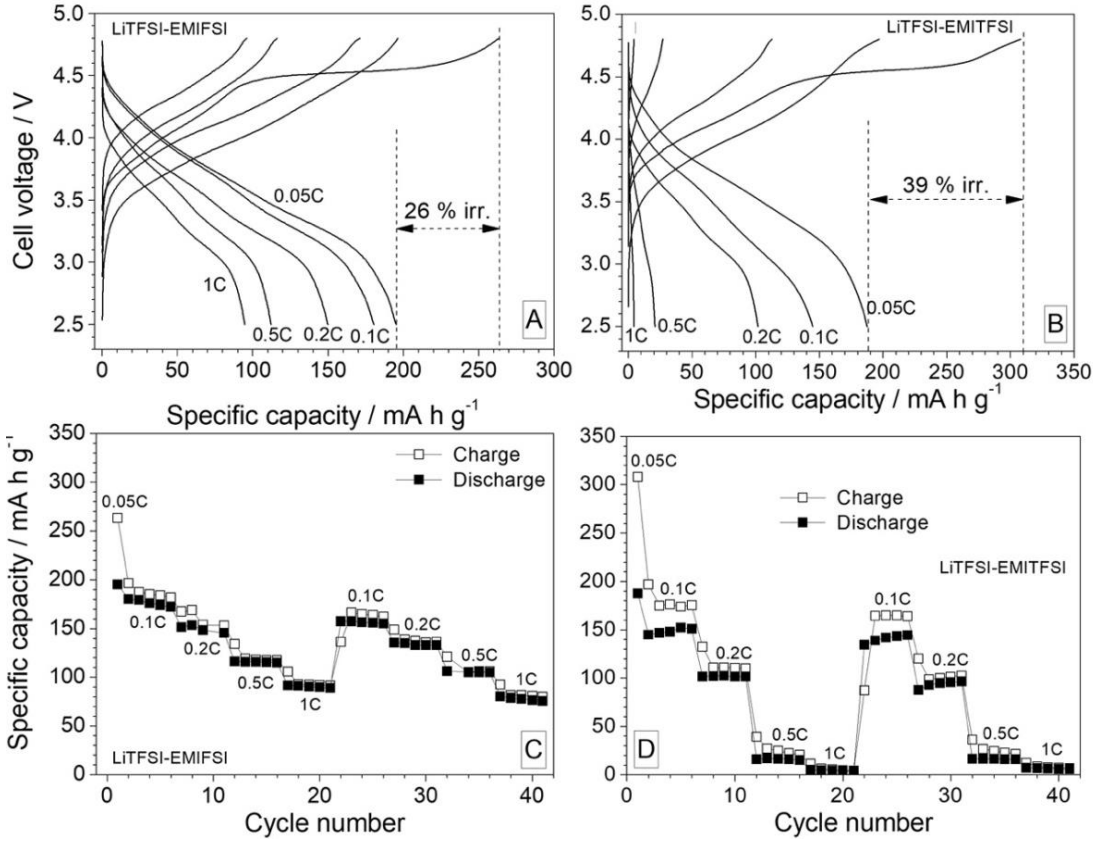

Figure 4.1: Selected voltage vs. capacity profiles (panels A and B) and cycling performance (panels C and D) of Li/LRMN cells containing the 0.2LiTFSI-0.8EMIFSI (panels A and C) and 0.2LiTFSI-0.8EMITFSI (panels B and D) ionic liquid electrolytes at different current rates (0.05C–1C). Temperature: 30 °C.

theoretical value and supporting for good performance in lithium metal cells. This is particularly true for 0.2LiTFSI- 0.8EMIFSI, where stable performances at all current rates are observed.

A better rate capability is observed for the 0.2LiTFSI-0.8EMIFSI electrolyte (about 100 mA h g^{-1} at 1C), ascribed to its faster ion transport lowering the effect of diffusion phenomena. Furthermore, the 0.2LiTFSI-0.8EMIFSI electrolyte shows a smaller irreversible capacity in the first cycle (< 70 mA h g^{-1}, corresponding to 26 % of the overall capacity value) in comparison to 0.2LiTFSI-0.8EMITFSI (> 110 mA h g^{-1}, equal to 39 % of the overall capacity), in combination with improved coulombic efficiencies upon cycling. One may qualitatively suggest that these differences in the reversibility of redox activity of the LRNM electrode are likely due to a more resistive electrolyte/electrode interface in the case of the 0.2LiTFSI-0.8EMIFSI solution. Thus, the properties of the cathode-electrolyte interphase (CEI) layer are apparently affected by the nature of the anion. A more detailed comprehension of these CEIs would likely shed light, but it is, however, beyond the scope of the present work.

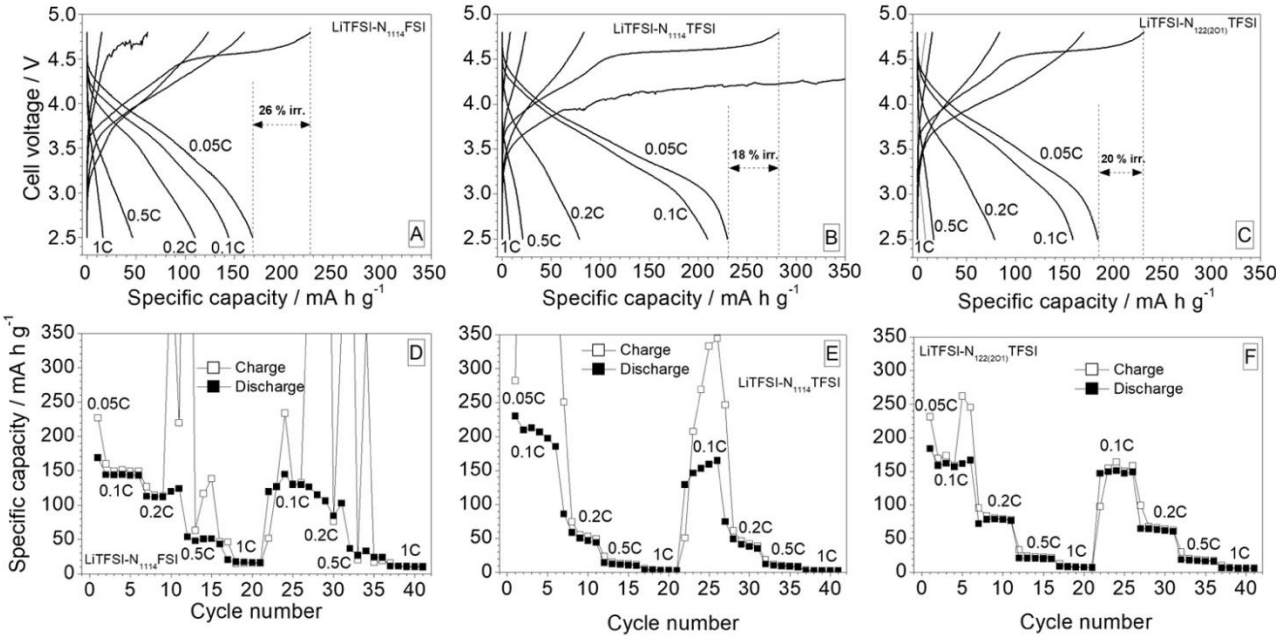

Figure 4.2: Selected voltage vs. capacity profiles (panels A-C) and cycling performance (panels D-F) of Li/LRMN cells containing the 0.2LiTFSI-0.8N_{1114}FSI (panels A and D), 0.2LiTFSI-0.8N_{1114}TFSI (panels B and E) and 0.2LiTFSI-0.8$N_{122(2O1)}$TFSI ionic liquid electrolytes at different current rates (0.05C–1C). Temperature: 30 °C.

Turning to the ammonium-based electrolytes, the performance in lithium metal cells (**Figure 4.2**) suggests a scattered instability upon charge, even if appreciable reversible capacity values

(approaching 200 mA h g^{-1} at the 1st cycle) are obtained. It is to note that, conversely to the behavior observed in EMI electrolytes (**Figure 4.1**), the ammonium TFSI formulations perform better than the FSI one, clearly indicating how an important role is played also by the cation. Upon cycling, the cells employing ammonium-based electrolytes show randomly extended oxidative steps, involving capacities of hundreds or thousands mA h g^{-1}. These results, as well as those recorded for the EMI-based IL electrolytes, have been confirmed in triplicate tests by applying prolonged and repeated drying procedures of all cell components (including the electrolyte blends and electrodes) and the use of different batches of lithium counter-electrodes. This behavior is a direct indication for the occurrence of parasitic oxidation reactions at the positive electrode surface and/or parasitic reduction at the negative electrode surface (lithium). The onset of these processes likely originates from the breaking of the CEI or the SEI (cathode/solid electrolyte interphase).

4.3.2 Prolonged cycling test

The 0.2LiTFSI-0.8EMIFSI electrolyte formulation, showing the most promising performance, was subjected to prolonged charge-discharge cycling tests in Li/LRMN cells (**Figure 4.3**). No appreciable modification of the voltage vs capacity profiles is observed after the 1st cycle, both in the following charge and discharge steps, thus highlighting the good reversibility of the Li^+ intercalation process. The specific capacity, displaying an initial value greater than 210 mA h g^{-1} (corresponding to 84 % of the theoretical one with an efficiency around 78 %) at 0.1C (panel A), is seen to progressively approach a plateau upon cycling. Around 150 mA h g^{-1} was delivered after more than 50 cycles, with a time-stable coulombic efficiency around 96-97 % after the 3rd (dis)charge cycle (panel B). No appreciable electrolyte degradation is detected, i.e., no modification of the voltage profiles is observed upon cycling, even if further studies about the latter issue need to be conducted. Much better performance is observed in optimized LRMN electrodes (panel C), displaying an initial reversible capacity exceeding 260 mA h g^{-1} (at 0.1C) with a coulombic efficiency around 83 %. An excellent cycling behavior is displayed even at medium rate (0.5C), i.e., above 165 mA h g^{-1} was delivered after 500 charge-discharge cycles (100 % Deep of Discharge, DoD), corresponding to more than 89 % of capacity initially delivered at 0.5C (capacity fading equal to 0.02 % per cycle) with a coulombic efficiency levelling 100 % (panel D). These data indicate very good compatibility of the 0.2LiTFSI-0.8EMIFSI electrolyte with high-voltage LRMN cathodes, once more confirming the high electrochemical stability of the electrolytic formulations developed in the Si-DRIVE Project. The cycling performance reported in **Figure 4.3** is higher than that recorded in organic standard electrolytes [218,220,221]

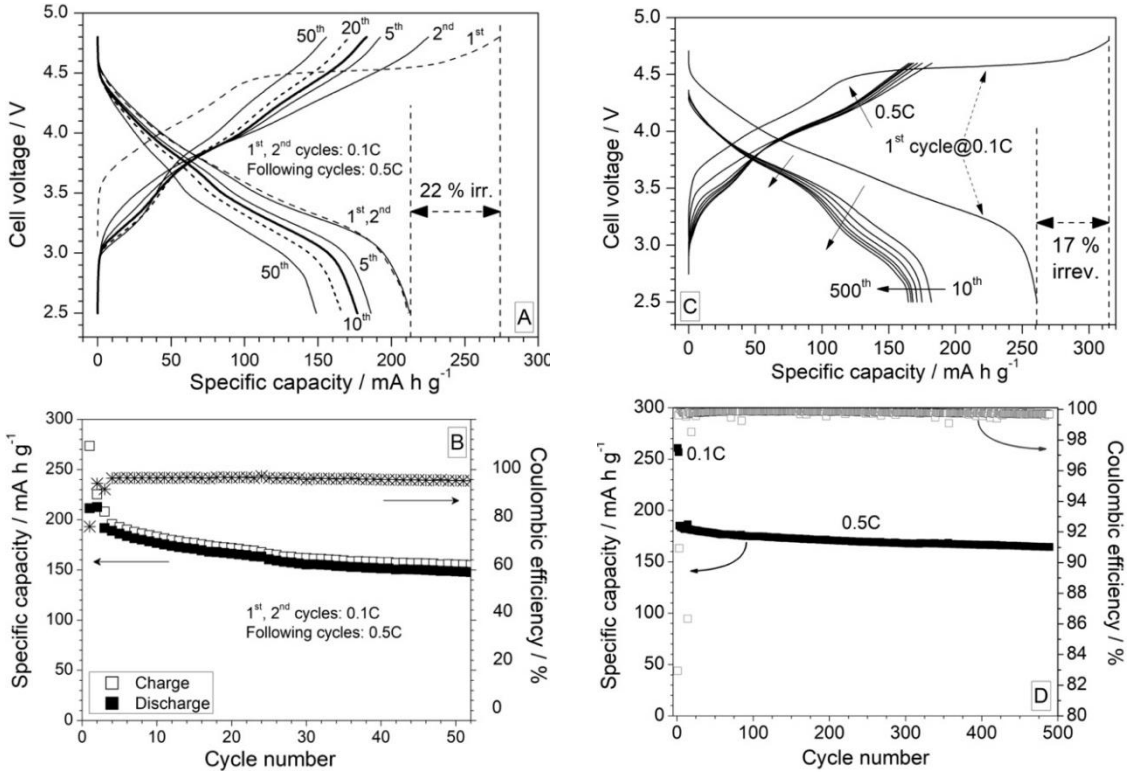

Figure 4.3: Selected voltage vs. capacity profiles (panels A and C) and cycling performance (panel B and D) of Li/LRNM cells containing the 0.2LiTFSI-0.8EMIFSI ionic liquid electrolyte at 0.5C current rate. Panels C and D are referred to optimized LRMN cathodes. Temperature: 20 °C [118].

4.3.3 Effect of lithium salt

The results depicted in **Figures** from **4.1** through **4.3** shows EMIFSI is the best performant IL with LRMN cathodes and, therefore, was selected as the IL component of the electrolytes. In addition, because of the very good behavior exhibited by the FSI anion, LiFSI was used in combination with EMIFSI (LiFSI: EMIFSI mole ratio = 1:4) and compared with LiTFSI till now employed as the lithium salt. The results, illustrated in **Figures 4.4** and **4.5** for sieved LRMN, show the performance recorded in Li/LRNM cells, using the 0.2LiTFSI-0.8EMIFSI and 0.2LiFSI-0.8EMIFSI electrolytes. **Figure 4.4** plots selected cell voltage *vs*. capacity profiles obtained at different current rates. The 1st charge profile differs with respect to the following ones for the structural reorganization occurring in the material, resulting from the involvement of oxygen in the redox reactions [118,218,220,221]. In the 1st discharge and in all following charge/discharge cycles (panels A and B) rather featureless voltage slopes are observed with no substantial modification with increasing the current rate up to 10C, apart a progressive increase of the ohmic drop and of the profile slope ascribable to diffusive phenomena within the cathode and (at higher current rates) the electrolytes. This supports for the good reversibility of the Li^+ intercalation process. Overall, also the use of LiFSI salt does not alter

the expected reaction mechanism occurring in these materials, in agreement with the CV results reported in **Figure 2.18**.

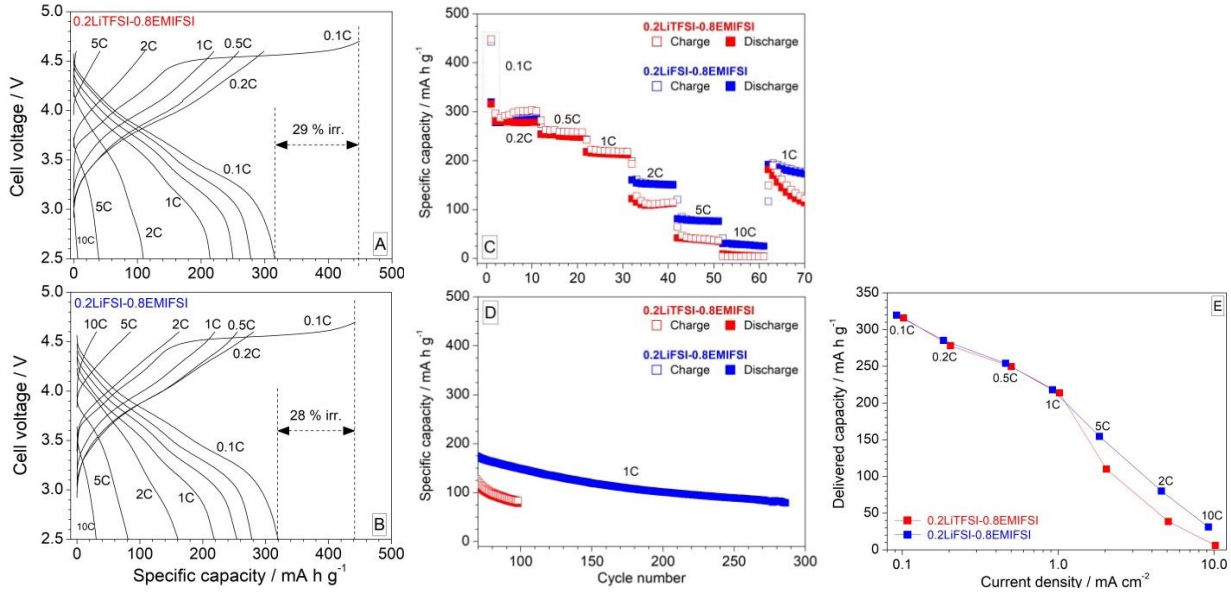

Figure 4.4: Selected voltage vs. capacity profiles (panel A and B), cycling performance (panel C and D) and delivered capacity vs. current rate dependence (panel E) of Li/LRNM cells containing the 0.2LiTFSI-0.8EMIFSI and 0.2LiFSI-0.8EMIFSI ionic liquid electrolytes at different current rates. Temperature: 20 °C. Sieved LRMN was employed.

The cycling tests (panel C) show an initial reversible capacity around 320 mA h g^{-1} (at 0.1C) with a coulombic efficiency above 72 % for both electrolyte formulations, which exhibit analogous performance up to a current rate of 1 C, i.e., delivering about 220 mA h g^{-1} corresponding to 68 % of the nominal capacity. At higher current rates (≥ 2C) higher capacity values are recorded for the 0.2LiFSI-0.8EMIFSI electrolyte, due to the faster ion transport properties of the LiFSI electrolytes [58]. For instance, more than 150 mA h g^{-1} are still delivered at 2C (corresponding to a current density above 2.0 mA cm^{-2}) whereas a further capacity decay, even if displaying still appreciable values, is observed at current rates ≥ 5C, suggesting that the electrolytes are governed by diffusive phenomena. Further cycling at 1C (panels C and D), run after those carried out at 10C, show a fully capacity recovery up to 200 mA h g^{-1} followed by a less relevant decay in 0.2LiFSI-0.8EMIFSI cells, i.e., 75 mA h g^{-1}, still exhibited after 290 cycles (capacity fading < 0.17 % per cycle), are however reached in 0.2LiTFSI-0.8EMIFSI cells after 110 cycles (capacity fading > 0.45 % per cycle). A higher charge-discharge efficiency (> 99 %) is seen for the 0.2LiFSI-0.8EMIFSI electrolyte. The discharge capacity evolution of the Li/LRMN cells as a function of the current density, reported in panel E, is characterized by two different linear trends, which may be associated with two distinguished regions: *i*) a lower rate region (< 1 mA cm^{-2}) where the capacity is limited by the diffusion phenomena taking

place within the electrode active material phase [222–224]; *ii*) a higher rate region (> 1 mA cm^{-2}) characterized by a more pronounced slope of the capacity *vs*. current density curve. The more remarkable decrease in capacity is due to the limitation originating from diffusive phenomena occurring in the ionic liquid electrolyte [222–224]. Therefore, a value of 1 mA cm^{-2}, corresponding to a current rate equal to 1C, may be considered as the current density limit for this electrolyte formulations. Above this threshold, the electrolyte is governed by diffusive phenomena.

Cycling tests (**Figure 4.5**), carried out on a different 1.4 LRMN batch (sieved active material) at constant medium rates (0.5C, i.e., of interests for Si-DRIVE applications), have shown slightly higher initial reversible capacity (around 350-360 mA h g^{-1} at 0.1C for both electrolyte formulations) but lower coulombic efficiency, i.e. 53 % (0.2LiTFSI-0.8EMIFSI) and 67 % (0.2LiFSI-0.8EMIFSI). This behavior, requiring a deeper investigation for a better understanding, is likely ascribable to different structural reorganization occurring in LRMN (i.e., involvement of oxygen in the redox reactions) as previously discussed in Section 4.3.1 [219–221], with respect to that of other active material batches reported in **Figures 4.1** and **4.3**. For instance, higher irreversible capacity is observed, this suggesting larger electrolyte degradation. A higher capacity retention (panel B) is evidenced, in the following tests run at 0.5C, in the 0.2LiFSI-0.8EMIFSI cells which exhibit more than 270 mA h g^{-1} (vs 245 mA h g^{-1} delivered by the 0.2LiTFSI-0.8EMIFSI cells) after 120 cycles, corresponding to about 89 % of the initial capacity (delivered at 0.5C) with a fading lower than 0.1 % per cycle (0.15 % per cycle recorded for the 0.2LiTFSI-0.8EMIFSI cells). Once more, better cycling behavior is exhibited by the 0.2LiFSI-0.8EMIFSI cells in LRMN high-voltage cathodes.

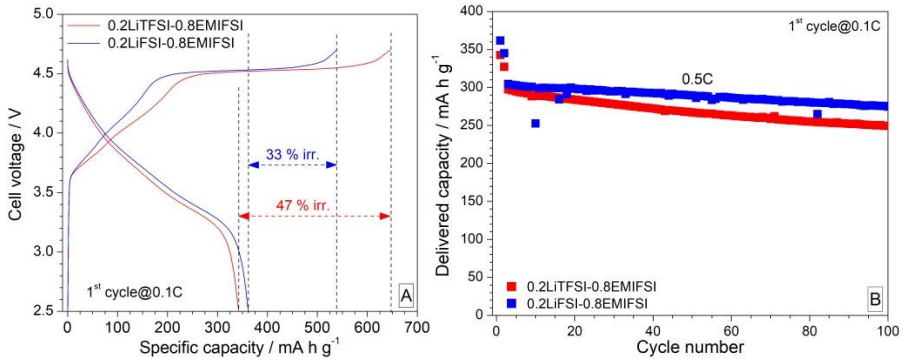

Figure 4.5: Voltage vs. capacity profile of the 1st charge-discharge cycle (panel A) and discharge capacity evolution (panel B) of Li/LRNM cells containing the 0.2LiTFSI-0.8EMIFSI and 0.2LiFSI-0.8EMIFSI ionic liquid electrolytes at 0.5C. Temperature: 20 °C. Sieved LRMN was employed.

To summarize, the results reported in **Figures** from **4.1** to **4.5**, indicate a better behavior for the 0.2LiFSI-0.8EMIFSI electrolyte formulation, exhibiting performances comparable, if not higher, with respect to those observed in organic standard lithium battery solutions [118,218,220,221].

4.3.4 Cyclic voltammetry investigation

The lithium intercalation process of the LRMN cathodes in the 0.2LiTFSI-0.8EMIFSI and 0.2LiFSI-0.8EMIFSI electrolyte formulations was investigated through CV tests (**Figure 4.6**) conducted at progressively increasing current rates and 20 °C. In agreement with the results reported in literature [115,218,220,221], the 1st anodic scan (thick trace), run at low rate (0.05 mV s^{-1}) for better evidencing the lithiation process, show weak and broad features (Li^+ alloying) in the 3.5-4.2 V voltage range, observed also in the corresponding cathodic scan (panels A and B). These specific current (normalized towards the LRMN active material weight) vs voltage profiles are coherent with the expected lithiation mechanism proposed in literature for the lithium-rich, layered oxide materials [219–221]. A well-pronounced peak, missing in all subsequent sweeps, is evidenced around 4.65 V (panels A and B), due to structural reorganization (i.e., crystalline phase modification) occurring in the LRMN material [217] and in agreement with the cycling test results (**Figure 4.1**-**4.5**). The increase of the scan rate leads to progressive enhancement of the current *vs.* voltage profiles (both in the cathodic and anodic verse) with only modest shift of the maximum value, indicating relatively fast kinetics of the lithium intercalation process. The raise in the current value recorded through the cells is a direct consequence of the increase of the scan rate based on the Randles-Sevcik equation as reported for the Si anodes in Section 3.3.1. The linear correspondence between current and scan rate values is attributable to the fact that the current is given by the charge per unit of time. The current flowing through the electrode is limited by the diffusion of the species located on its surface and, therefore, the ion flow due to the diffusion process is affected by the concentration gradients that are formed inside the electrolyte. These gradients are influenced by the voltage value of the cell (described by the Nernst equation) and, therefore, a faster variation of the voltage causes higher concentration in the proximity of the electrode. This results in increase in the number of electron equivalents exchanged and, likewise, in the value of current through the electrochemical cell.

The good reversibility of the lithiation process is highlighted by the correspondence between the cathodic and anodic features, suggesting high coulombic efficiency, and by the reproducibility of the CV traces even at high scan rates (i.e., the 21st cycle, run at 0.05 mV s^{-1} and subsequent to the CV tests carried out at much higher scan rate, is very close to the initial ones subjected to analogous scan rate). All current *vs.* voltage profiles are distinguishable even at 1 mV s^{-1} both in 0.2LiTFSI-0.8EMIFSI and in 0.2LiFSI-0.8EMIFSI cells, once more witnessing for quick Li^+ intercalation kinetics. It is worthy to note that the use of the IL-based electrolytes does not alter the expected reaction mechanism occurring in these materials. Prolonged CV tests (panels C and D), run after the CVs reported in panels A and B, display well-defined specific current vs voltage profiles even upon 100 consecutive cycles at 1 mV s^{-1}. Three main features, located around 3.3, 4.2 and 4.6 V

respectively, are evidenced in the anodic verse (Li^+ intercalation), and around 2.9, 3.6 and 4.4 V in the cathodic scans (Li^+ de-intercalation). The reversibility of the intercalation process is witnessed by the good correspondence between the cyclic voltammetry profiles, which only moderately are seen to decrease after 100 cycles, this highlighting remarkable reproducibility of the CV traces. The replacement of the LiTFSI salt with LiFSI does not lead to any relevant change of CV profile shape and/or shift of the voltage-current features, even at high scan rates. Also, no practical improvement in terms of cycling performance and capacity retention is observed. However, it should be noted a higher capacity stored during the anodic sweep for LiFSI electrolytes (comparison among the area of current-voltage profiles) with respect to the LiTFSI ones, whereas very similar and reproducible features are highlighted during the cathodic sweep.

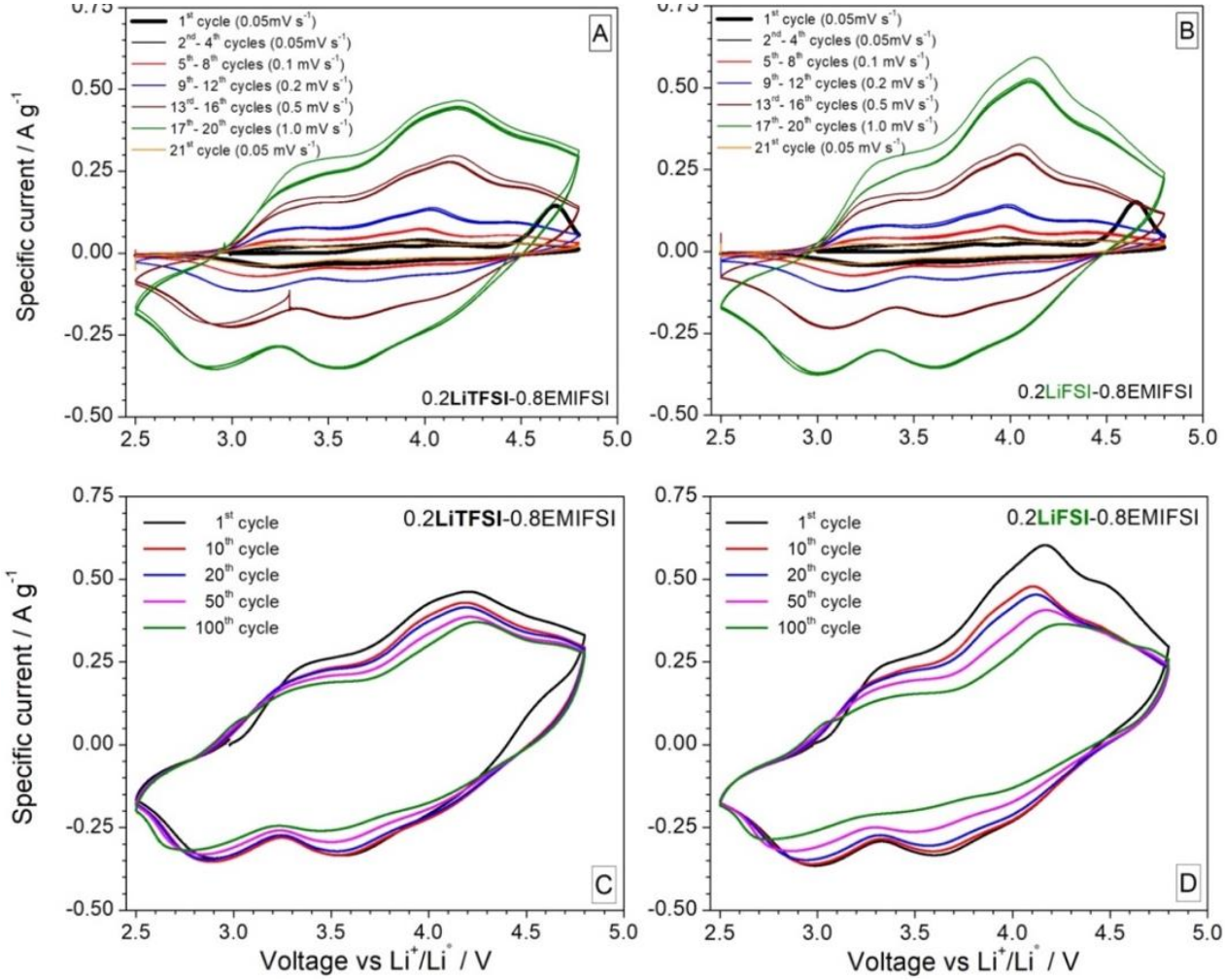

Figure 4.6: CV traces of Li/LRMN cells containing the 0.2LiTFSI-0.8EMIFSI (panels A and C) and 0.2LiFSI-0.8EMIFSI (panels B and D) electrolytes at different scan rates (panel A and B) and 1 mV s^{-1} (panels C and D). T = 20 °C.

4.4 Conclusions

Cycling tests run in Li/LRMN cells allowed to select EMIFSI as the most suitable IL component for the electrolytes. Nominal capacities exceeding 320 mA h g^{-1} were exhibited with excellent retention, i.e., about 90 % of the initial capacity was delivered after 500 cycles. Better rate capability was shown by the LiFSI electrolytes.

The lithiation process of LRNM in different IL-binary mixtures was analyzed by cyclic voltammetry measurements, run at increasing scan rates and for prolonged cycles. Voltammetry highlighted good reversibility and efficiency of the Li^+ intercalation process, indicating good compatibility of both, the LiTFSI-EMIFSI and LiFSI-EMIFSI, electrolytes with LRMN electrodes. However, the full-FSI display higher specific current even after prolonged CV test (> 200 cycles), indicating larger charge amount involved in the lithiation process.

To summarize, the full-FSI electrolyte exhibit comparable, if not higher performance with respect to those observed in organic standard solutions in LRMN cathodes, this again highlighting the good compatibility towards these kinds of lithium battery electrodes.

5. Hard carbon anode for Na-ion batteries

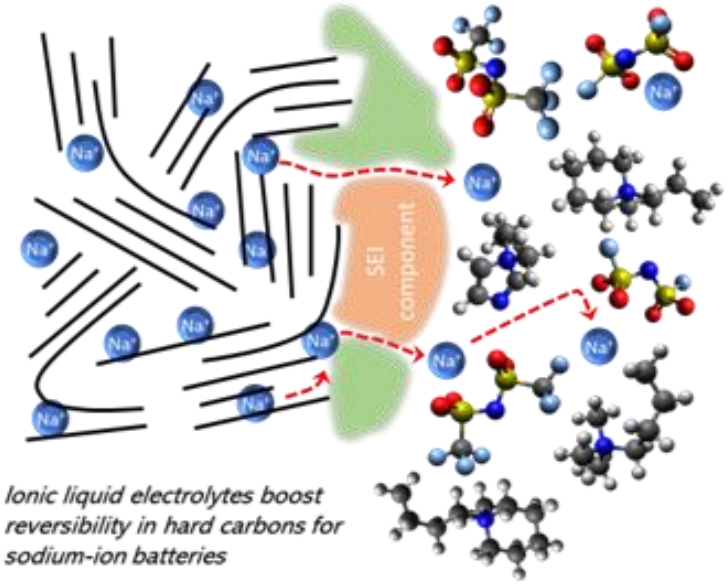

5.1 Introduction

Sodium-ion batteries (SIBs) are considered a promising alternative technology to the lithium-ion one for stationary energy storage systems. Among negative electrodes for Na-ion cells, graphite, the most widely used one in Li-ion batteries (LIBs) is unfortunately poorly active [225,226]: apparently, the reversible electrochemical intercalation of sodium ions within the graphite layers is limited to the NaC_{64} stoichiometry to be compared to the LiC_6 for LIBs [227]. The most effective alternatives to graphite for SIBs anodes are hard carbons (HCs), titanates and conversion materials [32,228]. The so-called non-graphitizable hard carbon attracted great attention thank to the large specific capacity in SIBs, low operative voltage and cycling stability. Moreover, hard carbons can be obtained starting from waste biomasses or natural products [229–231] and thus, their synthesis almost does not rely on non-renewable raw materials. Overall, HCs are eco-friendly, cheap and, therefore, suitable for large-scale production and commercialization.

HCs, obtained by chemical or thermal process from organic materials [232], show high mechanical hardness and micro-to-meso-porosities closely related to the precursor morphology [233]. In aprotic SIBs with carbonate-based electrolytes, HC anodes suffer high irreversible capacity losses in the first cycle followed by unsatisfactory coulombic efficiency upon cycling, i.e., in many cases below 99% [234,235] in Na metal cells [236,237]. This drawback originates from the parasitic reactions involving the electrolyte degradation (reduction) at low potentials, leading to the precipitation of decomposition product and consequent growth-up of the SEI layer (Solid Electrochemical Interface). Unfortunately, the SEI consolidation on HCs for SIBs is not affective like in the case of graphite for LIBs. In fact, previous X-ray photoemission studies proved the evolution of the SEI composition grown on HCs

for more than 10 galvanostatic cycles in sodium metal cells [128]. This detrimental phenomenon is a serious drawback for SIBs and also hinders the overall safety of the battery [236,238].

In the last two decades, various strategies have been demonstrated to improve the battery safety and reliability: as an example, by replacing the common organic-based solutions with ceramic, polymeric and ionic liquid (IL) electrolytes [52–54]. Among these, ILs are widely considered as safer electrolyte solvents compared to carbonates. Up to present only few ILs chemistries, mainly based on the pyrrolidinium cation [114,115], have been studied in SIBs despite the innumerable possible variety of potentially applicable ILs.

In the present PhD thesis activity, we have screened different IL families for being addressed to SIB systems. Based on the results reported in Chapter 2, the EMIFSI and N_{1114}FSI electrolyte formulations were selected for investigation with HC anodes.

5.2 Experimental Section

5.2.1 Materials and Methods

The EMIFSI and N_{1114}FSI electrolyte formulations were prepared as described in Chapter 2. The 1M NaTFSI in PC + 3 wt.% FEC organic solution, used for comparison purpose, was purchased by Solvionic.

The hard carbon material (developed and provided by La Sapienza University of Rome) was synthetized (starting from an organic precursor, i.e., D- (+)-Glucose (powder, Sigma Aldrich 99.5% purity). D-(+)-Glucose was de-watered) according to a route described in detail elsewhere [128]. Composite electrodes were prepared by casting *N*-methyl pyrrolidone slurries of the HC (75% in weight) mixed with super-P carbon (15 wt.%) and polyvinylidene difluoride binder (10 wt.%) on 20 µm thick Al foils. The mean mass loading of the electrodes was about 1.0 mg cm^{-2}, corresponding to a theoretical capacity of 0.3 mA cm^{-2} (300 mA h g^{-1}). The HC electrodes were punched in disks with 10 mm diameter, dried overnight under dynamic vacuum at 120 °C and stored in an Ar-filled glove box (Jacomex, Dagneux, France, O_2 and H_2O level < 1 ppm). All materials as well as the cell manufacturing were stored and handled in an Ar-filled glove box.

5.2.2 Electrochemical measurements

The Na^+ intercalation/deintercalation process in the HC active material and the SEI formation onto the electrodes were studied by cyclic voltammetric (CV) analysis paired with potentiostatic electrochemical impedance spectroscopy (PEIS) measurements. CV tests at different scan rates and run for prolonged cycles, associated with PEIS measurements, were performed on 0.1NaTFSI-0.9EMIFSI and 0.1NaTFSI-0.9N_{1114}FSI electrolytes in Na metal cells using HC as the working electrode material. Coin cells (CR2032) have been assembled (i.e., Na/0.1NaTFSI-0.9IL/HC galvanic

chain) by coupling a hard-carbon working electrode, two glass fiber disk (16 mm diameter, 100 µm thickness) separators (Whatman TM, Maidstone, UK) soaked with 150 µl of electrolyte, and a sodium metal (American Elements, Los Angeles, CA, USA) disk (10 mm diameter, 100-200 µm thickness) counter electrode. The CV tests were carried out between 0.01 to 2.2 V vs the $Na^+/Na°$ redox couple at increasing scan rates, i.e., from 0.05 to 1 mV s^{-1} (running four consecutive cycles for each selected scan rate). Finally, the Na/HC cells were subjected to 500 consecutive CV cycles carried out at 1 mV s^{-1}. Impedance measurements were run on the as manufactured cells, at the end of each CV family (at increasing scan rate) and after prolonged CV test, in the frequency range from 10 kHz to 0.1 Hz with 10 mV amplitude voltage.

The performances of HC material in Na metal cells, using the 0.1NaTFSI-0.9EMIFSI, 0.1NaTFSI-0.9 N_{1114}FSI and 1M NaTFSI in PC + 3 wt.% FEC (for comparison purpose) electrolytes, were evaluated by galvanostatic charge-discharge (GC) measurements. Three electrode cells were assembled using HC as the working electrode and Na metal as both counter and reference electrode (10 mm diameter). Two fiber glass disks (10 mm diameter), embedded with the IL electrolyte, were used as the separator. GC tests were performed at 0.1C, 0.2C, 0.5C and 1C current rates in the 0.01-2.2 V voltage range. The cycling tests were run in external environment (instead within a climate chamber) to point out the temperature effect on the electrode performance.

All the electrochemical tests were carried out using a Biologic (Seyssinet-Pariset, France) multichannel battery cycler.

5.2.3 Interfacial characterization

Raman spectroscopy measurements were registered using a DILOR LabRam confocal micro-Raman with a He-Ne laser source at 632.7 nm. All samples were loaded in 3D printed holders (poly lactic acid) sealed with a 0.155 mm transparent glass window to avoid undesired reactions with air moisture. The Raman energy shift was calibrated using a Si wafer. The Raman peak fitting procedure was carried out by using Voigt function. Besides the pristine electrodes, all spectroscopic experiments were performed on samples collected post-mortem from cells in different states of charge: *i*) pristine material; *ii*) 1 discharge at 0.1C; *iii*) 1 cycle at 0.1C; *iv*) 2 cycles at 0.1C + 8 cycles at 0.2C and *v*) 2 cycles at 0.1C + 8 cycles at 0.2C + 1 discharge.

The XPS analysis was registered using a Kratos AXIS ULTRA spectrometer with a monochromatic Al Kα X-ray radiation source (hν = 1486.6 eV). Pass energy of 160 eV for survey spectra and 20 eV for narrow regions were used. The C 1s line at 284.8 eV was used as a charge reference. The FIB-SEM measurements were performed by a Helios G4CX. Both the top surface and the cross-section of the HC electrodes were examined. The electrode morphology was investigated using secondary electron (SE) images. The elastic scattering between the primary electrons and the

atoms is proportional to the Z number: therefore, heavier elements provide a stronger signal, resulting in a brighter BSE image. Both measurements were performed on post-mortem HC electrode, obtained after dismantling the cells and rinsing in tetrahydrofuran. The measurements were conducted in high vacuum for avoiding air contamination.

5.3 Results and discussions

5.3.1 Sodium intercalation process

Cyclic voltammograms are shown in **Figure 5.1** at different scan rates (panels A and B) and after prolonged cycles (panels C and D) for both the EMIFSI and N_{1114}FSI based electrolytes. Current values have been normalized with respect to the HC mass loading of electrodes (specific current). A broad and intense feature, related to the electrochemical passivation layer (SEI) formation on the HC surface [96,128] and located around 0.6 V vs the Na^+/Na redox couple, can be observed for both IL electrolyte formulations during the 1st cathodic scan (black trace) conducted at low scan rate (0.05 mV s^{-1}). This peak disappears in the following cycles, suggesting negligible degradation processes of the electrolytes. Generally, sodium insertion into the HC electrode occurs through a two-step storage mechanism: *i)* Na^+ intercalation into graphene layers above 200 mV vs. Na^+/Na and *ii)* Na^+ insertion into micropores formed by the *pseudo-graphitic* domains with an oxidation state close to that of Na metal, which is detected below 200 mV [32,97,226,239]. The presence of two well-defined features around 0.15 V and 0.7 V (related to this two-step mechanism insertion) can be observed, in both electrolytes, during the first cycles at low scan rate in line with the expected sodium ion incorporation mechanism. A good reversibility of the electrochemical sodiation is observed even at high scan rates and during prolonged cycles. The increase of the scan rate results in the expected intensity enhancement of the current vs voltage profiles (both in the anodic and cathodic branches) with only modest shift of the maximum value, likely due to diffusion following the Randles-Sevcik equation [37,240]. The 0.1NaTFSI-0.9N_{1114}FSI cells show larger value of the specific current related to the electrochemical processes with respect to the 0.1NaTFSI-0.9EMIFSI ones, indicating larger Na^+ equivalent exchange and, therefore, a larger capacity delivered by the sodium (de)intercalation.

Prolonged cyclic voltammetry analysis has been performed in challenging conditions (500 cycles at 1 mV s^{-1}) to further demonstrate the reversibility of the sodiation processes in hard carbon electrodes. The results, displayed in **Figure 5.1C** (EMIFSI electrolyte) and **5.1D** (N_{1114}FSI electrolyte), show well-defined current-potential profile around 0.5 V (cathodic scan) and 0.6 V (anodic scan) for both electrolytes. Furthermore, the excellent reproducibility of voltammograms cycle-by-cycle confirms the outstanding reversibility of the Na^+ intercalation, even after hundreds of cycles for both IL electrolytes. This evidence is a possible clue of outstanding retention capacity for the hard carbon electrodes in any electrochemical cycling test. The Na/HC cells containing the

0.1NaTFSI-0.9N_{1114}FSI electrolyte show stronger voltammetry curves with higher specific current value, indicating a larger amount of charge involved in the sodiation process.

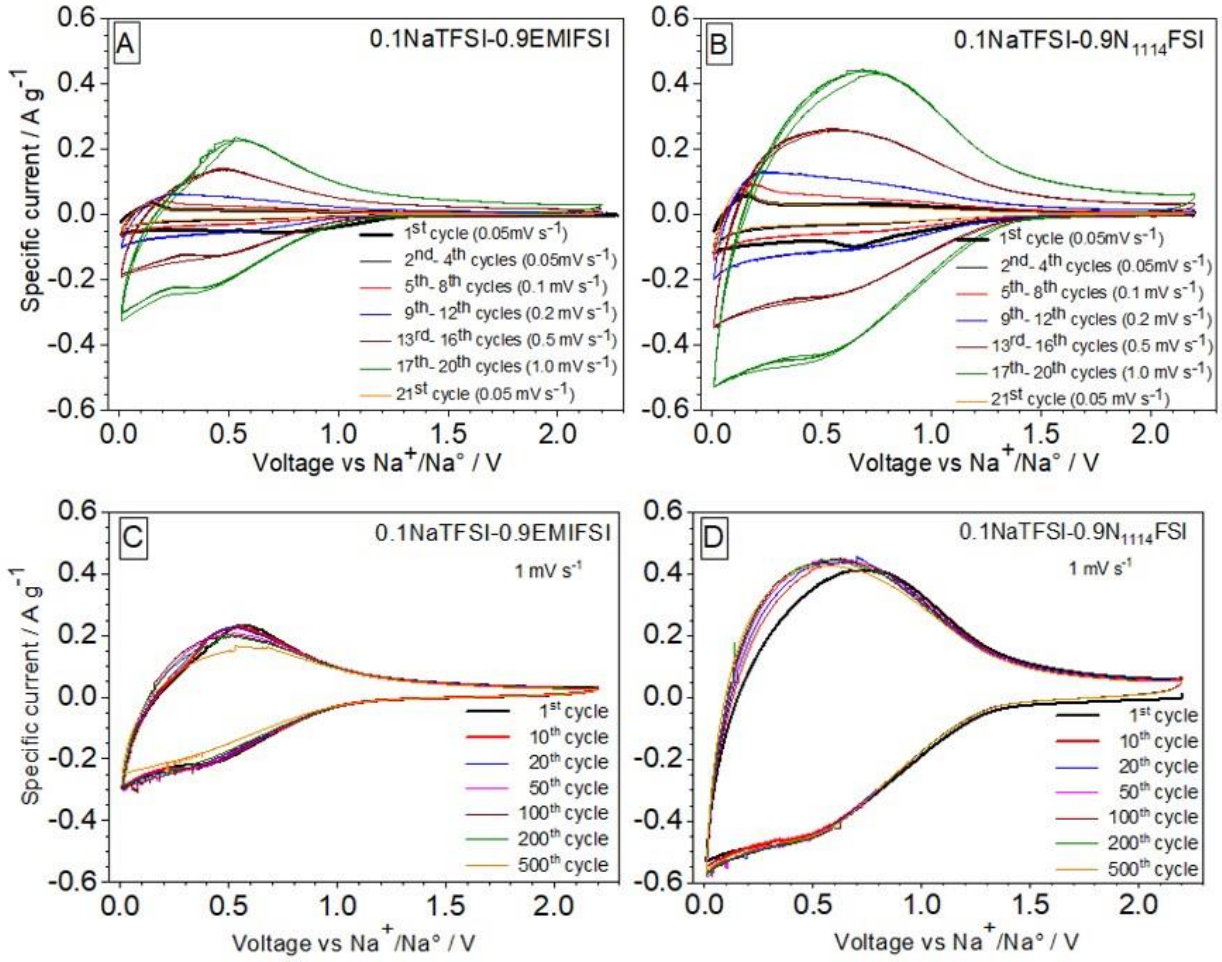

Figure 5.1: Cyclic voltammetries of Na/HC cells containing 0.1NaTFSI-0.9EMIFSI (panels A and C) and 0.1NaTFSI-0.9N_{1114}FSI (panels B and D) electrolytes at different scan rates (panel A and B) and for prolonged cycles with a scan rate of 1 mV s^{-1}(panel B and D). T = 20 °C.

As observed for the silicon (Chapter 3) and LRMN (Chapter 4) electrodes, the increase in the current value recorded in the CV tests reflects the raise in the scan rate, i.e., in line with the Randles-Sevcik equation [37,240]. Therefore, all voltammograms (recorded at different scan rates) have been analyzed to evaluate the diffusion coefficient D_0 (cm^2 s^{-1}) of the sodium ions at electrolyte/ anodes. The peak current (i_p) values, related to the *C* parameter and associated to the sodium insertion-extraction with the respective redox potential (E_p), are summarized in **Table 5.2**. The peak current ratio of the anodic (i_{pa}) and cathodic (i_{pc}) scans is almost equal to unity in both IL electrolyte formulations, suggesting reversible intercalation process and no chemical reaction coupled with the electron transfer [241].

Table 5.2. Anodic (i_{pa}) and cathodic (i_{pc}) peak current values, and related anodic (E_{pa}) and cathodic (E_{pc}) peak voltage, determined at different scan rates for Na/HC cells using the 0.1NaTFSI-0.9EMIFSI and 0.1NaTFSI-0.9N_{1114}FSI electrolytes. T = 20 °C.

Scan rate / mV s^{-1}		0.05	0.1	0.2	0.5	1
0.1NaTFSI-0.9EMIFSI	i_{pa} / A	(2.8± 0.1)×10^{-2}	(3.7±0.2)×10^{-2}	(6.6±0.3)×10^{-2}	(13.2±0.7)×10^{-2}	(21.7±1.1)×10^{-2}
	E_{pa} / V	(13.0±0.6)×10^{-2}	(18.0±0.9)×10^{-2}	(24 ± 1)×10^{-2}	(46 ± 2)×10^{-2}	(55.0±2.7)×10^{-2}
	i_{pc} / A	(-1.9±0.1)×10^{-2}	(-3.8±0.2)×10^{-2}	(-6.6±0.3)×10^{-2}	(-12.3±0.6)×10^{-2}	(-212 ± 1)×10^{-2}
	E_p / V	(11.0±0.5)×10^{-2}	(13.0±0.6)×10^{-2}	(22 ± 1)×10^{-2}	(43 ± 2)×10^{-2}	(37 ± 2)×10^{-2}
0.1NaTFSI-0.9N_{1114}FSI	i_{pa} / A	(3.4±0.2)×10^{-2}	(3.8±0.2)×10^{-2}	(5.5±0.3)×10^{-2}	(10.9±0.5)×10^{-2}	(18.5±0.9)×10^{-2}
	E_{pa} / V	(14.0±0.2)×10^{-2}	(17.0±0.8)×10^{-2}	(22 ± 1)×10^{-2}	(52 ± 3)×10^{-2}	(68± 3)×10^{-2}
	i_{pc} / A	(-2.1±0.1)×10^{-2}	(-3.8±0.2)×10^{-2}	(-5.5±0.3)×10^{-2}	(-10.5±0.5)×10^{-2}	(-18.1±0.9)×10^{-2}
	E_p / V	(10.0±0.5)×10^{-2}	(13.0±0.6)×10^{-2}	(30 ± 2)×10^{-2}	(52 ± 3)×10^{-2}	(49 ± 3)×10^{-2}

Figure 5.2 plots the i_{pa} and i_{pc} current values against the square root of the scan rate for Na/HC cells in 0.1NaTFSI-0.9EMIFSI and 0.1NaTFSI-0.9N_{1114}FSI electrolytes. A straight-line dependence (crossing the axes origin) is observed, supporting for the diffusive nature of the sodium insertion in the hard carbon electrode. The D_0 parameter was calculated through the slope $i_p/v^{1/2}$ (proportional to the square root of the diffusion coefficient) [242–244], obtained by linear fitting (**Figure 5.2**). Comparable diffusion coefficients, related to the electrolyte/electrode interface, were found for both IL Na-formulations, with a moderately higher value ((4.9 ± 0.3) × 10^{-9} vs (3.5 ± 0.2) × 10^{-9} cm^2 s^{-1}) for 0.1NaTFSI- 0.9EMIFSI likely due to the faster ion transport properties of the EMIFSI ionic liquid [93]. The error on the D values was found to be equal to 5 %. It is to note that they are one order of magnitude lower with respect to those reported in literature for organic electrolytes and determined through different techniques [245–247], likely due to the higher viscosity of the IL electrolyte medium.

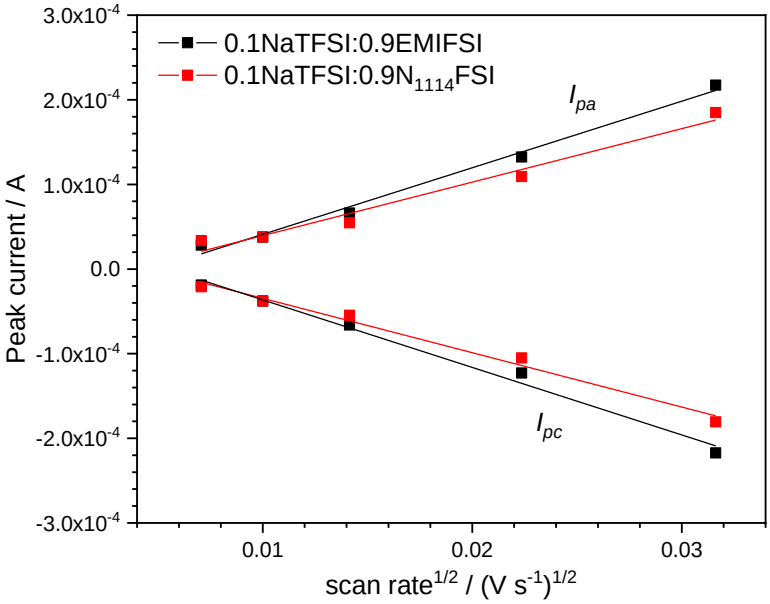

Figure 5.2: Dependence of the peak current on the square root of the voltage scan rate, referred to the sodium insertion/ extraction into/from HC electrodes, in 0.1NaTFSI-0.9EMIFSI and 0.1NaTFSI-0.9N_{1114}FSI electrolytes. T = 20 °C.

5.3.2 Impedance measurements

The AC responses, recorded during each CV tests run at different scan rates (**Figure 5.1**), of Na/HC cells in 0.1NaTFSI-0.9EMIFSI (panel A) and 0.1NaTFSI-0.9N1114FSI (panel B) electrolytes are reported in **Figure 5.3** as Nyquist plots. A medium-high frequency (10 kHz -100 Hz) semicircle pattern, related to the overall interfacial resistance [178,248,249], is observed, followed by a straight line (100 – 1Hz) which is related to the HC electrode capacitance [178,248,249]. The high-frequency intercept of the semicircle with the real axis gives the bulk resistance of the IL-based electrolyte. The AC responses have been fitted by a proper equivalent circuit model (Figure 5.3) where R_{bulk} and R_{int} are the electrolyte and overall interfacial resistance, respectively, Q_{dl} is the constant phase element taking on account for the double layer capacitance and C_l is the electrode limit capacitance [178,248,249]. R_{bulk} is found to be around 3 and 25 Ω cm^2 (at 20 °C) for 0.1NaTFSI-0.9EMIFSI and 0.1NaTFSI-0.9N1114FSI cells, respectively, i.e., in good agreement with the ionic conductivity values reported in previous paper [93] supporting for faster ion transport properties for the EMIFSI electrolyte (8.6×10^{-3} vs 1.8×10^{-3} S cm^{-1}). As summarized in **Table 5.3** and evidenced in **Figure 5.4**, no relevant increase of the R_{bulk} value is observed during CV cycles run at increasing scan rates, suggesting no appreciable degradation processes on the electrode surfaces in both IL electrolytes.

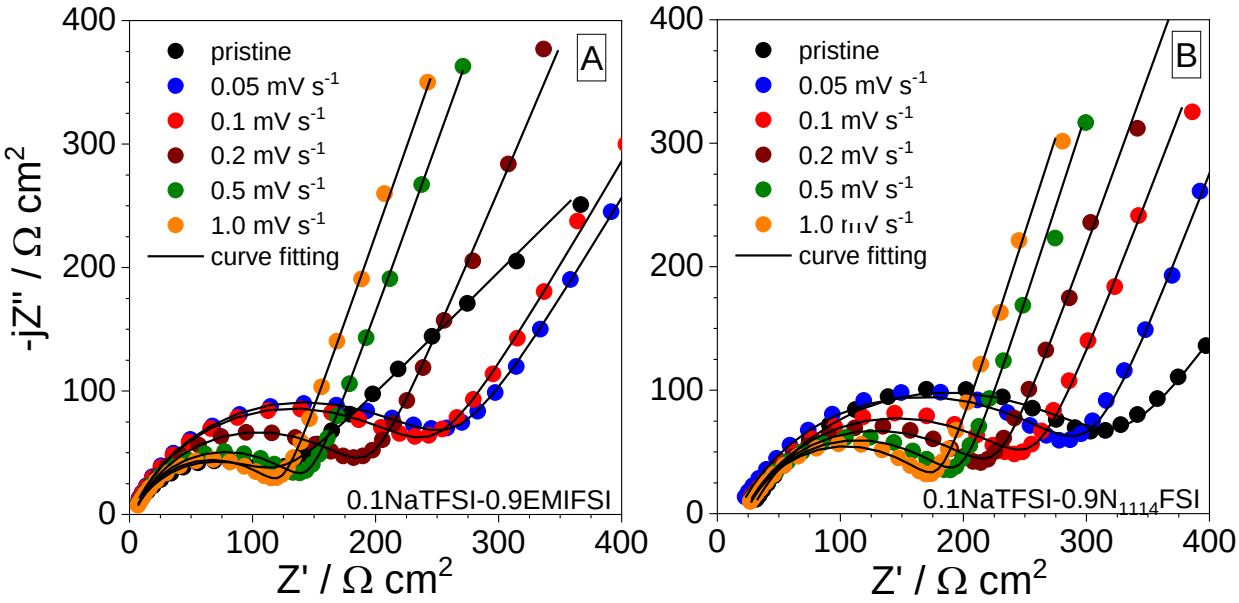

Figure 5.3: AC response, carried out during the CV tests reported in Figures 5.1A and 5.1B, of a Na/HC cell in 0.1NaTFSI:0.9EMIFSI (panel A) and 0.1NaTFSI:0.9N_{1114}FSI (panel B) electrolytes. The equivalent circuit model is also reported in both panels. T = 20 °C

The evolution of the R_{bulk} and R_{int} parameters against the scan rates is displayed in **Figure 5.4**. A progressive reduction of the interfacial resistance during the CV tests is observed, i.e., from 240 to 110 Ω cm^2 and from about 270 to 145 Ω cm^2 for the 0.1NaTFSI-0.9EMIFSI and 0.1NaTFSI-0.9N_{1114}FSI cells, respectively, due to an improvement of the electrolyte/HC interface probably ascribable to the increase

in electronic conductivity of the HC active material during the sodiation process, which promotes the electrochemical reaction kinetics [179]. Finally, the Q_{dl} element is found to be of the order of 10^{-6} F, i.e., as expected for double layer capacitance in lithium or sodium battery systems [178,248,249].

Table 5.3. R_{bulk} (Ω cm) and R_{int} (Ω cm^2) parameters, associated to Na/HC cells containing the 0.1NaTFSI-0.9EMIFSI or 0.1NaTFSI-0.9N_{1114}FSI electrolyte, determined in OCV condition after CV tests run at increasing scan rates (Figure 5.1). T = 20 °C.

Scan rate / mV s^{-1}		**Pristine**	**0.05**	**0.1**	**0.2**	**0.5**	**1**
0.1NaTFSI-0.9EMIFSI	R_{bulk}	2.6 ± 0.1	2.1 ± 0.1	2.6 ± 0.1	3.3 ± 0.2	4.0 ± 0.2	4.4 ± 0.2
	R_{int}	118 ± 6	240 ± 20	230 ± 20	181 ± 9	131 ± 7	109 ± 6
0.1NaTFSI-0.9N_{1114}FSI	R_{bulk}	27 ± 2	18 ± 1	24 ± 2	29 ± 2	26 ± 2	24 ± 2
	R_{int}	290 ± 20	270 ± 20	230 ± 20	171 ± 9	158 ± 8	145 ± 6

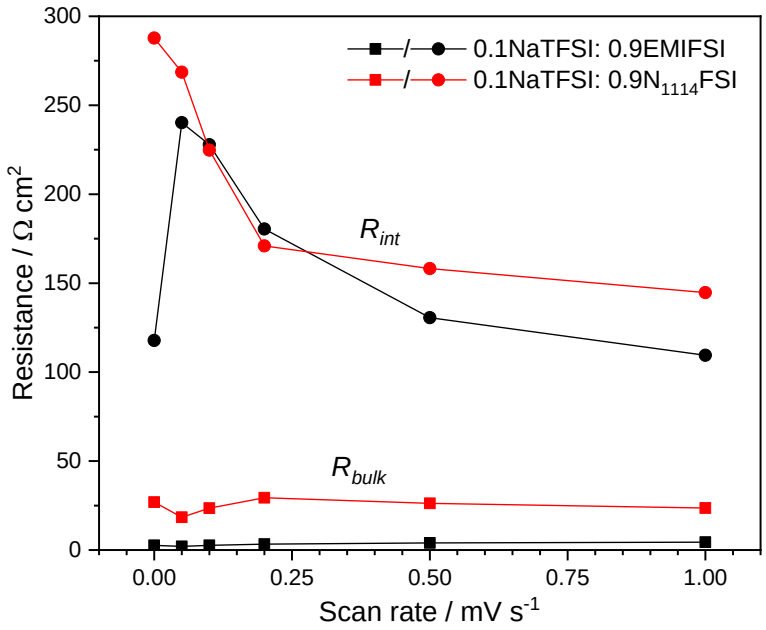

Figure 5.4: Evolution of the electrolyte (R_{bulk}) and overall interfacial (R_{int}) resistance, during CV tests run at different scan rates (Figure 5.1), for Na/HC cells in 0.1NaTFSI-0.9EMIFSI and 0.1NaTFSI-0.9N_{1114}FSI. T =20 °C.

Figures 5.5 compares the Nyquist plots, related to 0.1NaTFSI-0.9EMIFSI and 0.1NaTFSI-0.9N_{1114}FSI cells, obtained during the CV tests reported in **Figure 5.1**. The AC responses taken after each CV family run at increasing scan rates (**Figures 5.1A** and **5.1B**), reported in panels A and B, were above discussed for **Figure 5.3**. **Figures 5.5C** and **5.5D** display the Nyquist plots obtained during prolonged CV analysis (**Figure 5.1C** and **5.1D**). Again, no variation of the AC response shape was observed for both Na/HC cells. The R_{bulk} value, recorded after 500 cycles, is close to the initial one, confirming the absence of degradation phenomena within the IL electrolytes. No practical increase of the R_{int} resistance (close to

180 Ω cm^2) is seen for the EMIFSI cells, indicating stable electrolyte/electrode interface during the CV tests. Conversely, a marked decrease (from 260 to 180 Ω cm^2) is observed for the N_{1114}FSI ones, suggesting a morphological and/or structural gradual variation of SEI on the electrode surface and upholding the behaviour displayed **Figure 5.5A** and **5.5B**. Therefore, the N_{1114}^+ cation seems to play a favourable role for the SEI composition on the HC and Na surfaces.

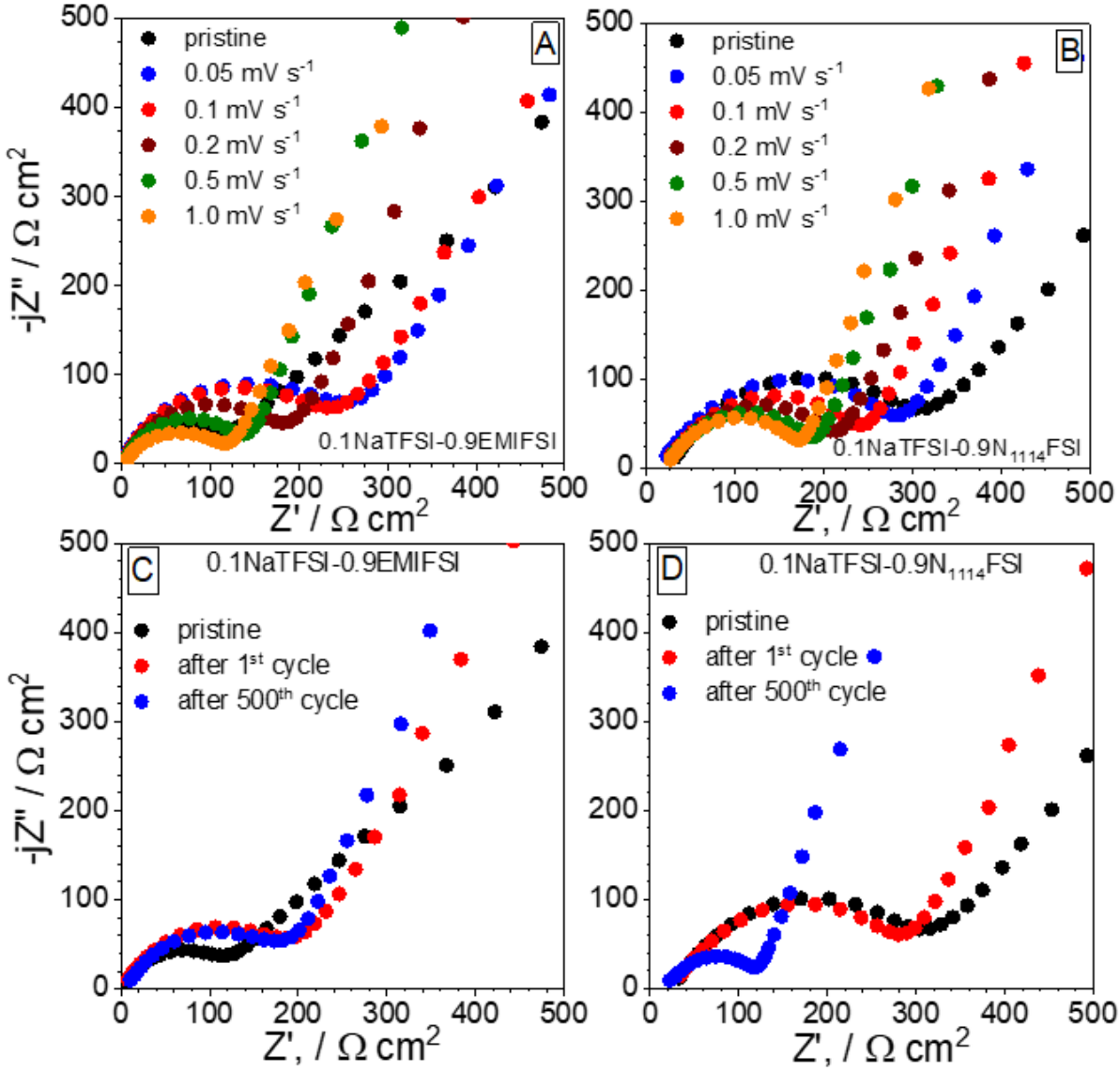

Figure 5.5: AC responses taken, under OCV condition, on Na/HC cells containing the 0.1NaTFSI-0.9EMIFSI and 0.1NaTFSI-0.9N_{1114}FSI electrolytes. The impedance measurements were run during after the CV tests (reported in Figure 5.1) carried out at different scan rates (panel A and B) and at 1 mVs^{-1} (panels C and D). Frequency range: 10 kHz – 1 Hz. Voltage amplitude: ΔV = 10 mV. T = 20 °C.

Figure 5.6 displays the AC response of Na/0.1NaTFSI-0.9EMIFSI/HC and Na/0.1NaTFSI-0.9N_{1114}FSI/HC cells recorded before (panel A) and after (panel C) the sodiation process of the HC electrode occurred during the 1st cathodic scan (panel B). A further depressed semicircle (**Figure 5.6C**)

appears in the medium-low frequency range after the first cathodic scan, due to the growth-up of a passive layer at the HC/electrolyte interface [248,250]; conversely, no change of electrolyte resistance is seen.

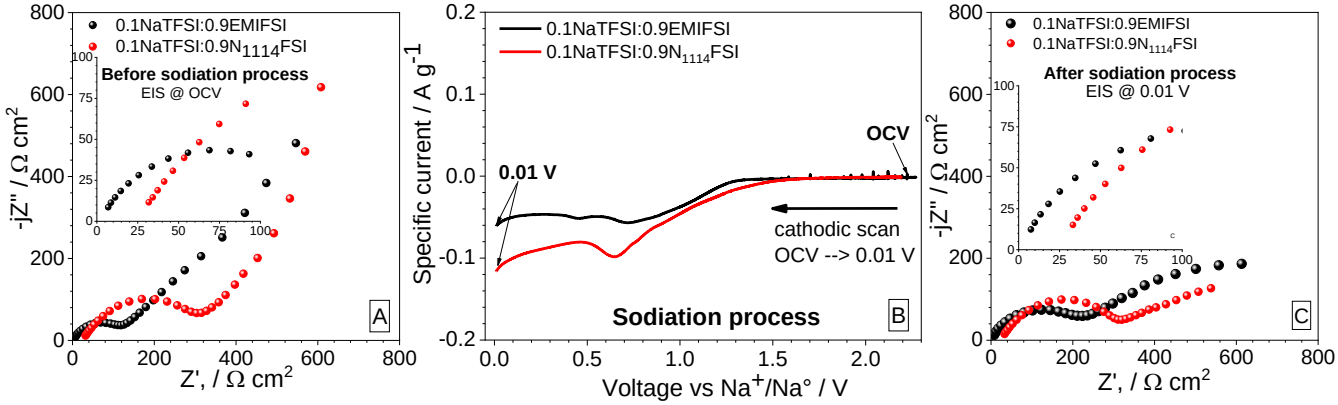

Figure 5.6: AC response of Na/0.1NaTFSI-0.9EMIFSI/HC and Na/0.1NaTFSI-0.9N_{1114}FSI/HC cells before (panel A) and after (panel C) sodiation process of the HC electrode occurred during the 1st cathodic scan (panel B). The insets in panels A and C magnify the high to middle frequency region. Frequency range: 10 kHz – 1 Hz. Voltage amplitude: ΔV = 10 mV. T = 20 °C.

5.3.3 Cycling behavior

The electrochemical performances of hard carbon electrodes in 0.1NaTFSI-0.9EMIFSI and 0.1NaTFSI-0.9N_{1114}FSI electrolytes have been investigated by galvanostatic cycling measurements at different current rates. The voltage-capacity profiles (panels A and B of **Figure 5.7**) display the expected two-step sodium intercalation process, i.e., a sloping curve at higher voltage (related to the Na^+ intercalation into pseudo-graphitic regions) from the OCV until 200 mV vs $Na^+/Na°$, followed by a reduced pseudo-plateau around 100 mV as a result of the ion-electron absorption inside the HC electrode micro-porosity [32,251]. Above 200 mV, 67 % (305 mA h g^{-1}) and 77 % (360 mA h g^{-1}) of the overall capacity are delivered in the EMIFSI and N_{1114}FSI cells, respectively, during the first Na-insertion whereas the remaining fraction (33 and 24 %, respectively) is discharged in the pseudo-plateau around 100 mV, according to the data reported in literature [128,251]. A large irreversible capacity (Q_{irr}) is observed during the first discharge, i.e., missing in the following cycles, due to the SEI formation onto the HC electrode [32], in agreement with the results reported in previous paper [94] for these IL electrolyte formulations. For instance, a Q_{irr} value levelling 61 % (270 mA h g^{-1}) is recorded for the N_{1114}FSI cells (**Table 5.2**), i.e., comparable with that observed in organic electrolytes [128,252,253], increasing up to 73 % (335 mA h g^{-1}) for the EMIFSI electrolyte (**Figure 5.7D**). No appreciable change of the discharge/charge voltage profiles is seen in passing from 0.1C to 1C (panel B), indicating fast kinetics of the Na^+ intercalation process in conjunction with the good ion transport properties of the IL electrolytes. Interesting reversible capacities are exhibited with good rate capability (**Table 5.4**): for instance, 127, 115, 96, 79 mA h g^{-1} (EMIFSI) and 175, 163, 135, 109 mA h g^{-1} (N_{1114}FSI) are observed at 0.1C, 0.2C, 0.5C and 1C, respectively, i.e., comparable with the values reported for organic electrolytes [128].

Therefore, around 64-66 % of the initial (nominal) capacity (0.1C) is displayed at 1C (panel E). The coulombic efficiency quickly overcomes 95 % after few cycles in both IL formulations, levelling at 99 % (panel C) even during very prolonged cycling tests (over 2000 cycles). By increasing the current rate down to 0.2C from 1C (panel C), the capacity returns to the value initially exhibited (at 0.2C), once more confirming the very good reversibility of the sodium intercalation process in HC electrodes. It is to be noted that an excellent capacity retention is shown, i.e., 87% (EMIFSI electrolyte) and 98.2 % (N_{1114}FSI) of the initial capacity are delivered after 1500 consecutive cycles at 0.2C, corresponding to a fading lower than 0.0090 % (EMIFSI) and 0.0012 (N_{1114}FSI) per cycle. This superior cycling behavior, largely exceeding that reported for organic carbonate-based electrolytes [128,179,254] has never been reported so far in literature. In fact, several electrolytes were investigated in other works [32,40,255], based on PC and/or ethylene carbonate (EC), dimethyl carbonate (DMC), diethyl carbonate (DEC) solvents, etc., in combination with $NaClO_4$, NaTFSI or $NaPF_6$ as sodium salts, which show values of reversible capacity close to those reported for the N_{1114}FSI-cell but with significant capacity fading upon cycling and higher initial irreversible capacity, demonstrating that the choice of the electrolyte plays a key role for good battery performances. Other innovative and efficient approaches were evaluated to boost the rate performances and the specific capacity of hard carbon anodes, such as doping with heteroatoms (i.e., pyridinic N and thiophene S) through different techniques [256,257], which allowed to enhance the sodium storage capacity. So, different strategies can be followed to raise the efficiency of hard carbon as anode, improving its structure and/or designing suitable electrolytes. The superior performances shown in our case are likely related to the good compatibility of FSI-based ionic liquids, especially N_{1114}FSI, with respect to the standard commercial battery solvents towards the HC electrodes. This is confirmed also in consideration of the experimental results recorded on Na metal cells with 1M NaTFSI in PC + 3wt.%FEC electrolyte cycled in analogues operative conditions (**Figure 5.7C**). Turning back to ILs-based electrolytes, the reversible capacity vs current density dependence, displayed in **Figure 5.7E**, does not show any step decay up to 1C, suggesting that the IL electrolytes are not affected by relevant diffusion phenomena up to this current rate. To summarize, the Na / 0.1NaTFSI-0.9N_{1114}FSI / HC cell configuration shows better performance, in terms of capacity, retention, rate capability and coulombic efficiency, than that based on EMIFSI.

Table 5.4: Initial irreversible capacity (Qirr) and reversible capacity, delivered at different scan rates, of Na/HC cells in different electrolyte formulations.

Electrolyte formulation	**1st cycle Q_{irr} / %**	**Q / mA h g^{-1}**			
		0.1C	**0.2C**	**0.5C**	**1C**
0.1NaTFSI-0.9EMIFSI	73	127	115	96	79
0.1NaTFSI-0.9N_{1114}FSI	61	175	163	135	109
PC:NaTFSI+3 wt.% FEC	73	153	144	134	125

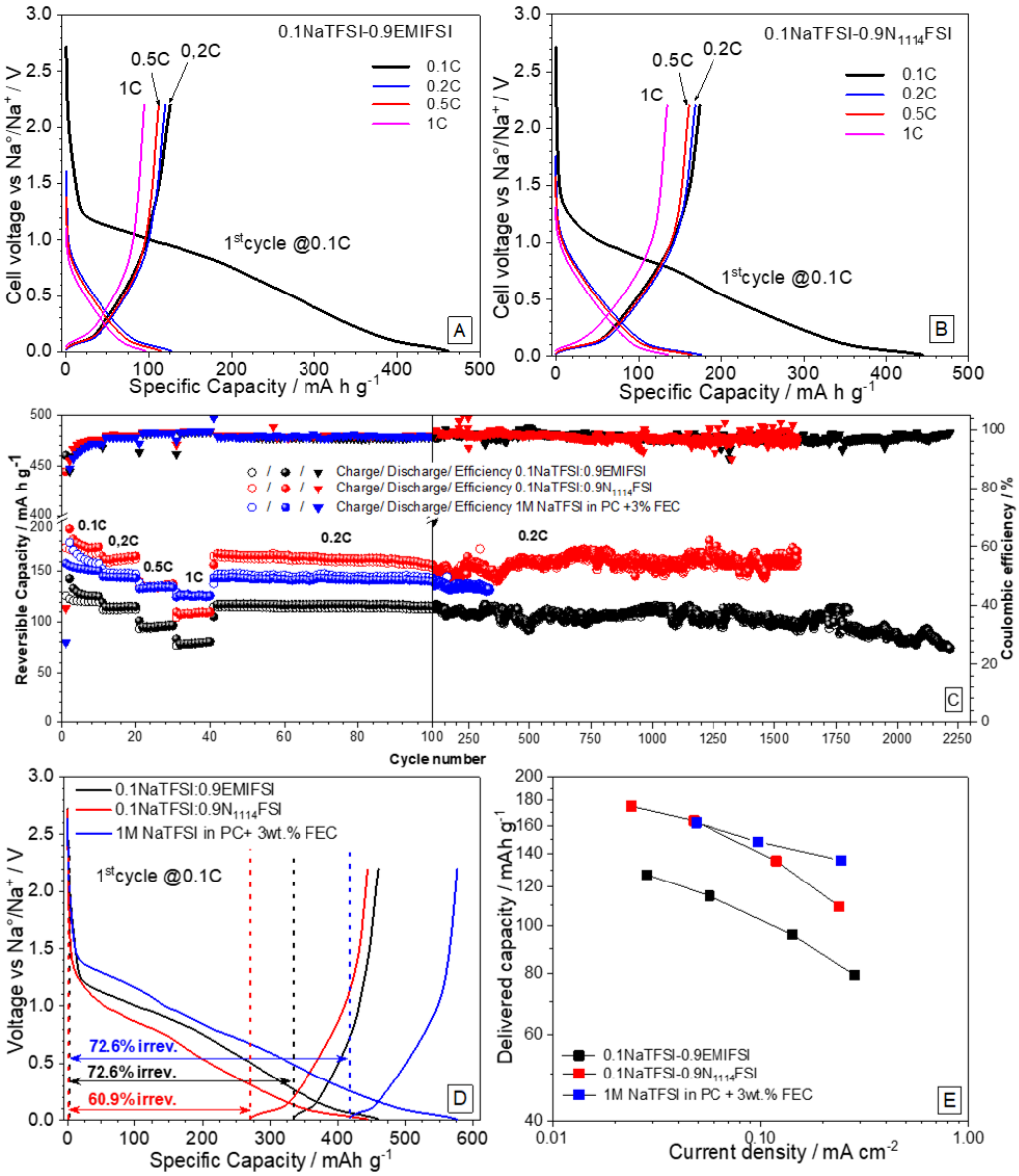

Figure 5.7: Voltage-capacity profiles at different rates (panels A and B), cycling performance (panel C), 1st discharge-charge curves (panel D) and reversible capacity vs current density dependence (panel E) of Na/HC cells in 0.1NaTFSI-0.9EMIFSI and 0.1NaTFSI-0.9N_{1114}FSI electrolytes. The cycling behaviour of Na/HC cells in (1M)NaTFSI-PC + 3 wt.% FEC organic electrolyte is reported (panel C) for comparison purpose. Room temperature.

5.3.4 Raman characterization

In order to better understand the structural alteration of hard carbon electrodes during the electrochemical insertion/removal of Na^+ ions in different electrolytes, micro-Raman spectroscopy measurements have been carried out on pristine and postmortem samples collected from cells. **Figure 5.8** shows the Raman spectra, recorded both in the full discharged (sodiated) and charged (de-sodiated) state after the 1st and 10th cycle, of HC electrodes in the 0.1NaTFSI-0.9EMIFSI and 0.1NaTFSI-0.9N_{1114}FSI electrolytes, while the Raman spectra related to the pristine HC sample was displayed in **Figure 5.9**. The

Raman spectra have been analyzed according to the model proposed by Sadezky *et al*. [256], which identifies the main components of the hard carbon signals at ~1595 cm^{-1} (G band), ~1340 cm^{-1} (D1 band), ~ 1630 cm^{-1} (D2 band), ~1500 cm^{-1} (D3 band), and ~1200 cm^{-1} (D4 band), respectively. The curve-fitted Raman spectrum of the pristine HC electrode (**Figure 5.9**) shows the D1, D3, and G bands as the main components, related to microcrystalline graphitic domains, amorphous carbon, and extended graphitic domains, respectively [258,259], confirming the structure observed in the previous work [128] through measurements of X-ray diffraction (XRD), Raman spectroscopy, N_2 adsorption (BET) and scanning electron microscopy (SEM). Where the synthesized HC was found to have the characteristic "falling card structural motif" [260], which consists of randomly graphene sheets packed with large amounts of micropores. The I_G/I_{D3} area ratio, representing the degree of graphitization [261], of the pristine hard carbon is equal to 0.42, indicating a highly disordered structure. In **Figure 5.8** (panel A) the Raman spectra of sodiated and de-sodiated electrodes cycled in the N_{1114}FSI-based electrolyte show differences in the profile shape, owed to the sodium insertion. The rise in intensity of the D4 component at ~1150 cm^{-1} results in the appearance of a left shoulder with respect to the main D1 band component. Moreover, a slight rise of the D3 contribution at ~1500 cm^{-1}, leading to a more pronounced coalescence between D and G bands, is observed in the case of sodiated samples. These bands are likely attributed to the amorphous carbon (D3) and the disordered graphitic lattice (D4) [258,259]. No shift of the D1 and G bands is shown (i.e., comparing the spectra of the sodiated and de-sodiated electrode), suggesting that sodium is likely incorporated through an adsorption mechanism on the hard carbon surfaces and defects, or pore filling, whereas intercalation occurs in a secondary process [262].

Conversely, a modification of the Na^+ insertion mechanism is noted in the 0.1NaTFSI-0.9EMIFSI electrolyte: a D band shift is detected for the sodiated electrode after the 1^{st} cycle, whereas both D and G bands look shifted after the 10^{th} cycle. This suggests that Na^+ insertion firstly involves only the microcrystalline graphitic domains (D1 band), whereas the extended graphitic domains (G band) are subsequently involved as the cycle number increases. In addition, the shift of the D and G bands demonstrates an increase of the d-spacing between the graphene layers owed to intercalation [263]. Avoiding, however, any speculation, it is possible that such a behaviour is originated not only by Na^+ intercalation, but also by the simultaneous co-intercalation of the EMI^+ cation, as reported in previous paper [261–263], likely because of its reduced size and planarity [24]. The fitting of the Raman spectra, recorded for the desodiated electrodes after the 1^{st} and 10^{th} cycle, allows to investigate the modification occurring in the hard carbon structure upon cycling. The results, reported in panels B (N_{1114}FSI electrolyte) and D (EMIFSI electrolyte), clearly show no significant shift (**Table 5.5)** and/or intensity variation of the Raman feature in N_{1114}FSI electrolyte, supporting for good structural stability. The I_G/I_{D3} area ratio is seen to decrease from 1.22 to 1.06 upon cycling, however significantly higher than that of the pristine electrode, suggesting that the HC structure evolves likely enhancing the graphite-like

character in the N_{1114}FSI electrolyte formulation. Conversely, a relevant shift of the D_3 and D_4 bands, both attributed to amorphous carbon, is detected for the electrode cycled in 0.1NaTFSI-0.9EMIFSI. The I_G/I_{D3} area ratio ranges from 0.51 to 0.43, i.e., very close to the graphitization degree of the pristine HC. Therefore, the Na^+ intercalation process in EMIFSI electrolyte involves microcrystalline (D1 band) or extended (G band) graphitic domains without leading to deep structural modifications, while the amorphous carbon region is more significantly affected. As the most relevant shift is related to the D4 band, i.e., mainly attributed to C-H termination groups and to the contribution of adsorbed molecules [226], it can be argued that one of the main causes of the observed variations is likely a change in the SEI layer morphology or composition. Work is in progress in our labs to investigate this issue.

Table 5.5. Positions of the G, D1, D3 and D4 bands of HC full-charged electrodes after cycling in 0.1NaTFSI-0.9N_{1114}FSI and 0.1NaTFSI-0.9EMIFSI electrolyte.

Electrolyte	**G (cm^{-1})**	**D1 (cm^{-1})**	**D3 (cm^{-1})**	**D4 (cm^{-1})**
0.9N_{1114}FSI-0.1NaTFSI *1st cycle*	1601	1335	1520	1195
0.9N_{1114}FSI-0.1NaTFSI *10th cycle*	1601	1338	1515	1195
0.9EMIFSI-0.1NaTFSI *1st cycle*	1595	1340	1498	1120
0.9 EMIFSI-0.1NaTFSI *10th cycle*	1596	1340	1476	1050

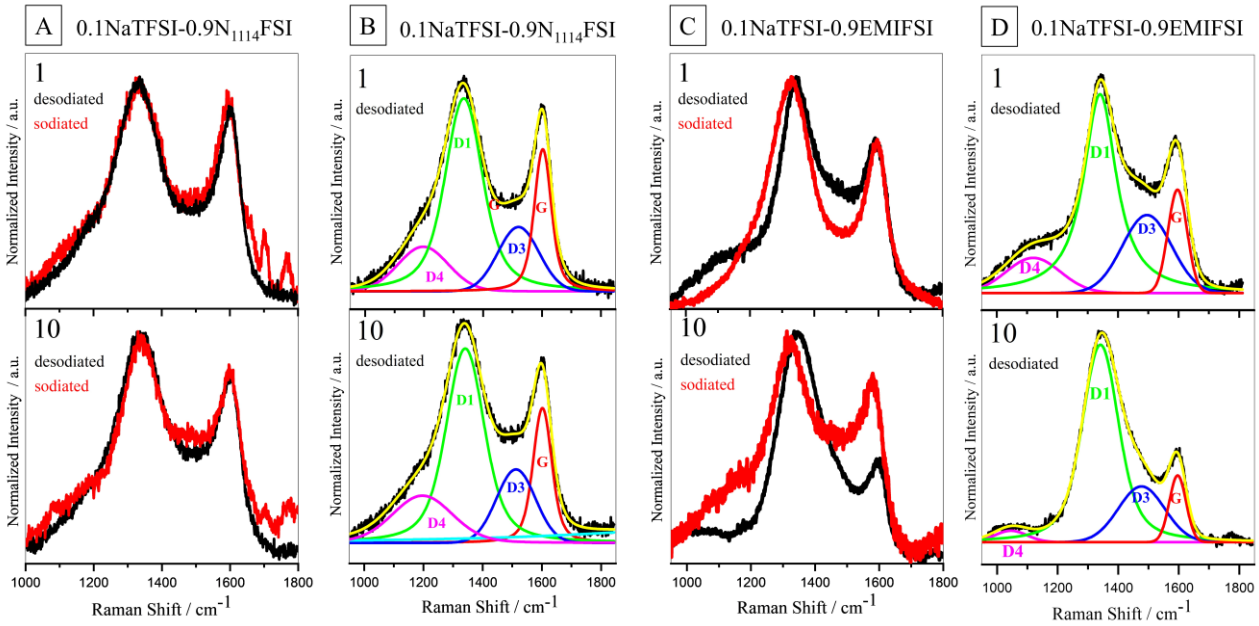

Figure 5.8: Raman spectra, recorded after the 1st and the 10th cycle, of HC electrodes (in the full-discharged and full-charged state) in 0.1NaTFSI-0.9N_{1114}FSI (a) and 0.1NaTFSI-0.9EMIFSI (c) electrolytes. Fitting curves of Raman spectra of HC electrodes (in the full-charged state) after the 1st and 10th cycle in 0.1NaTFSI-0.9N_{1114}FSI (b) and 0.1NaTFSI-0.9EMIFSI (d) electrolytes.

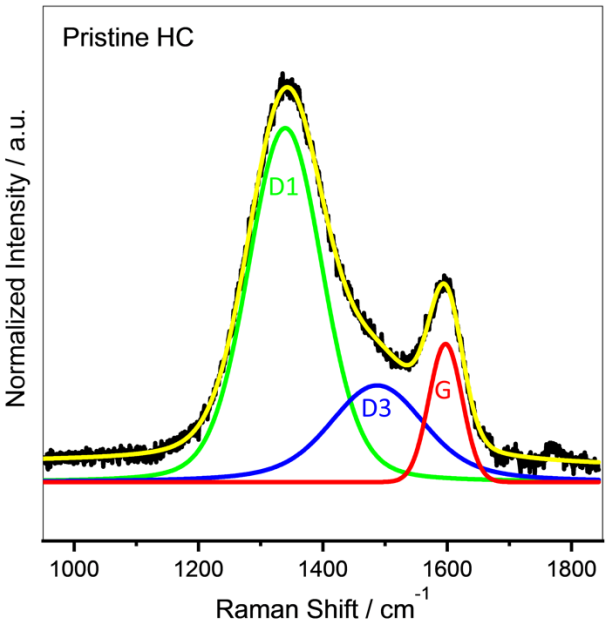

Figure 5.9: Curve-fitted Raman response of a pristine hard carbon electrode.

5.3.5 XPS analysis on HC anode surface

The HC electrodes subjected to the a few cycling tests were undergone to post-mortem analysis for getting information about the SEI layer composition. All samples were examined in the de-sodiated state, after 1 and 12 discharge-charge full cycles, respectively. **Table 5.6** reports the atomic percentage of the surface composition of HC anodes. The pristine electrode exhibits high concentrations of C and F, the latter related to the presence of the PVdF binder, as expected. After cycling, the HC samples in organic solution show higher concentration of C and F with respect to those cycled in IL electrolytes, indicating a thinner SEI layer onto the HC surface. Meanwhile, the electrodes cycled in IL-based electrolyte display a high concentration of S arising from the NaTFSI degradation products [264,265].

Table 5.6: Surface composition (atom percentage) of pristine and cycled HC electrodes.

		O 1s	C 1s	Na 1s	F 1s	N 1s	S 2p
Pristine		1.9	81.9	--	16.1	--	--
0.1NaTFSI-0.9EMIFSI	1st cycle	32.3	18.5	19.6	12.7	5.4	10.4
	12th cycle	33.7	24.5	16.4	8.0	5.0	11.2
0.1NaTFSI-0.8N_{1114}FSI	1st cycle	31.8	23.6	18.2	11.3	4.5	9.3
	12th cycle	34.1	21.5	18.5	8.7	5.3	11.6
0.1NaTFSI in PC + 3wt. % FEC	1st cycle	29.3	42.4	14.3	11.3	0.5	1.1
	12th cycle	28.2	40.3	15.4	12.0	1.0	1.8

The high-resolution spectra of C 1s, O 1s, Na 1s, F 1s, and N 1s, S 2p, collected on pristine and cycled HC electrodes, were displayed in **Figures 5.10** and **5.11**, respectively. The C 1s spectra

(**Figure 5.10**) show a feature at 284.5 eV related to the sp^2 C-C bonds of hard carbon, and the peaks corresponding to C-N/C-O (286.0 eV), C=O (287.5 eV), O=C-O/ CO_3^{2-} (289.0 eV), and CF_2 (291.3 eV), the last one associated to the PVdF presence [128,266–268]. The presence of C-O, C=O, and

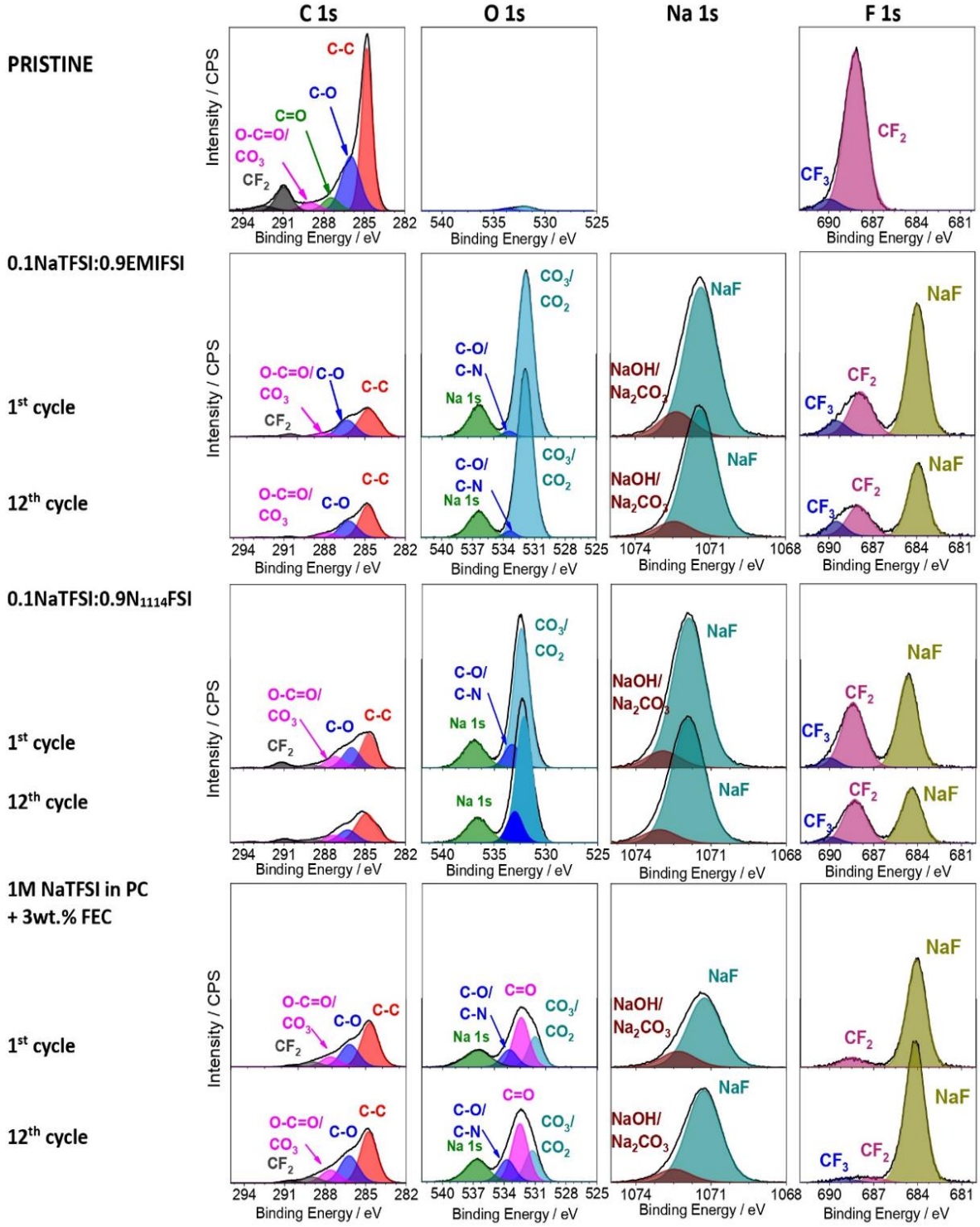

Figure 5.10: High-resolution C 1s, O 1s, Na 1s, and F 1s core level spectra obtained on the HC anodes after 1 discharge-charge cycle and after consecutive sodiation/de-sodiation steps in different electrolyte formulations (see legend).

O=C-O/ CO_3^{2-} species onto the pristine electrodes depends on the external contamination during the synthesis [128], meanwhile for the cycled electrodes resulting from the decomposition of the electrolyte and were associated with RCH_2Na, Na_2CO_2R, and carbonate species (i.e., Na_2CO_3, $ROCO_2Na$) [269–272]. The oxygenated compounds in HC cycled in ILs derived from the pristine electrode surface as elsewhere observed [268]. The presence of C-O and CO_2/CO_3 compound was also confirmed by O 1s spectra at 533.5 eV and 532.5 eV, respectively [269–272], and by the Na 1s spectra at 1072.5 eV [40]. The deconvolution of F 1s exhibits a big NaF peak at 684.5 eV [268,269], according to the Na 1s spectra at 1071.5 eV [273], due to the electrochemical degradation of the $TFSI^-$, FSI^- and FEC species [274]. Also, two other peaks are detected, associated to $-CF_2$ (PVdF: 688.4 eV) and $-CF_3$ (690.0 eV) species [268], this last derived by $TFSI^-$ anion [268]. The semi-ionic C-F bonds are considered active sites that may induce the electrolyte decomposition to form a stable SEI [275,276]. Hence, the NaF species can be found in all electrolyte systems [269]. The $-CF_2$ peak is less intense in the PC system, suggesting a thicker SEI richer in organic/inorganic compounds.

Three well-define features can be observed from the deconvolution of N 1s XPS spectra (**Figure 5.11**) for the HC electrodes cycled into IL-based electrolytes. The first two peaks are associated with the cations, EMI^+ (401.8 eV) and N^+_{1114} (402.3 eV) [192,268,277], and anions $FSI^-/TFSI^-$ both fall around 400.0 eV [193,278]. The last peak is ascribable to the nitrides (i.e., Na_3N) or -NS=O bond (398.5 eV) in a polymeric network [268]. The IL signals are from residual IL caught in the porosity of hard carbon which cannot be eliminated by THF washing and/ or high vacuum [279,280]. Lastly, the HC electrode surface results covered by a large amount of sulfur products, derived by the decomposition of anions $FSI^-/TFSI^-$ ($-SO_2F-$, and $-SO_x-$) [268], as observed from the S 2p XPS spectra, more intense in IL samples than for PC. In addition, the IL samples show "small" sulfur-containing species below 164 eV [279,281], inorganic species which into the SEI reduced the interfacial resistance, and improved Na^+ migration kinetics [268,282]. It was found in the literature that the SEI in SIBs is typically formed by an inner layer composed of inorganic species (i.e., Na_2CO_3, NaF-, S-, N-containing species, etc.) [40,269], covered by an organic outer layer ($ROCO_2Na$) [283]. The SEI results are richer in inorganic compounds and less homogeneous and thinner [284] with respect to the one in LIBs, which is moreover dominated by organic compounds [143,285]. The SEI layer composition, its evolution, and thickness strictly depend on the Na salt [281], and the presence of IL plays a key role. It has been demonstrated by Sun et al [268] that the SEI formed in the carbonate-based electrolyte is mainly composed of organic products and partial inorganic compounds derived from the reduction of $TFSI^-$. Conversely, it was found that for electrodes in IL electrolytes, the outer layer is formed by inorganic products, such as Na_2O, NaF, and sodium sulfides, and an inner layer with oxygenated species. We may guess to have the same behavior in our systems. In fact, the

HC electrode surface cycled in PC-based electrolyte shows a thicker SEI, richer in organic/inorganic species. Whereas in the case of HC cycled in ILs, the PVdF signals result to be more prominent (in particular for the $N_{1114}FSI$ system), suggesting a thinner SEI, richer in inorganic species, among which "small" sulfide-based compounds that improved the interfacial properties of the SEI towards the Na^+ migration.

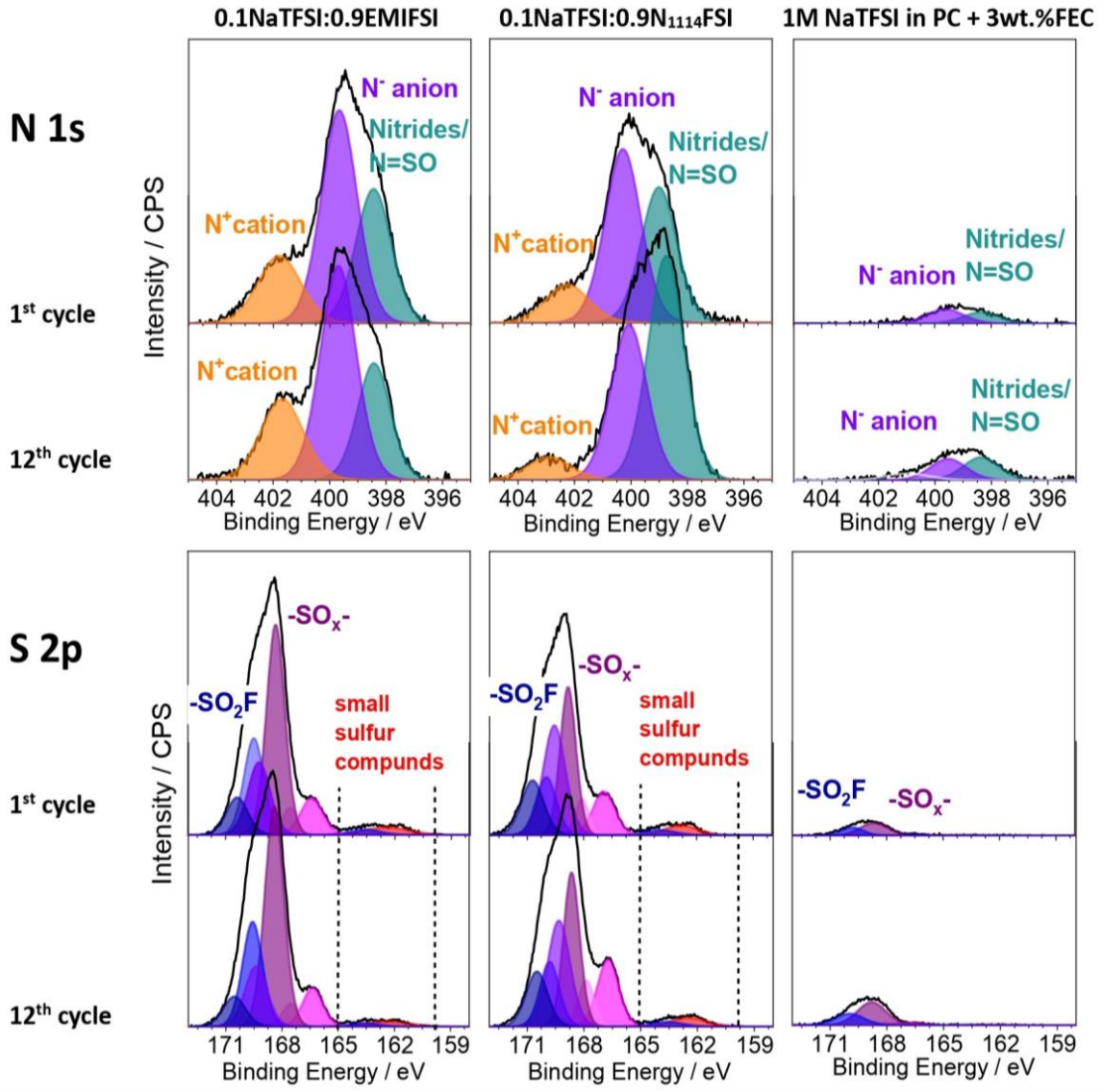

Figure 5.11: High-resolution N 1s, and S 2p core level spectra obtained on the HC anodes after 1 discharge-charge cycle and after consecutive sodiation/de-sodiation steps in different electrolyte formulations (see legend).

5.3.6 FIB-SEM analysis

In order to gain a more fundamental understanding of the morphology of the SEI layer formed on the HC electrode surface, cycled in different electrolyte systems, a FIB-SEM was conducted on post-mortem samples. A comparison of the morphology surface between the pristine HC anode and the HC electrodes cycled in different electrolyte systems was reported in **Figure 5.12**. A low-

magnification SEM image shows severe cracks on the HC surface and the delamination of the HC cycled in the 0.1NaTFSI-0.9EMIFSI formulation. This observation offers a plausible explanation for the significant capacity degradation experienced with this electrolyte, shedding light on the underlying mechanisms responsible for the diminished performance. The repeated contraction and expansion during the accommodation of Na ions results in a structural change that can lead to cracks formation, adversely affecting the performance and lifespan of the battery [286]. The surface morphology changes for the different electrolyte compositions became more evident in the higher magnification SEM images presented in **Figure 5.13**. A comparison of these images suggests the formation of a SEI layer with varying thickness, which is more pronounced in the cases of 0.1Na TFSI-0.9 EMIFSI (**Figure 5.13b**) and 1M NaTFSI in PC + 3wt.% FEC (**Figure 5.13d**) electrolytes, confirming as observed through XPS analysis. Moreover, upon analyzing the cross-section in **Figure 5.14**, it becomes increasingly apparent that the evolution of the internal structure is strongly influenced by the electrolyte composition. The pronounced cracks of the electrode surface after cycling in 0.1NaTFSI-0.9 EMIFSI and 1M NaTFSI in PC + 3wt. % FEC electrolytes reflect a deeper penetration of the electrolyte below the surface (**Figure 5.14b** and **5.14d** respectively), occupying the voids inside the material. For these two electrolyte formulations (**Figure 5.14b** and **5.14d** respectively) the typical porosity of the material, present in the pristine and in the sample cycled in NaTFSI-N_{1114}FSI (**Figure 5.14a** and **5.14c** respectively) seems completely disappearing.

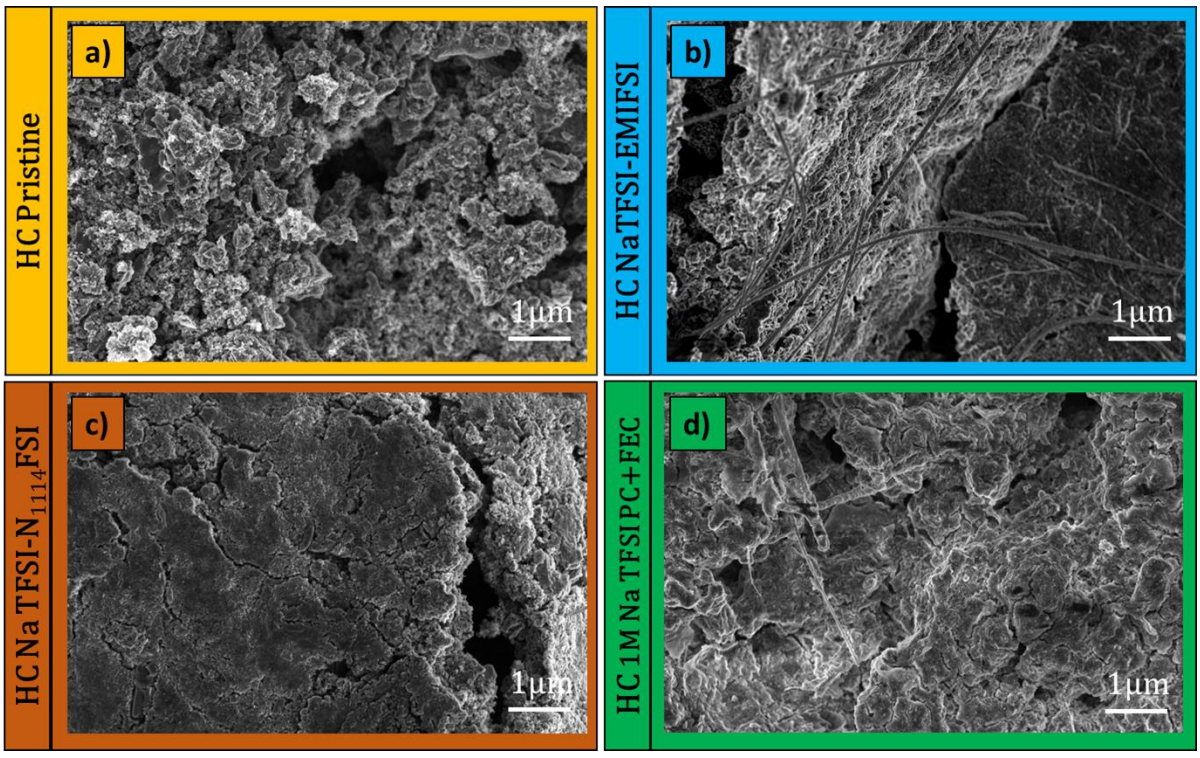

Figure 5.12: Low magnification (2500x) SE-SEM images collected for a) HC pristine anode, b) after 12 charge/discharge cycles in 0.1NaTFSI-0.9 EMIFSI. c) After 12 charge/discharge cycles in 0.1NaTFSI-0.9 N_{1114}FSI. d) After 12 charge/discharge cycles in 1M NaTFSI in PC + 3 wt.% FEC.

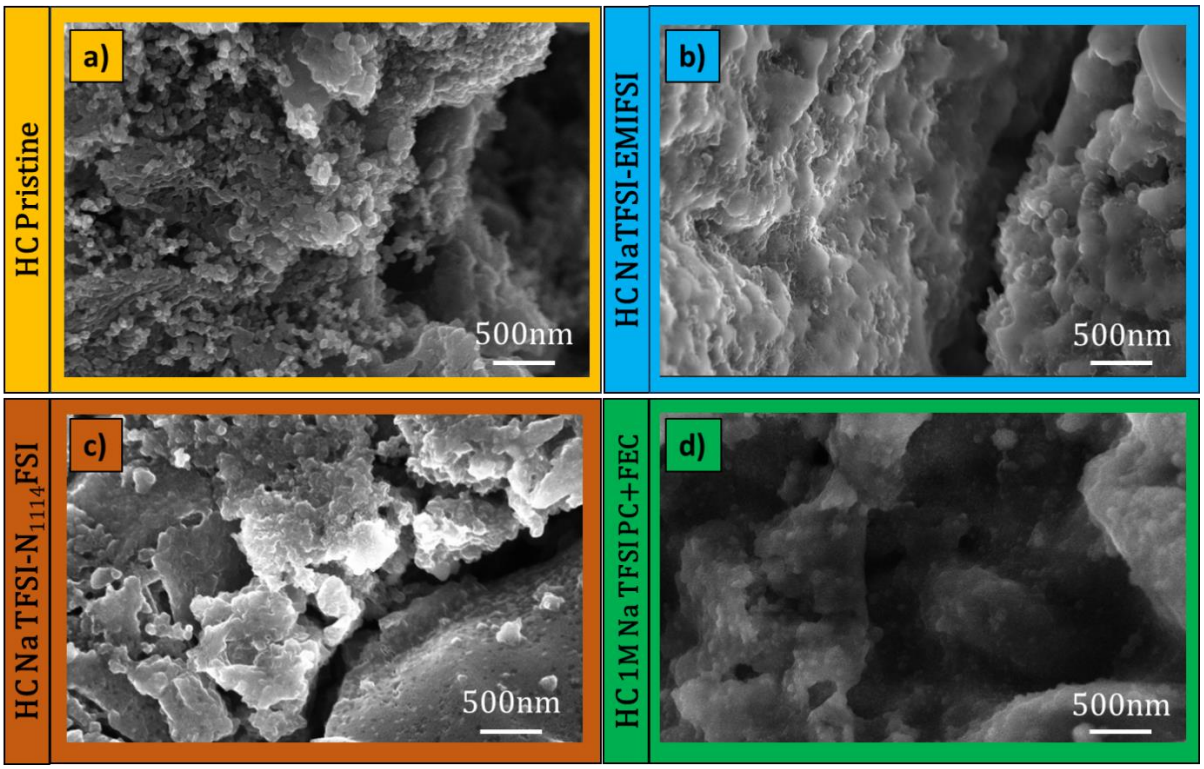

Figure 5.13: High magnification (50000x) SE SEM images collected for a) HC pristine anode, b) after 12 charge/discharge cycles in 0.1NaTFSI-0.9 EMIFSI. c) After 12 charge/discharge cycles in 0.1NaTFSI-0.9 N_{1114}FSI. d) After 12 charge/discharge cycles in 1M NaTFSI in PC + 3 wt.% FEC.

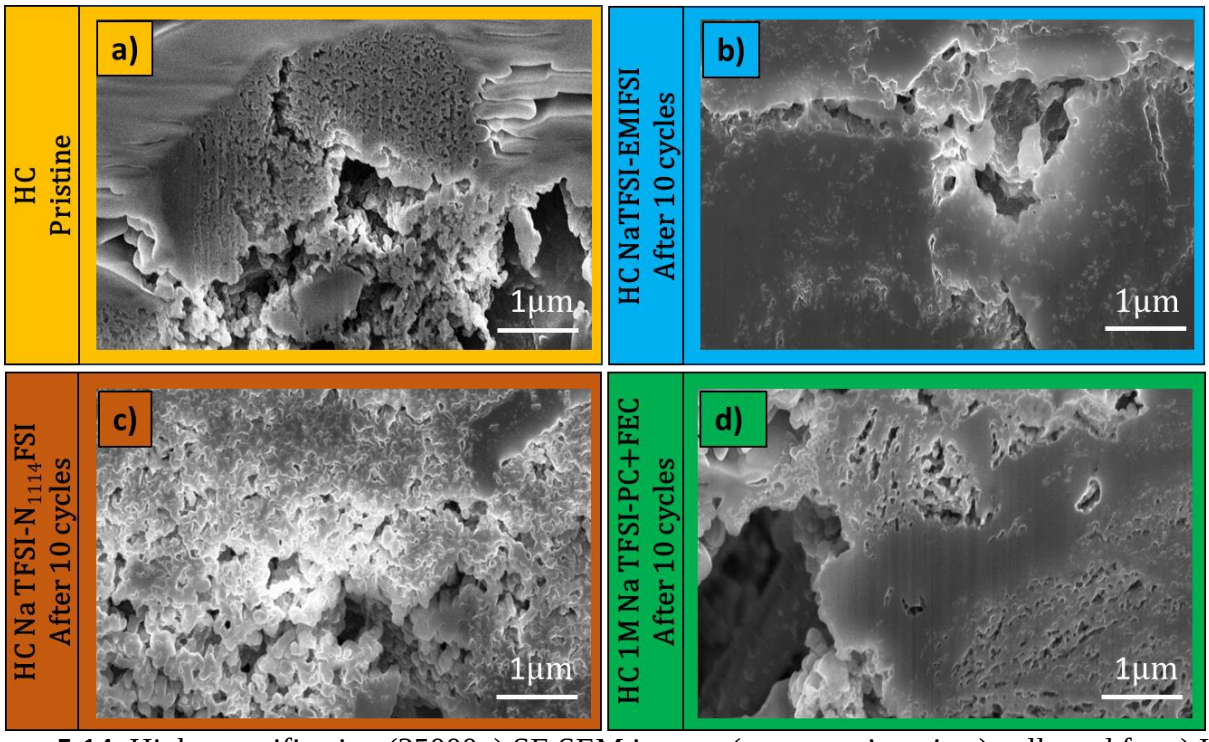

Figure 5.14: High magnification (35000x) SE SEM images (cross-section view) collected for a) HC pristine anode, b) after 12 charge/discharge cycles in 0.1NaTFSI-0.9 EMIFSI. c) After 12 charge/discharge cycles in 0.1NaTFSI-0.9 N_{1114}FSI. d) After 12 charge/discharge cycles in 1M NaTFSI in PC + 3 wt.% FEC.

5.4 Conclusions

The Na^+-intercalation process of hard carbon (HC) electrodes in 0.1NaTFSI-0.9EMIFSI and 0.1NaTFSI-0.9N_{1114}FSI ionic liquid (IL) electrolytes was investigated through repeated cyclic voltammetry (CV) tests paired with impedance spectroscopy (PEIS) analysis. High reversibility and reproducibility of the sodiation process were observed in both electrolyte formulations. More defined CV profiles were exhibited in 0.1NaTFSI-0.9N_{1114}FSI electrolyte, indicating a larger charge amount involved in the sodiation process. This trend agrees with the charge-discharge test results, where the Na/HC cells in the N_{1114}FSI electrolyte show excellent cycling performances with capacity retention exceeding 98 % of the initial value (175 mA h g^{-1}) after more than 1500 cycles with a coulombic efficiency above 99 %. This superior cyclability represents one of the best, if not the best, results obtained for hard carbon electrodes in ionic liquid electrolytes, exceedingly even that exhibited in organic electrolytes.

The chemical/electrochemical stability of the EMIFSI and N_{1114}FSI ionic liquids toward HC electrodes was confirmed by PEIS measurements, where no appreciable change of the electrolyte resistance was recorded during the CV measurements. The interface resistance is seen to be reduced upon cycling, likely due to the improvement of the electrolyte/electrode interface arising from the electric conductivity increase of the HC electrodes with the Na^+ insertion. The Na^+ diffusion coefficient (D_0), evaluated through the Randles-Sevcik equation, was found to be 4.9×10^{-9} cm^2 s^{-1} and 3.5×10^{-9} cm^2 s^{-1} in the 0.1NaTFSI-0.9EMIFSI and 0.1NaTFSI-0.9 N_{1114}FSI electrolytes, respectively. These values are one order of magnitude lower with respect to those reported in the literature and referred to organic electrolytes, likely ascribable to the slower ion transport properties of the ILs. Raman measurements revealed a more favourable Na^+ intercalation process for the N_{1114}FSI electrolyte whereas a co-insertion of the IL cation can occur in EMIFSI, thus depleting the HC electrode performance. To summarize, the EMIFSI and, especially, N_{1114}FSI electrolytes have shown very good compatibility towards hard carbon electrodes, resulting rather appealing for the realization of safer, more reliable, and highly performant Na-ion cells.

The solid electrolyte interphase (SEI) on HC electrodes cycled in different electrolytes, 0.1NaTFSI-0.9EMIFSI, 0.1NaTFSI-0.9N_{1114}FSI, and 1M NaTFSI in PC + 3wt.% FEC was analyzed through X-ray Photoelectron Spectroscopy (XPS) and focused ion beam milling scanning electron microscopy (FIB-SEM) analysis, to explain the different battery performances in Na-metal cells observed in our previous study [287].

The composition analysis carried out by XPS analysis on pristine and cycled HC electrodes has shown that the SEI on HC electrode surface in carbonate-based electrolyte displays a thicker layer, mainly composed of organic/inorganic compounds, such as $ROCO_2Na$, Na_2CO_3, and NaF.

Meanwhile, the HC electrodes cycled in ILs have shown a thinner SEI layer richer in inorganic and oxygenated species, among which small sulfide-based products, derived by the decomposition of IL, which reduced the interfacial resistance and improved the Na^+ migration kinetics.

The morphology characterization on post-mortem HC samples through FIB-SEM analysis has revealed the presence of several cracks on its surface and delamination of the active material for the electrodes cycled in 0.1NaTFSI-0.9EMIFSI electrolyte. In addition, the SEI thickness onto HC electrodes was seen to depend on the electrolyte formulation, i.e., thinner SEI was observed in 0.1NaTFSI-0.9N_{1114}FSI.

Thanks to the combination of the XPS and FIB-SEM analysis, we understood that the HC electrode cycled in 0.1NaTFSI-0.9N_{1114}FSI electrolyte shows a thinner and compact SEI layer on its surface, characterized by the presence of inorganic and oxygenated species, especially of small sulfide-based products, which provide favorable Na^+ migration through the passivation layer. This supports for the best cycling performance, in terms of capacity retention, rate capability, and coulombic efficiency, with high reversibility of the electrochemical processes, showed by 0.1NaTFSI-0.9N_{1114}FSI in comparison with 0.1NaTFSI-0.9EMIFSI and 1M NaTFSI in PC + 3 wt.%.

6. α-NaMnO2 cathodes for Na-ion batteries

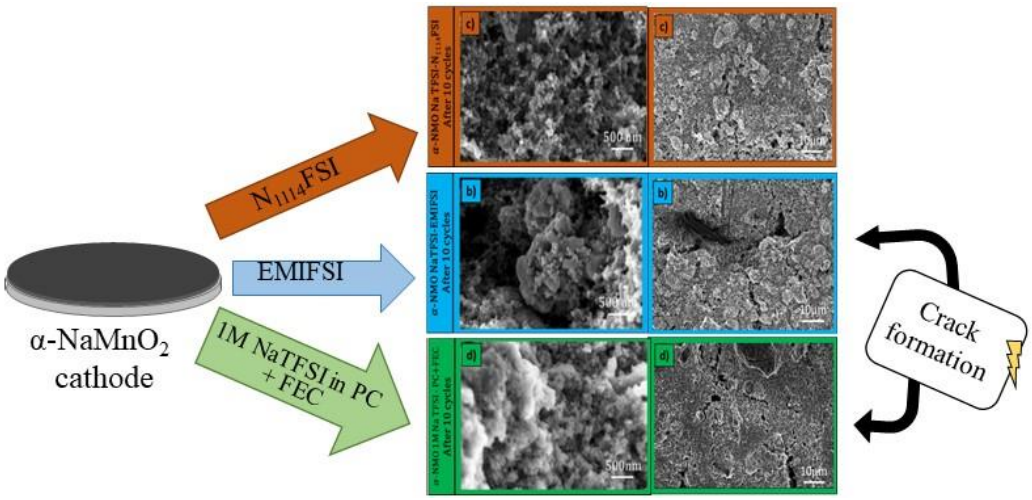

6.1 Introduction

Analogous to LIBs, the SIB cathode materials represent the technological limit because of their limited capacity. Therefore, many efforts have been addressed to the development of nano-structured electrode materials able to improve the SIB performances and decrease their costs [288–290]. Until now, layered metal oxides ($NaMO_x$), in particular Mn-based layered oxides, have been widely applied in commercial SIBs for their stable structure and low-cost. Na_xMnO_y oxides derive from abundant and cheap metal precursor minerals and are cobalt- and nickel-free (which are toxic for the environment) [291,292], this reducing the request of precious raw materials.

Focusing on layered $NaMnO_2$ cathodes, they exhibit high capacity (over 140 mA h g^{-1}) and excellent electrochemical performance in SIBs [293,294]. The $NaMnO_2$ can crystallize in two different layered phases, the α-$NaMnO_2$ stable between 600 and 850°C, and the polymorph β-$NaMnO_2$ thermodynamically stable at higher temperatures (above 850°C) [295]. The α-$NaMnO_2$ crystallizes in a monocline structure [296], while the β-$NaMnO_2$ in an orthorhombic system [297]. The α-$NaMnO_2$ cathode material has attracted our attention for its easier synthesis procedure and the lower processing temperature: however, this electrode material has shown the worst battery performances in Na-metal cells using commercial organic electrolyte (1M NaTFSI in PC + 3 wt.% FEC) with relevant capacity loss during the galvanostatic cycles [295].

Thereafter, we decided to investigate the electrochemical properties of α-$NaMnO_2$ in ionic liquid-based (IL) electrolytes, which already show excellent results when combined with hard carbon anodes in Na-metal cells [287]. On the basis of the results reported in Chapters 2 and 5, the EMIFSI and N_{1114}FSI electrolyte formulations were selected for the investigation with α-$NaMnO_2$ cathodes.

6.2 Experimental Section

6.2.1 Materials and Methods

The monocline sodium manganite α-$NaMnO_2$ (hereafter NMO) has been prepared by a solid-state reaction according to a route reported elsewhere [295]. Working electrodes were prepared through hand-grind mixing of NMO, super P carbon (Timcal), and PVdF-HFP (Kynar Flex 2801) binder in the weight ratio of 80:10:10, in according to a procedure described in the literature [295]. 10 mm disks (supported on 20 µm thick Al foil) were punched and vacuum-dried at 120 °C overnight. The mass loading of active material was around 2 mg cm^{-2}, corresponding to a capacity of 0.4 mA cm^{-2} (accounting for a NMO theoretical capacity equal to 208 mA h g^{-1}). All materials as well as the cell manufacturing were stored and handled in an Ar-filled glove box (Jacomex, Dagneux, France, O_2 and H_2O level < 1 ppm).

6.2.2 Electrochemical measurements

The electrochemical characterization was carried out in sodium half-cells assembled using CR2032 coin-cell containers. The α-NMO_2 working electrode was coupled with two glass fiber disk (16 mm diameter) separators (Whatman TM, Maidstone, UK), soaked with the electrolyte, and a sodium metal (American Elements, Los Angeles, CA, USA) disk (10 mm diameter) as the counter electrode.

The sodium insertion process in α-NMO_2 cathodes was investigated by cyclic voltammetric (CV) analysis, run at different scan rates and for prolonged cycles, combined with potentiostatic electrochemical impedance spectroscopy (PEIS) measurements. The CV tests were recorded between 2 to 3.8 V vs. the $Na^+/Na°$ redox couple at increasing scan rates, i.e., from 0.05 to 1 mV s^{-1} (four cycles for each scan rate). At the end of all family cycles the cells have undergone to 100 cycles at 1 mV s^{-1}. PEIS was performed on fresh cells and at the end of each scan rate family cycle, in the frequency range from 10 kHz to 0.1 Hz with 10 mV amplitude voltage. Galvanostatic charge-discharge tests were carried out on Na/NMO cells (the organic electrolyte 1M NaTFSI in PC + 3 wt.% FEC was used for comparison purposes. The cells were cycled between 2 and 3.8 V vs $Na^+/Na°$ at current rates ranging from 0.1C to 1C.

All the electrochemical tests, duplicated at least three times for checking the reproducibility of the results, were carried out using a Biologic (Seyssinet-Pariset, France) multichannel battery cycler.

6.2.3 Interfacial characterization

The X-ray photoelectron spectroscopy (XPS) and the focused ion beam milling scanning electron microscopy (FIB-SEM) analysis were carried out to get information on the electrochemical passive layer (SEI) and morphology of the NMO surface. The XPS analysis was registered using the Kratos AXIS ULTRA spectrometer with a monochromatic Al Kα X-ray radiation source (hν = 1486.6 eV).

Pass energy of 160 eV for survey spectra and 20 eV for narrow regions. The C 1s line at 284.8 eV was used as a charge reference. The FIB-SEM measurements were done using Helios G4CX. Both the top surface and the cross-section of the electrode were examined. The morphology of the electrodes was investigated using secondary electron (SE) images while the composition was confirmed through backscattered electron (BSE) imaging. The elastic scattering between the primary electrons and the atoms is proportional to the Z number. Therefore, heavier elements provide a stronger signal, resulting in a brighter BSE image. Both measurements were performed in a high vacuum avoiding air contamination. These analyses were performed on the NMO pristine electrode and after *i*) 1 charge-discharge cycle at 0.1C and *ii*) 1 cycle at 0.1C + 9 cycles at 0.2C. The cells were dismantled and the NMO electrodes were rinsed with Tetrahydrofuran (Sigma Aldrich, anhydrous, ≥99.9%) at least three times, vacuum-dried, and then transferred directly to the XPS and/or FIB-SEM analysis chamber using a vacuum glass-oven (Buchi) to avoid contamination from external.

6.3 Results and Discussions

6.3.1 Sodium intercalation process

The ability of NMO to reversibly deintercalate/intercalate sodium ions in 0.1NaTFSI-0.9EMIFSI and 0.1NaTFSI-0.9N_{1114}FSI electrolytes were studied by cyclic voltammetry tests (**Figure 6.1**). The current values were normalized with respect to the NMO mass. The initial CV cycle shows several peaks, in both anodic and cathodic verse, typical of the multistep de-sodiation/sodiation process in monoclinic NMO [293,295]. The de-sodiation process of α-$NaMnO_2$ consists of eight different oxidation stages at 2.59 V, 2.63 V, 2.73 V, 2.80 V, 2.97 V, 3.14 V, 3.48 V, and 3.59 V (vs $Na^+/Na°$), respectively: however, only five features (i.e., located at 2.47 V, 2.62 V, 2.87 V, 3.08 V, and 3.45 V vs $Na^+/Na°$, respectively) can be observed during the reduction process. Both electrolyte systems show, in the following cycles, well-evidenced features up to a 0.2 mV s^{-1} scan rates (blue curve) whereas the peaks are no longer clearly distinguishable when further increasing the scan rate. Moreover, a sharp rise in current profiles, followed by a moderate shift of the maximum value, results in a higher scan rate up to 1 mV s^{-1}, due to the diffusive phenomena that take place in the electrolyte [298]. The complete overlapping of the voltammograms indicates higher reversibility of the electrochemical processes [63,295,299], confirmed also from the 21st cycle (orange curve), which was superimposed with the cycles at the same scan rate of 0.05 mV s^{-1} (black curves) for both electrolyte systems. The Na cell with the 0.1NaTFSI-0.9N_{1114}FSI electrolyte (**Figure 6.1B**) exhibits more pronounced voltammograms with respect to the cell with 0.1NaTFSI-0.9EMIFSI (**Figure 6.1A**), suggesting a higher capacity involved in the Na^+ deintercalation/ intercalation processes. Prolonged CV tests, under stressed conditions (500 cycles at 1 mV s^{-1}) were performed on Na/NMO

cells for evaluating the reversibility of Na^+ electrochemical processes. The current vs voltage curves, displayed in **Figures 6.1C** (0.1NaTFSI-0.9EMIFSI) and **6.1D** (0.1NaTFSI-0.9N_{1114}FSI), show not well-split broader peaks, suggesting slow kinetics for the various stage of the Na^+ intercalation process into the α-NMO cathodes. However, the good correspondence between the area underlying the anodic and cathodic curves indicates good reversibility of the electrochemical processes and the moderate decrease in the current value during cycling implies good capacity retention of the NMO in the investigated electrolyte mixtures. An increasing current raise, during the CV tests, is detected for the EMIFSI cells starting from the 100th cycle, ascribable to dendrite growth-up onto the sodium electrode. Conversely, only a modest increase is observed for the N_{1114}FSI cells (starting from the 200th cycle), indicating a better compatibility, at the interface with the Na° anode, for the N_{1114}FSI ionic liquid than EMIFSI.

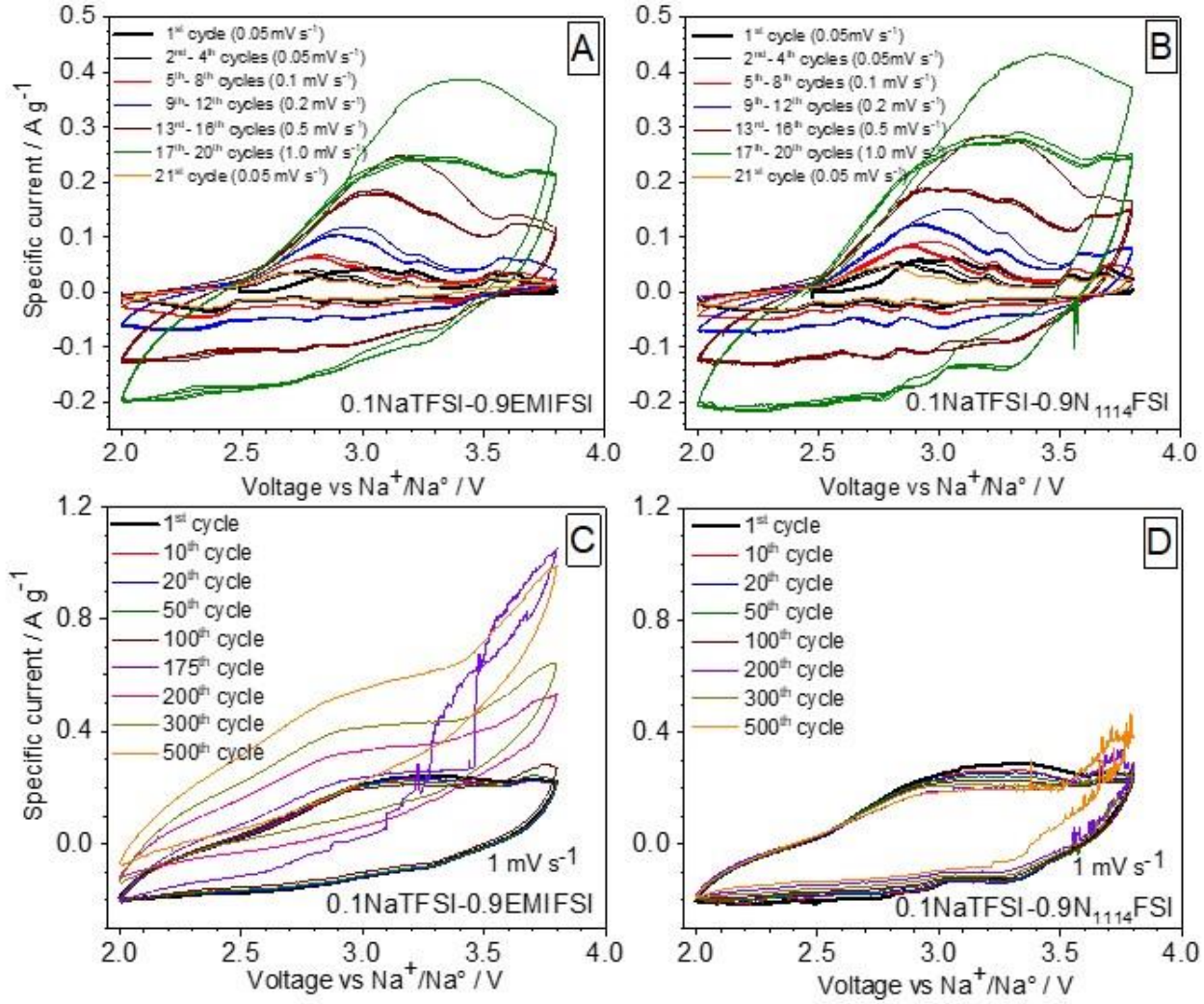

Figure 6.1: Cyclic voltammetries of Na/NMO cells containing 0.1NaTFSI-0.9EMIFSI (panels A and C) and 0.1NaTFSI-0.9N_{1114}FSI (panels B and D) electrolytes at different scan rates (panel A and B) and for prolonged cycles with a scan rate of 1 mV s^{-1}(panel B and D). T = 20 °C.

The impedance response recorded after cyclic voltammetry tests on Na/NMO cells in 0.1NaTFSI-0.9EMIFSI and 0.1NaTFSI-0.9N_{1114}FSI are reported in **Figures 6.2A** and **6.2B**, respectively. The Nyquist plots are composed of a semicircle in the medium-high frequency range (10 kHz – 100 Hz) followed by a straight line (100 – 1 Hz) related to the NMO electrode capacitance (C). The IL electrolyte resistance (R_{bulk}) is given by the distance of the semicircle high-frequency intercept with the real axis [178,179,250] whereas the semicircle diameter represents the overall interfacial resistance (R_{int}) [178,179,250]. The AC responses were fitted using the equivalent circuit model [177–179] depicted in **Figure 6.2C** where Q_{dl} is the constant phase element considering the double layer capacitance and C_l is the electrode limit capacitance [178,179,250]. The obtained resistance values are summarized in **Table 6.1** and their evolution (during the CV tests) is plotted in **Figure 6.3**.

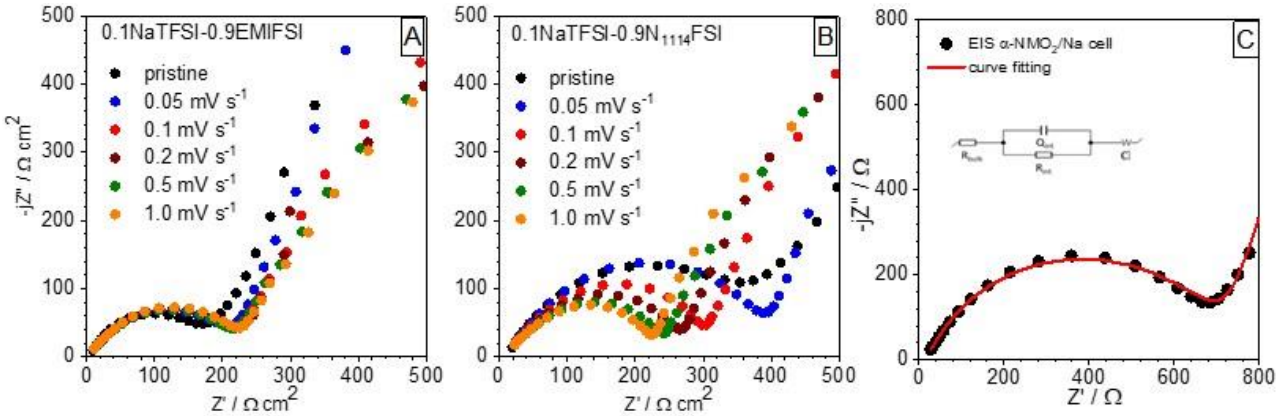

Figure 6.2: AC responses, taken under OCV condition, of Na/NMO cells containing the 0.1NaTFSI-0.9EMIFSI (panel A) and 0.1NaTFSI-0.9N_{1114}FSI (panel B) electrolytes. The impedance measurements were run after each CV family run at increasing scan rates (Figures 6.1A and 6.1B). Frequency range: 10 kHz – 1 Hz. Voltage amplitude: ΔV = 10 mV. T = 20 °C. Equivalent circuit model used for fitting the AC responses (panel C).

Apart an initial increment from 220 to 290 Ω cm^2, no relevant increase (i.e., from 290 to 310 Ω cm^2) of the overall interfacial resistance is observed during CV cycles for the EMIFSI electrolyte cells (**Figure 6.2A**), suggesting good compatibility of the IL electrolyte even at the interface with the lithium metal anode. Meanwhile, the N_{1114}FSI cells (**Figure 6.2B**) display reduction of the semicircle amplitude (with corresponding decrease of the interfacial resistance from ~ 500 to ~300 Ω cm^2), likely due to progressive morphological and/or structural modification (i.e., composition, structure, thickness of the SEI) at Na/electrolyte interface leading to enhanced Na^+ mobility (trough the interface). At the end of the CV tests (**Figures 6.1A** and **6.1B**), the interfacial resistance of the N_{1114}FSI is found to be comparable with that of the EMIFSI ones, confirming the key role of the cation in the SEI formation as reported elsewhere for hard carbon anodes [287]. No practical variation in terms of bulk resistance is observed during CV tests. The EMIFSI electrolyte cells exhibits lower

R_{bulk} values (~5 Ω cm^1) with respect to the N_{1114}FSI ones (~17 Ω cm^1), in agreement with the higher conductivity of the EMIFSI ionic liquid with respect to N_{1114}FSI [93].

Table 6.1. R_{bulk} (Ω cm^1) and R_{int} (Ω cm^2) parameters, related to Na/NMO cells containing the 0.1NaTFSI-0.9EMIFSI and 0.1NaTFSI-0.9N_{1114}FSI electrolyte, determined in OCV condition after each CV family run at increasing scan rates (Figures 6.1A and 6.1B). T = 20 °C.

Scan rate / mVs $^{-1}$		Pristine	0.05	0.1	0.2	0.5	1
0.1NaTFSI-0.9EMIFSI	R_{bulk}	6.9 ± 0.3	5.9 ± 0.3	4.9 ± 0.2	4.7 ± 0.2	5.2 ± 0.3	5.2 ± 0.3
	R_{int}	220 ± 10	290 ± 20	300 ± 20	310 ± 20	300 ± 20	310 ± 20
0.1NaTFSI-0.9N_{1114}FSI	R_{bulk}	16.4 ± 0.8	17.7 ± 0.9	17.1 ± 0.8	16.1 ± 0.8	16.1 ± 0.8	16.8 ± 0.8
	R_{int}	500 ± 30	520 ± 30	400 ± 20	360 ± 20	320 ± 20	290 ± 20

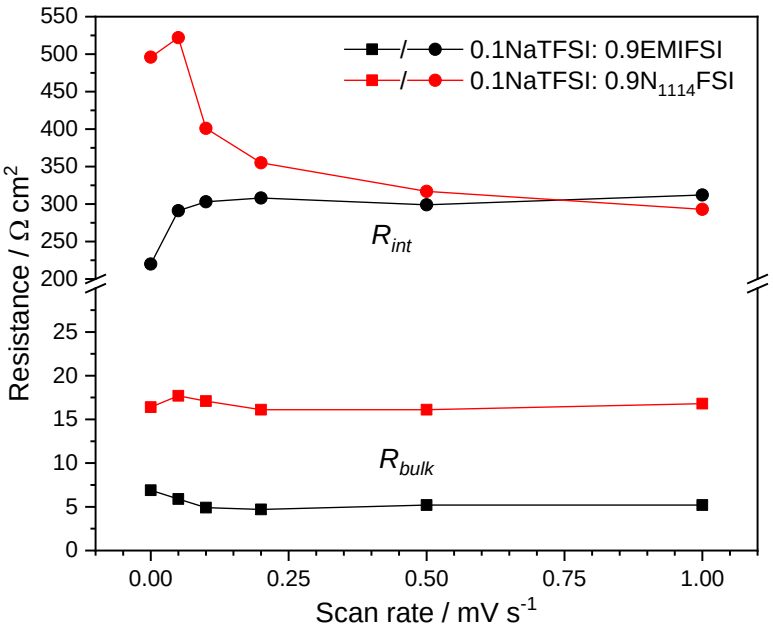

Figure 6.3: Evolution of the electrolyte R_{bulk} (panel A) and overall interfacial R_{int} (panel B) resistance, after each CV family run at increasing scan rates (Figures 6.1A and 6.1B), for Na/NMO cells in 0.1NaTFSI-0.9EMIFSI and 0.1NaTFSI-0.9N_{1114}FSI. T = 20 °C.

6.3.2 Cycling behavior

The voltage vs capacity charge/discharge profiles of Na/NMO cells in 0.1NaTFSI-0.9EMIFSI and 0.1NaTFSI-0.9N_{1114}FSI electrolytes are reported in **Figures 6.4A** and **6.4B**, respectively. The first cycle (run at 0.1C) shows a series of subsequent plateaus related to the multistage de-sodiation/sodiation process, as above discussed for the CV tests [293,295], which are also observed in the following cycles at higher scan rates. The plateau referred to the Na^+ electrochemical processes resulted better pronounced in the 0.1NaTFSI-0.9N_{1114}FSI cells. Not-well-defined plateaus are exhibited at higher current rates (i.e., 0.5C), suggesting diffusive phenomena into electrolytes. The cycling performances, displayed in **Figure 6.4C**, show an initial reversible capacity equal to 139

(0.1NaTFSI-0.9EMIFSI), 160 (0.1NaTFSI-0.9N_{1114}FSI) and 105 (1M NaTFSI in PC + 3 wt.% FEC organic electrolyte, reported for comparison purpose) mA h g^{-1}, respectively, with a corresponding coulombic efficiency of 73%, 83%, and 62% An increase in charge irreversible capacity is recorded for the EMIFSI electrolyte cells after a few cycles, likely due to dendrite growth-up onto the sodium metal electrode surface as also observed during the CV tests (**Figure 6.1C**) and reported in **Figure 6.5**. Avoiding any speculation, this behaviour might be ascribed to non-homogeneous distribution of the Na^+ ions, i.e., induced by the coordination with the EMIFSI ions, onto the Na anode surface, leading to local concentration increase of Na^+ ions which involves a priority sodium plating during charge and, therefore, promotes dendrite formation [118,269]. Meanwhile, the presence of proper compounds can promote a more stable SEI onto the sodium metal surface [269]. However, further investigation is required for better understanding this behavior.

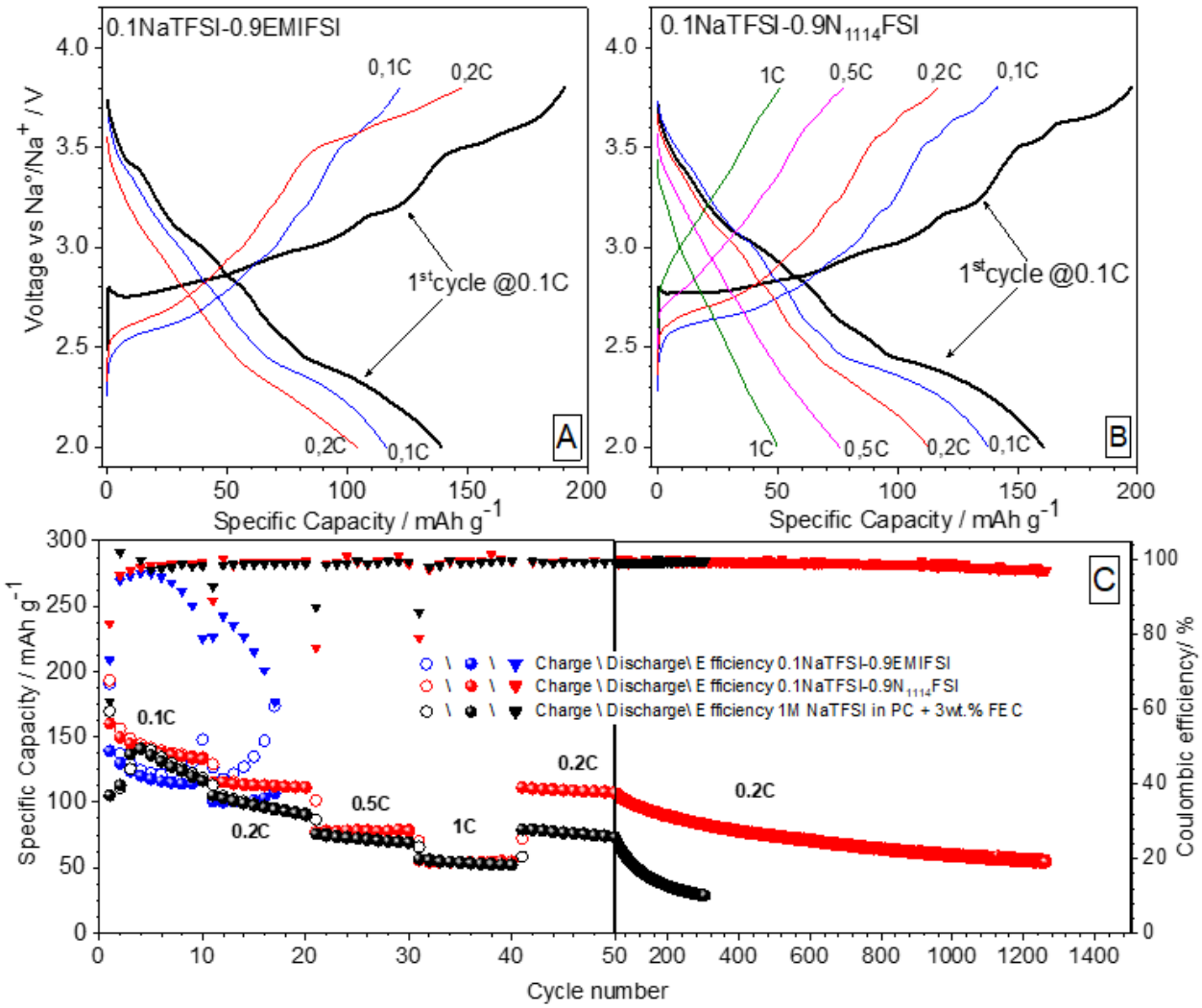

Figure 6.4: Voltage-capacity profiles at different rates (panels A and B) and cycling performance (panel C) of Na/NMO cells in 0.1NaTFSI-0.9EMIFSI and 0.1NaTFSI-0.9N_{1114}FSI electrolytes. The cycling behaviour of Na/NMO cells in 1M NaTFSI-PC + 3 wt.% FEC organic electrolyte is reported (panel C) for comparison purpose. T = 20 °C.

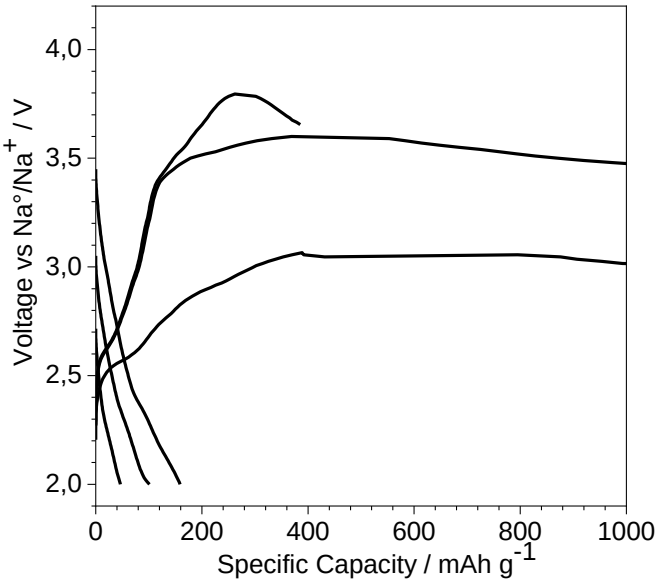

Figure 6.5: Selected charge-discharge voltage vs capacity profiles of Na/NMO cells cycled in 0.1NaTFSI-0.9EMIFSI electrolyte. T = 20 °C**.**

The N_{1114}FSI cells displays better performance (**Table 6.2**) than the organic ones: reversible capacities of 113, 78, 54 mA h g^{-1} (N_{1114}FSI) and 97, 72, 54 mA h g^{-1} (comparable with the results reported in the literature for organic electrolytes [295]) are exhibited at 0.2C, 0.5C and 1C, respectively. Higher initial coulombic efficiency (ICE) is observed in N_{1114}FSI and, in general, in IL electrolytes. About 25 % of the capacity is retained after 300 cycles by the organic electrolyte cells whereas the N_{1114}FSI ones release 60 % of the capacity initially delivered at 0.2C after 1200 cycles, in conjunction with a coulombic efficiency levelling 100 %. Also, turning the current rate from 1C to 0.2C, the capacity is seen matching the value initially delivered at 0.2C, confirming the good reversibility of sodiation process in agreement with the cyclic voltammetry tests. These represent the best result obtained till now for monolithic α-$NaMnO_2$ cathodes in Na-cells.

Table 6.2: Initial irreversible (Q_{irr}) and reversible (Q_{rev}) capacities, delivered at different scan rates, of Na/NMO cells containing different electrolyte formulations.

Cell setup	1st cycle	Q_{rev} / mA h g^{-1}				
	Q_{irr} / %	0.1C	0.2C	0.5C	1C	$0.2C_{300th}$
Na / 0.1NaTFSI-0.9EMIFSI / α-NMO	27	118	101	--	--	--
Na / 0.1NaTFSI-0.9N_{1114}FSI / α-NMO	17	139	113	78	54	83
Na / PC:NaTFSI + 3 wt.% FEC / α-NMO	38	136	97	72	54	29

6.3.3 XPS analysis on NMO cathode surface

For better understanding the favorable performance of NMO cathodes in N_{1114}FSI electrolyte with respect to the EMIFSI and organic ones, ex-situ XPS analysis was performed on pristine and on post-mortem electrodes (in the desodiated state) after both one and few galvanostatic charge-discharge

cycles. As known, the characteristics (i.e., composition, thickness) of passive layer can affect the battery performances [300]. Generally, the cathode-electrolyte interface (CEI) is composed of organic species (i.e., -CH, -CO, and -CF) and inorganic species (i.e., NaF, Na_2CO_3, and Na_2CO_3R) [237,281,301]. Na_2CO_3 and NaF are key components for a robust and stable CEI layer onto the α-NMO_2 electrodes, preventing further electrolyte decomposition and promotes fast charge transfer [237,301]. The high-resolution spectra of O 1s, Na 1s, Mn 2p, F 1s, and C 1s collected on pristine and cycled (**Figure 6.6**) electrodes are shown in **Figure 6.7**. A comparison of the surface composition (**Table 6.3**), reported as atom percentage, highlights the cathode cycled in organic electrolyte shows higher sodium, fluorine, and manganese content.

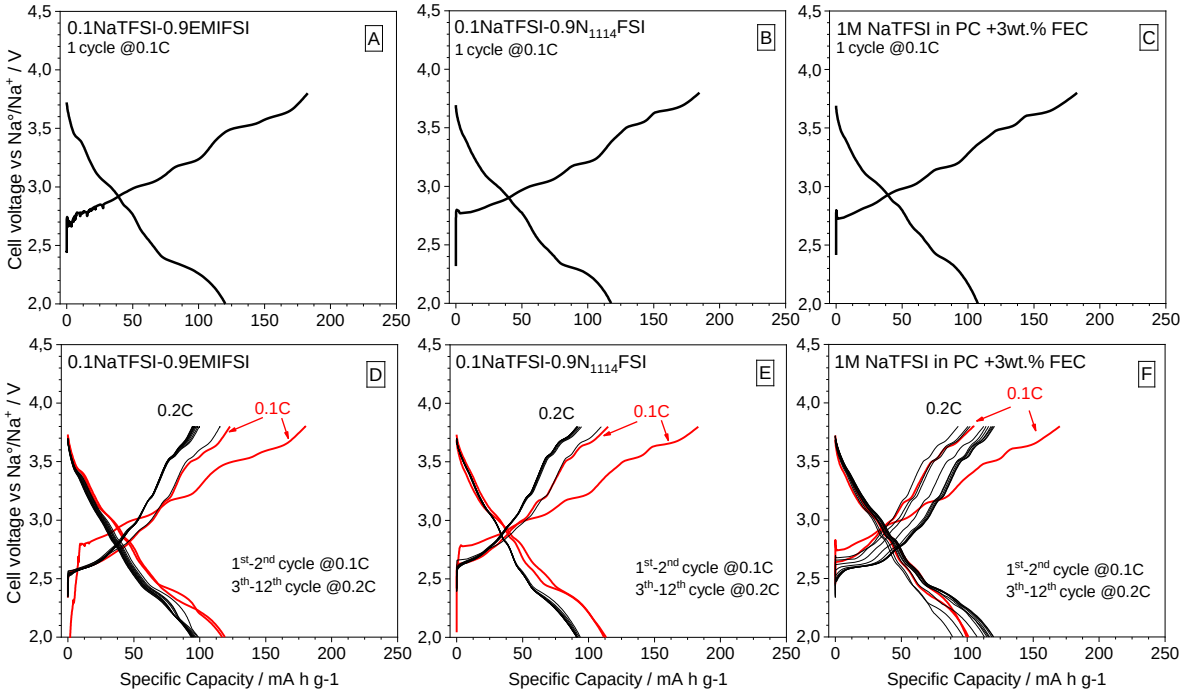

Figure 6.6: Voltage vs. capacity profiles, referred to selected charge-discharge cycles, of Na/NMO cells cycled in different electrolytes. T = 20°C.

Table 6.3: *Surface composition (atom percentage) of pristine and cycled NMO electrodes.*

		O 1s	*C 1s*	*F 1s*	*Na 1s*	*N 1s*	*S 2p*	*Mn 2p*
Pristine		5.7	73.1	17.3	3.7	--	--	--
0.1 NaTFSI-0.9 EMITFSI	*1st cycle*	11.7	64.8	13.7	4.2	1.3	1.3	0.2
	10th cycle	7.9	68.5	17.4	3.2	1.3	0.8	0.2
0.1 NaTFSI-0.9 N_{1114}FSI	*1st cycle*	19.6	50.7	12.7	9.2	1.8	3.5	0.2
	10th cycle	6.8	70.6	17.9	3.0	0.4	0.5	0.2
1M NaTFSI in PC + 3 wt.% FEC	*1st cycle*	21.2	38.0	18.2	17.8	0.5	0.5	0.1
	10th cycle	19.7	40.0	18.7	18.9	0.1	0.8	0.3

The Na 1s XPS spectra of the pristine NMO display a broad peak at 1072.2 eV, related to the oxidic Na compound (Na-O species) which strongly interacts with MnO [302,303]. The binding energy of Na-O remains pretty constant in all samples investigated, indicating that the Na chemical

state is nominally constant within the surface of the electrode [302]. The Na 1s spectra related to NMO cycled in different electrolytes show a second less-marked feature around 1073.4 eV attributed to NaF[304] and confirmed by the signal around 685 eV in the F 1s spectra [300,304]. Weaker Na_2O and NaF features are recorded in IL electrolytes, suggesting thinner and less resistive SEI onto the NMO electrode. The F 1s spectra shows the PVdF peak (visible also for the pristine electrode) at ~ 688 eV [300], which increases in intensity after few cycles in all investigated electrolyte systems, suggesting cleaning of the electrode surface. In particular, the NMO cathodes cycled in IL electrolytes exhibit a more pronounced PVdF feature with respect to that cycled in organic solution, supporting for larger improvement of the electrolyte/electrode interface during cycling in ionic liquids than in organics and for the better performance recorded in N_{1114}FSI and EMIFSI electrolytes (**Figure 6.4**). This phenomenon is proved by the appearance of the Mn peaks, which become detectable and more pronounced during cycling. Larger peaks related to Na_2CO_3, NaO, NaF, and less evidence feature of the PVdF binder were shown by the XPS spectra of the NMO cathodes cycled in organic electrolyte. This could suggest the presence of thicker CEI onto the electrode surface, which is apparently in contrast with the well-defined peaks observed for the Mn species. However, the structure and morphology of CEI (especially if porous and/or less dense) could allow the permeation (and the detection) of the Mn species through the passive layer [305,306].

The Mn 2p spectra displays two major features deconvoluted into four peaks of Mn $2p_{3/2}$ and Mn $2p_{1/2}$. The peaks located around 642.5 eV and 645.5 eV are assigned to Mn^{3+}, while the other two peaks at ~ 653.5 eV and 656.5 eV correspond to Mn^{4+} [304,307,308]. The Mn species are not observable for the pristine electrode because it is covered by carbonaceous species, such as Na_2CO_3, that are immediately formed during the electrode preparation. A well-pronounced peak at around 532 eV, corresponding to Na_2CO_3 species [300,304], can be observed in the O 1s spectra. Also, the strength of the Na_2CO_3 decreases, thus confirming the cleaning of the electrode surface (and a better interface improvement) during cycling especially in IL electrolytes.

The C 1s core-level spectrum exhibits five main features. The main peak at 284.8 eV is attributed to C-C bonds, corresponding to Super P conductive carbon. The signals around 286 and 291 eV are related to CH_2-CF_2 of the PVdF binder [309], i.e., the 286 eV signal is overlapped with the -CO species at the surface [310]. The last two features are given to the carbonate species (Na_2CO_3) at 289 eV [309] and -C=O group at ~ 287. A very small peak at 292.7 eV can be observed for the electrode cycled in N_{1114}FSI-based electrolyte, associated with the CF_3 [193,277] group derived by the $TFSI^-$ degradation, also confirmed by the broad peak at 690 eV in the F 1s spectra.

To summarize, the XPS results indicate improvement of the electrolyte/NMO interface after cycling tests. A fluorine rich CEI is observed in commercial organic electrolyte, resulting from the

hydrolysis of the TFSI anion (probably less pronounced in IL electrolytes) in conjunction with more pronounced Mn features, suggesting a not well covered surface which allows the dissolution on Mn in solution [305] and supports for the capacity fading during the cycling tests.

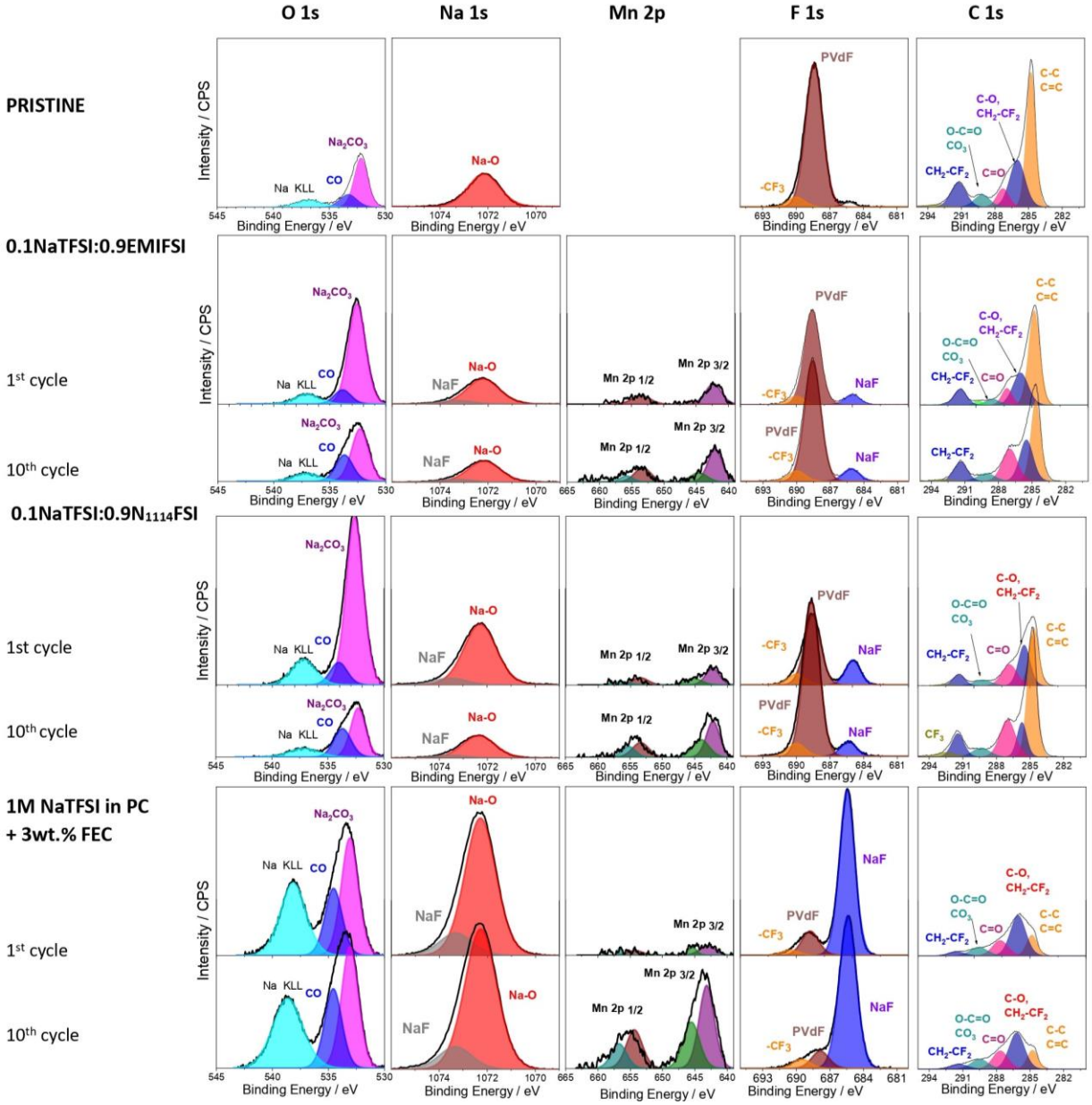

Figure 6.7: High-resolution O 1s, Na 1s, Mn 2p, F 1s, and C1s core level spectra obtained on the pristine NMO cathodes, and after consecutive lithiation/delithiation steps in different electrolyte formulations (see legend).

6.3.4 FIB-SEM analysis

The high magnification top-view SEM images (**Figure 6.8**) indicate that there are no significant differences in the primary particle shape, dimension, and distribution before and after the cycling process. Although, the low magnification SEM images of the top surface of the electrode (**Figure 6.9**) revealed the formation of more pronounced cracks in the samples cycled in 0.1NaTFSI-0.9

EMIFSI (**Figure 6.9b**) and 1M NaTFSI in PC +3 wt. % FEC (**Figure 6.9d**) as compared to the one cycled in NaTFSI-N_{1114}FSI. This could be related to improved cathode-electrolyte interphase (CEI) in the NaTFSI-N_{1114}FSI electrolyte formulation, in agreement with the better cycling behavior (**Figure 6.4**) and confirmed by XPS analysis (**Figure 6.7**).

The deintercalation process (of the Na^+ ions) results in significant mechanical stress on the oxide layer structure, often accompanied by a series of phase changes and gradually leading to structural degradation. Ensuring the formation of a stable CEI is crucial for enhancing the performance and lifespan of the battery [286]. Cracks are more prominent for the sample cycled in 0.1NaTFSI-0.9EMIFSI even below the surface, as can be observed through the cross-section view reported on **Figure 6.10** (c-d). This finding provides a rational explanation for the significant capacity loss and very short lifespan associated with this specific electrolyte, offering insights into the fundamental factors contributing to the reduced overall performance. In **Figure 6.8**, a higher magnification view of the top surface reveals the primary particles embedded within the carbon nanoparticles of the slurry. When compared to the pristine sample, no significant differences are observed in the ionic liquid electrolyte formulation. However, in the case of the standard carbonate-based electrolyte (**Figure 6.8d**), a moderate passivation layer on the electrode's surface becomes apparent.

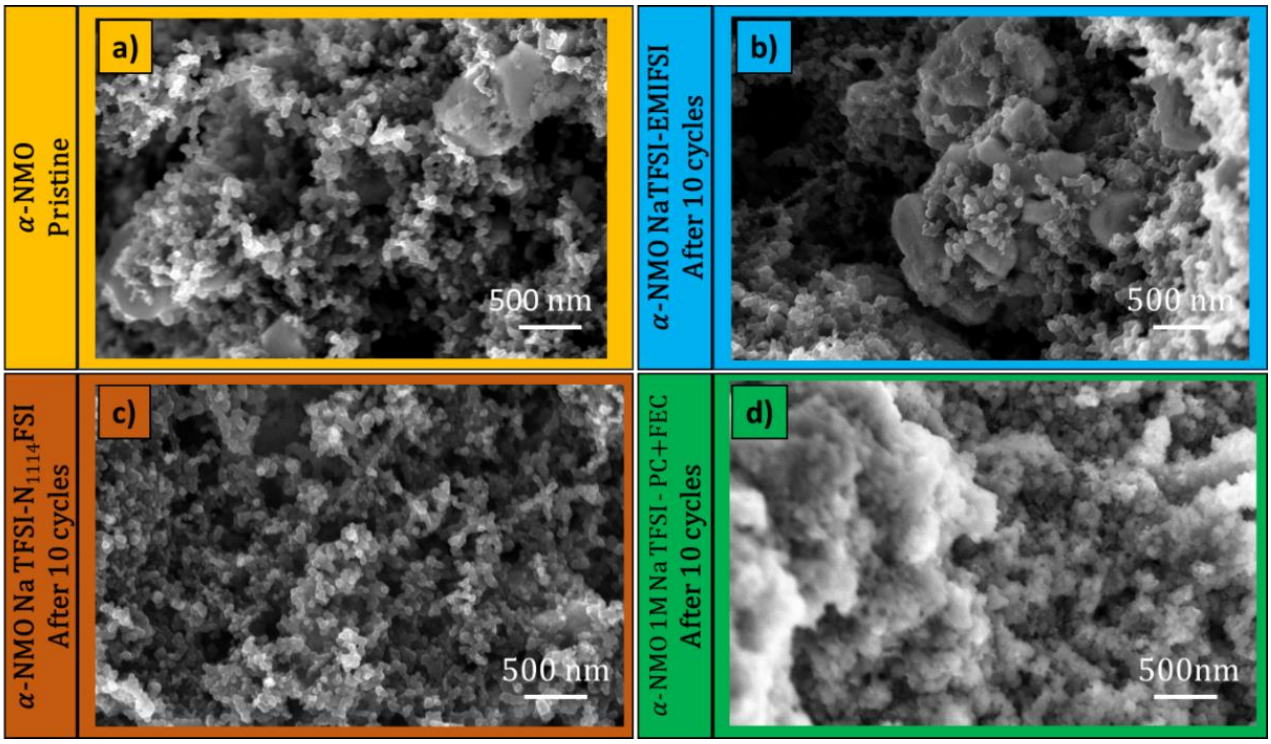

Figure 6.8: High magnification (50000x) SE images (top view) collected for a) α-$NaMnO_2$ pristine cathode, and after 10 charge/discharge cycles in b) 0.1Na TFSI-0.9 EMIFSI, c) 0.1Na TFSI-0.9 N1114FSI, and d) 1M NaTFSI in PC +3 wt. % FEC.

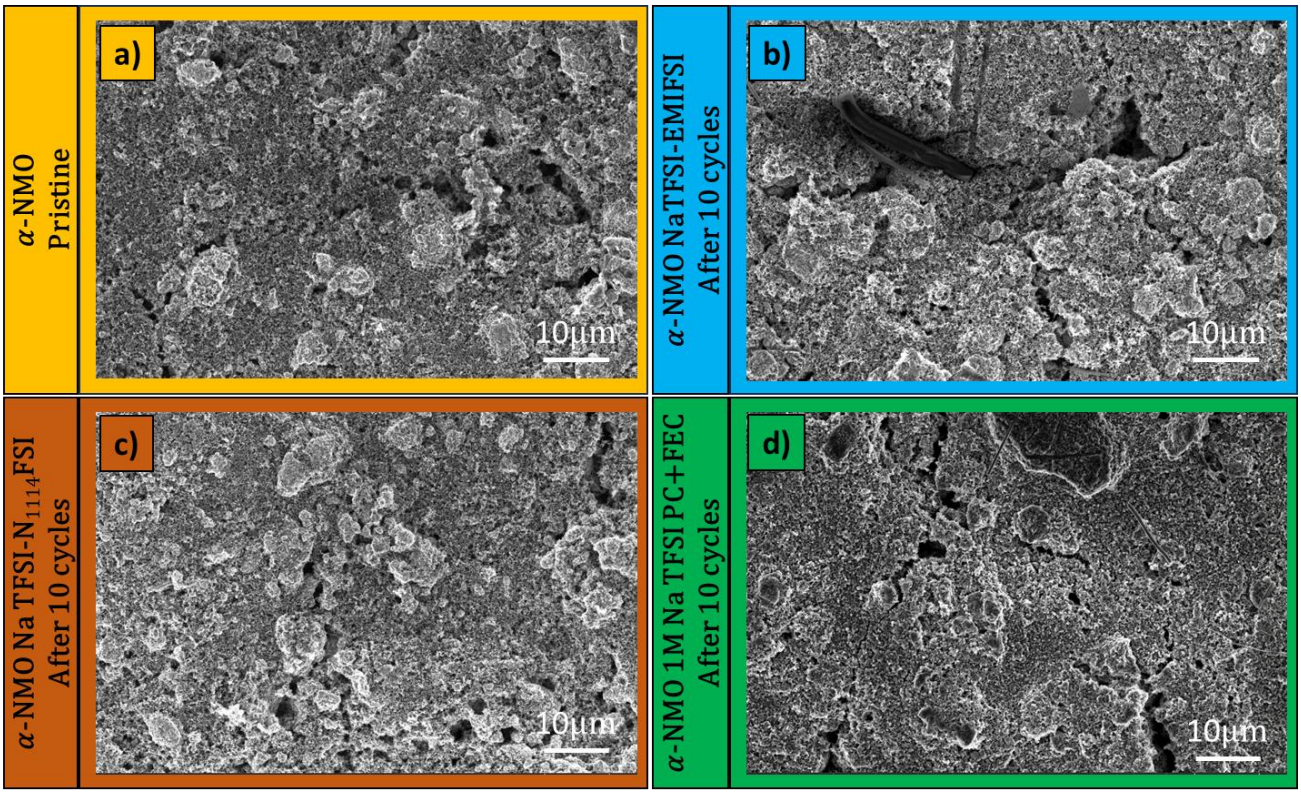

Figure 6.9: Low magnification (2500x) SE SEM images (top view) collected for a) NMO pristine cathode, and after 10 charge/discharge cycles in b) 0.1NaTFSI-0.9EMIFSI, c) 0.1NaTFSI-0.9N_{1114}FSI, and d) 1M NaTFSI in PC +3 wt.% FEC.

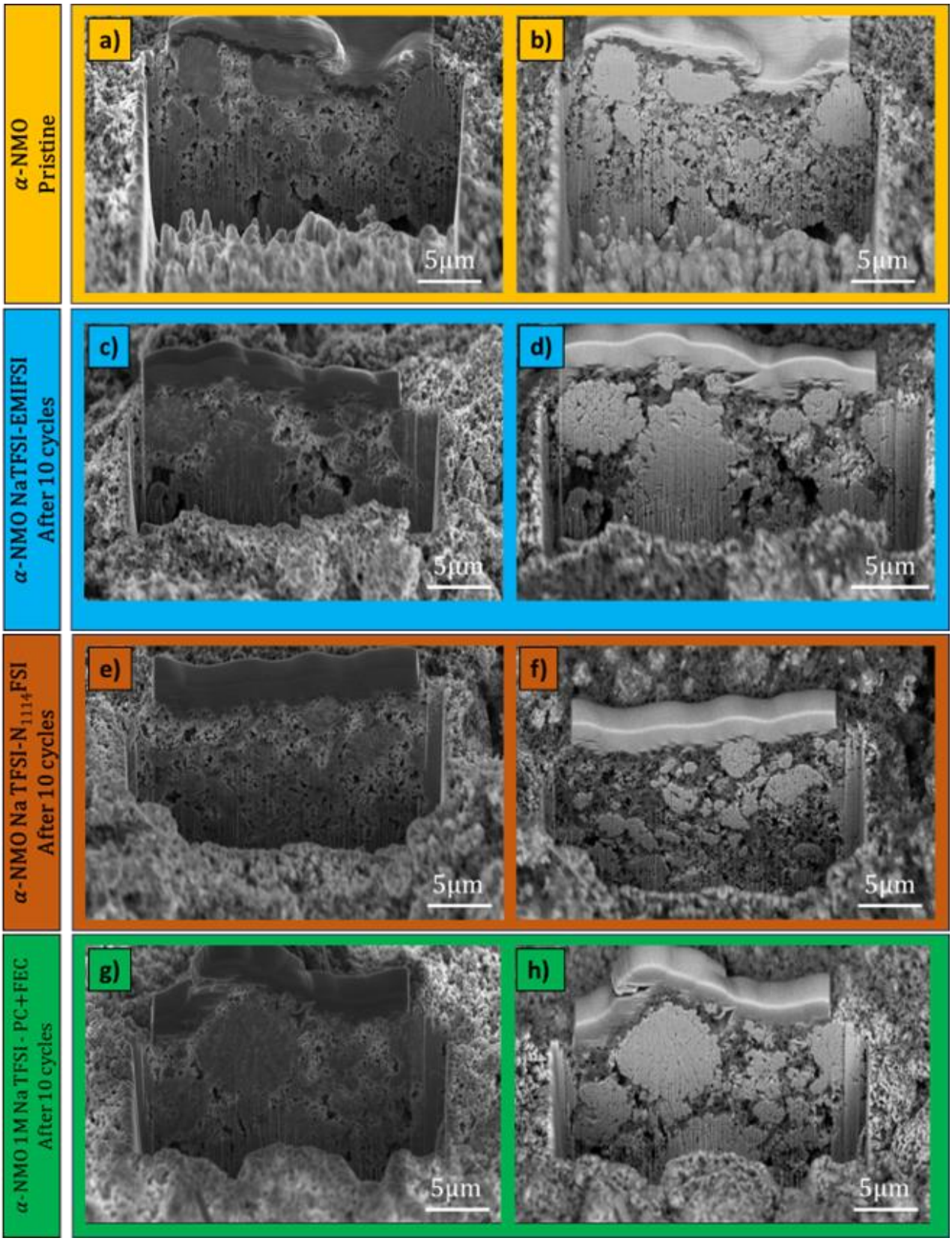

Figure 6.10: High magnification (6500x) SEM images (cross-section view) of: a-b) NMO pristine cathode, SE and BSE image, respectively; c-d) after 10 cycles in 0.1NaTFSI-0.9EMIFSI; SE and BSE image, respectively; e-f) after 10 cycles in 0.1NaTFSI-0.9N_{1114}FSI, SE and BSE image, respectively; g-h) after 10 cycles in 1M NaTFSI–PC +3 wt.% FEC, SE and BSE image, respectively.

The SEM images taken after cycling in carbonate-based electrolyte (**Figure 6.11**) evidence progressive increase of the passive layer thickness (i.e., from the 1st to the 10th cycle) onto the NMO cathode, supporting for experimental results obtained from XPS analysis.

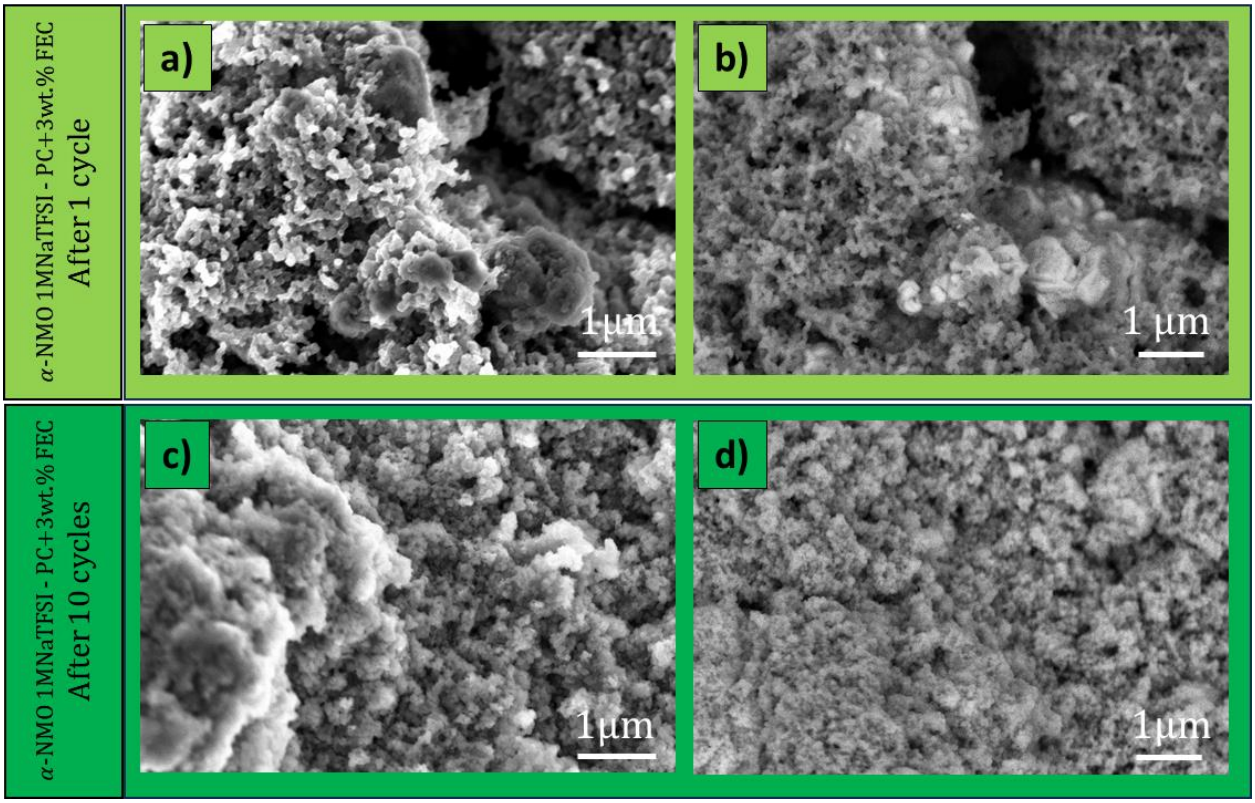

Figure 6.11: High magnification (30000x) SEM images (top view), collected for the NMO cathodes cycled in 1M NaTFSI in PC +3 wt. % FEC electrolyte, after 1 charge/discharge cycle and r 10 charge/discharge cycles in SE (panels A and C) and BSE (panels B and D) imaging.

The analysis of the cross-section at higher magnification, reported in **Figure 6.12**, reveals the presence of intergranular cracks between the primary particles after 10 charge/discharge cycles, whereas in the pristine samples the primary particles appear agglomerated and sintered together. Previous works reported in literature assign generally the cracks to anisotropic changes of the unit cell [311,312]. The repeated de-sodiation process corresponds to continuous expansion/contraction of the lattice c-axis, generating localized internal strain that severely affects the mechanical stability of the material [313]. In-depth understanding of the structural changes, induced by de-sodiation process, reported that the phase change upon the cycles is responsible for the formation of poorly crystallized mixtures of $Na_{0.7}MnO_2/Mn_3O_4$ species followed by $Na_{0.1\text{-}0.5}MNO_2$ compounds as consequences of the structural degradation. The fading mechanisms are determined by the continuous loss of sodium from the manganese lattice [314]. The formation of cracks enables the electrolyte penetration into the internal regions, leading to crack dimensions increase over cycling and, ultimately, active material pulverization [313]. To sum up, the FIB-SEM images indicate the presence

of more pronounced cracks inside the NMO electrodes cycled in EMIFSI and organic electrolytes with respect to those cycled in the N_{1114}FSI formulation, suggesting less stable CEI.

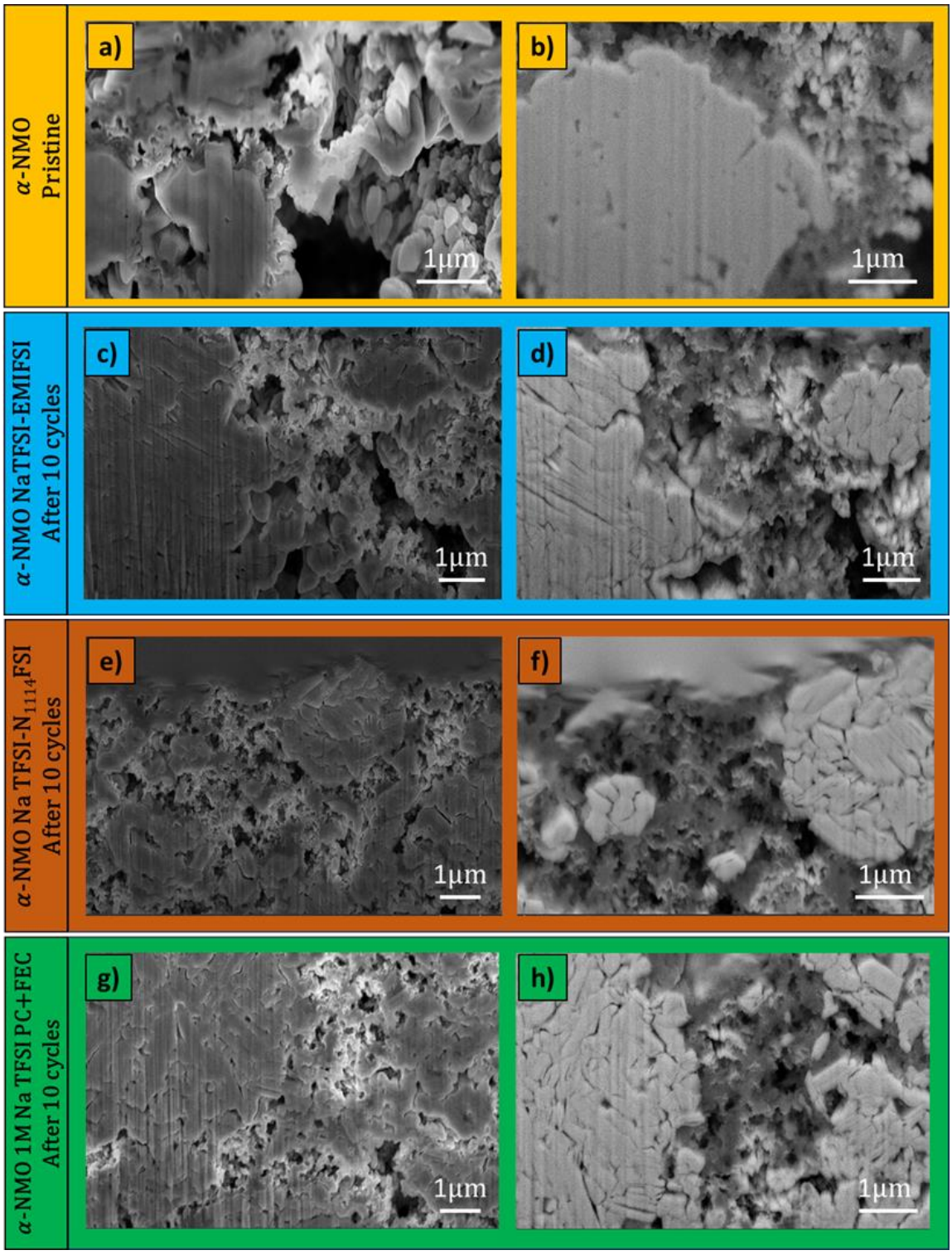

Figure 6.12: High magnification (30000x) SEM images, cross-section view, of: a-b) NMO_2 pristine cathode, SE and BSE image, respectively; c-d) after 10 cycles in 0.1NaTFSI-0.9 EMIFSI, SE and BSE image, respectively; e-f) after 10 cycles in 0.1NaTFSI-0.9 N_{1114}FSI, SE and BSE image, respectively; g-h) after 10 charge/discharge cycles in 1M NaTFSI in PC +3 wt. % FEC, SE and BSE image, respectively.

6.4 Conclusions

The sodium insertion/de-insertion of α-$NaMnO_2$ cathodes in 0.1NaTFSI-0.9EMIFSI and 0.1NaTFSI-0.9N_{1114}FSI electrolytes was investigated through electrochemical measurements and spectroscopy analysis.

The cyclic voltammetry tests conducted at increasing scan rates and for prolonged cycles revealed higher reversibility of the electrochemical process for both electrolyte systems. Higher specific current values were observed in N_{1114}FSI electrolyte, suggesting larger capacities involved in the Na^+ deintercalation/ intercalation processes. These results agree the behavior recorded in galvanostatic charge-discharge tests, which highlight excellent cycling performances in the N_{1114}FSI-based electrolyte: for instance, 60 % of the initial capacity is delivered after 1200 cycles with a coulombic efficiency above 99%, representing at our sight the best result obtained with a monolithic α-$NaMnO_2$ cathode in Na-cells.

The interfacial properties at electrolyte/electrode interface were studied through impedance spectroscopy analysis paired with CV measurements. A time-stable overall interfacial resistance was observed in the EMIFSI electrolyte whereas progressive reduction (upon cycling) was detected in the N_{1114}FSI formulation, likely due to progressive morphological and/or structural modifications of the SEI at the interface with the α-$NaMnO_2$ electrode. No practical increase in electrolyte resistance was detected during the CV tests, once more supporting for high electrochemical stability of the IL systems.

XPS analysis showed an improvement of the α-$NaMnO_2$ electrode surface during cycling, displaying a CEI rich in carbonates which, for the 1M NaTFSI in PC + 3wt.% FEC electrolyte, shows high amount of fluorine derived by NaTFSI hydrolysis.

FIB-SEM images collected on the top-view and on the cross-section of post-mortem α-$NaMnO_2$ electrodes have shown the presence of more pronounced cracks for the EMIFSI and PC-based electrolytes, supporting for the capacity loss recorded during the cycling tests.

To summarize, the 0.1NaTFSI-0.9N_{1114}FSI electrolyte has shown very high compatibility towards α-$NaMnO_2$, allowing the formation of a stable passivation layer on its surface which prevent the dissolution of Mn in solution and the formation of cracks. Therefore, this ionic liquid electrolyte formulation results rather appealing for the realization of safer, more reliable, and highly performant Na-ion cells.

7. Final Remarks

Ionic liquids (IL) electrolytes based on imidazolium, tetra-alkyl-ammonium, and piperidinium cations, coupled with bis(perfluroalkylsulfonyl)imide anions, were specifically tailored for lithium-ion (LIB) and sodium (SIB) battery systems. The ILs were synthesized and purified through an ecofriendly procedure which use water as the only processing solvent. The purity level, investigated through x-ray fluorescence, UV-Vis spectrophotometry and Karl-Fisher titration, was seen to be above 99.9 %, with a water, halide and lithium content below 5 ppm. All investigated ILs are thermally stable (checked by temperature heating scan and isothermal steps) at least up to 150 °C: in particular, the TFSI sample exhibit thermal robustness up to about 250 °C. The incorporation of an oxygen atom in the main side cation alkyl chain does not relevantly deplete the thermal stability.

Li^+- and Na^+-conducting electrolyte formulations, based on 1-ethyl-3-methyl-imidazolium (EMI^+), trimethyl-butyl-ammonium (N_{1114}^+), and *N*-alkyl-*N*-methyl-piperidinium (PIP_{1A}^+) ionic liquid (IL) families, were designed and investigated. Lithium bis(trifluoromethylsulfonyl)imide (LiTFSI), lithium bis(fluorosulfonyl)imide (LiFSI) and sodium bis(trifluoromethylsulfonyl)imide (NaTFSI) were selected as the salts. Their ion transport properties and electrochemical stability have been investigated, analyzing the dependence on the anion and the cation aliphatic side chain length. Conductivities of interest for lithium and sodium batteries, i.e., largely overcoming 10^{-4} or 10^{-3} S cm^{-1} even below room temperature, were displayed, particularly for the electrolyte formulations based on the EMI^+ and N_{1114}^+ cations, and the FSI^- anion. Most of the investigated IL electrolytes were found to be electrochemically stable up to 4.8 V (vs Li^+/Li°) and 4.6 V (vs Na^+/Na°) for being addressed to LIBs and SIBs, respectively. Based on the obtained results, the EMITFSI, EMIFSI and N_{1114}FSI ionic liquids were selected for exploring/investigating their behavior and compatibility with electrodes for LIBs, i.e., silicon nanowire (Si-NW) anodes and lithium-rich, cobalt-free, layered oxide $Li_{1.2}Ni_{0.2}Mn_{0.6}O_2$ (LRLO) cathodes, and SIBs, i.e., hard-carbon (HC) anodes and α-$NaMnO_2$ (NMO) cathodes.

The Li^+ insertion process of Si-NW anodes showed good reversibility even at high scan rates, in conjunction with excellent cycling behavior especially in EMIFSI-based electrolytes. For instance, reversible capacity exceeding 1000 mA h g^{-1} after 2000 cycles, corresponding to 46 % of the initial value, was recorded. These data, supported by the x-ray photoelectron spectroscopy (XPS) analysis at the silicon/electrolyte interface, are one of the best results obtained for silicon electrodes in IL electrolytes.

The best performance of LRLO cathodes was recorded in EMIFSI electrolyte formulations, i.e., an initial reversible capacity values exceeding 300 mA h g^{-1} was observed with retention close to 90

% after 500 cycles and coulombic efficiency levelling 100 %. Cyclic voltammetry measurements have confirmed good reversibility and efficiency of the Li^+ insertion process even at high rates.

HC anodes, obtained from natural bio-waste, have shown high reversibility and reproducibility of the sodiation process in N_{1114}FSI electrolytes. For instance, a capacity retention exceeding 98% of the initial value has been recorded after more than 1500 cycles with a coulombic efficiency above 99%, largely beyond standard carbonate-based electrolytes. Raman spectroscopy measurements confirmed N_{1114}^+ promotes SEI layers with superior ability for supporting the reversible Na^+ intercalation. Post-mortem analysis, carried out by XPS and FIB-SEM, have evidenced thicker SEI layer (mainly composed of organic compounds) onto HC anodes cycled in carbonate-based electrolytes Conversely, thinner SEI (richer in inorganic species) was detected in ILs electrolytes, improving the the Na^+ migration kinetics especially in N_{1114}FSI electrolytes.

NMO cathodes have exhibited very good cell performances in N_{1114}FSI-based electrolytes, largely overcoming those observed in organic standard solutions: for instance, 60 % of the initial capacity was delivered after 1200 cycles in conjunction with a coulombic efficiency above 99 %. XPS and FIB-SEM measurements have addressed this very promising issue to the growth-up of stable passive layer onto the NMO surface. These results, as well as those evidenced for HC anodes, are, at our sight, the best result obtained for monolithic α-$NaMnO_2$ cathodes in sodium cells.

In conclusion, the work activities carried out in the present PhD thesis demonstrated that ionic liquids, in particular EMIFSI and N_{1114}FSI, show very good compatibility with topic Li^+-intercalating (Si-NW, LRLO) and Na^+-intercalating (HC and NMO) electrodes. Therefore, they are suitable and very promising electrolyte solvents for the realization of safer, more reliable, and highly performant Li- and Na-ion batteries.

8. Bibliography

[1] C. Damak, D. Leducq, H.M. Hoang, D. Negro, A. Delahaye, Liquid Air Energy Storage (LAES) as a large-scale storage technology for renewable energy integration – A review of investigation studies and near perspectives of LAES, International Journal of Refrigeration 110 (2020). https://doi.org/10.1016/j.ijrefrig.2019.11.009.

[2] EIA, International Energy Outlook 2021, International Energy Outlook (2021) 1–42. www.eia.gov/outlooks.

[3] B. Dunn, H. Kamath, J.M. Tarascon, Electrical energy storage for the grid: A battery of choices, Science (1979) 334 (2011) 928–935. https://doi.org/10.1126/science.1212741.

[4] X. Wu, F. Kang, W. Duan, J. Li, Density functional theory calculations: A powerful tool to simulate and design high-performance energy storage and conversion materials, Progress in Natural Science: Materials International 29 (2019). https://doi.org/10.1016/j.pnsc.2019.04.003.

[5] S. Koohi-Fayegh, M.A. Rosen, A review of energy storage types, applications and recent developments, J Energy Storage 27 (2020). https://doi.org/10.1016/j.est.2019.101047.

[6] G.L. Soloveichik, Battery technologies for large-scale stationary energy storage, Annu Rev Chem Biomol Eng 2 (2011). https://doi.org/10.1146/annurev-chembioeng-061010-114116.

[7] J.B. Goodenough, Y. Kim, Challenges for rechargeable Li batteries, Chemistry of Materials 22 (2010). https://doi.org/10.1021/cm901452z.

[8] J.M. Tarascon, M. Armand, Issues and challenges facing rechargeable lithium batteries, Nature 414 (2001) 359–367. https://doi.org/10.1038/35104644.

[9] M. Winter, R.J. Brodd, What are batteries, fuel cells, and supercapacitors?, Chem Rev 104 (2004). https://doi.org/10.1021/cr020730k.

[10] J. Eyer, Energy Storage for the Electricity Grid : Benefits and Market Potential Assessment Guide A Study for the DOE Energy Storage Systems Program, Sandia Laboratories 321 (2010).

[11] H. Kung, Basic research needs for electrical energy storage, in: ACS National Meeting Book of Abstracts, 2007.

[12] V. Etacheri, R. Marom, R. Elazari, G. Salitra, D. Aurbach, Challenges in the development of advanced Li-ion batteries: A review, Energy Environ Sci 4 (2011). https://doi.org/10.1039/c1ee01598b.

[13] M. Armand, J.M. Tarascon, Building better batteries, Nature 451 (2008) 652–657. https://doi.org/10.1038/451652a.

[14] A.S. Aricò, P. Bruce, B. Scrosati, J.M. Tarascon, W. Van Schalkwijk, Nanostructured materials for advanced energy conversion and storage devices, in: Materials for Sustainable Energy: A Collection of Peer-Reviewed Research and Review Articles from Nature Publishing Group, World Scientific Publishing Co., 2010: pp. 148–159. https://doi.org/10.1142/9789814317665_0022.

[15] H. Li, Z. Wang, L. Chen, X. Huang, Research on advanced materials for Li-ion batteries, Advanced Materials 21 (2009). https://doi.org/10.1002/adma.200901710.

[16] P. Poizot, S. Laruelle, S. Grugeon, L. Dupont, J.M. Tarascon, Nano-sized transition-metal oxides as negative-electrode materials for lithium-ion batteries, Nature 407 (2000). https://doi.org/10.1038/35035045.

[17] M.N. Obrovac, L. Christensen, Structural changes in silicon anodes during lithium insertion/extraction, Electrochemical and Solid-State Letters 7 (2004). https://doi.org/10.1149/1.1652421.

[18] P. Barpanda, J. Chotard, N. Recham, C. Delacourt, M. Ati, L. Dupont, M. Armand, J. Tarascon, ChemInform Abstract: Structural, Transport, and Electrochemical Investigation of Novel AMSO 4 F (A: Na, Li; M: Fe, Co, Ni, Mn) Metal Fluorosulfates Prepared Using Low Temperature Synthesis Routes. , ChemInform 41 (2010). https://doi.org/10.1002/chin.201041013.

[19] A. Yamada, S.C. Chung, K. Hinokuma, Optimized LiFePO[sub 4] for Lithium Battery Cathodes, J Electrochem Soc 148 (2001). https://doi.org/10.1149/1.1348257.

[20] J.M. Tarascon, Key challenges in future Li-battery research, Philosophical Transactions of the Royal Society A: Mathematical, Physical and Engineering Sciences 368 (2010). https://doi.org/10.1098/rsta.2010.0112.

[21] J.M. Tarascon, N. Recham, M. Armand, J.N. Chotard, P. Barpanda, W. Walker, L. Dupont, Hunting for better Li-based electrode materials via low temperature inorganic synthesis, Chemistry of Materials 22 (2010). https://doi.org/10.1021/cm9030478.

[22] J.Y. Hwang, S.T. Myung, Y.K. Sun, Sodium-ion batteries: Present and future, Chem Soc Rev 46 (2017). https://doi.org/10.1039/c6cs00776g.

[23] H. Pan, Y.S. Hu, L. Chen, Room-temperature stationary sodium-ion batteries for large-scale electric energy storage, Energy Environ Sci 6 (2013). https://doi.org/10.1039/c3ee40847g.

[24] C.X. Zu, H. Li, Thermodynamic analysis on energy densities of batteries, Energy Environ Sci 4 (2011). https://doi.org/10.1039/c0ee00777c.

[25] E. De La Llave, V. Borgel, K.J. Park, J.Y. Hwang, Y.K. Sun, P. Hartmann, F.F. Chesneau, D. Aurbach, Comparison between Na-Ion and Li-Ion Cells: Understanding the Critical Role of the Cathodes Stability and the Anodes Pretreatment on the Cells Behavior, ACS Appl Mater Interfaces 8 (2016). https://doi.org/10.1021/acsami.5b09835.

[26] M.D. Slater, D. Kim, E. Lee, C.S. Johnson, Correction: Sodium-Ion Batteries, Adv Funct Mater 23 (2013). https://doi.org/10.1002/adfm.201301540.

[27] D. Linden, Handbook of Batteries, 3rd Edition, 2009.

[28] J.F. Whitacre, A. Tevar, S. Sharma, Na4Mn9O18 as a positive electrode material for an aqueous electrolyte sodium-ion energy storage device, Electrochem Commun 12 (2010). https://doi.org/10.1016/j.elecom.2010.01.020.

[29] P. Adelhelm, P. Hartmann, C.L. Bender, M. Busche, C. Eufinger, J. Janek, From lithium to sodium: Cell chemistry of room temperature sodium-air and sodium-sulfur batteries, Beilstein Journal of Nanotechnology 6 (2015). https://doi.org/10.3762/bjnano.6.105.

[30] D. Saurel, B. Orayech, B. Xiao, D. Carriazo, X. Li, T. Rojo, From Charge Storage Mechanism to Performance: A Roadmap toward High Specific Energy Sodium-Ion Batteries through Carbon Anode Optimization, Adv Energy Mater 8 (2018). https://doi.org/10.1002/aenm.201703268.

[31] E. Monyoncho, R. Bissessur, Unique properties of α-NaFeO2: De-intercalation of sodium via hydrolysis and the intercalation of guest molecules into the extract solution, Mater Res Bull 48 (2013). https://doi.org/10.1016/j.materresbull.2013.03.027.

[32] E. Irisarri, A. Ponrouch, M.R. Palacin, Review—Hard Carbon Negative Electrode Materials for Sodium-Ion Batteries, J Electrochem Soc 162 (2015) A2476–A2482. https://doi.org/10.1149/2.0091514jes.

[33] D.P. Divincenzo, E.J. Mele, Cohesion and structure in stage-1 graphite intercalation compounds, Phys Rev B 32 (1985). https://doi.org/10.1103/PhysRevB.32.2538.

[34] R. Alcántara, J.M. Jiménez-Mateos, P. Lavela, J.L. Tirado, Carbon black: A promising electrode material for sodium-ion batteries, Electrochem Commun 3 (2001). https://doi.org/10.1016/S1388-2481(01)00244-2.

[35] P. Thomas, J. Ghanbaja, D. Billaud, Electrochemical insertion of sodium in pitch-based carbon fibres in comparison with graphite in NaClO4-ethylene carbonate electrolyte, Electrochim Acta 45 (1999). https://doi.org/10.1016/S0013-4686(99)00276-5.

[36] P. Thomas, D. Billaud, Electrochemical insertion of sodium into hard carbons, Electrochim Acta 47 (2002) 3303–3307. https://doi.org/10.1016/S0013-4686(02)00250-5.

[37] D.A. Stevens, J.R. Dahn, The Mechanisms of Lithium and Sodium Insertion in Carbon Materials, J Electrochem Soc 148 (2001) A803. https://doi.org/10.1149/1.1379565.

[38] L. Joncourt, M. Mermoux, P. Touzain, L. Bonnetain, D. Dumas, B. Allard, Sodium reactivity with carbons, Journal of Physics and Chemistry of Solids 57 (1996). https://doi.org/10.1016/0022-3697(95)00366-5.

[39] X. Xia, J.R. Dahn, Study of the Reactivity of Na/Hard Carbon with Different Solvents and Electrolytes, J Electrochem Soc 159 (2012). https://doi.org/10.1149/2.jes111637.

[40] S. Komaba, W. Murata, T. Ishikawa, N. Yabuuchi, T. Ozeki, T. Nakayama, A. Ogata, K. Gotoh, K. Fujiwara, Electrochemical Na insertion and solid electrolyte interphase for hard-carbon electrodes and application to Na-ion batteries, Adv Funct Mater 21 (2011) 3859–3867. https://doi.org/10.1002/adfm.201100854.

[41] M.Z. Kufian, S.R. Majid, Performance of lithium-ion cells using 1 M LiPF6 in EC/DEC (v/v = 1/2) electrolyte with ethyl propionate additive, Ionics (Kiel) 16 (2010). https://doi.org/10.1007/s11581-009-0413-6.

[42] R.P. Seward, E.C. Vieira, The dielectric constants of ethylene carbonate and of solutions of ethylene carbonate in water, methanol, benzene and propylene carbonate, Journal of Physical Chemistry 62 (1958). https://doi.org/10.1021/j150559a041.

[43] S. ichi Tobishima, T. Okada, Lithium cycling efficiency and conductivity for high dielectric solvent/low viscosity solvent mixed systems, Electrochim Acta 30 (1985). https://doi.org/10.1016/0013-4686(85)87019-5.

[44] K. Xu, Nonaqueous liquid electrolytes for lithium-based rechargeable batteries, Chem Rev 104 (2004). https://doi.org/10.1021/cr030203g.

[45] S. Shahid, M. Agelin-Chaab, A review of thermal runaway prevention and mitigation strategies for lithium-ion batteries, Energy Conversion and Management: X 16 (2022). https://doi.org/10.1016/j.ecmx.2022.100310.

[46] S.S. Zhang, A review on electrolyte additives for lithium-ion batteries, J Power Sources 162 (2006). https://doi.org/10.1016/j.jpowsour.2006.07.074.

[47] R. Wagner, S. Brox, J. Kasnatscheew, D.R. Gallus, M. Amereller, I. Cekic-Laskovic, M. Winter, Vinyl sulfones as SEI-forming additives in propylene carbonate based electrolytes for lithium-ion batteries, Electrochem Commun 40 (2014). https://doi.org/10.1016/j.elecom.2014.01.004.

[48] K. Ciosek Högström, H. Lundgren, S. Wilken, T.G. Zavalis, M. Behm, K. Edström, P. Jacobsson, P. Johansson, G. Lindbergh, Impact of the flame retardant additive triphenyl phosphate (TPP) on the performance of graphite/LiFePO4 cells in high power applications Dedication: Professor per

Jacobsson in memoriam., J Power Sources 256 (2014). https://doi.org/10.1016/j.jpowsour.2014.01.022.

[49] J. Kalhoff, D. Bresser, M. Bolloli, F. Alloin, J.Y. Sanchez, S. Passerini, Enabling LiTFSI-based electrolytes for safer lithium-ion batteries by Using linear fluorinated carbonates as (Co)solvent, ChemSusChem 7 (2014). https://doi.org/10.1002/cssc.201402502.

[50] S. Li, W. Zhao, X. Cui, H. Zhang, X. Wang, W. Zhong, H. Feng, H. Liu, Lithium difluoro(sulfato)borate as a novel electrolyte salt for high-temperature lithium-ion batteries, Electrochim Acta 129 (2014). https://doi.org/10.1016/j.electacta.2014.02.090.

[51] P. Murmann, P. Niehoff, R. Schmitz, S. Nowak, H. Gores, N. Ignatiev, P. Sartori, M. Winter, R. Schmitz, Investigations on the electrochemical performance and thermal stability of two new lithium electrolyte salts in comparison to LiPF6, Electrochim Acta 114 (2013). https://doi.org/10.1016/j.electacta.2013.09.155.

[52] J.W. Fergus, Ceramic and polymeric solid electrolytes for lithium-ion batteries, J Power Sources 195 (2010) 4554–4569. https://doi.org/10.1016/j.jpowsour.2010.01.076.

[53] F. Lv, Z. Wang, L. Shi, J. Zhu, K. Edström, J. Mindemark, S. Yuan, Challenges and development of composite solid-state electrolytes for high-performance lithium ion batteries, J Power Sources 441 (2019) 227175. https://doi.org/10.1016/j.jpowsour.2019.227175.

[54] A. Lewandowski, A. Świderska-Mocek, Ionic liquids as electrolytes for Li-ion batteries-An overview of electrochemical studies, J Power Sources 194 (2009) 601–609. https://doi.org/10.1016/j.jpowsour.2009.06.089.

[55] S.K. Singh, A.W. Savoy, Ionic liquids synthesis and applications: An overview, J Mol Liq 297 (2020). https://doi.org/10.1016/j.molliq.2019.112038.

[56] M. Armand, F. Endres, D.R. MacFarlane, H. Ohno, B. Scrosati, Ionic-liquid materials for the electrochemical challenges of the future, Nat Mater 8 (2009). https://doi.org/10.1038/nmat2448.

[57] A.J. Greer, J. Jacquemin, C. Hardacre, Industrial Applications of Ionic Liquids, Molecules 25 (2020). https://doi.org/10.3390/molecules25215207.

[58] G.B. Appetecchi, M. Montanino, S. Passerini, Ionic liquid-based electrolytes for high energy, safer lithium batteries, in: ACS Symposium Series, 2012: pp. 67–128. https://doi.org/10.1021/bk-2012-1117.ch004.

[59] H. Ohno, Electrochemical Aspects of Ionic Liquids, 2005. https://doi.org/10.1002/0471762512.

[60] M.A. Navarra, Ionic liquids as safe electrolyte components for Li-metal and Li-ion batteries, MRS Bull 38 (2013) 548–553. https://doi.org/10.1557/mrs.2013.152.

[61] D. Monti, E. Jónsson, M.R. Palacín, P. Johansson, Ionic liquid based electrolytes for sodium-ion batteries: Na+ solvation and ionic conductivity, J Power Sources 245 (2014) 630–636. https://doi.org/10.1016/j.jpowsour.2013.06.153.

[62] K. Vignarooban, R. Kushagra, A. Elango, P. Badami, B.E. Mellander, X. Xu, T.G. Tucker, C. Nam, A.M. Kannan, Current trends and future challenges of electrolytes for sodium-ion batteries, Int J Hydrogen Energy 41 (2016) 2829–2846. https://doi.org/10.1016/j.ijhydene.2015.12.090.

[63] I. Hasa, S. Passerini, J. Hassoun, Characteristics of an ionic liquid electrolyte for sodium-ion batteries, in: J Power Sources, 2016: pp. 203–207. https://doi.org/10.1016/j.jpowsour.2015.10.100.

[64] A.I. Bhatt, I. May, V.A. Volkovich, M.E. Hetherington, B. Lewin, R.C. Thied, N. Ertok, Group 15 quaternary alkyl bistriflimides: Ionic liquids with potential application in electropositive metal

deposition and as supporting electrolytes, Journal of the Chemical Society. Dalton Transactions (2002). https://doi.org/10.1039/b208968h.

[65] S. Panozzo, M. Armand, O. Stéphan, Light-emitting electrochemical cells using a molten delocalized salt, Appl Phys Lett 80 (2002). https://doi.org/10.1063/1.1436534.

[66] P. Wang, S.M. Zakeeruddin, I. Exnar, M. Grätzel, High efficiency dye-sensitized nanocrystalline solar cells based on ionic liquid polymer gel electrolyte, Chemical Communications (2002). https://doi.org/10.1039/b209322g.

[67] J. Fuller, A.C. Breda, R.T. Carlin, Ionic liquid-polymer gel electrolytes from hydrophilic and hydrophobic ionic liquids, Journal of Electroanalytical Chemistry 459 (1998). https://doi.org/10.1016/S0022-0728(98)00285-X.

[68] H. Nakagawa, S. Izuchi, K. Kuwana, T. Nukuda, Y. Aihara, Liquid and Polymer Gel Electrolytes for Lithium Batteries Composed of Room-Temperature Molten Salt Doped by Lithium Salt, J Electrochem Soc 150 (2003). https://doi.org/10.1149/1.1568939.

[69] A. Balducci, W.A. Henderson, M. Mastragostino, S. Passerini, P. Simon, F. Soavi, Cycling stability of a hybrid activated carbon//poly(3-methylthiophene) supercapacitor with N-butyl-N-methylpyrrolidinium bis(trifluoromethanesulfonyl) imide ionic liquid as electrolyte, Electrochim Acta 50 (2005). https://doi.org/10.1016/j.electacta.2004.10.006.

[70] C. Chiappe, D. Pieraccini, Ionic liquids: Solvent properties and organic reactivity, J Phys Org Chem 18 (2005). https://doi.org/10.1002/poc.863.

[71] W. Xu, E.I. Cooper, C.A. Angell, Ionic liquids: Ion mobilities, glass temperatures, and fragilities, Journal of Physical Chemistry B 107 (2003). https://doi.org/10.1021/jp0275894.

[72] G.B. Appetecchi, M. Montanino, M. Carewska, M. Moreno, F. Alessandrini, S. Passerini, Chemical-physical properties of bis(perfluoroalkylsulfonyl)imide-based ionic liquids, Electrochim Acta 56 (2011) 1300–1307. https://doi.org/10.1016/j.electacta.2010.10.023.

[73] J.C. Dearden, The QSAR prediction of melting point, a property of environmental relevance, Science of the Total Environment, The 109–110 (1991). https://doi.org/10.1016/0048-9697(91)90170-J.

[74] Z. Bin Zhou, H. Matsumoto, K. Tatsumi, Cyclic quaternary ammonium ionic liquids with perfluoroalkyltrifluoroborates: Synthesis, characterization, and properties, Chemistry - A European Journal 12 (2006). https://doi.org/10.1002/chem.200500930.

[75] Y. Wang, K. Zaghib, A. Guerfi, F.F.C. Bazito, R.M. Torresi, J.R. Dahn, Accelerating rate calorimetry studies of the reactions between ionic liquids and charged lithium ion battery electrode materials, Electrochim Acta 52 (2007). https://doi.org/10.1016/j.electacta.2007.04.067.

[76] Y. Gao, B. Twamley, ne M. Shreeve, Ionic Liquids: Industrial Applications to Green Chemistry, Freemantle, M. Chem. Eng. News 767 (1914).

[77] V.R. Koch, C. Nanjundiah, G.B. Appetecchi, B. Scrosati, The Interfacial Stability of Li with Two New Solvent-Free Ionic Liquids: 1,2-Dimethyl-3-propylimidazolium Imide and Methide, J Electrochem Soc 142 (1995). https://doi.org/10.1149/1.2044332.

[78] P. Bonĥte, A.P. Dias, N. Papageorgiou, K. Kalyanasundaram, M. Grätzel, Hydrophobic, Highly Conductive Ambient-Temperature Molten Salts, Inorg Chem 35 (1996). https://doi.org/10.1021/ic951325x.

[79] J. Sun, M. Forsyth, D.R. MacFarlane, Room-temperature molten salts based on the quaternary ammonium ion, Journal of Physical Chemistry B 102 (1998). https://doi.org/10.1021/jp981159p.

[80] D.R. Macfarlane, J. Huang, M. Forsyth, Lithium-doped plastic crystal electrolytes exhibiting fast ion conduction for secondary batteries, Nature 402 (1999). https://doi.org/10.1038/45514.

[81] D.R. MacFarlane, P. Meakin, J. Sun, N. Amini, M. Forsyth, Pyrrolidinium imides: A new family of molten salts and conductive plastic crystal phases, Journal of Physical Chemistry B 103 (1999). https://doi.org/10.1021/jp984145s.

[82] P.C. Howlett, D.R. MacFarlane, A.F. Hollenkamp, High lithium metal cycling efficiency in a room-temperature ionic liquid, Electrochemical and Solid-State Letters 7 (2004). https://doi.org/10.1149/1.1664051.

[83] J.H. Shin, W.A. Henderson, S. Passerini, Ionic liquids to the rescue? Overcoming the ionic conductivity limitations of polymer electrolytes, Electrochem Commun 5 (2003). https://doi.org/10.1016/j.elecom.2003.09.017.

[84] J.-H. Shin, W.A. Henderson, S. Passerini, PEO-Based Polymer Electrolytes with Ionic Liquids and Their Use in Lithium Metal-Polymer Electrolyte Batteries, J Electrochem Soc 152 (2005). https://doi.org/10.1149/1.1890701.

[85] W.A. Henderson, S. Passerini, Phase behavior of ionic liquid-LiX mixtures: Pyrrolidinium cations and TFSI- anions, Chemistry of Materials 16 (2004). https://doi.org/10.1021/cm049942j.

[86] H. Matsumoto, H. Sakaebe, K. Tatsumi, Preparation of room temperature ionic liquids based on aliphatic onium cations and asymmetric amide anions and their electrochemical properties as a lithium battery electrolyte, in: J Power Sources, 2005. https://doi.org/10.1016/j.jpowsour.2005.03.103.

[87] G.B. Appetecchi, M. Carewska, M. Montanino, F. Alessandrini, S. Passerini, (Invited) LiFSI-PYR 1A FSI Binary Electrolyte Mixtures for Lithium Batteries , ECS Trans 25 (2010). https://doi.org/10.1149/1.3393839.

[88] Q. Zhou, W.A. Henderson, G.B. Appetecchi, M. Montanino, S. Passerini, Physical and electrochemical properties of N-alkyl-N-methylpyrrolidinium bis(fluorosulfonyl)imide ionic liquids: PY13FSI and PY 14FSI, Journal of Physical Chemistry B 112 (2008). https://doi.org/10.1021/jp805419f.

[89] W.A. Henderson, E. Paillard, Q. Zhou, G. Appetecchi, M. Montanino, S. Passerini, Electrochemical and Physicochemical Properties of PY14FSI-Based Electrolytes with LiFSI, ECS Meeting Abstracts MA2009-01 (2009). https://doi.org/10.1149/ma2009-01/3/122.

[90] L. Conte, G.P. Gambaretto, G. Caporiccio, F. Alessandrini, S. Passerini, Perfluoroalkanesulfonylimids and their lithium salts: Synthesis and characterisation of intermediates and target compounds, J Fluor Chem 125 (2004). https://doi.org/10.1016/j.jfluchem.2003.07.003.

[91] F. Toulgoat, B.R. Langlois, M. Médebielle, J.Y. Sanchez, An efficient preparation of new sulfonyl fluorides and lithium sulfonates, Journal of Organic Chemistry 72 (2007). https://doi.org/10.1021/jo701318n.

[92] G.B. Appetecchi, M. Montanino, D. Zane, M. Carewska, F. Alessandrini, S. Passerini, Effect of the alkyl group on the synthesis and the electrochemical properties of N-alkyl-N-methyl-pyrrolidinium bis(trifluoromethanesulfonyl)imide ionic liquids, Electrochim Acta 54 (2009). https://doi.org/10.1016/j.electacta.2008.09.011.

[93] M. Bellusci, E. Simonetti, M. De Francesco, G.B. Appetecchi, Ionic liquid electrolytes for safer and more reliable sodium battery systems, Applied Sciences (Switzerland) 10 (2020) 6323. https://doi.org/10.3390/APP10186323.

[94] G. Maresca, P. Casu, E. Simonetti, S. Brutti, G.B. Appetecchi, Sodium-Conducting Ionic Liquid Electrolytes: Electrochemical Stability Investigation, Applied Sciences (Switzerland) 12 (2022) 4174. https://doi.org/10.3390/app12094174.

[95] G. Maresca, A. Petrongari, S. Brutti, G. Battista Appetecchi, Outstanding Compatibility of Hard-Carbon Anodes for Sodium-Ion Batteries in Ionic Liquid Electrolytes, ChemSusChem (2023) e202300840. https://doi.org/10.1002/cssc.202300840.

[96] M. Montanino, F. Alessandrini, S. Passerini, G.B. Appetecchi, Water-based synthesis of hydrophobic ionic liquids for high-energy electrochemical devices, Electrochim Acta 96 (2013) 124–133. https://doi.org/10.1016/j.electacta.2013.02.082.

[97] M. De Francesco, E. Simonetti, G. Gorgi, G. Appetecchi, About the Purification Route of Ionic Liquid Precursors, Challenges 8 (2017) 11. https://doi.org/10.3390/challe8010011.

[98] S. Jeong, S. Li, G.B. Appetecchi, S. Passerini, Asymmetric ammonium-based ionic liquids as electrolyte components for safer, high-energy, electrochemical storage devices, Energy Storage Mater 18 (2019) 1–9. https://doi.org/10.1016/j.ensm.2019.01.015.

[99] L. Chancelier, O. Boyron, T. Gutel, C. Santini, Thermal stability of imidazolium-based ionic liquids, French-Ukrainian Journal of Chemistry 4 (2016). https://doi.org/10.17721/fujcv4i1p51-64.

[100] C. Maton, N. De Vos, C. V. Stevens, Ionic liquid thermal stabilities: Decomposition mechanisms and analysis tools, Chem Soc Rev 42 (2013). https://doi.org/10.1039/c3cs60071h.

[101] A. Cimini, O. Palumbo, E. Simonetti, M. De Francesco, G.B. Appetecchi, S. Fantini, R. Lin, A. Falgayrat, A. Paolone, Decomposition temperatures and vapour pressures of selected ionic liquids for electrochemical applications, J Therm Anal Calorim 142 (2020). https://doi.org/10.1007/s10973-020-10334-5.

[102] M. Montanino, M. Moreno, F. Alessandrini, G.B. Appetecchi, S. Passerini, Q. Zhou, W.A. Henderson, Physical and electrochemical properties of binary ionic liquid mixtures: (1 - X) PYR 14TFSI-(x) PYR 14IM 14, Electrochim Acta 60 (2012) 163–169. https://doi.org/10.1016/j.electacta.2011.11.030.

[103] M. Montanino, M. Carewska, F. Alessandrini, S. Passerini, G.B. Appetecchi, The role of the cation aliphatic side chain length in piperidinium bis(trifluoromethansulfonyl)imide ionic liquids, in: Electrochim Acta, 2011. https://doi.org/10.1016/j.electacta.2011.03.089.

[104] Z. Bin Zhou, H. Matsumoto, K. Tatsumi, Low-melting, low-viscous, hydrophobic ionic liquids: Aliphatic quaternary ammonium salts with perfluoroalkyltrifluoroborates, Chemistry - A European Journal 11 (2005). https://doi.org/10.1002/chem.200400817.

[105] N. Terasawa, S. Tsuzuki, T. Umecky, Y. Saito, H. Matsumoto, Alkoxy chains in ionic liquid anions; Effect of introducing ether oxygen into perfluoroalkylborate on physical and thermal properties, Chemical Communications 46 (2010). https://doi.org/10.1039/b916759e.

[106] M. Kunze, E. Paillard, S. Jeong, G.B. Appetecchi, M. Schoönhoff, M. Winter, S. Passerini, Inhibition of self-aggregation in ionic liquid electrolytes for high-energy electrochemical devices, Journal of Physical Chemistry C 115 (2011). https://doi.org/10.1021/jp2055969.

[107] W.A. Henderson, V.G. Young, D.M. Fox, H.C. De Long, P.C. Trulove, Alkyl vs. alkoxy chains on ionic liquid cations, Chemical Communications (2006). https://doi.org/10.1039/b606381k.

[108] M. Kunze, S. Jeong, G.B. Appetecchi, M. Schönhoff, M. Winter, S. Passerini, Mixtures of ionic liquids for low temperature electrolytes, in: Electrochim Acta, 2012. https://doi.org/10.1016/j.electacta.2012.02.035.

[109] M. Moreno, E. Simonetti, G.B. Appetecchi, M. Carewska, M. Montanino, G.-T. Kim, N. Loeffler, S. Passerini, Ionic Liquid Electrolytes for Safer Lithium Batteries, J Electrochem Soc 164 (2017) A6026–A6031. https://doi.org/10.1149/2.0051701jes.

[110] H. Vogel, The law of the relation between the viscosity of liquids and the temperature, Phys. Z. 22 (1921).

[111] G.S. Fulcher, ANALYSIS OF RECENT MEASUREMENTS OF THE VISCOSITY OF GLASSES, Journal of the American Ceramic Society 8 (1925). https://doi.org/10.1111/j.1151-2916.1925.tb16731.x.

[112] G. Tammann, W. Hesse, Die Abhängigkeit der Viscosität von der Temperatur bie unterkühlten Flüssigkeiten, Z Anorg Allg Chem 156 (1926). https://doi.org/10.1002/zaac.19261560121.

[113] S. Slgaryov, Vogel-Fulcher-Tammann behavior of ionic conductivity in KTiOPO4, J Phys D Appl Phys 26 (1993). https://doi.org/10.1088/0022-3727/26/8/028.

[114] J. Serra Moreno, G. Maresca, S. Panero, B. Scrosati, G.B. Appetecchi, Sodium-conducting ionic liquid-based electrolytes, Electrochem Commun 43 (2014) 1–4. https://doi.org/10.1016/j.elecom.2014.02.010.

[115] S. Brutti, M.A. Navarra, G. Maresca, S. Panero, J. Manzi, E. Simonetti, G.B. Appetecchi, Ionic liquid electrolytes for room temperature sodium battery systems, Electrochim Acta 306 (2019) 317–326. https://doi.org/10.1016/j.electacta.2019.03.139.

[116] B.B. Hallac, O.E. Geiculescu, R. V. Rajagopal, S.E. Creager, D.D. DesMarteau, Lithium-conducting ionic melt electrolytes from polyether-functionalized fluorosulfonimide anions, Electrochim Acta 53 (2008). https://doi.org/10.1016/j.electacta.2008.03.061.

[117] F. Toulgoat, B.R. Langlois, M. Médebielle, J.Y. Sanchez, Efficient preparation of new fluorinated lithium and ammonium sulfonimides, Journal of Organic Chemistry 73 (2008). https://doi.org/10.1021/jo800272q.

[118] S. Brutti, E. Simonetti, M. De Francesco, A. Sarra, A. Paolone, O. Palumbo, S. Fantini, R. Lin, A. Falgayrat, H. Choi, M. Kuenzel, S. Passerini, G.B. Appetecchi, Ionic liquid electrolytes for high-voltage, lithium-ion batteries, J Power Sources 479 (2020) 228791. https://doi.org/10.1016/j.jpowsour.2020.228791.

[119] E. Cho, J. Mun, O.B. Chae, O.M. Kwon, H.T. Kim, J.H. Ryu, Y.G. Kim, S.M. Oh, Corrosion/passivation of aluminum current collector in bis(fluorosulfonyl) imide-based ionic liquid for lithium-ion batteries, Electrochem Commun 22 (2012). https://doi.org/10.1016/j.elecom.2012.05.018.

[120] T. Evans, J. Olson, V. Bhat, S.H. Lee, Effect of organic solvent addition to PYR13FSI + LiFSI electrolytes on aluminum oxidation and rate performance of Li(Ni 1/3Mn1/3Co1/3)O2 cathodes, J Power Sources 265 (2014). https://doi.org/10.1016/j.jpowsour.2014.04.138.

[121] R.S. Kühnel, A. Balducci, Comparison of the anodic behavior of aluminum current collectors in imide-based ionic liquids and consequences on the stability of high voltage supercapacitors, J Power Sources 249 (2014). https://doi.org/10.1016/j.jpowsour.2013.10.072.

[122] C.H. Krause, P. Röring, S. Röser, D. Diddens, J.H. Thienenkamp, I. Cekic-Laskovic, G. Brunklaus, M. Winter, Toward adequate control of internal interfaces utilizing nitrile-based electrolytes, Journal of Chemical Physics 152 (2020). https://doi.org/10.1063/5.0003098.

[123] E. Simonetti, G. Maresca, G.B. Appetecchi, G.T. Kim, N. Loeffler, S. Passerini, Towards Li(Ni0.33Mn0.33Co0.33)O2/graphite batteries with ionic liquid-based electrolytes. I. Electrodes'

behavior in lithium half-cells, J Power Sources 331 (2016) 426–434. https://doi.org/10.1016/j.jpowsour.2016.09.078.

[124] J.S. Moreno, Y. Deguchi, S. Panero, B. Scrosati, H. Ohno, E. Simonetti, G.B. Appetecchi, N-Alkyl-N-ethylpyrrolidinium cation-based ionic liquid electrolytes for safer lithium battery systems, Electrochim Acta 191 (2016). https://doi.org/10.1016/j.electacta.2016.01.119.

[125] G.B. Appetecchi, M. Montanino, M. Carewska, M. Moreno, F. Alessandrini, S. Passerini, Chemical-physical properties of bis(perfluoroalkylsulfonyl)imide-based ionic liquids, Electrochim Acta 56 (2011) 1300–1307. https://doi.org/10.1016/j.electacta.2010.10.023.

[126] S. Randström, M. Montanino, G.B. Appetecchi, C. Lagergren, A. Moreno, S. Passerini, Effect of water and oxygen traces on the cathodic stability of N-alkyl-N-methylpyrrolidinium bis(trifluoromethanesulfonyl)imide, Electrochim Acta 53 (2008) 6397–6401. https://doi.org/10.1016/j.electacta.2008.04.058.

[127] S. Doblinger, T.J. Donati, D.S. Silvester, Effect of Humidity and Impurities on the Electrochemical Window of Ionic Liquids and Its Implications for Electroanalysis, Journal of Physical Chemistry C 124 (2020) 20309–20319. https://doi.org/10.1021/acs.jpcc.0c07012.

[128] M. Carboni, J. Manzi, A.R. Armstrong, J. Billaud, S. Brutti, R. Younesi, Analysis of the Solid Electrolyte Interphase on Hard Carbon Electrodes in Sodium-Ion Batteries, ChemElectroChem (2019) 1745–1753. https://doi.org/10.1002/celc.201801621.

[129] C.J. Jafta, X.G. Sun, H. Lyu, H. Chen, B.P. Thapaliya, W.T. Heller, M.J. Cuneo, R.T. Mayes, M.P. Paranthaman, S. Dai, C.A. Bridges, Insight into the Solid Electrolyte Interphase Formation in Bis(fluorosulfonyl)Imide Based Ionic Liquid Electrolytes, Adv Funct Mater 31 (2021). https://doi.org/10.1002/adfm.202008708.

[130] G.M.A. Girard, M. Hilder, N. Dupre, D. Guyomard, D. Nucciarone, K. Whitbread, S. Zavorine, M. Moser, M. Forsyth, D.R. MacFarlane, P.C. Howlett, Spectroscopic Characterization of the SEI Layer Formed on Lithium Metal Electrodes in Phosphonium Bis(fluorosulfonyl)imide Ionic Liquid Electrolytes, ACS Appl Mater Interfaces 10 (2018) 6719–6729. https://doi.org/10.1021/acsami.7b18183.

[131] G.A.O. Tiago, I.A.S. Matias, A.P.C. Ribeiro, L.M.D.R.S. Martins, Application of Ionic Liquids in Electrochemistry-Recent Advances, Molecules 25 (2020). https://doi.org/10.3390/molecules25245812.

[132] M. Armand, P. Axmann, D. Bresser, M. Copley, K. Edström, C. Ekberg, D. Guyomard, B. Lestriez, P. Novák, M. Petranikova, W. Porcher, S. Trabesinger, M. Wohlfahrt-Mehrens, H. Zhang, Lithium-ion batteries – Current state of the art and anticipated developments, J Power Sources 479 (2020) 228708. https://doi.org/10.1016/j.jpowsour.2020.228708.

[133] Y. Miao, P. Hynan, A. Von Jouanne, A. Yokochi, Current li-ion battery technologies in electric vehicles and opportunities for advancements, Energies (Basel) 12 (2019) 1074. https://doi.org/10.3390/en12061074.

[134] S. S. Rangarajan, S.P. Sunddararaj, A.V.V. Sudhakar, C.K. Shiva, U. Subramaniam, E.R. Collins, T. Senjyu, Lithium-Ion Batteries—The Crux of Electric Vehicles with Opportunities and Challenges, Clean Technologies 4 (2022) 908–930. https://doi.org/10.3390/cleantechnol4040056.

[135] F.H. Gandoman, J. Jaguemont, S. Goutam, R. Gopalakrishnan, Y. Firouz, T. Kalogiannis, N. Omar, J. Van Mierlo, Concept of reliability and safety assessment of lithium-ion batteries in electric vehicles: Basics, progress, and challenges, Appl Energy 251 (2019) 113343. https://doi.org/10.1016/j.apenergy.2019.113343.

[136] C. Fang, X. Wang, Y.S. Meng, Key Issues Hindering a Practical Lithium-Metal Anode, Trends Chem 1 (2019) 152–158. https://doi.org/10.1016/j.trechm.2019.02.015.

[137] X. Feng, M. Ouyang, X. Liu, L. Lu, Y. Xia, X. He, Thermal runaway mechanism of lithium ion battery for electric vehicles: A review, Energy Storage Mater 10 (2018) 246–267. https://doi.org/10.1016/j.ensm.2017.05.013.

[138] X. Feng, D. Ren, X. He, M. Ouyang, Mitigating Thermal Runaway of Lithium-Ion Batteries, Joule 4 (2020) 743–770. https://doi.org/10.1016/j.joule.2020.02.010.

[139] X. Su, Q. Wu, J. Li, X. Xiao, A. Lott, W. Lu, B.W. Sheldon, J. Wu, Silicon-Based nanomaterials for lithium-ion batteries: A review, Adv Energy Mater 4 (2014) 1300882. https://doi.org/10.1002/aenm.201300882.

[140] R. Teki, R. Krishnan, T.C. Parker, T.M. Lu, M.K. Datta, P.N. Kumta, N. Koratkar, Nanostructured silicon anodes for lithium Ion rechargeable batteries, Small 5 (2009) 2236–2242. https://doi.org/10.1002/smll.200900382.

[141] J. Schwan, G. Nava, L. Mangolini, Critical barriers to the large scale commercialization of silicon-containing batteries, Nanoscale Adv 2 (2020) 4368–4389. https://doi.org/10.1039/d0na00589d.

[142] C.K. Chan, H. Peng, G. Liu, K. McIlwrath, X.F. Zhang, R.A. Huggins, Y. Cui, High-performance lithium battery anodes using silicon nanowires, Nat Nanotechnol 3 (2008) 31–35. https://doi.org/10.1038/nnano.2007.411.

[143] H. Adenusi, G.A. Chass, S. Passerini, K. V. Tian, G. Chen, Lithium Batteries and the Solid Electrolyte Interphase (SEI)—Progress and Outlook, Adv Energy Mater 13 (2023) 2203307. https://doi.org/10.1002/aenm.202203307.

[144] Q. Liu, T. Meng, L. Yu, S. Guo, Y. Hu, Z. Liu, X. Hu, Interface Engineering to Boost Thermal Safety of Microsized Silicon Anodes in Lithium-Ion Batteries, Small Methods 6 (2022) 2200380. https://doi.org/10.1002/smtd.202200380.

[145] E. Peled, The Electrochemical Behavior of Alkali and Alkaline Earth Metals in Nonaqueous Battery Systems—The Solid Electrolyte Interphase Model, J Electrochem Soc 126 (1979) 2047–2051. https://doi.org/10.1149/1.2128859.

[146] E. Peled, S. Menkin, Review—SEI: Past, Present and Future, J Electrochem Soc 164 (2017) A1703–A1719. https://doi.org/10.1149/2.1441707jes.

[147] J. Shin, T.H. Kim, Y. Lee, E.A. Cho, Key functional groups defining the formation of Si anode solid-electrolyte interphase towards high energy density Li-ion batteries, Energy Storage Mater 25 (2020) 764–781. https://doi.org/10.1016/j.ensm.2019.09.009.

[148] C. Xu, F. Lindgren, B. Philippe, M. Gorgoi, F. Björefors, K. Edström, T. Gustafsson, Improved performance of the silicon anode for li-ion batteries: Understanding the surface modification mechanism of fluoroethylene carbonate as an effective electrolyte additive, Chemistry of Materials 27 (2015) 2591–2599. https://doi.org/10.1021/acs.chemmater.5b00339.

[149] T. Kennedy, M. Brandon, F. Laffir, K.M. Ryan, Understanding the influence of electrolyte additives on the electrochemical performance and morphology evolution of silicon nanowire based lithium-ion battery anodes, J Power Sources 359 (2017) 601–610. https://doi.org/10.1016/j.jpowsour.2017.05.093.

[150] J. Kalhoff, G.G. Eshetu, D. Bresser, S. Passerini, Safer electrolytes for lithium-ion batteries: State of the art and perspectives, ChemSusChem 8 (2015) 2154–2175. https://doi.org/10.1002/cssc.201500284.

[151] D.N.G. Krishna, J. Philip, Review on surface-characterization applications of X-ray photoelectron spectroscopy (XPS): Recent developments and challenges, Applied Surface Science Advances 12 (2022) 100332. https://doi.org/10.1016/j.apsadv.2022.100332.

[152] K. Stokes, T. Kennedy, G.T. Kim, H. Geaney, D. Storan, F. Laffir, G.B. Appetecchi, S. Passerini, K.M. Ryan, Influence of Carbonate-Based Additives on the Electrochemical Performance of Si NW Anodes Cycled in an Ionic Liquid Electrolyte, Nano Lett 20 (2020) 7011–7019. https://doi.org/10.1021/acs.nanolett.0c01774.

[153] J.M. Whiteley, J.W. Kim, D.M. Piper, S.-H. Lee, High-Capacity and Highly Reversible Silicon-Tin Hybrid Anode for Solid-State Lithium-Ion Batteries, J Electrochem Soc 163 (2016) A251–A254. https://doi.org/10.1149/2.0701602jes.

[154] Z. Xu, J. Yang, H. Li, Y. Nuli, J. Wang, Electrolytes for advanced lithium ion batteries using silicon-based anodes, J Mater Chem A Mater 7 (2019) 9432–9446. https://doi.org/10.1039/c9ta01876j.

[155] M. Falco, G. Lingua, M. Destro, L. Silvestri, G. Meligrana, R. Lin, S. Fantini, G. Maresca, A. Paolone, S. Brutti, G.B. Appetecchi, G.A. Elia, C. Gerbaldi, An electrochemical compatibility investigation of RTIL-based electrolytes with Si-based anodes for advanced Li-ion batteries, Materials Today Sustainability 21 (2023) 100299. https://doi.org/10.1016/j.mtsust.2022.100299.

[156] E. Mullane, T. Kennedy, H. Geaney, C. Dickinson, K.M. Ryan, Synthesis of tin catalyzed silicon and germanium nanowires in a solvent-vapor system and optimization of the seed/nanowire interface for dual lithium cycling, Chemistry of Materials 25 (2013) 1816–1822. https://doi.org/10.1021/cm400367v.

[157] H. Geaney, C. Dickinson, C. O'Dwyer, E. Mullane, A. Singh, K.M. Ryan, Growth of crystalline copper silicide nanowires in high yield within a high boiling point solvent system, Chemistry of Materials 24 (2012) 4319–4325. https://doi.org/10.1021/cm302066n.

[158] K. Stokes, H. Geaney, M. Sheehan, D. Borsa, K.M. Ryan, Copper Silicide Nanowires as Hosts for Amorphous Si Deposition as a Route to Produce High Capacity Lithium-Ion Battery Anodes, Nano Lett 19 (2019) 8829–8835. https://doi.org/10.1021/acs.nanolett.9b03664.

[159] E. Mullane, T. Kennedy, H. Geaney, C. Dickinson, K.M. Ryan, Synthesis of tin catalyzed silicon and germanium nanowires in a solvent-vapor system and optimization of the seed/nanowire interface for dual lithium cycling, Chemistry of Materials 25 (2013) 1816–1822. https://doi.org/10.1021/cm400367v.

[160] G.T. Kim, T. Kennedy, M. Brandon, H. Geaney, K.M. Ryan, S. Passerini, G.B. Appetecchi, Behavior of Germanium and Silicon Nanowire Anodes with Ionic Liquid Electrolytes, ACS Nano 11 (2017) 5933–5943. https://doi.org/10.1021/acsnano.7b01705.

[161] W.J. Zhang, Lithium insertion/extraction mechanism in alloy anodes for lithium-ion batteries, J Power Sources 196 (2011) 877–885. https://doi.org/10.1016/j.jpowsour.2010.08.114.

[162] A. Ševčík, Oscillographic polarography with periodical triangular voltage, Collect Czechoslov Chem Commun 13 (1948) 349–377. https://doi.org/10.1135/cccc19480349.

[163] J.E.B. Randles, A cathode ray polarograph. Part II. - The current-voltage curves, Transactions of the Faraday Society 44 (1948) 327–338. https://doi.org/10.1039/TF9484400327.

[164] Q. Ai, D. Li, J. Guo, G. Hou, Q. Sun, Q. Sun, X. Xu, W. Zhai, L. Zhang, J. Feng, P. Si, J. Lou, L. Ci, Artificial Solid Electrolyte Interphase Coating to Reduce Lithium Trapping in Silicon Anode for High Performance Lithium-Ion Batteries, Adv Mater Interfaces 6 (2019) 1–9. https://doi.org/10.1002/admi.201901187.

[165] D.M.R. de Rooij, Electrochemical Methods: Fundamentals and Applications, Anti-Corrosion Methods and Materials 50 (2003). https://doi.org/10.1108/acmm.2003.12850eae.001.

[166] N.G. Tsierkezos, Cyclic voltammetric studies of ferrocene in nonaqueous solvents in the temperature range from 248.15 to 298.15 K, J Solution Chem 36 (2007) 289–302. https://doi.org/10.1007/s10953-006-9119-9.

[167] P. Rama Kant, Theory for staircase voltammetry and linear scan voltammetry onfractal electrodes: Emergence of anomalous Randles-Sevčik behavior, Electrochim Acta 111 (2013) 223–233. https://doi.org/10.1016/j.electacta.2013.07.163.

[168] A. V. Churikov, A. V. Ivanishchev, I.A. Ivanishcheva, V.O. Sycheva, N.R. Khasanova, E. V. Antipov, Determination of lithium diffusion coefficient in LiFePO4 electrode by galvanostatic and potentiostatic intermittent titration techniques, Electrochim Acta 55 (2010) 2939–2950. https://doi.org/10.1016/j.electacta.2009.12.079.

[169] A. V. Churikov, A. V. Ivanishchev, A. V. Ushakov, V.O. Romanova, Diffusion aspects of lithium intercalation as applied to the development of electrode materials for lithium-ion batteries, Journal of Solid State Electrochemistry 18 (2014) 1425–1441. https://doi.org/10.1007/s10008-013-2358-y.

[170] W. Zeng, L. Wang, X. Peng, T. Liu, Y. Jiang, F. Qin, L. Hu, P.K. Chu, K. Huo, Y. Zhou, Enhanced Ion Conductivity in Conducting Polymer Binder for High-Performance Silicon Anodes in Advanced Lithium-Ion Batteries, Adv Energy Mater 8 (2018) 1702314. https://doi.org/10.1002/aenm.201702314.

[171] E. Sivonxay, M. Aykol, K.A. Persson, The lithiation process and Li diffusion in amorphous SiO2 and Si from first-principles, Electrochim Acta 331 (2020) 135344. https://doi.org/10.1016/j.electacta.2019.135344.

[172] G. Wang, B. Xu, J. Shi, M. Wu, H. Su, C. Ouyang, New insights into Li diffusion in Li-Si alloys for Si anode materials: Role of Si microstructures, Nanoscale 11 (2019) 14042–14049. https://doi.org/10.1039/c9nr03986d.

[173] T. Nakajima, H. Groult, Advanced Fluoride-Based Materials for Energy Conversion, 2015. https://doi.org/10.1016/C2013-0-18650-3.

[174] J.R. Macdonald, W.B. Johnson, Fundamentals of Impedance Spectroscopy, in: Impedance Spectroscopy, 2018: pp. 1–20. https://doi.org/10.1002/9781119381860.ch1.

[175] E. Barsoukov, J.R. Macdonald, Impedance Spectroscopy: Theory, Experiment, and Applications, 2005. https://doi.org/10.1002/0471716243.

[176] L.A. Middlemiss, A.J.R. Rennie, R. Sayers, A.R. West, Characterisation of batteries by electrochemical impedance spectroscopy, in: Energy Reports, 2020: pp. 232–241. https://doi.org/10.1016/j.egyr.2020.03.029.

[177] J.R. Macdonald, W.B. Johnson, Fundamentals of Impedance Spectroscopy, in: Impedance Spectroscopy, 2018: pp. 1–20. https://doi.org/10.1002/9781119381860.ch1.

[178] E. Barsoukov, J.R. Macdonald, Impedance Spectroscopy: Theory, Experiment, and Applications, 2005. https://doi.org/10.1002/0471716243.

[179] L.A. Middlemiss, A.J.R. Rennie, R. Sayers, A.R. West, Characterisation of batteries by electrochemical impedance spectroscopy, in: Energy Reports, 2020: pp. 232–241. https://doi.org/10.1016/j.egyr.2020.03.029.

[180] S. Brutti, E. Simonetti, M. De Francesco, A. Sarra, A. Paolone, O. Palumbo, S. Fantini, R. Lin, A. Falgayrat, H. Choi, M. Kuenzel, S. Passerini, G.B. Appetecchi, Ionic liquid electrolytes for high-

voltage, lithium-ion batteries, J Power Sources 479 (2020) 228791. https://doi.org/10.1016/j.jpowsour.2020.228791.

[181] J. Li, J.R. Dahn, An In Situ X-Ray Diffraction Study of the Reaction of Li with Crystalline Si, J Electrochem Soc 154 (2007) A156. https://doi.org/10.1149/1.2409862.

[182] W. Xu, J.C. Flake, Composite Silicon Nanowire Anodes for Secondary Lithium-Ion Cells, J Electrochem Soc 157 (2010) A41. https://doi.org/10.1149/1.3251341.

[183] J. Li, J.R. Dahn, An In Situ X-Ray Diffraction Study of the Reaction of Li with Crystalline Si, J Electrochem Soc 154 (2007) A156. https://doi.org/10.1149/1.2409862.

[184] G.B. Appetecchi, J.H. Shin, F. Alessandrini, S. Passerini, 0.6 Ah Li/V2O5 battery prototypes based on solvent-free PEO-LiN(SO2CF2CF3)2 polymer electrolytes, J Power Sources 143 (2005) 236–242. https://doi.org/10.1016/j.jpowsour.2004.11.039.

[185] G.B. Appetecchi, S. Passerini, Poly(ethylene oxide)-LiN(SO[sub 2]CF[sub 2]CF[sub 3])[sub 2] Polymer Electrolytes, J Electrochem Soc 149 (2002) A891. https://doi.org/10.1149/1.1483098.

[186] T. Hou, G. Yang, N.N. Rajput, J. Self, S.W. Park, J. Nanda, K.A. Persson, The influence of FEC on the solvation structure and reduction reaction of LiPF6/EC electrolytes and its implication for solid electrolyte interphase formation, Nano Energy 64 (2019) 103881. https://doi.org/10.1016/j.nanoen.2019.103881.

[187] B. Philippe, R. Dedryveìre, M. Gorgoi, H. Rensmo, D. Gonbeau, K. Edström, Improved performances of nanosilicon electrodes using the salt LiFSI: A photoelectron spectroscopy study, J Am Chem Soc 135 (2013) 9829–9842. https://doi.org/10.1021/ja403082s.

[188] Z.Y. Wu, L. Deng, J.T. Li, S. Zanna, A. Seyeux, L. Huang, S.G. Sun, P. Marcus, J. Światowska, Solid Electrolyte Interphase Layer Formation on the Si-Based Electrodes with and without Binder Studied by XPS and ToF-SIMS Analysis, Batteries 8 (2022) 271. https://doi.org/10.3390/batteries8120271.

[189] H. Nakai, T. Kubota, A. Kita, A. Kawashima, Investigation of the Solid Electrolyte Interphase Formed by Fluoroethylene Carbonate on Si Electrodes, J Electrochem Soc 158 (2011) A798–A801. https://doi.org/10.1149/1.3589300.

[190] B. Philippe, R. Dedryvère, J. Allouche, F. Lindgren, M. Gorgoi, H. Rensmo, D. Gonbeau, K. Edström, Nanosilicon electrodes for lithium-ion batteries: Interfacial mechanisms studied by hard and soft X-ray photoelectron spectroscopy, Chemistry of Materials 24 (2012) 1107–1115. https://doi.org/10.1021/cm2034195.

[191] J.E. Morales-Ugarte, E. Bolimowska, H. Rouault, J. Santos-Peña, C.C. Santini, A. Benayad, EIS and XPS Investigation on SEI Layer Formation during First Discharge on Graphite Electrode with a Vinylene Carbonate Doped Imidazolium Based Ionic Liquid Electrolyte, Journal of Physical Chemistry C 122 (2018) 18223–18230. https://doi.org/10.1021/acs.jpcc.8b03636.

[192] D.M. Piper, T. Evans, K. Leung, T. Watkins, J. Olson, S.C. Kim, S.S. Han, V. Bhat, K.H. Oh, D.A. Buttry, S.H. Lee, Stable silicon-ionic liquid interface for next-generation lithium-ion batteries, Nat Commun 6 (2015) 6230. https://doi.org/10.1038/ncomms7230.

[193] K. Forster-Tonigold, F. Buchner, J. Bansmann, R.J. Behm, A. Groß, A Combined XPS and Computational Study of the Chemical Reduction of BMP-TFSI by Lithium**, Batter Supercaps 5 (2022) e20220030. https://doi.org/10.1002/batt.202200307.

[194] N. Karimi, M. Zarrabeitia, H. Geaney, K.M. Ryan, B. Iliev, T.J.S. Schubert, A. Varzi, S. Passerini, Stable cycling of Si nanowire electrodes in fluorine-free cyano-based ionic liquid electrolytes enabled

by vinylene carbonate as SEI-forming additive, J Power Sources 558 (2023) 232621. https://doi.org/10.1016/j.jpowsour.2022.232621.

[195] J. Wu, M. Ihsan-Ul-Haq, Y. Chen, J.K. Kim, Understanding solid electrolyte interphases: Advanced characterization techniques and theoretical simulations, Nano Energy 89 (2021) 106489. https://doi.org/10.1016/j.nanoen.2021.106489.

[196] S. Bhattacharyya, J. Hong, G. Turban, Determination of the structure of amorphous nitrogenated carbon films by combined Raman and x-ray photoemission spectroscopy, J Appl Phys 83 (1998) 3917–3919. https://doi.org/10.1063/1.367312.

[197] A.P. Dementjev, A. De Graaf, M.C.M. Van de Sanden, K.I. Maslakov, A. V. Naumkin, A.A. Serov, X-ray photoelectron spectroscopy reference data for identification of the C3N4 phase in carbon-nitrogen films, Diam Relat Mater 9 (2000) 1904–1907. https://doi.org/10.1016/S0925-9635(00)00345-9.

[198] F. Buchner, K. Forster-Tonigold, M. Bozorgchenani, A. Gross, R.J. Behm, Interaction of a Self-Assembled Ionic Liquid Layer with Graphite(0001): A Combined Experimental and Theoretical Study, Journal of Physical Chemistry Letters 7 (2016) 226–233. https://doi.org/10.1021/acs.jpclett.5b02449.

[199] R.I.R. Blyth, H. Buqa, F.P. Netzer, M.G. Ramsey, J.O. Besenhard, P. Golob, M. Winter, XPS studies of graphite electrode materials for lithium ion batteries, Appl Surf Sci 167 (2000) 99–106. https://doi.org/10.1016/S0169-4332(00)00525-0.

[200] C.C. Nguyen, S.W. Song, Characterization of SEI layer formed on high performance Si-Cu anode in ionic liquid battery electrolyte, Electrochem Commun 12 (2010) 1593–1595. https://doi.org/10.1016/j.elecom.2010.09.003.

[201] S. Bhattacharyya, C. Cardinaud, G. Turban, Spectroscopic determination of the structure of amorphous nitrogenated carbon films, J Appl Phys 83 (1998) 4491–4500. https://doi.org/10.1063/1.367211.

[202] L. Martin, H. Martinez, M. Ulldemolins, B. Pecquenard, F. Le Cras, Evolution of the Si electrode/electrolyte interface in lithium batteries characterized by XPS and AFM techniques: The influence of vinylene carbonate additive, Solid State Ion 215 (2012) 36–44. https://doi.org/10.1016/j.ssi.2012.03.042.

[203] U.S. Vogl, S.F. Lux, P. Das, A. Weber, T. Placke, R. Kostecki, M. Winter, The Mechanism of SEI Formation on Single Crystal Si(100), Si(110) and Si(111) Electrodes, J Electrochem Soc 162 (2015) A2281–A2288. https://doi.org/10.1149/2.0361512jes.

[204] R. Dedryvère, L. Gireaud, S. Grugeon, S. Laruelle, J.M. Tarascon, D. Gonbeau, Characterization of lithium alkyl carbonates by X-ray photoelectron spectroscopy: Experimental and theoretical study, Journal of Physical Chemistry B 109 (2005) 15868–15875. https://doi.org/10.1021/jp051626k.

[205] V. Etacheri, U. Geiger, Y. Gofer, G.A. Roberts, I.C. Stefan, R. Fasching, D. Aurbach, Exceptional electrochemical performance of Si-nanowires in 1,3-dioxolane solutions: A surface chemical investigation, Langmuir 28 (2012) 6175–6184. https://doi.org/10.1021/la300306v.

[206] R. Dedryvère, S. Leroy, H. Martinez, F. Blanchard, D. Lemordant, D. Gonbeau, XPS valence characterization of lithium salts as a tool to study electrode/electrolyte interfaces of Li-ion batteries, Journal of Physical Chemistry B 110 (2006) 12986–12992. https://doi.org/10.1021/jp061624f.

[207] H. Kim, S. Grugeon, G. Gachot, M. Armand, L. Sannier, S. Laruelle, Ethylene bis-carbonates as telltales of SEI and electrolyte health, role of carbonate type and new additives, Electrochim Acta 136 (2014) 157–165. https://doi.org/10.1016/j.electacta.2014.05.072.

[208] V. Sharova, A. Moretti, T. Diemant, A. Varzi, R.J. Behm, S. Passerini, Comparative study of imide-based Li salts as electrolyte additives for Li-ion batteries, J Power Sources 375 (2018) 43–52. https://doi.org/10.1016/j.jpowsour.2017.11.045.

[209] G.G. Eshetu, T. Diemant, S. Grugeon, R.J. Behm, S. Laruelle, M. Armand, S. Passerini, In-Depth Interfacial Chemistry and Reactivity Focused Investigation of Lithium-Imide- and Lithium-Imidazole-Based Electrolytes, ACS Appl Mater Interfaces 8 (2016) 16087–16100. https://doi.org/10.1021/acsami.6b04406.

[210] K. Leung, S.B. Rempe, M.E. Foster, Y. Ma, J.M. Martinez del la Hoz, N. Sai, P.B. Balbuena, Modeling Electrochemical Decomposition of Fluoroethylene Carbonate on Silicon Anode Surfaces in Lithium Ion Batteries, J Electrochem Soc 161 (2014) A213–A221. https://doi.org/10.1149/2.092401jes.

[211] D. Ensling, M. Stjerndahl, A. Nytén, T. Gustafsson, J.O. Thomas, A comparative XPS surface study of Li2FeSiO4/C cycled with LiTFSI- and LiPF6-based electrolytes, J Mater Chem 19 (2009) 82–88. https://doi.org/10.1039/b813099j.

[212] M. Nie, B.L. Lucht, Role of Lithium Salt on Solid Electrolyte Interface (SEI) Formation and Structure in Lithium Ion Batteries, J Electrochem Soc 161 (2014) A1001–A1006. https://doi.org/10.1149/2.054406jes.

[213] N.S. Choi, K.H. Yew, K.Y. Lee, M. Sung, H. Kim, S.S. Kim, Effect of fluoroethylene carbonate additive on interfacial properties of silicon thin-film electrode, J Power Sources 161 (2006) 1254–1259. https://doi.org/10.1016/j.jpowsour.2006.05.049.

[214] Q. Li, X. Liu, X. Han, Y. Xiang, G. Zhong, J. Wang, B. Zheng, J. Zhou, Y. Yang, Identification of the Solid Electrolyte Interface on the Si/C Composite Anode with FEC as the Additive, ACS Appl Mater Interfaces 11 (2019) 14066–14075. https://doi.org/10.1021/acsami.8b22221.

[215] C. Bongiorno, G. Mannino, U. D'Alessio, F. Monforte, G.G. Condorelli, C. Spinella, A. La Magna, S. Brutti, On the Redox Activity of the Solid Electrolyte Interphase in the Reduction/Oxidation of Silicon Nanoparticles in Secondary Lithium Batteries, Energy Technology 10 (2022) 2100791. https://doi.org/10.1002/ente.202100791.

[216] M. Marinaro, D. Bresser, E. Beyer, P. Faguy, K. Hosoi, H. Li, J. Sakovica, K. Amine, M. Wohlfahrt-Mehrens, S. Passerini, Bringing forward the development of battery cells for automotive applications: Perspective of R&D activities in China, Japan, the EU and the USA, J Power Sources 459 (2020). https://doi.org/10.1016/j.jpowsour.2020.228073.

[217] N. Rapulenyane, E. Ferg, H. Luo, High-performance Li1.2Mn0.6Ni0.2O2 cathode materials prepared through a facile one-pot co-precipitation process for lithium ion batteries, J Alloys Compd 762 (2018) 272–281. https://doi.org/10.1016/j.jallcom.2018.05.207.

[218] F. Wu, G.T. Kim, M. Kuenzel, H. Zhang, J. Asenbauer, D. Geiger, U. Kaiser, S. Passerini, Elucidating the Effect of Iron Doping on the Electrochemical Performance of Cobalt-Free Lithium-Rich Layered Cathode Materials, Adv Energy Mater 9 (2019). https://doi.org/10.1002/aenm.201902445.

[219] W. Yin, A. Grimaud, G. Rousse, A.M. Abakumov, A. Senyshyn, L. Zhang, S. Trabesinger, A. Iadecola, D. Foix, D. Giaume, J.M. Tarascon, Structural evolution at the oxidative and reductive limits in the first electrochemical cycle of Li1.2Ni0.13Mn0.54Co0.13O2, Nat Commun 11 (2020). https://doi.org/10.1038/s41467-020-14927-4.

[220] S. Muhammad, H. Kim, Y. Kim, D. Kim, J.H. Song, J. Yoon, J.H. Park, S.J. Ahn, S.H. Kang, M.M. Thackeray, W.S. Yoon, Evidence of reversible oxygen participation in anomalously high capacity Li-

and Mn-rich cathodes for Li-ion batteries, Nano Energy 21 (2016). https://doi.org/10.1016/j.nanoen.2015.12.027.

[221] A.R. Armstrong, M. Holzapfel, P. Novk, S. Christopher, S. Kang, M.M. Thackeray, P.G. Bruce, L. Ni, L. Mn, P. Nova, C.S. Johnson, Demonstrating Oxygen Loss and Associated Structural Reorganization in the Lithium Battery Cathode Li [Ni Li Mn] O, JACS 128 (2006). https://doi.org/10.1021/ja062027.

[222] P. Villano, M. Carewska, G.B. Appetecchi, S. Passerini, PEO-LiN(SO[sub 2]CF[sub 2]CF[sub 3])[sub 2] Polymer Electrolytes, J Electrochem Soc 149 (2002). https://doi.org/10.1149/1.1502688.

[223] G.B. Appetecchi, Y. Aihara, B. Scrosati, Investigation of Swelling Phenomena in Poly(ethylene oxide)-Based Polymer Electrolytes:, J Electrochem Soc 150 (2003). https://doi.org/10.1149/1.1544633.

[224] G.B. Appetecchi, J.H. Shin, F. Alessandrini, S. Passerini, 0.6 Ah Li/V2O5 battery prototypes based on solvent-free PEO-LiN(SO2CF2CF3)2 polymer electrolytes, J Power Sources 143 (2005) 236–242. https://doi.org/10.1016/j.jpowsour.2004.11.039.

[225] H. Moriwake, A. Kuwabara, C.A.J. Fisher, Y. Ikuhara, Why is sodium-intercalated graphite unstable?, RSC Adv 7 (2017) 36550–36554. https://doi.org/10.1039/c7ra06777a.

[226] X. Dou, I. Hasa, D. Saurel, C. Vaalma, L. Wu, D. Buchholz, D. Bresser, S. Komaba, S. Passerini, Hard carbons for sodium-ion batteries: Structure, analysis, sustainability, and electrochemistry, Materials Today 23 (2019) 87–104. https://doi.org/10.1016/j.mattod.2018.12.040.

[227] E. Olsson, J. Cottom, H. Au, Z. Guo, A.C.S. Jensen, H. Alptekin, A.J. Drew, M.M. Titirici, Q. Cai, Elucidating the Effect of Planar Graphitic Layers and Cylindrical Pores on the Storage and Diffusion of Li, Na, and K in Carbon Materials, Adv Funct Mater 30 (2020) 1908209. https://doi.org/10.1002/adfm.201908209.

[228] M.Á. Muñoz-Márquez, D. Saurel, J.L. Gómez-Cámer, M. Casas-Cabanas, E. Castillo-Martínez, T. Rojo, Na-Ion Batteries for Large Scale Applications: A Review on Anode Materials and Solid Electrolyte Interphase Formation, Adv Energy Mater 7 (2017) 1700463. https://doi.org/10.1002/aenm.201700463.

[229] X. Dou, I. Hasa, M. Hekmatfar, T. Diemant, R.J. Behm, D. Buchholz, S. Passerini, Pectin, Hemicellulose, or Lignin? Impact of the Biowaste Source on the Performance of Hard Carbons for Sodium-Ion Batteries, ChemSusChem 10 (2017) 2668–2676. https://doi.org/10.1002/cssc.201700628.

[230] E.M. Lotfabad, J. Ding, K. Cui, A. Kohandehghan, W.P. Kalisvaart, M. Hazelton, D. Mitlin, High-density sodium and lithium ion battery anodes from banana peels, ACS Nano 8 (2014) 7115–7129. https://doi.org/10.1021/nn502045y.

[231] H. Hou, X. Qiu, W. Wei, Y. Zhang, X. Ji, Carbon Anode Materials for Advanced Sodium-Ion Batteries, Adv Energy Mater 7 (2017) 1602898. https://doi.org/10.1002/aenm.201602898.

[232] V. Hernndez-Montoya, J. Garca-Servin, J. Ivn, Thermal Treatments and Activation Procedures Used in the Preparation of Activated Carbons, in: Lignocellulosic Precursors Used in the Synthesis of Activated Carbon - Characterization Techniques and Applications in the Wastewater Treatment, 2012. https://doi.org/10.5772/39365.

[233] I.A. Edwards, Introduction to Carbon Science, 1989. https://doi.org/10.1016/c2013-0-04111-4.

[234] G. Hasegawa, K. Kanamori, N. Kannari, J. ichi Ozaki, K. Nakanishi, T. Abe, Hard Carbon Anodes for Na-Ion Batteries: Toward a Practical Use, ChemElectroChem 2 (2015) 1917–1920. https://doi.org/10.1002/celc.201500412.

[235] C. Bommier, W. Luo, W.Y. Gao, A. Greaney, S. Ma, X. Ji, Predicting capacity of hard carbon anodes in sodium-ion batteries using porosity measurements, Carbon N Y 76 (2014) 165–174. https://doi.org/10.1016/j.carbon.2014.04.064.

[236] R. Mogensen, D. Brandell, R. Younesi, Solubility of the Solid Electrolyte Interphase (SEI) in Sodium Ion Batteries, ACS Energy Lett 1 (2016) 1173–1178. https://doi.org/10.1021/acsenergylett.6b00491.

[237] J. Song, B. Xiao, Y. Lin, K. Xu, X. Li, Interphases in Sodium-Ion Batteries, Adv Energy Mater 8 (2018) 1703082. https://doi.org/10.1002/aenm.201703082.

[238] T.M. Bandhauer, S. Garimella, T.F. Fuller, A Critical Review of Thermal Issues in Lithium-Ion Batteries, J Electrochem Soc 158 (2011) R1–R25. https://doi.org/10.1149/1.3515880.

[239] F.A. Soto, P. Yan, M.H. Engelhard, A. Marzouk, C. Wang, G. Xu, Z. Chen, K. Amine, J. Liu, V.L. Sprenkle, F. El-Mellouhi, P.B. Balbuena, X. Li, Tuning the Solid Electrolyte Interphase for Selective Li- and Na-Ion Storage in Hard Carbon, Advanced Materials 29 (2017) 1606860. https://doi.org/10.1002/adma.201606860.

[240] D.A. Stevens, J.R. Dahn, High Capacity Anode Materials for Rechargeable Sodium-Ion Batteries, J Electrochem Soc 147 (2000) 1271. https://doi.org/10.1149/1.1393348.

[241] J.E.B. Randles, A cathode ray polarograph. Part II. - The current-voltage curves, Transactions of the Faraday Society 44 (1948) 327–338. https://doi.org/10.1039/TF9484400327.

[242] A.J. Bard, L.R. Faulkner, Electrochemical Methods: Fundamentals and Applications, 2nd Edition, 2001.

[243] N.G. Tsierkezos, Cyclic voltammetric studies of ferrocene in nonaqueous solvents in the temperature range from 248.15 to 298.15 K, J Solution Chem 36 (2007) 289–302. https://doi.org/10.1007/s10953-006-9119-9.

[244] P. Rama Kant, Theory for staircase voltammetry and linear scan voltammetry onfractal electrodes: Emergence of anomalous Randles-Sevčik behavior, Electrochim Acta 111 (2013) 223–233. https://doi.org/10.1016/j.electacta.2013.07.163.

[245] A. V. Churikov, A. V. Ivanishchev, I.A. Ivanishcheva, V.O. Sycheva, N.R. Khasanova, E. V. Antipov, Determination of lithium diffusion coefficient in LiFePO4 electrode by galvanostatic and potentiostatic intermittent titration techniques, Electrochim Acta 55 (2010) 2939–2950. https://doi.org/10.1016/j.electacta.2009.12.079.

[246] A. V. Churikov, A. V. Ivanishchev, A. V. Ushakov, V.O. Romanova, Diffusion aspects of lithium intercalation as applied to the development of electrode materials for lithium-ion batteries, Journal of Solid State Electrochemistry 18 (2014) 1425–1441. https://doi.org/10.1007/s10008-013-2358-y.

[247] K. Ohishi, D. Igarashi, R. Tatara, S. Nishimura, A. Koda, S. Komaba, J. Sugiyama, Na Diffusion in Hard Carbon Studied with Positive Muon Spin Rotation and Relaxation, ACS Physical Chemistry Au 2 (2022) 98–107. https://doi.org/10.1021/acsphyschemau.1c00036.

[248] D.G. Kizzire, A.M. Richter, D.P. Harper, D.J. Keffer, Lithium and Sodium Ion Binding Mechanisms and Diffusion Rates in Lignin-Based Hard Carbon Models, ACS Omega 6 (2021) 19883–19892. https://doi.org/10.1021/acsomega.1c02787.

[249] S. Alvin, H.S. Cahyadi, J. Hwang, W. Chang, S.K. Kwak, J. Kim, Revealing the Intercalation Mechanisms of Lithium, Sodium, and Potassium in Hard Carbon, Adv Energy Mater 10 (2020) 2000283. https://doi.org/10.1002/aenm.202000283.

[250] J. Huang, Y. Gao, J. Luo, S. Wang, C. Li, S. Chen, J. Zhang, Editors' Choice—Review—Impedance Response of Porous Electrodes: Theoretical Framework, Physical Models and Applications, J Electrochem Soc 167 (2020) 166503. https://doi.org/10.1149/1945-7111/abc655.

[251] M.E. Orazem, B. Tribollet, Electrochemical Impedance Spectroscopy, John Wiley and Sons, 2008. https://doi.org/10.1002/9780470381588.

[252] L. Xiao, Y. Cao, W.A. Henderson, M.L. Sushko, Y. Shao, J. Xiao, W. Wang, M.H. Engelhard, Z. Nie, J. Liu, Hard carbon nanoparticles as high-capacity, high-stability anodic materials for Na-ion batteries, Nano Energy 19 (2016) 279–288. https://doi.org/10.1016/j.nanoen.2015.10.034.

[253] A. Wang, S. Kadam, H. Li, S. Shi, Y. Qi, Review on modeling of the anode solid electrolyte interphase (SEI) for lithium-ion batteries, NPJ Comput Mater 4 (2018). https://doi.org/10.1038/s41524-018-0064-0.

[254] K.L. Hong, L. Qie, R. Zeng, Z.Q. Yi, W. Zhang, D. Wang, W. Yin, C. Wu, Q.J. Fan, W.X. Zhang, Y.H. Huang, Biomass derived hard carbon used as a high performance anode material for sodium ion batteries, J Mater Chem A Mater 2 (2014) 12733–12738. https://doi.org/10.1039/c4ta02068e.

[255] S.J.R. Prabakar, J. Jeong, M. Pyo, Nanoporous hard carbon anodes for improved electrochemical performance in sodium ion batteries, Electrochim Acta 161 (2015) 23–31. https://doi.org/10.1016/j.electacta.2015.02.086.

[256] A. Sadezky, H. Muckenhuber, H. Grothe, R. Niessner, U. Pöschl, Raman microspectroscopy of soot and related carbonaceous materials: Spectral analysis and structural information, Carbon N Y 43 (2005) 1731–1742. https://doi.org/10.1016/j.carbon.2005.02.018.

[257] M. Curcio, S. Brutti, L. Caripoti, A. De Bonis, R. Teghil, Laser irradiation of a bio-waste derived carbon unlocks performance enhancement in secondary lithium batteries, Nanomaterials 11 (2021). https://doi.org/10.3390/nano11123183.

[258] R.F. Susanti, S. Alvin, J. Kim, Toward high-performance hard carbon as an anode for sodium-ion batteries: Demineralization of biomass as a critical step, Journal of Industrial and Engineering Chemistry 91 (2020) 317–329. https://doi.org/10.1016/j.jiec.2020.08.016.

[259] B. Zhang, C.M. Ghimbeu, C. Laberty, C. Vix-Guterl, J.M. Tarascon, Correlation between Microstructure and Na Storage Behavior in Hard Carbon, Adv Energy Mater 6 (2016). https://doi.org/10.1002/aenm.201501588.

[260] J.S. Weaving, A. Lim, J. Millichamp, T.P. Neville, D. Ledwoch, E. Kendrick, P.F. McMillan, P.R. Shearing, C.A. Howard, D.J.L. Brett, Elucidating the sodiation mechanism in hard carbon by operando raman spectroscopy, ACS Appl Energy Mater 3 (2020) 7474–7484. https://doi.org/10.1021/acsaem.0c00867.

[261] X. Shi, W. Zhang, J. Wang, W. Zheng, K. Huang, H. Zhang, S. Feng, H. Chen, (EMIm)+(PF6)− Ionic Liquid Unlocks Optimum Energy/Power Density for Architecture of Nanocarbon-Based Dual-Ion Battery, Adv Energy Mater 6 (2016). https://doi.org/10.1002/aenm.201601378.

[262] H.C. De Long, Ionic Liquid Battery Electrolytes as Sources for Reversible Graphite Intercalation Anodes for Battery Applications, ECS Proceedings Volumes 1994–13 (1994) 736–743. https://doi.org/10.1149/199413.0736pv.

[263] M.C. Lin, M. Gong, B. Lu, Y. Wu, D.Y. Wang, M. Guan, M. Angell, C. Chen, J. Yang, B.J. Hwang, H. Dai, An ultrafast rechargeable aluminium-ion battery, Nature 520 (2015) 325–328. https://doi.org/10.1038/nature14340.

[264] G.G. Eshetu, T. Diemant, S. Grugeon, R.J. Behm, S. Laruelle, M. Armand, S. Passerini, In-Depth Interfacial Chemistry and Reactivity Focused Investigation of Lithium-Imide- and Lithium-Imidazole-Based Electrolytes, ACS Appl Mater Interfaces 8 (2016) 16087–16100. https://doi.org/10.1021/acsami.6b04406.

[265] M. Nie, B.L. Lucht, Role of Lithium Salt on Solid Electrolyte Interface (SEI) Formation and Structure in Lithium Ion Batteries, J Electrochem Soc 161 (2014) A1001–A1006. https://doi.org/10.1149/2.054406jes.

[266] J. Fondard, E. Irisarri, C. Courrèges, M.R. Palacin, A. Ponrouch, R. Dedryvère, SEI Composition on Hard Carbon in Na-Ion Batteries After Long Cycling: Influence of Salts (NaPF 6 , NaTFSI) and Additives (FEC, DMCF), J Electrochem Soc 167 (2020) 070526. https://doi.org/10.1149/1945-7111/ab75fd.

[267] L. Chen, B. Kishore, M. Walker, C.E.J. Dancer, E. Kendrick, Nanozeolite ZSM-5 electrolyte additive for long life sodium-ion batteries, Chemical Communications 56 (2020) 11609–11612. https://doi.org/10.1039/d0cc03976d.

[268] J. Sun, L.A. O'Dell, M. Armand, P.C. Howlett, M. Forsyth, Anion-Derived Solid-Electrolyte Interphase Enables Long Life Na-Ion Batteries Using Superconcentrated Ionic Liquid Electrolytes, ACS Energy Lett 6 (2021) 2481–2490. https://doi.org/10.1021/acsenergylett.1c00816.

[269] G.G. Eshetu, G.A. Elia, M. Armand, M. Forsyth, S. Komaba, T. Rojo, S. Passerini, Electrolytes and Interphases in Sodium-Based Rechargeable Batteries: Recent Advances and Perspectives, Adv Energy Mater 10 (2020). https://doi.org/10.1002/aenm.202000093.

[270] Z. Tang, H. Wang, P.F. Wu, S.Y. Zhou, Y.C. Huang, R. Zhang, D. Sun, Y.G. Tang, H.Y. Wang, Electrode–Electrolyte Interfacial Chemistry Modulation for Ultra-High Rate Sodium-Ion Batteries, Angewandte Chemie - International Edition 61 (2022). https://doi.org/10.1002/anie.202200475.

[271] M. Ma, H. Cai, C. Xu, R. Huang, S. Wang, H. Pan, Y.S. Hu, Engineering Solid Electrolyte Interface at Nano-Scale for High-Performance Hard Carbon in Sodium-Ion Batteries, Adv Funct Mater 31 (2021). https://doi.org/10.1002/adfm.202100278.

[272] J. Meng, G. Jia, H. Yang, M. Wang, Recent advances for SEI of hard carbon anode in sodium-ion batteries: A mini review, Front Chem 10 (2022). https://doi.org/10.3389/fchem.2022.986541.

[273] B. Qin, A. Schiele, Z. Jusys, A. Mariani, T. Diemant, X. Liu, T. Brezesinski, R.J. Behm, A. Varzi, S. Passerini, Highly Reversible Sodiation of Tin in Glyme Electrolytes: The Critical Role of the Solid Electrolyte Interphase and Its Formation Mechanism, ACS Appl Mater Interfaces 12 (2020) 3697–3708. https://doi.org/10.1021/acsami.9b20616.

[274] B. Philippe, R. Dedryvère, J. Allouche, F. Lindgren, M. Gorgoi, H. Rensmo, D. Gonbeau, K. Edström, Nanosilicon electrodes for lithium-ion batteries: Interfacial mechanisms studied by hard and soft X-ray photoelectron spectroscopy, Chemistry of Materials 24 (2012) 1107–1115. https://doi.org/10.1021/cm2034195.

[275] Y. Sato, K. Itoh, R. Hagiwara, T. Fukunaga, Y. Ito, On the so-called "semi-ionic" C-F bond character in fluorine-GIC, Carbon N Y 42 (2004) 3243–3249. https://doi.org/10.1016/j.carbon.2004.08.012.

[276] C. Lee, Y.J. Han, Y.D. Seo, K. Nakabayashi, J. Miyawaki, R. Santamaría, R. Menéndez, S.H. Yoon, J. Jang, C4F8 plasma treatment as an effective route for improving rate performance of natural/synthetic graphite anodes in lithium ion batteries, Carbon N Y 103 (2016) 28–35. https://doi.org/10.1016/j.carbon.2016.02.060.

[277] J.E. Morales-Ugarte, E. Bolimowska, H. Rouault, J. Santos-Peña, C.C. Santini, A. Benayad, EIS and XPS Investigation on SEI Layer Formation during First Discharge on Graphite Electrode with a

Vinylene Carbonate Doped Imidazolium Based Ionic Liquid Electrolyte, Journal of Physical Chemistry C 122 (2018) 18223–18230. https://doi.org/10.1021/acs.jpcc.8b03636.

[278] B. Philippe, R. Dedryveìre, M. Gorgoi, H. Rensmo, D. Gonbeau, K. Edström, Improved performances of nanosilicon electrodes using the salt LiFSI: A photoelectron spectroscopy study, J Am Chem Soc 135 (2013) 9829–9842. https://doi.org/10.1021/ja403082s.

[279] P.C. Howlett, N. Brack, A.F. Hollenkamp, M. Forsyth, D.R. MacFarlane, Characterization of the Lithium Surface in N-Methyl-N-alkylpyrrolidinium Bis(trifluoromethanesulfonyl)amide Room-Temperature Ionic Liquid Electrolytes, J Electrochem Soc 153 (2006) A595. https://doi.org/10.1149/1.2164726.

[280] N. Karimi, M. Zarrabeitia, A. Mariani, D. Gatti, A. Varzi, S. Passerini, Nonfluorinated Ionic Liquid Electrolytes for Lithium Metal Batteries: Ionic Conduction, Electrochemistry, and Interphase Formation, Adv Energy Mater 11 (2021). https://doi.org/10.1002/aenm.202003521.

[281] G.G. Eshetu, T. Diemant, M. Hekmatfar, S. Grugeon, R.J. Behm, S. Laruelle, M. Armand, S. Passerini, Impact of the electrolyte salt anion on the solid electrolyte interphase formation in sodium ion batteries, Nano Energy 55 (2019). https://doi.org/10.1016/j.nanoen.2018.10.040.

[282] T. Wang, D. Legut, Y. Fan, J. Qin, X. Li, Q. Zhang, Building Fast Diffusion Channel by Constructing Metal Sulfide/Metal Selenide Heterostructures for High-Performance Sodium Ion Batteries Anode, Nano Lett 20 (2020) 6199–6205. https://doi.org/10.1021/acs.nanolett.0c02595.

[283] J. Zhang, D.W. Wang, W. Lv, S. Zhang, Q. Liang, D. Zheng, F. Kang, Q.H. Yang, Achieving superb sodium storage performance on carbon anodes through an ether-derived solid electrolyte interphase, Energy Environ Sci 10 (2017) 370–376. https://doi.org/10.1039/c6ee03367a.

[284] A. Ponrouch, R. Dedryvère, D. Monti, A.E. Demet, J.M. Ateba Mba, L. Croguennec, C. Masquelier, P. Johansson, M.R. Palacín, Towards high energy density sodium ion batteries through electrolyte optimization, Energy Environ Sci 6 (2013) 2361–2369. https://doi.org/10.1039/c3ee41379a.

[285] E. Peled, S. Menkin, Review—SEI: Past, Present and Future, J Electrochem Soc 164 (2017). https://doi.org/10.1149/2.1441707jes.

[286] J. Zhang, J. Gai, K. Song, W. Chen, Advances in electrode/electrolyte interphase for sodium-ion batteries from half cells to full cells, Cell Rep Phys Sci 3 (2022). https://doi.org/10.1016/j.xcrp.2022.100868.

[287] G. Maresca, A. Petrongari, S. Brutti, G. Battista Appetecchi, Outstanding Compatibility of Hard-Carbon Anodes for Sodium-Ion Batteries in Ionic Liquid Electrolytes, ChemSusChem (2023) e202300840. https://doi.org/10.1002/cssc.202300840.

[288] P.J.P. Naeyaert, M. Avdeev, N. Sharma, H. Ben Yahia, C.D. Ling, Synthetic, structural, and electrochemical study of monoclinic Na4Ti5O12 as a sodium-ion battery anode material, Chemistry of Materials 26 (2014) 7067–7072. https://doi.org/10.1021/cm5035358.

[289] L. Zhang, H. Bin Wu, X.W. Lou, Iron-oxide-based advanced anode materials for lithium-ion batteries, Adv Energy Mater 4 (2014). https://doi.org/10.1002/aenm.201300958.

[290] T. Lan, J. Dou, F. Xie, P. Xiong, M. Wei, Ultrathin TiO2-B nanowires with enhanced electrochemical performance for Li-ion batteries, J Mater Chem A Mater 3 (2015). https://doi.org/10.1039/c5ta01061f.

[291] Q. Liu, Z. Hu, M. Chen, C. Zou, H. Jin, S. Wang, S.L. Chou, S.X. Dou, Recent Progress of Layered Transition Metal Oxide Cathodes for Sodium-Ion Batteries, Small 15 (2019). https://doi.org/10.1002/smll.201805381.

[292] S. Wang, C. Sun, N. Wang, Q. Zhang, Ni- and/or Mn-based layered transition metal oxides as cathode materials for sodium ion batteries: Status, challenges and countermeasures, J Mater Chem A Mater 7 (2019) 10138–10158. https://doi.org/10.1039/c8ta12441h.

[293] X. Ma, H. Chen, G. Ceder, Electrochemical Properties of Monoclinic NaMnO2, J Electrochem Soc 158 (2011) A1307. https://doi.org/10.1149/2.035112jes.

[294] I.H. Jo, H.S. Ryu, D.G. Gu, J.S. Park, I.S. Ahn, H.J. Ahn, T.H. Nam, K.W. Kim, The effect of electrolyte on the electrochemical properties of Na/α-NaMnO2 batteries, Mater Res Bull 58 (2014) 74–77. https://doi.org/10.1016/j.materresbull.2014.02.024.

[295] J. Manzi, A. Paolone, O. Palumbo, D. Corona, A. Massaro, R. Cavaliere, A.B. Muñoz-García, F. Trequattrini, M. Pavone, S. Brutti, Monoclinic and Orthorhombic NaMnO2 for Secondary Batteries: A Comparative Study, Energies (Basel) 14 (2021) 1230. https://doi.org/10.3390/en14051230.

[296] C. Delmas, C. Fouassier, P. Hagenmuller, Structural classification and properties of the layered oxides, Physica B+C 99 (1980). https://doi.org/10.1016/0378-4363(80)90214-4.

[297] J.P. Parant, R. Olazcuaga, M. Devalette, C. Fouassier, P. Hagenmuller, Sur quelques nouvelles phases de formule NaxMnO2 (x ≤ 1), J Solid State Chem 3 (1971). https://doi.org/10.1016/0022-4596(71)90001-6.

[298] D.M.R. de Rooij, Electrochemical Methods: Fundamentals and Applications, Anti-Corrosion Methods and Materials 50 (2003). https://doi.org/10.1108/acmm.2003.12850eae.001.

[299] R. Usiskin, Y. Lu, J. Popovic, M. Law, P. Balaya, Y.S. Hu, J. Maier, Fundamentals, status and promise of sodium-based batteries, Nat Rev Mater 6 (2021) 1020–1035. https://doi.org/10.1038/s41578-021-00324-w.

[300] I. Moeez, D. Susanto, W. Chang, H.D. Lim, K.Y. Chung, Artificial cathode electrolyte interphase by functional additives toward long-life sodium-ion batteries, Chemical Engineering Journal 425 (2021). https://doi.org/10.1016/j.cej.2021.130547.

[301] Y. Huang, L. Zhao, L. Li, M. Xie, F. Wu, R. Chen, Electrolytes and Electrolyte/Electrode Interfaces in Sodium-Ion Batteries: From Scientific Research to Practical Application, Advanced Materials 31 (2019). https://doi.org/10.1002/adma.201808393.

[302] X. Feng, D.F. Cox, Na Deposition on MnO(100), Surf Sci 645 (2016) 23–29. https://doi.org/10.1016/j.susc.2015.10.041.

[303] X. Feng, D.F. Cox, Oxidation of MnO(100) and NaMnO2 formation: Characterization of Mn2+ and Mn3+ surfaces via XPS and water TPD, Surf Sci 675 (2018) 47–53. https://doi.org/10.1016/j.susc.2018.04.022.

[304] G. Kucinskis, B. Kruze, P. Korde, A. Sarakovskis, A. Viksna, J. Hodakovska, G. Bajars, Enhanced Electrochemical Properties of Na0.67MnO2 Cathode for Na-Ion Batteries Prepared with Novel Tetrabutylammonium Alginate Binder, Batteries 8 (2022). https://doi.org/10.3390/batteries8010006.

[305] J. Wang, S.L. Dreyer, K. Wang, Z. Ding, T. Diemant, G. Karkera, Y. Ma, A. Sarkar, B. Zhou, M. V. Gorbunov, A. Omar, D. Mikhailova, V. Presser, M. Fichtner, H. Hahn, T. Brezesinski, B. Breitung, Q. Wang, P2-type layered high-entropy oxides as sodium-ion cathode materials, Materials Futures 1 (2022). https://doi.org/10.1088/2752-5724/ac8ab9.

[306] C. Wang, L. Xing, J. Vatamanu, Z. Chen, G. Lan, W. Li, K. Xu, Overlooked electrolyte destabilization by manganese (II) in lithium-ion batteries, Nat Commun 10 (2019). https://doi.org/10.1038/s41467-019-11439-8.

[307] Y. Liu, C. Wang, S. Zhao, L. Zhang, K. Zhang, F. Li, J. Chen, Mitigation of Jahn-Teller distortion and Na+/vacancy ordering in a distorted manganese oxide cathode material by Li substitution, Chem Sci 12 (2021) 1062–1067. https://doi.org/10.1039/d0sc05427e.

[308] Z. Zhao, X. Huang, Y. Shao, S. Xu, L. Chen, L. Shi, Q. Yi, C. Shang, D. Zhang, Surface modification of Na0.44MnO2 via a nonaqueous solution-assisted coating for ultra-Stable and High-Rate sodium-ion batteries, Chemical Engineering Journal Advances 10 (2022) 100292. https://doi.org/10.1016/j.ceja.2022.100292.

[309] S. Doubaji, B. Philippe, I. Saadoune, M. Gorgoi, T. Gustafsson, A. Solhy, M. Valvo, K. Edström, Passivation Layer and Cathodic Redox Reactions in Sodium-Ion Batteries Probed by HAXPES, ChemSusChem 9 (2016) 97–108. https://doi.org/10.1002/cssc.201501282.

[310] G. Cherkashinin, K. Nikolowski, H. Ehrenberg, S. Jacke, L. Dimesso, W. Jaegermann, The stability of the SEI layer, surface composition and the oxidation state of transition metals at the electrolyte-cathode interface impacted by the electrochemical cycling: X-ray photoelectron spectroscopy investigation, Physical Chemistry Chemical Physics 14 (2012). https://doi.org/10.1039/c2cp41134b.

[311] S.L. Dreyer, R. Zhang, J. Wang, A. Kondrakov, Q. Wang, T. Brezesinski, J. Janek, The effect of configurational entropy on acoustic emission of P2-type layered oxide cathodes for sodium-ion batteries, JPhys Energy 5 (2023). https://doi.org/10.1088/2515-7655/acd41a.

[312] T. Liu, L. Yu, J. Lu, T. Zhou, X. Huang, Z. Cai, A. Dai, J. Gim, Y. Ren, X. Xiao, M. V. Holt, Y.S. Chu, I. Arslan, J. Wen, K. Amine, Rational design of mechanically robust Ni-rich cathode materials via concentration gradient strategy, Nat Commun 12 (2021). https://doi.org/10.1038/s41467-021-26290-z.

[313] X. Li, L. Liang, M. Su, L. Wang, Y. Zhang, J. Sun, Y. Liu, L. Hou, C. Yuan, Multi-Level Modifications Enabling Chemomechanically Stable Ni-Rich O3-Layered Cathode toward Wide-Temperature-Tolerance Quasi-Solid-State Na-Ion Batteries, Adv Energy Mater 13 (2023). https://doi.org/10.1002/aenm.202203701.

[314] M. Palluzzi, L. Silvestri, A. Celeste, M. Tuccillo, A. Latini, S. Brutti, Structural Degradation of O3-NaMnO2 Positive Electrodes in Sodium-Ion Batteries, Crystals (Basel) 12 (2022). https://doi.org/10.3390/cryst12070885.

9. List of Publications

1. O. Palumbo, A. Sarra, J.B. Brubach, F. Trequattrini, A. Cimini, S. Brutti, G.B. Appetecchi, E. Simonetti, **G. Maresca**, S. Fantini, R. Lin, A. Falgayrat, P. Roy, A. Paolone, So similar, yet so different: the case of the ionic liquids N-trimethyl-N(2-methoxyethyl)ammonium bis(trifluoromethanesulfonyl)imide and N,N-diethyl-Nmethyl-N(2-methoxyethyl)ammonium bis(trifluoromethanesulfonyl)imide. Frontiers in Physics 10, 851279 (2022).
2. **G. Maresca**, P. Casu; E. Simonetti; S. Brutti; G. B. Appetecchi, Sodium-Conducting Ionic Liquid Electrolytes: Electrochemical Stability Investigation. Applied Sciences, 12(9), 4174, (2022).
3. O. Palumbo, G. B. Appetecchi, **G. Maresca**, J.B. Brubach, P. Roy, S. Di Muzio, F. Trequattrini, D. Bordignon, F. Legrand, A. Falgayrat, R. Lin, S. Fantini, A. Paolone. Synthesis, "Physical Properties and Electrochemical Applications of Two Ionic Liquids Containing the Asymmetric (Fluoromethylsulfonyl)(Trifluoromethylsulfonyl)imide Anion", Applied Sciences (2022)/ Special Issue Innovative Materials for Batteries,12(9), 4524 (2022).
4. M. Falco, G. Lingua, M. Destro, L. Silvestri, G. Meligrana, R. Lind, S. Fantini, **G. Maresca**, A. Paolone, S. Brutti, G. B. Appetecchi, G. A. Elia, C. Gerbaldi, "An electrochemical compatibility investigation of {RTIL}-based electrolytes with Si-based anodes for advanced Li-ion batteries", Materials Today Sustainability, 100299 (2022).
5. **G. Maresca**, A. Petrongari, S. Brutti, G.B. Appetecchi, "Outstanding Compatibility of Hard-Carbon Anodes for Sodium-Ion Batteries in Ionic Liquid Electrolytes", ChemSusChem 2023, 16(23), e202300840.
6. **G. Maresca**, A. Sankaran, L.J. Santa Maria, M. Ottaviani, S. Fantini, K.M. Ryan, S. Brutti, G.B. Appetecchi, "Superior compatibility of silicon nanowire anodes in ionic liquid electrolytes", Energy Materials 2024, in press.
7. **G. Maresca**, M. Ottaviani, K.M. Ryan, S. Brutti, G.B. Appetecchi, "Improved compatibility of α-$NaMnO_2$ cathodes in ionic liquid electrolytes", ACS Applied Materials & Interfaces, 2024, submitted.
8. **G. Maresca**, M. Ottaviani, K.M. Ryan, S. Brutti, G.B. Appetecchi, "Physicochemical investigation on the hard carbon interface in ionic liquid interface", in preparation.

10. Conference contributions

1) **G. Maresca**, P. Casu, M. Bellusci, E. Simonetti, S. Brutti, G.B. Appetecchi; Sodium-conducting, ionic liquid electrolytes for Na battery systems. *SCI 2021 - XXVII Congresso Nazionale della Società Chimica Italiana, September 14-23, 2021.*
2) **G. Maresca**, A. Di Schiavi, E. Simonetti, S. Brutti, A. Paolone, O. Palumbo, S. Fantini, R. Lin, P.I. Martin, A. Falgayrat, H. Choi, M. Kuenzel, S. Passerini, A. Sankaran, H. Geaney, K.M. Ryan, G.B. Appetecchi; Compatibility of ionic liquid electrolytes towards large-capacity silicon anodes and high-voltage, lithium-rich, nickel-manganese oxide cathodes. *E-MRS 2021 (European Material Research Society), September 20-23, 2021.*
3) O. Palumbo, A. Sarra, A. Cimini, S. Brutti, G.B. Appetecchi, E. Simonetti, **G. Maresca**, S. Fantini, R. Lin, A. Falgayrat, A. Paolone; Ionic liquids as electrolytes for high voltage Li-ion batteries within the Si-Drive Project: links between the physical properties and the microscopic interactions. *Spring Meeting 2022 of the European Materials Research Society (E-MRS), Virtual Conference, May 30 – June 3, 2022.*
4) N. Carboni, S. Brutti, O. Palumbo, G.B. Appetecchi, **G. Maresca**, Geaney, K.M. Ryan, F. Capitani, F. Borondic, S. Fantini, R. Lin, P.-A. Martin, A. Paolone; SEI formed on Si Nanowire electrodes in ionic liquid electrolytes: a micro-spectroscopic investigation. *32nd Topical Meeting of the International Society of Electrochemistry, Stockholm (Sweden), June 20-22, 2022.*
5) **G. Maresca**, S. Brutti, G.B. Appetecchi; Ionic liquid electrolytes for sodium battery systems. *7th ICNaB 2022 (International Conference on Sodium Batteries) Ulm, Germany, December 5-8, 2022.*
6) **G. Maresca**, S. Brutti, G.B. Appetecchi; Ionic liquid electrolytes for sodium battery systems. *2nd Italian Workshop on Energy Storage (IWES 2023), Bressanone (TN), January 23- 28, 2023.*
7) **G. Maresca**, A. Di Schiavi, S. Brutti, A. Paolone, O. Palumbo, S. Fantini, R. Lin, P.A. Martin, H. Choi, M. Kuenzel, S. Passerini, A. Sankaran, H. Geaney, K.M. Ryan, G.B. Appetecchi; Compatibility of ionic liquid electrolytes towards large-capacity, nanowire, silicon anodes and high-voltage, lithium-rich, nickel-manganese oxide cathodes. *ICTAE (Accumulatori Ca-ione per una TEcnologia Alternativa al litio) Workshop, ENEA – Frascati Research Center, March 31, 2023.*
8) O. Palumbo, N. Carboni, S. Brutti, G.B. Appetecchi, **G. Maresca**, H. Geaney, K. M. Ryan, F. Capitani, S. Fantini, R. Lin, P.-A. Martin, A. Paolone; Impact of the silicon electrode morphology on the solid electrolyte interphase formation using ionic-liquid based electrolytes. *ICTAE*

(Accumulatori Ca-ione per una TEcnologia Alternativa al litio) Workshop, ENEA – Frascati Research Center, March 31, 2023.

9) **G. Maresca**, A. Petrongari, S. Brutti, G.B. Appetecchi; Ionic Liquid Electrolytes for Sodium-Ion Battery Systems. *Giornate dell'Elettrochimica Italiana (GEI) 2023, Cefalù (Italy), September 17-21, 2023.*

10) E. De Santis, M. Mastrandrea, V. Lombardi, L. Silvestri, **G. Maresca**, M. Navarra, A. Rinaldi, R. Araneo, G.B. Appetecchi; Performance of LRNM cathodes in ionic liquid electrolytes**.** *3rd Italian Workshop on Energy Storage (IWES 2024), Rome (Italy), February 7-9, 2024.* 178).

11) **G. Maresca**, M. Ottaviani, K.M. Ryan, S. Brutti, G.B. Appetecchi; Improved compatibility of α-$NaMnO_2$ cathodes in ionic liquid electrolytes. *3rd Italian Workshop on Energy Storage (IWES 2024), Rome (Italy), February 7-9, 2024.*

11. Acknowledgements

This work has been carried out with the financial support of the Si-DRIVE (Silicon Alloying Anodes for High Energy Density Batteries comprising Lithium Rich Cathodes and Safe Ionic Liquid based Electrolytes for Enhanced High VoltagE Performance) European Project (H2020-NMBP-ST-IND-2018, Topic LC-NMBP-30-201), and the ENEA-MISE Program Agreement on Electric System Research, funding by the Italian Ministry of the Economic Development (MISE).

I would like to thank:

- Dr. Paolone of CNR-ISC (Rome) for the TGA measurements on ionic liquids samples.
- Prof. Passerini of KIT-HIU (Germany) for providing LRMN cathodes and carrying out SEM images on Al current collector, and charge/ discharge measurements on Li/LRNM cells.
- Prof. Ryan of University of Limerick (EIRE) for providing Si anodes.

I would like to acknowledge Prof. Kevin M. Ryan for hosting me in his laboratories and the opportunity of working in his research team.

A would like to express my deep gratitude to my supervisor Dr. Giovanni B. Appetecchi of ENEA (Materials and Physicochemical Processes Technical Unit, Rome) for having trust in me, and for his constant support and guidance during all my PhD activity. I would like to thank Dr. Elisabetta Simonetti and Massimo De Francesco of ENEA for making me feel at home even when staying at work.

A special thanks to Prof. Sergio Brutti of La Sapienza University of Rome for the stimulating discussions and valuable suggestions.